Controlling the Self-Assembly and Aggregation of Pre-gelled Low Molecular Weight Gelators

Rebecca Elaine Ginesi

Submitted in fulfilment with the requirements for the Degree of Doctor in Philosophy.

School of Chemistry

College of Science and Engineering

University of Glasgow

May 2024

Declaration of Authorship

This Thesis has been written and compiled by the author, Rebecca Ginesi, who carried out the research at the University of Glasgow between 2020 and 2024 under the supervision of Prof Emily Draper. I declare that, except where explicit reference is made to the contributions of others, this thesis is the result of my own work and has not been submitted for any other degree at the University of Glasgow or any other institution.

Rebecca Elaine Ginesi

Abstract

Hydrogels from low molecular weight gelators (LMWGs) continue to attract notable interest, with many potential applications. However, there are still significant gaps in our understanding of these systems and the correlation between the pre-gel and final gel states. The kinetics of the gelation process play a crucial role in the bulk properties of the hydrogel, presenting an opportunity to fine-tune these systems to meet the requirements of the chosen application. Therefore, it is possible to use a single gelator for multiple applications. In this thesis, we report on the ability to modify the pre-gel structures before triggering gelation to develop materials with a range of interesting properties to suit multiple potential applications.

First, we show how a well-studied amino acid-appended perylene bisimide (PBI) can form diverse hydrogels with distinct mechanical and optical properties. These differences are achieved by adjusting the solubility and aggregate structure, influenced by the initial pH and the history of the solution before gelling. Through the utilisation of small-angle neutron scattering, rheology, ^{1}H NMR spectroscopy, and absorption spectroscopy, we exemplify the impact of initial pH on the gelation kinetics and final gel properties.

We then expand upon previous work, which used heat-cool cycles to alter the properties of LMWG solutions to modulate the self-assembly of three amino acid-appended PBIs. We exemplify the use of heat-cool cycles as a tool for modulating the self-assembly behaviour of amino acid-appended PBIs using small-angle neutron scattering, rheology, and absorption spectroscopy. We determine the impact on the resulting hydrogels and thin films using rheology, nanoindentation, and voltammetry. We find that heating and cooling both influence the aggregation, which consequently changes the resistivity of the resulting films. This work highlights the importance of controlling the temperature of solutions but also opens up more aggregation states, allowing the same molecule to have many different uses.

Finally, we utilise a non-gelling polymer additive to create hydrogels tailored for 3D printing applications. Using rheology and small-angle neutron scattering, we aim to gain a deeper understanding of how printing affects the overall properties of the hydrogels. We demonstrate that upon drying, the resultant xerogels exhibit alignment attributed to the shear force exerted during printing, leading to enhanced film uniformity. Furthermore, these materials display mechanoresponsive behaviour, with an increased photoresponse upon

bending. Consequently, these hydrogels show potential for diverse applications, including wearable sensors and electronics.

Overall, we demonstrate that LMWG systems display a variety of structures in both the solution and gel states, which significantly influences their resulting properties. This work provides a greater understanding of the relationship between gelator structures and the material's bulk properties. Moreover, it challenges the notion that the discovery of new gelator molecules is essential for attaining novel or specific properties.

Acknowledgements

Firstly, my biggest thank you goes to my supervisor, Prof. Emily Draper. If I had not worked with you during my final year project, I would never have done a PhD. Thank you for your constant support and guidance. Your encouragement, excitement, and insight into my research are greatly appreciated. Thank you for being there and supporting me, even when it wasn't about my work. I could not have asked for a better supervisor. I have loved my time in the lab and working with you, and I am grateful for all the amazing opportunities you have given me. There is no doubt in my mind that your help and guidance over the years have shaped me into the scientist I am today.

I would like to thank the University of Glasgow for the opportunities provided to me over the last nine years. My thanks go to all the technical staff, analytical staff, and lecturers I had who made my undergraduate and postgraduate degrees so enjoyable. Thank you to Lucy Parkins and Eilidh Malcolm for always being there for me during my undergraduate degree and celebrating the small wins of my PhD with me.

This experience would not have been the same without all the amazing Draper group members past (Sam, Becky, Gregor, Olivia, Patrick, Kelly, Cara, Jakki, Jess, Joulie, Qayyum, Amina, and David) and present (Bart, Nick, Connor, Ziyao, Ben, and Lineta) who I had the pleasure to work with. Jakki and Becky, thank you for being so welcoming when I first joined the group in my MSci. To Bart Dietrich, thank you for printing anything imaginable and proofreading my thesis. I cannot wait to make millions selling your 3D printed goods. To Nick, thank you for becoming one of my closest friends and being the ray of sunshine you are. To Connor, thank you for your friendship and for celebrating my wins, however small. To Ziyao, thank you for being the sweetest person and cooking amazing food for me to drool over in the office. To Lineta, you have been a perfect addition to the group, and I am sad we did not get to spend more of our PhDs together.

I would like to give a special thanks to Chloe Wallace for being the most amazing flatmate and best friend. Thank you for being my rock during my PhD and placement in Canada and supporting me during the tough times. I cannot imagine going through this without you and cannot think of anyone better to have started and finished my PhD with. I am extremely proud of you and everything you have achieved.

I would also like to thank the Adams group (Ana, Lisa, Dan, Courtenay, Libby, Chloe, Max, Qingwen, Simona, Rui, Maria Laura, Emma, and Fin) for being a huge part of my PhD. Lisa – you were such an inspiration to me, and I thoroughly enjoyed our time working together. Courtenay – thank you for your friendship and for always being there for me no matter what. Libby – you are such a talented scientist and a great friend, and your positivity made every day in the lab enjoyable. Max – thank you for checking in on me and getting excited whenever I showed you my work.

I would also like to thank Dr James Doutch, Dr Najet Mahmoudi, and Dr Robert Dalgliesh for their help with my trips down to ISIS Neutron and Muon Source and for providing support during and after my beam times.

Thank you to Prof. Gregory Welch from the University of Calgary for your support during my placement and guidance on my next steps. I would also like to say a massive thank you to Prof. Dave Adams for his help, guidance, and support throughout my MSci and PhD. Thank you for your help with many of my scattering experiments.

Despite not being directly involved in my PhD, I would like to thank my school friends for their constant support. A special thank you to Colette and Natasha for always checking in on me and their continued friendship.

Finally, thank you to my family (Mum, Dad, Emma, Lucy, Gran, Granda, and Nana) for being so supportive throughout my degree. To my parents, Elaine and David, thank you for everything you have done for me. Thank you for always believing in me and pushing me to success. You are my biggest supporters, and I hope I have made you proud.

List of Publications from This Degree

1. **R. E. Ginesi**, T. Jacquin, J. Doutch, M. Amjadi and E. R. Draper, 3D Printing for Aligned and Flexible Perylene Bismide/Polymer Hydrogel Devices, manuscript in preparation.

2. **R. E. Ginesi**, F. Angus, J. Doutch, P. Docampo and E. R. Draper, The impact of heat-cool processing on the behaviour and properties of perylene bisimides, manuscript in preparation.

3. **R. E. Ginesi** and E. R. Draper, Methods of changing low molecular weight gel properties through gelation kinetics, *Soft Matter*, 2024, **20**, 3887-3896.

4. T. A. Gudmundsson, G. Kuppadakkarth, D. Ghosh, M. Ruether, A. Seddon, **R. E. Ginesi**, J. Doutch, D. J. Adams, T. Gunnlaugsson and K. K. Damodaran, Nanoscale Assembly of Enantiomeric Supramolecular Gels Driven by the Nature of Solvents, *Nanoscale*, 2024, **16**, 8922-8930.

5. X. Karagiorgis, D. Shakthivel, G. Khandelwal, **R. E. Ginesi**, P. Skabara and R. Dahiya, Highly conductive PEDOT:PSS – Ag Nanowires based nanofibres for transparent flexible electronics, *ACS Appl. Mater. Interfaces*, 2024, **16**, 19551-19562.

6. J. A. M. Jimenez, J. G. Egan, R. I. Randle, A. O. Rezig, B. Orimolade, **R. E. Ginesi**, R. Schweins, M. O. Riehle and E. R. Draper, Tuning conductivity whilst maintaining mechanical properties in perylene bisimide hydrogels at physiological pH, *Chem. Comm.*, 2024, **60**, 3027-3030.

7. **R. E. Ginesi**, M. R. Niazi, G. C. Welch and E. R. Draper, All slot-die coated organic solar cells using a water/amine processed cathode interlayer based upon an amino acid functionalized perylene bisimide, *RSC Appl. Interfaces*, 2024, **1**, 323-328.

8. T. A. Welsh, J. G. Egan, B. Dietrich, N. Rafferty, **R. E. Ginesi**, J. Doutch, R. Schweins and E. R. Draper, The Effects of Amino Acid Functionalisation on the Optoelectronic Properties and Self-Assembly of Perylene Bisimides, *J. Phys. Mater.*, 2024, **7**, 015004.

9. L. J. Marshall, S. Bianco, **R. E. Ginesi**, J. Doutch, E. R. Draper and D. J. Adams, Investigating multigelator systems across multiple length scales, *Soft Matter*, 2023, **19**, 4972-4981.

10. H. Nassar, G. Khandelwal, R. Chirila, X. Karagiorgis, **R. E. Ginesi,** A. S. Dahiya and R. Dahiya, Fully 3D printed piezoelectric pressure sensor for dynamic tactile sensing, *Addit. Manuf.*, 2023, **71**, 103601.

11. L. Thomson, **R. E. Ginesi**, D. Osborne, E. R. Draper and D. J. Adams, Photothermal Perylene Bisimide Hydrogels, *Eur. J. Chem.*, 2023, e202300663.

12. **R. E. Ginesi**, N. R. Murray, R. M. Dalgliesh, J. Doutch and E. R. Draper, Using Solution History to Control Hydrogel Properties of a Perylene Bisimide, *Chem. Eur. J.*, 2023, e202301042.

13. R. I. Randle, **R. E. Ginesi**, O. Matsarskaia, R. Schweins and E. R. Draper, Process dependent complexity in multicomponent gels, *Macromol. Rapid Commun.*, 2023, **44**, 2200709.

Table of Contents

List of Abbreviations

°C	Degrees Celsius
δ	Chemical shift
θ	Scattering angle
μL	Microlitres
μN	Micronewton
1D	One dimensional
^{1}H	Proton
^{13}C	Carbon
2Nap	2-Napthoxyacetic acid
3D	Three dimensional
A	Alanine amino acid
Å	Angstrom
AFM	Atomic force microscopy
aq	Aqueous
ArH	Aromatic hydrogen
au	Arbitrary units
br	Broad
cm	Centimetre
CP	Cone-plate
CV	Cyclic voltammetry
D_2O	Deuterated water
DMF	*N*-*N*-Dimethylformamide
DMSO	Dimethyl sulfoxide
DMSO-d_6	Deuterated DMSO
E_{IT}	Indentation modulus
ESI	Electrospray ionisation
et al.	And others
eq	Equivalent
F	Phenylalanine amino acid
FF	Fill factor
Fig.	Figure
Fmoc	Fluorenylmethyloxycarbonyl

FTO	Fluorine-doped tin oxide
g	Gram
G′	Storage modulus
G″	Loss modulus
GdL	Glucono-δ-lactone
H	Histidine amino acid
HCl	Hydrochloric acid
H_{IT}	Indentation hardness
HRMS	High resolution mass spectrometry
HTM	Hole transporting material
IPA	Isopropyl alcohol
IR	Infrared
J	Coupling constant
J_{SC}	Short circuit current density
K	Kelvin
L	Leucine amino acid
LED	Light emitting diiode
LMWG	Low molecular weight gelator
M	Molar
m	Metres
mA	Milliamps
MAI	Methylammonium
MAPI	Methylammonium lead iodide
mBar	Millibar
MeOH	Methanol
mg	Milligram
MHz	Megahertz
min	Minutes
mL	Millilitre
mm	Millimetre
M_n	Number average molecular weight
MRI	Magnetic resonance imaging
N	Normal force

N/A	Not applicable
NaCl	Sodium chloride
NaOD	Sodium deuteroxide
NaOH	Sodium hydroxide
NDI	Naphthalene diimide
NIST	National Institute of Standards and Technology
nm	Nanometre
NMR	Nuclear magnetic resonance
Pa	Pascal
PBI	Perylene bisimide
PCE	Power conversion efficiency
PEG	Poly(ethylene) glycol
PEO	Poly(ethylene) oxide
PP	Parallel plate
ppm	Parts per million
PTCDA	Perylene-3,4-9,10-tetracarboxylic dianhydride
PVA	Poly(vinyl) alcohol
Q	Scattering vector
rad	Radian
rpm	Revolutions per minute
s	Seconds
SANS	Small-angle neutron scattering
SAXS	Small-angle X-ray scattering
SEM	Scanning electron microscopy
SLD	Scattering length density
TEM	Transmission electron microscopy
T_{gel}	Gelation temperature
UV	Ultraviolet
UV-vis	Ultraviolet-visible
V	Volts
vs.	Versus
V_{OC}	Open-circuit voltage
Y	Tyrosine amino acid

Chapter 1: Introduction

This Chapter is adapted from the following publication:

“Methods of changing low molecular weight gel properties through gelation kinetics”.

R. E. Ginesi and E. R. Draper, *Soft Matter*, 2024, **20**, 3887-3896.

REG was responsible for researching, creating figures, and writing the publication. ERD supervised the project. REG wrote the initial draft of the manuscript, to which both authors contributed for the final publication.

1.1 Hydrogels

Hydrogels are a class of soft materials that continue to attract significant interest.[1,2] They are used in many applications, such as sensing,[3] cosmetics,[4] electronics,[5] and the food and pharmaceutical industries.[6,7] Hydrogels exhibit solid-like behaviour despite containing a substantial fraction of water.[8] Such solid-like properties arise from a cross-linked network which entraps the water by surface tension effects. More commonly, these networks are formed from cross-linked polymers or biopolymers.[8] Polymeric hydrogels are formed when long polymer chains are either chemically cross-linked or entangled to form physical cross-links. The covalent bonds formed in chemically cross-linked hydrogels result in robust and irreversible materials. Another route to form hydrogels is to use low molecular weight gelators (LMWGs). LMWGs can self-assemble to form entangled gel networks governed by various non-covalent interactions.[2,9–12] Compared to polymer hydrogels, LMWGs possess discrete molecular components and well-defined chemical structures.[13] As such, it is possible to tune these materials at the molecular level more easily and thus control the resulting gel properties.[14–16] Such control is crucial since the gel properties determine the applications for which the gel is suitable. Furthermore, some LMWGs can actively contribute to the functionality of the material.[3,17–21]

1.2 Low Molecular Weight Gelators

When forming hydrogels from LMWGs, the molecules are initially molecularly dissolved or dispersed in water (Fig. 1.1).[8] A trigger or stimulus is then applied, resulting in a decrease in solubility of the gelator. As the LMWG becomes less soluble, the molecules assemble into 1D structures to minimise their interactions with the water, driven by the hydrophobic effect. Further interactions occur between these 1D structures, causing entanglement and association to form a 3D network which entraps the solvent. This self-assembly process is driven by the formation of non-covalent interactions, such as hydrogen bonding, electrostatic forces, van der Waals forces, π-π stacking, and the hydrophobic effect.[22,23] These interactions allow the gelation process to be reversible compared to the often irreversible gelation of polymeric hydrogels. This reversibility is crucial for applications such as the controlled release of guest molecules or sensors.[24,25] Such weak forces may also allow the gels to recover upon breaking.[26] This thixotropic behaviour presents an opportunity to use these gels in 3D printing or other processing techniques. Overall, the self-assembly process to form these supramolecular hydrogels is still poorly understood due to the inability to predict

whether a molecule will form a gel or what conditions are necessary to favour gelation over crystallisation. It has been suggested that one could use crystal structures and crystal engineering to inform design. However, this method may not be accurate, as it has been shown that the crystal phase and gel phase are different.[27]

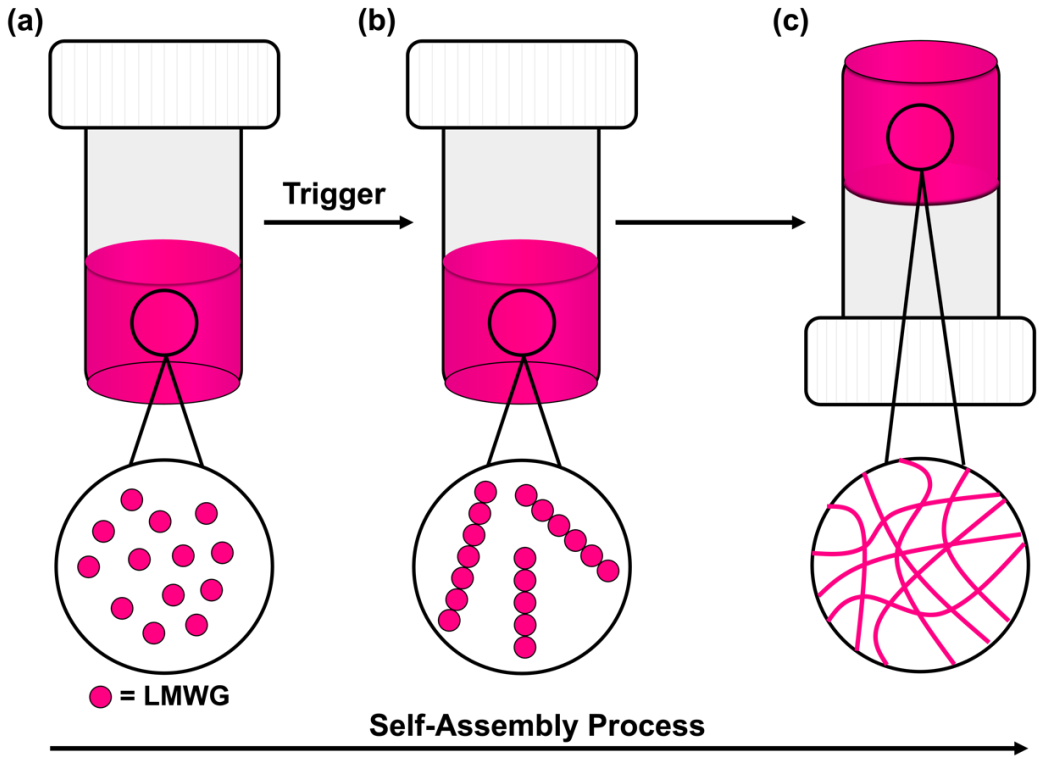

Figure 1.1. Typical schematic for gelation using a LMWG. (a) The LMWG is initially suspended in the solvent. (b) A trigger is applied, which reduces the solubility of the LMWG, resulting in the formation of 1D structures. (c) When these structures become sufficiently long and are in a high enough concentration, entanglement or other cross-linking leads to the formation of a network to give a self-supporting gel. Figure adapted from Reference 8.

1.2.1 Gelation Triggers

As discussed above, the self-assembly to form supramolecular hydrogels is induced by a trigger which changes the environment of the LMWG from one in which it is relatively soluble to one in which it is insoluble.[28] Several triggers exist, such as heat-cool cycles,[29,30] addition of an enzyme,[31,32] solvent-switch,[33,34] change in pH,[35,36] or addition of metal salts.[37,38] The choice of gelation trigger can also impact the networks formed and thus the properties of the bulk gel.[39]

Temperature-triggered gelation requires the gelator to be soluble in a solvent at high temperatures and insoluble with a decrease in temperature.[40] When lowered to the gelation

temperature (T_{gel}), the solvent is immobilised to form the gel.[9] The properties of these hydrogels can be tuned by altering the kinetics of the cooling process, the gelator concentration, and the pH of the water or solvent mixture used.

Enzymatic triggers work by synthesising the gelator *in situ*, either by reacting two soluble precursors or cleaving a solubilising group from a precursor molecule.[41–43] When using enzymes, the pH and temperature of the environment must be considered to ensure the enzyme is not denatured.[44] Here, the properties of the resulting gels are determined by the rate at which the enzyme produces the gelator. When less enzyme is present, it has been shown that the assembly affords more uniform fibres and reproducible gels due to slower gelation kinetics. In comparison, high enzyme concentrations produce gels more rapidly, resulting in stiffer gels.[44]

Solvent-triggered hydrogels require a water-miscible organic solvent in which the LMWG is soluble, followed by the rapid addition of an anti-solvent, again reducing the solubility and inducing self-assembly.[45,46] The properties of these gels are determined by the ratio of the two solvents, the pH of the water, and the concentration of the gelator.[46]

A pH trigger can be used when a LMWG has functional groups that can be protonated and deprotonated, such as carboxylic acids and amines.[47] For carboxylic acid groups, the LMWG is freely dissolved in water above the "apparent" pK_a of the gelator. When an acid is added to lower the pH below this pK_a, the carboxylate is re-protonated, decreasing the solubility of the gelator and inducing self-assembly.[48,49] Again, the final properties are controlled by the kinetics of the decrease in pH and concentration of the gelator.[48,50,51]

In comparison, chelation of divalent metal ions from salts such as calcium chloride increases the strength of the ionic interactions between pre-formed fibres.[52] As the fibres must already have formed, this gelation process depends on the presence of worm-like micelles. The self-assembly of these micelles can be altered by the valence and concentration of the chosen metal ion, pH of the water, and gelator concentration.[53]

In this thesis, pH-triggered gels were prepared using glucono-δ-lactone (GdL). GdL hydrolysis to gluconic acid is slower than its dissolution in water, resulting in a uniform change in pH throughout the system (Fig. 1.2).[48] As such, a homogenous mixture forms,

which allows for uniform and reproducible gels to be produced. This is a well-studied process to produce hydrogels. The properties of these hydrogels can be controlled by the amount of GdL added to a solution, the temperature at which gelation occurs, the starting pH of the solution, the final pH of the gel, and the concentration of the gelator used.

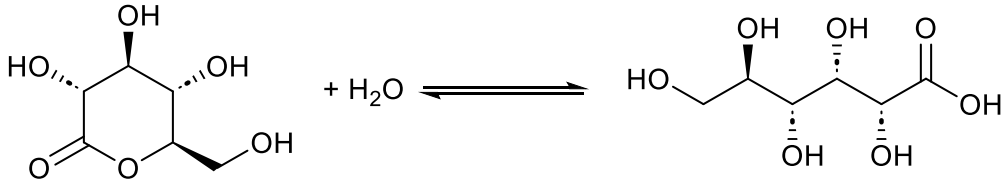

Figure 1.2. Hydrolysis of glucono-δ-lactone in water to form gluconic acid.

1.2.2 Gelator Design

The design of LMWG is crucial for creating hydrogels with desired properties for a particular application. However, LMWGs are commonly discovered through serendipity.[54,55] Therefore, designing these materials is difficult, since it can be challenging to predict whether a molecule will gel.[56] There are some typical features of LMWGs. For example, to self-assemble in water, these molecules must contain both hydrophilic and hydrophobic regions to balance solubility and hydrophobicity.[57] This balance is crucial, as if the LMWG is too hydrophobic, precipitation will be favoured over gelation. In comparison, if the LMWG is too soluble in the chosen solvent, there will be no driving force for self-assembly.

Typically, water soluble LMWGs are based upon molecules such as amino acids,[58] peptide amphiphiles,[59] saccharides,[60] nucleobases,[57] perylene bisimides,[61] and naphthalene diimides.[62] However, even slight modifications in their structures are known to significantly impact their ability to gel. For example, changing the sequence or chirality of amino acids within a gelator can impact or prevent gelation.[63,64] It is also impossible to change only one parameter of a gelator at a time, as changing functional groups can alter sterics, hydrophobicity, solubility, and hydrogen bonding.[11]

Recently, computational models have been used to identify dipeptide gelators that can successfully form gels.[63,65] However, some predictors require the synthesis of a library of materials and screening, making them time- and labour-intensive. Furthermore, using models to predict gel properties is limited because of the pathway dependence of gelation.[66–68] Therefore, there is a need to better understand the assembly process and correlate the precursor, assembly conditions, and self-assembled structures.[8]

1.2.3 Characterisation of LMWGs over Multiple Length Scales

As various length scales are associated with the self-assembly process of LMWGs (Fig. 1.3), it is crucial to characterise the properties of the solutions and corresponding gels at different length scales.[2,11] However, care must be taken, as each technique has its own advantages and disadvantages. Ideally, each analysis should occur at the same concentration since self-assembly is concentration dependent.[69,70] This brings about its own issues, as factors such as sample vessel size and surface chemistry can also impact self-assembly and gelation.[8,56,71] For example, gels constrained in thin cuvettes will likely have a different network to those prepared in plastic vials. Therefore, it is important to use multiple techniques to fully understand these systems.

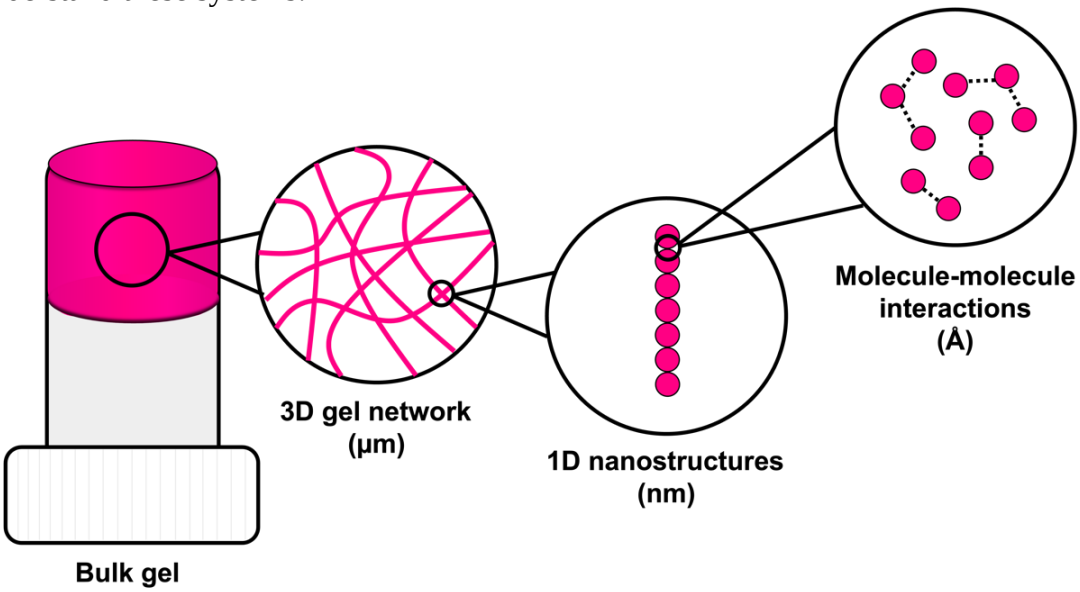

Figure 1.3. Schematic of the various length scales associated with the self-assembly and gelation of LMWGs.

The molecular packing and self-assembly can be probed using spectroscopic techniques, including UV-visible (UV-vis) absorption,[72,73] infrared (IR),[74] and nuclear magnetic resonance (NMR) spectroscopy.[75,76] Furthermore, these techniques can also be used to study the kinetics of the self-assembly process.[76–78]

The morphology and size of 1D structures are typically determined using imaging techniques, such as scanning electron microscopy (SEM), transmission electron microscopy (TEM), or confocal microscopy.[79] However, for TEM and SEM, the samples must be dried, which can result in drying artefacts or changes in the structure lengths and morphologies.[80,81] Therefore, it is possible to use cryo-TEM, which allows analysis of structures in their hydrated form.[82] However, the low film thickness used makes it difficult to capture the 3D

gel network.[83] When using confocal microscopy, this requires the addition of a dye or synthesis of a dye-functionalised LMWG, which can also impact the self-assembly process.[56]

Small-angle x-ray scattering (SAXS) or small-angle neutron scattering (SANS) are preferred for characterising the fibre-level assembly of LMWGs, as both techniques are non-destructive and allow characterisation on solvated bulk samples.[84] In this technique, a beam of x-rays or neutrons is fired at the sample (Fig. 1.4).[85,86] For SANS, neutrons interact with the nucleus of atoms, whilst x-rays interact with the electrons in SAXS.[87] However, both techniques are comparable in terms of the Huygens-like description of wave propagation. The scattering from x-rays is proportional to the size of the atom, whereas neutron scattering is not. The angle of scattering (θ) is inversely related to the size of the object. Thus, larger objects scatter to smaller angles. Small-angle scattering probes structures of the order of 1-100 nm in size. The scattering intensity is measured as a function of the scattering vector, Q. Another way in which neutron and x-ray scattering differ is with the scattering magnitude. With x-rays, this is dependent on the scattering angle, whereas with neutrons it is not. Most of the radiation is transmitted through the sample without interaction and blocked from hitting the detector by a beamstop. However, a small proportion of the radiation interacts with the sample, is elastically scattered, and measured by a 2D detector. The intensity is related to the difference in the scattering length density (SLD) between the scattering object and the solvent. For neutron scattering, the difference between the SLD of hydrogen and deuterium is exploited, with deuterium being essentially invisible to neutrons. Therefore, deuterated solvents are used for good contrast. For x-ray scattering, this contrast comes from the difference in electron density. The scattering data can be fitted to mathematical models to deduce information about the length, radius, and flexibility of the secondary structures formed during self-assembly.[85]

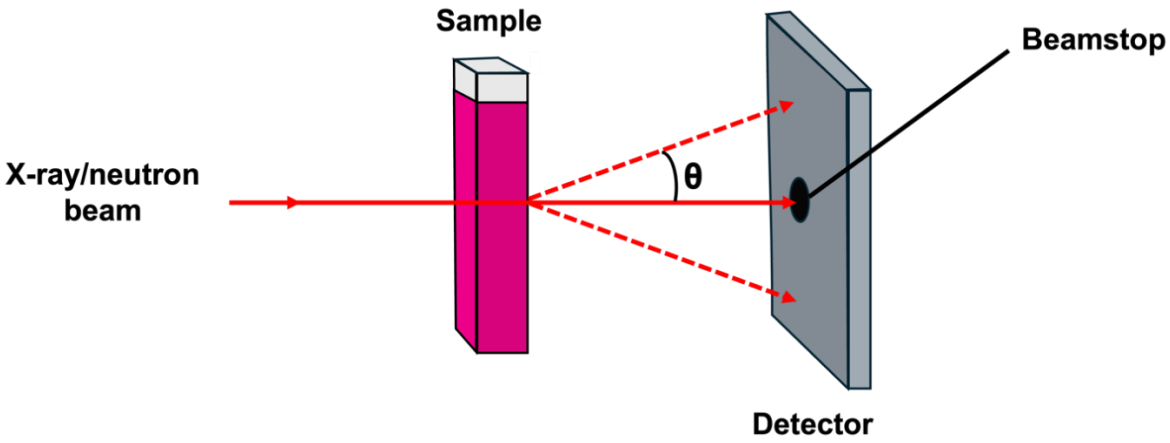

Figure 1.4. Schematic showing a typical small-angle scattering experiment. Figure adapted from Reference 86.

There are many advantages and disadvantages of both SANS and SAXS, which depend on factors such as the type of sample and the requirements of the experiment. For example, some biological molecules are more susceptible to damage from x-rays than neutrons.[88] An advantage of SAXS over SANS is it has a high flux, allowing measurements to be performed within seconds. The length of a SANS measurement is much longer, with the timescale depending on the number of neutrons available and how well the sample scatters. Therefore, SAXS is preferential when measuring a large number of samples or kinetics over short periods. In comparison, SANS kinetic experiments are more suited to study *in situ* processes occurring over several hours or overnight due to better penetration of the neutrons compared to x-rays.[89]

Some samples can have different properties in D_2O than H_2O,[90] meaning SANS data may not be comparable to other experimental data collected in H_2O or be totally representative of the sample. Selectively deuterated SANS experiments, also known as contrast matching, involve deuterating molecules (or parts of molecules) or altering the ratio of D_2O and H_2O in the solvent. This renders the deuterated component effectively invisible, removing any scattering contribution from this component, and allows for in-depth analysis of multicomponent systems,[91] or monitoring gelation processes.[85]

Scattering experiments can also be used in combination with other techniques, such as rheology (rheo-SANS or rheo-SAXS)[85,92] or electrochemistry,[93] allowing changes to be monitored *in situ*. However, one caveat of scattering techniques is that they require access to a beamline, often in advanced and large facilities. Scattering techniques also require a lot more training and experience. Each scattering pattern is reduced to give a 2D graph

representation. This data then needs fitting to a model to reveal what structures are present. This analysis is much more difficult to do than that for a microscopy image, for example.

The bulk mechanical properties of gels are measured using rheology.[94–97] The rheological properties of supramolecular gels are determined by the morphology, mechanical strength, flexibility, and distribution in space of the primary fibres of the gel network.[83] Gels are considered viscoelastic materials as they exhibit both flow and elastic behaviour.[98] During rheological measurements, the storage modulus (G′, a measure of the material's elastic response and how "solid-like" a material is) and the loss modulus (G″, a measure of the ability of the material to flow under stress and how "liquid-like" a material is) are collected. For a material to be viscoelastic, G′ must greater than G″, *i.e.*, the energy stored by the material must be greater than the energy dissipated.[99] Furthermore, when G′ is an order of magnitude larger than G″, and the G″/G′ value (defined as tanδ) is less than 0.1, the material can be considered a "true gel".[2,100] However, it is common for tanδ to be slightly greater than 0.1 for supramolecular gels owing to the non-covalent interactions that hold the gel network together. A strain test can measure how much strain is required to deform the gel, thus determining how strong the gel is. The strain percentage at which the gel breaks is the point where G′ deviates from linearity and is defined as the yield point. The flow point describes when G′ falls below G″, resulting in gel breakdown. Frequency sweeps can be used to see how the gels react under increasing applied frequency. Gels are typically frequency independent over a large frequency range when the strain imposed on the sample is within the linear viscoelastic region. Rheology can also be used to monitor the gelation kinetics.[101,102] Understanding the assembly kinetics is crucial, as not only does this play a role in determining the final bulk properties, but also many factors can impact gelation.

1.2.4 Factors Impacting Gelation

Many hydrogelators are relatively hydrophobic, which drives gelation.[103] As such, self-assembly in a gel is considered a non-equilibrium process in which the system moves from a "highly soluble" to a "less soluble" state. Therefore, gelation is regarded as kinetically dependent.[104,105] The self-assembly is also an energetically downhill process, allowing the gels to form under thermodynamic equilibrium.[66,106–109] The competition between the thermodynamic and kinetic pathways presents an opportunity to switch from thermodynamic to kinetic control, allowing the system to exist as a kinetically trapped

species.[110] Therefore, materials with different properties can be prepared from the same precursor depending on the assembly pathway kinetics.[66,106,107,109–111]

1.3 Modification of Pre-Gel Structures

Whilst altering the final gel properties by changing the gelation trigger and controlling the gelation kinetics has been extensively studied,[48,101,112–115] changing the pre-gel solution before triggering gelation is rarely discussed. One limitation of changing the gelation trigger to change the gel properties is that some triggers may not be suitable for the final applications. For example, DMSO and high temperatures can be detrimental to cells.[10,116] An advantage is that due to their hydrophobicity, the pre-gel state may contain micellar aggregates (such as spherical, cylindrical, and worm-like micelles) above the critical micelle concentration and Krafft temperature.[117–120] How these molecules pack is dependent on their size and shape, but also on the non-covalent interactions present.[118,119] Owing to their weak nature, these interactions can be tuned by parameters such as temperature, ionic strength, or pH, thus impacting the bulk properties of the pre-gel solution.[107] These changes in solution-phase properties could potentially be translated into the resulting gels. For example, it has been shown in functionalised dipeptide-based gelators that the structures formed in the gel state can be templated by the micellar state.[121] Varying the micellar aggregate presents an opportunity to control the "apparent" pK_a value of the aggregate, changing the pH at which the gel forms and the properties of the gel.[103] By tuning the gel, this creates new applications for the material. Currently, the properties of gels (such as stiffness) are controlled by varying the concentration of the gelator.[100] However, this method also tends to lead to other changes in properties. Thus, the opportunity to selectively control the properties of hydrogels is extremely desirable.

1.3.1 Using Heat-Cool Cycles

When LMWGs are heated, this increases their solubility, and therefore, the molecules are more dispersed in solution due to reduced intermolecular interactions.[122] As a result, these molecules may reassemble differently after cooling as they are molecularly dissolved. Thus, the kinetics will be affected by both the temperature the solution is heated to and the cooling rate, directly influencing the structures formed.

At elevated temperatures, some charged amphiphilic molecules can form structures that template alignment of supramolecular fibrils.[123] The Stupp group utilised this behaviour to

form supramolecular noodles, which, when mixed with cells at physiological temperature, formed monodomain gels of aligned cells and filaments.[123] A peptide amphiphile with an alkyl tail was studied, which self-assembles into 1D nanofibres in aqueous solution and can form gels. Alignment of 1D nanostructures has potential applications from cell culturing to organic electronics.[124–127] Gel noodles were formed by dispensing the self-assembled amphiphile solution from a pipette into a $CaCl_2$ solution to trigger gelation. Upon heating to 80°C and cooling to 25°C, alignment of the nanostructures parallel to the long direction of the gel noodles occurred, which was attributed to a heat-induced change in the self-assembled structure. In comparison, non-heat-cooled solutions could not form mechanically stable noodles. TEM showed that the solutions formed thin plaque-like structures after a heat-cool treatment. Heat-cool cycles also resulted in a threefold increase in viscosity. It was postulated that the formation of plaque-like structures and increase in viscosity meant that the shear force experienced by the solution when pipetted aligned the nanostructures. SAXS suggested that the local packing was not changed by heating and cooling, but instead, the aggregates were dehydrated when heated, leading to filaments with larger diameters. Microscopy highlighted large birefringent domains in the resulting gel noodles. Such birefringence suggests alignment along the noodle axis, which was shown to control the orientation of cells in 3D cultures. These findings offer a route to develop therapies which require directed cell migration or cell growth.

Another example of modifying pre-gel solutions using heat-cool cycles comes from Draper *et al.*, who have reported on the change in the physical properties of dipeptide-based gelator (2NapFF, where Nap = naphthalene and F = phenylalanine) solutions.[128] These gelators can form worm-like micelles at high pH due to their hydrophobicity.[52,129] Upon a heat-cool cycle, the viscosity of the samples at low shear significantly increased. SAXS showed that heat-cooling resulted in an increase in the length of the hollow structures formed due to dehydration of the aggregate core. This increase in length increased the extensional viscosity (Fig. 1.5a), making it a potential candidate for electrospinning.[130] When $CaCl_2$ was used to trigger gelation (Fig. 1.5b), the gels formed from heat-cooled solutions were significantly stiffer than those from pre-heated solutions (G' values of 122.7 ± 4.1 kPa for gels formed from heat-cooled solutions and 18.9 ± 3.4 kPa for gels formed from pre-heated solutions). Other gelators were also tested to prove this behaviour was not just observed with 2NapFF.

This work again highlights a method to tune the properties of hydrogels by simply changing how the solution is prepared to offer more potential applications from a single gelator.

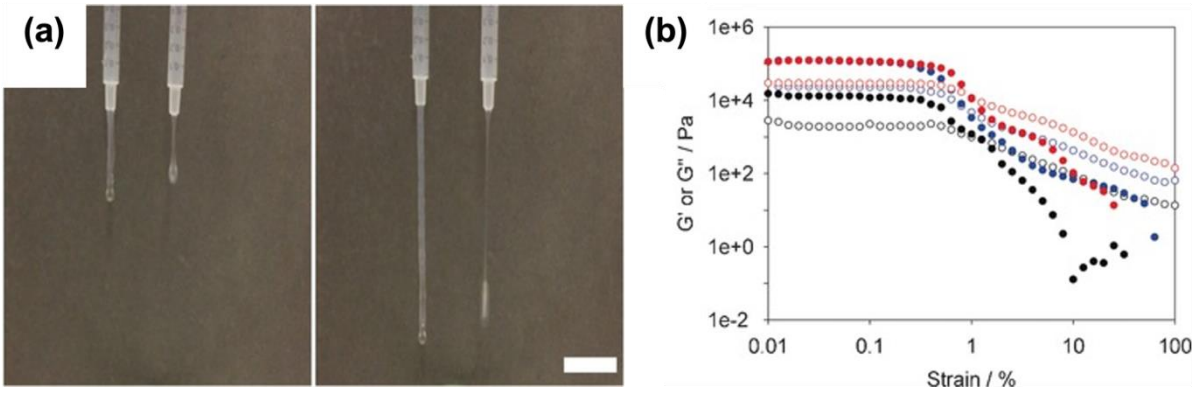

Figure 1.5. (a) Photographs demonstrating the increase in extensional viscosity upon heat-cooling 2NapFF solutions. Scale bar represents 2 cm. (b) Strain sweeps of gels formed by adding $CaCl_2$ to non-heat-cooled (black), heated (blue), and heat-cooled (red) solutions of 2NapFF. Filled circles represent G′, and empty circles represent G″. Figure adapted from Reference 128.

A more recent example of kinetically tuning the behaviour of LMWGs using heat-cooling comes from the Ulijn group, showing that thermal history is a simple method to control the structure and function of supramolecular hydrogels.[131] Using the Fmoc dipeptide, FmocYL (Fig. 1.6a), the group showed that tunable gels can form by altering the assembly temperature, with the resulting structures being "locked in" by cooling. The differential self-assembly was tuned by altering the dominant non-covalent interactions present. Using ^{1}H NMR spectroscopy, they found that at higher temperatures (333-363 K), π-stacking interactions dominated, whereas at lower temperatures (313-323 K), hydrogen bonding was the primary interaction (Fig. 1.6b). Previously, such modifications were achieved by introducing functional groups to alter the self-assembly.[132–135] However, Uljin's group showed that it was possible to obtain a variety of supramolecular structures from a single molecule.[131] The balance of non-covalent interactions also influenced the proteolytic degradation of the gels, with gels containing more ordered H-bonding structures having lower degradation rates. Upon gelation, the hydrogels formed from higher pre-assembly temperatures were mechanically stiffer and showed higher melting temperatures. Atomic force microscopy (AFM) also showed that the morphology of the gel networks had changed, with dried films of gels formed at lower pre-assembly temperatures having shorter and wider fibres. Overall, this work highlights the influence of temperature on the self-assembled

structures formed whilst emphasising that thermodynamic and kinetic considerations must be in place when designing functional nanomaterials.

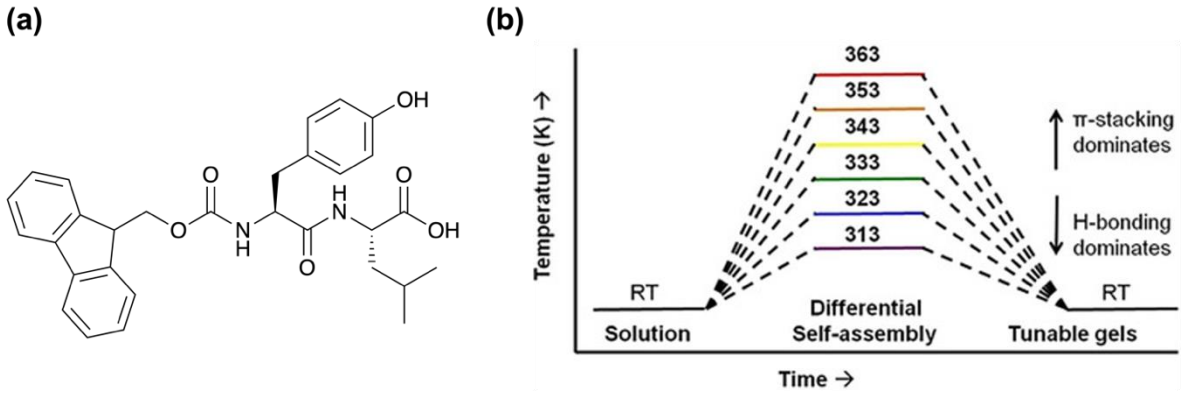

Figure 1.6. (a) Chemical structure of the Fmoc-YL gelator. (b) Cartoon illustrating the pathway-dependent self-assembly of Fmoc-YL and the dominant intermolecular interactions at various temperatures. Figure adapted from Reference 131.

1.3.2 Using Solution pH

As previously mentioned, the pH of the pre-gel solution is crucial when triggering gelation using a pH trigger or a divalent salt. LMWGs containing ionisable groups (such as carboxylic acids and amines) are sensitive to changes in pH due to protonation and deprotonation of these groups.[136–138] These ionisable groups have different acid strengths, which are described by "apparent" pK_a values (with "apparent" referring to the pK_a values of the aggregates and not the single molecule). As such, changing the pH of the pre-gel solution can result in a change in the self-assembly due to differences in solubility.[139–141] Peptide-based LMWGs are soluble in water at high pH when the terminal carboxylic acid groups are deprotonated and form hydrogels upon lowering the pH due to the gradual protonation of these groups. As the pH is lowered, there are typically changes in the aggregation around each "apparent" pK_a value.[142] When using a pH trigger, these groups should be sufficiently deprotonated to ensure the gelator is fully solubilised. Similarly, when using a metal salt to trigger gelation, the LMWG should have a deprotonated group to allow for metal chelation. Therefore, this is another potential way to tune the properties of the resulting hydrogels.

An example of using solution pH to control the gel properties comes from the Banerjee group, who reported on a phenylalanine-based conjugated LMWG.[143] This molecule can form hydrogels across a wide range of phosphate buffers at different pHs (7.46-15.0). SEM showed how pH impacted the morphology of the nanofibres (Fig. 1.7). Gel structures formed

at pH 7.46-12.0 were helical in nature, whereas when the pH was greater than 12, straight, tape-like structures formed. Furthermore, the gels formed at higher pHs had wider gel fibres. It was found that the starting pH had a significant influence on the thixotropic behaviour of the hydrogels, with only the gels formed at pH 7.46 showing full recoverability after high strain was applied. Such behaviour allows these hydrogels to be suitable candidates for 3D printing,[144–147] or to be used to encapsulate and release biomolecules over time without the need for heat-cool cycles, which could damage biomolecules.

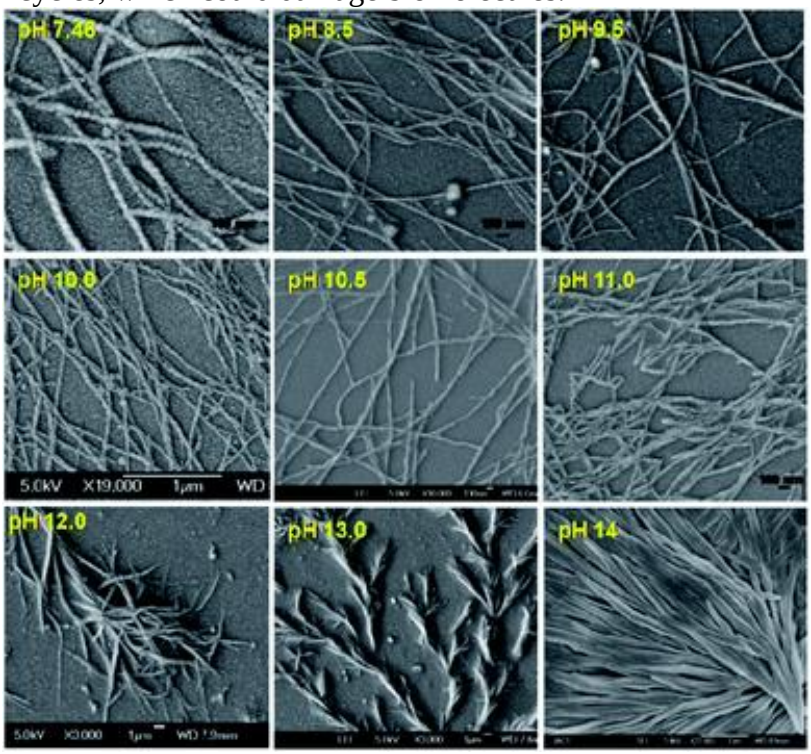

Figure 1.7. SEM image of the phenylalanine-based hydrogels formed at different pHs. Figure adapted from Reference 143.

1.3.3 Using Counterions

Due to their hydrophobicity, many LMWGs require the addition of a base to solubilise them in water to form the pre-gel solution. These salts can also affect aggregation in accordance with the Hofmeister series.[103,148–150] The Hofmeister series can affect the stability of secondary and tertiary structures of self-assembled materials.[151] Therefore, it should be possible to tune the micellar aggregates formed from a single gelator by changing the cation.[103,152–154] Depending on the ability of the salt to influence the solubility in aqueous solutions, counterions can be divided into two categories: “salting-in” or “salting-out”.[155] Weakly hydrated cations are more likely to “salt-out”, whereas divalent cations typically “salt-in” (Fig. 1.8). “Salting-out” describes the increase in surface tension at the fibre-

solution interface, leading to an increase in the aggregate stability due to strengthening of the hydrophobic effect.[156] By contrast, "salting-in" describes a decrease in surface tension at the fibre-solution interface. As a result, the hydrophobic effect is weakened, and the gelators become more soluble. With this increased solubility, the gelator can more easily interact with water and the stability of the aggregate formed is decreased. These changes in solubility can change the self-assembled structures formed and again impact the gelation kinetics.

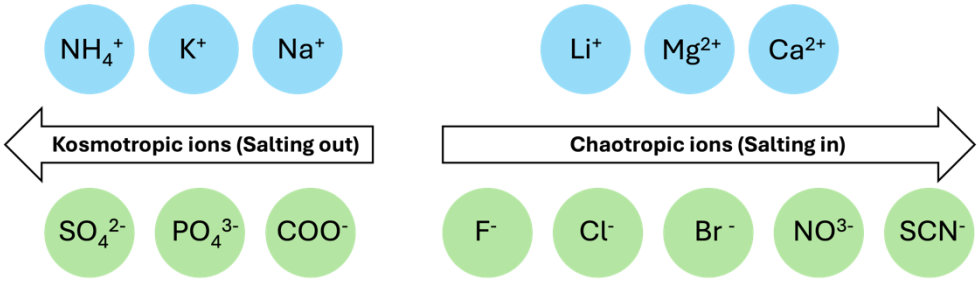

Figure 1.8. Hofmeister series showing ions which are more likely to "salt-in" on the right and ions more likely to "salt-out" on the left.

McAulay *et al.* have shown this effect directly using 2NapFF.[103] By changing the size of the cation used to prepare the solutions, they saw there was a change in the structure of the micellar aggregates.[103] These aggregates showed different behaviours upon heating and cooling and changes in their "apparent" pK_a values. Similarly, Mañas-Torres *et al.* recently investigated the gelation kinetics of the dipeptide FmocFF in the presence of different metallic cations (Cs^+ and Ca^{2+}) using *in-situ* fluorescence lifetime imaging microscopy (FLIM).[157] They anticipated that Ca^{2+} would show "salting-in" behaviour, whilst Cs^+ would result in "salting-out". FLIM showed that fibril formation with Ca^{2+} ions was faster, whilst Cs^+-promoted fibril formation was an order of magnitude slower. The difference in the self-assembly mechanisms was explained using differential scanning calorimetry (DSC) (Fig. 1.9a). The more complex DSC profile for Cs^+-mediated gelation suggested a multistep assembly process into several increasingly stable intermediate species (a mixture of nanospheres and amorphous fibres). In comparison, only nanofibres were formed when Ca^{2+} was used. This mixture of fibres and nanospheres for FmocFF with Cs^+ was observed using both TEM and FLIM. The difference in the self-assembly process was reflected in the physical properties of the resulting gels. Rheological measurements showed hydrogels formed in the presence of Ca^{2+} were 500 times stiffer than the analogous Cs^+ hydrogels (Fig. 1.9b and c). It was postulated that this difference was the result of the different properties of the counterions regarding their coordination abilities and capability to stabilise the water-

solute interactions. Overall, this work shows the influence of different metallic ions on the mechanism of nucleation and growth of dipeptides and thus presents another method to tune the properties of hydrogels.

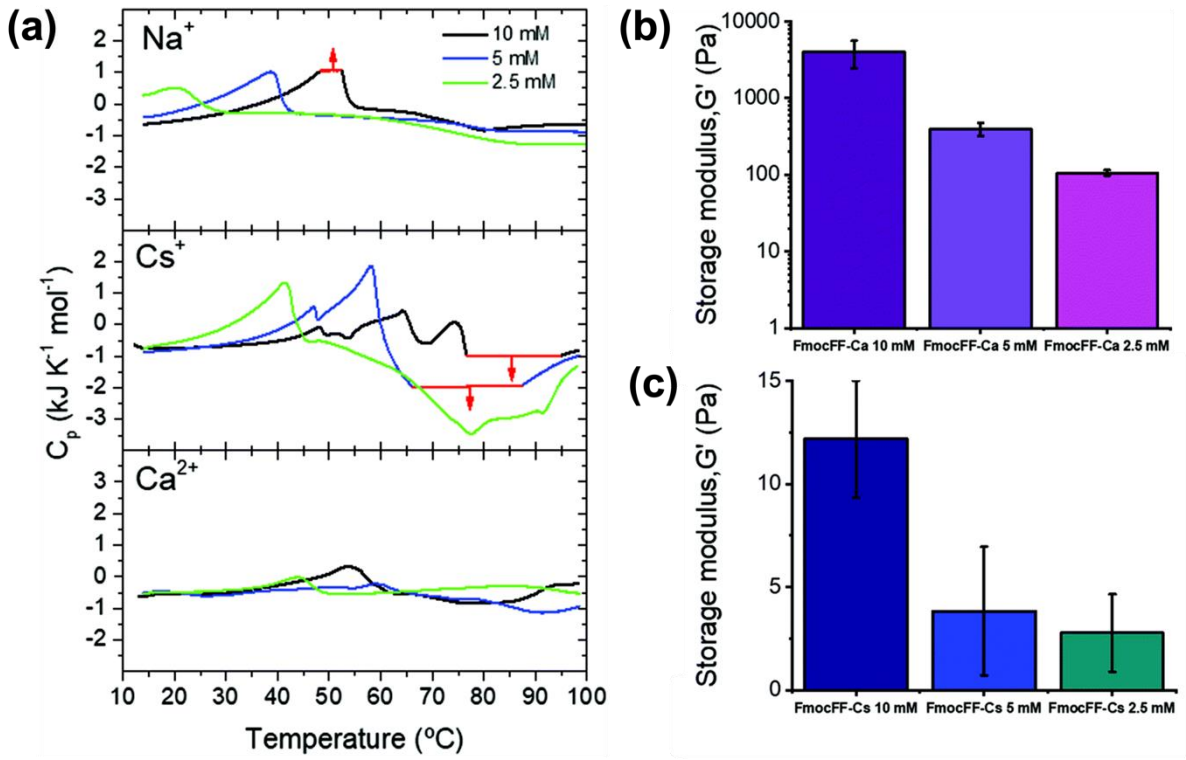

Figure 1.9. (a) DSC scans of FmocFF at a concentration of 10 mM (black), 5 mM (blue), and 2.5 mM (green) in the presence of Na^+, Cs^+, and Ca^{2+}. G′ values of hydrogels formed at different FmocFF concentrations in the presence of (b) Ca^{2+} and (c) Cs^+ ions. Figure adapted from Reference 157.

The Adams group have reported the impact of different counterions on the assembly of 2NapFF.[120] Both metal (Li^+, Na^+, K^+, Rb^+, and Cs^+) and non-coordinating organic (tetra-*n*-butylammonium (TBA) and benzyltrimethylammonium (BTMA)) ions were used to access different micellar structures at high pH. Differences in micellar aggregation were evident from viscosity measurements. They found that the viscosity increased with increasing size of the metallic counterions, with Li^+ ions giving the lowest viscosity and Rb^+ and Cs^+ the highest. This increase in viscosity was thought to be the result of the more labile and soft Rb^+ and Cs^+ ions causing a more viscous micellar aggregation of 2NapFF. The organic ions showed a significant increase in viscosity compared to the metal ions. TBA had a slightly higher viscosity, which was attributed to its larger size and greater hydrophobicity compared to BTMA. Hydrogels were formed by cross-linking the dipeptides with Ca^{2+} to replace the counterions with this ion in the gel state. As such, any differences in the gel's network and

properties would be due to the distinct self-assembled structures formed in the pre-gel form. Rheology showed that the gels became weaker with increasing size of metal ions. Furthermore, the gels formed from the organic salts were stiffer than the Li^+ and Na^+ salts. Upon preparation of gel noodles from metal-salt solutions, the resulting noodles were more rigid than those formed from the organic salts (Fig. 1.10a), which were too fragile to be measured or manipulated. The noodles from the metal salts could resist external perturbation and deformation. However, the organic salts formed significantly fragile noodles, which broke when slight strain was applied or when they were shaken. Nanoindentation and tensile testing experiments showed that the stiffness of the metal-salt noodles varied with the different ions (Fig. 1.10b). It was found that Cs^+ ions produced the stiffest noodles. This work highlights that the variation of micellar arrangement in the pre-gel state can be translated to the hierarchical networks.

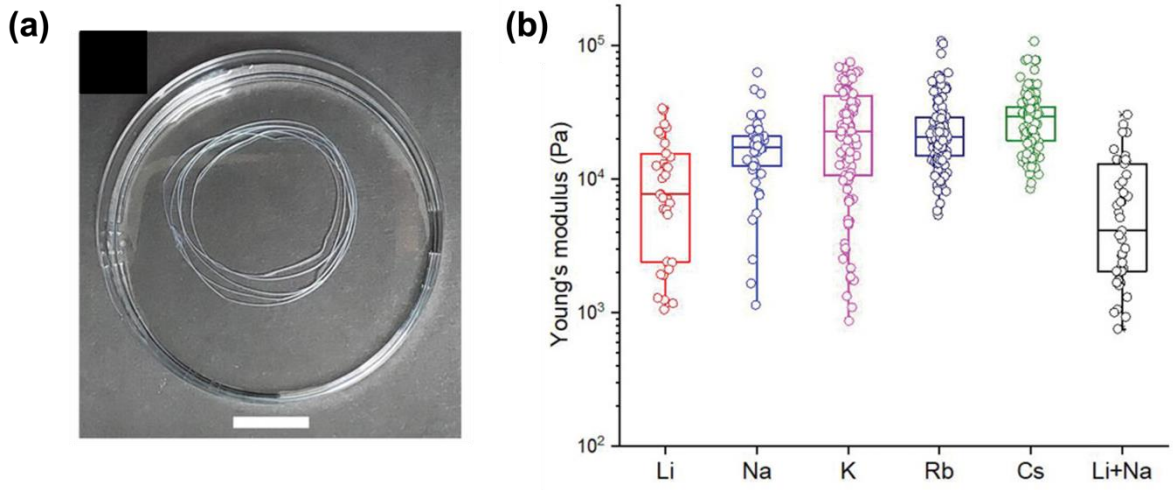

Figure 1.10. (a) Photographs of gel noodles obtained from 2NapFF (20 mg/mL) and Li^+. (b) Statistical bar plot of nanoindentation data of gel noodles obtained from different 2NapFF salts and counterions. Figure adapted from Reference 120.

Uljin and co-workers also exploited the Hofmeister series to tune the self-assembly of various Fmoc-dipeptide hydrogels.[158] The efficiency of the anions in promoting the hydrophobic interactions, and thus self-assembly, was monitored by fluorescence spectroscopy. The ratio of the emission intensity of the excimer/monomer suggested that strongly hydrated ions (also known as kosmotropes) promoted stacking of fluorenyl groups, aided by increased hydrogen bonding. In comparison, weakly hydrated ions (referred to as chaotropes) resulted in weaker hydrophobic interactions. Such differences were demonstrated in the AFM results, which showed gels produced in the presence of kosmotropes formed dense, fibrous networks (Fig. 1.11). However, when chaotropes were

present, spherical aggregates instead formed. The dense fibrous networks resulted in mechanically stiffer gels when hydrogels were formed with kosmotropes. Overall, this study demonstrates that salts have a dramatic effect on the hydrophobic interactions of dipeptides, resulting in differential order and supramolecular chirality. Therefore, the salts directly impact the mechanical properties of the resulting gels. In summary, ionic composition is another important parameter to consider when designing supramolecular hydrogels.

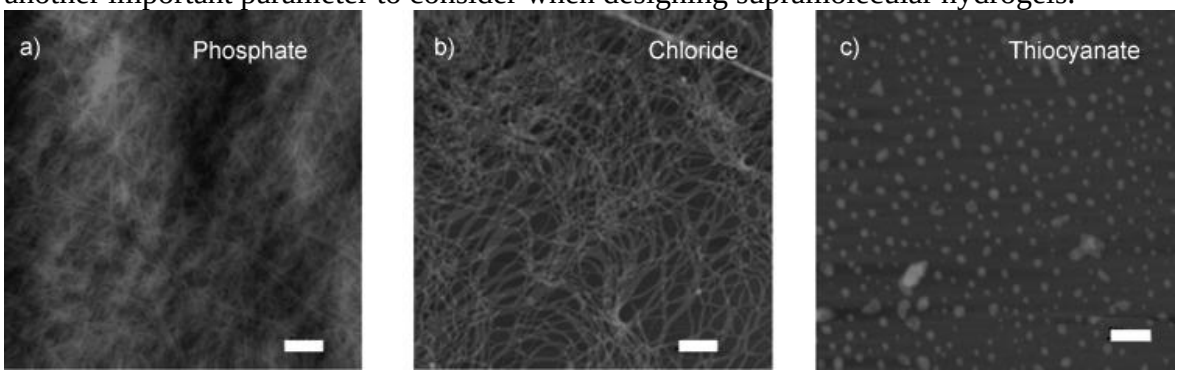

Figure 1.11. AFM images of Fmoc-YL gels in the presence of (a) phosphate, (b) chloride, and (c) thiocyanate salts of sodium. Scale bars represent 500 nm. Figure adapted from Reference 158.

1.3.4 Using Polymer Additives

Polymer additives have generated interest due to the ability to enhance the desired properties of a material by "blending" the properties of the gelator and polymer without the need for synthesis.[159] However, this is often not the case, with the polymer altering the gelation process by changing the pre-gel structures. Such additives have been reported to both impede and promote gelation.[11,160–162] These polymers can modify the nucleation and growth process during gelation,[163] facilitate aggregation,[164] or increase fibre branching.[165] As such, the addition of additives could impact the gelation kinetics and thus change the resulting gel properties or gel network. Recently, the Durand group investigated the impact of dextran on the gel kinetics and properties of two *L*-lysine-based gelators (A and B, Fig. 1.12).[58] Samples were prepared with varying dextran quantities ranging from 0 to 240 mg. Increasing the dextran concentration resulted in weaker gels, thought to be due to the polymer reducing the topological interactions between fibre-like aggregates. Such behaviour has also been reported by the Adams group.[166,167] Increasing the dextran concentration also resulted in a decrease in the gelation kinetics, suggesting gel formation was more difficult.[58] This behaviour suggests that the polymer increased the viscosity of the pre-gel solution, resulting in diffusion-limited self-assembly. It was also hypothesised that there were no interactions between the dextran macromolecules and the LMWG, and the polymer was instead sterically

hindering aggregate formation and growth. In summary, these studies show that careful consideration must be given when choosing polymer additives, as they can directly impact the self-assembly process to alter the properties of the gel.

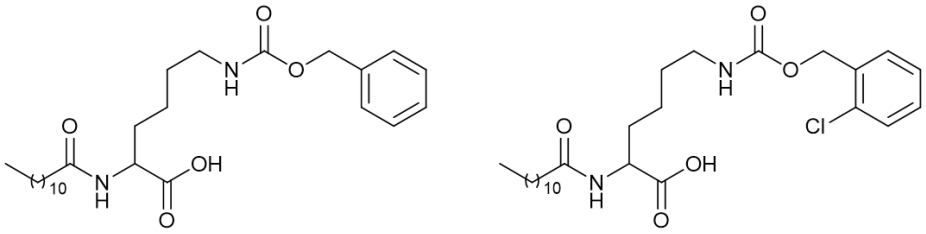

Figure 1.12. Chemical structures of the two *L*-lysine-based gelators (A and B) used by Durand and co-workers.[58]

Chakraborty *et al.* have also used polymer additives with the aim to improve the desired mechanical properties of tripeptide-based gels and their durability in cell culture media.[168] This work focused on composite hydrogels formed from Fmoc-RGD and chitosan (Fig. 1.13a). Gels formed from Fmoc-RGD alone were too weak to be used for cell culturing. The composite Fmoc-RGD/chitosan hydrogels showed a significant increase in the storage modulus (G′ values of 529 Pa and 3436 Pa for Fmoc-RGD and Fmoc-RGD/chitosan, respectively). TEM showed that the fibre diameter of the composite gel had decreased, resulting in a higher aspect ratio of the fibres (Fig. 1.13b and c). These higher aspect ratio fibres entrapped the solvent more tightly, explaining the increase in G′ from the rheology. Furthermore, chitosan provided additional nucleation sites during gelation, enhancing the number of fibres, and consequently, the fibre network density. This was further suggested when monitoring the gelation over time, with the composite gels forming much faster than the Fmoc-RGD gels (239 minutes versus 46 minutes for Fmoc-RGD and Fmoc-RGD/chitosan, respectively). When placed in cell media, the Fmoc-RGD gels completely dissolved after 30 minutes. However, the Fmoc-RGD/chitosan gels were stable in media for several months. Washing with cell media made these composite gels ideal for cell adherence. This work demonstrates the use of polymers to tailor the properties of supramolecular gels by forming a gel with attributes from both the gelator and the polymer to make them suitable for multiple applications.

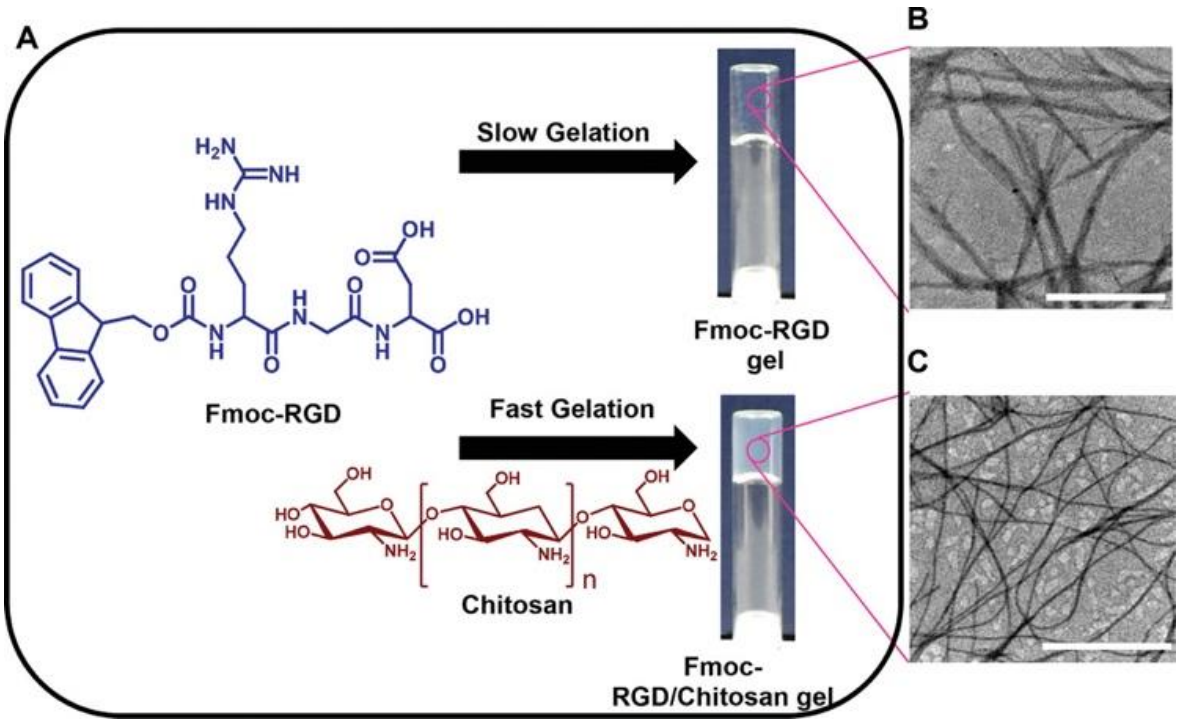

Figure 1.13. (a) Chemical structures of the Fmoc-RGD gelator and chitosan additive and images of resulting hydrogels. TEM micrographs of (b) Fmoc-RGD and (c) Fmoc-RGD/chitosan hydrogels. Scale bars represent 1 μm. Figure adapted from Reference 168.

When using polymer additives, the molecular weight, concentration, and order of mixing can all impact the self-assembly process. The Thordarson group focused on how these factors influenced the gels formed with FmocFF.[169] The gelator was dissolved in various poly(ethylene) glycol (PEG)/water mixtures, and the gelation compared. Furthermore, the group explored the gelation behaviour in different molecular weight PEGs. The viscosity significantly increased upon increasing the polymer weight from PEG 400 to PEG 800, after which the viscosity only slightly increased. In the resulting gels, G' was found to increase with increasing molecular weight of PEG from PEG 200 to PEG 400. However, for gels formed with PEG 400 to PEG 10000, there was very little change in G', suggesting that the storage modulus of these gels cannot be correlated with the viscosity of PEG. This behaviour differs from that reported by Adams and co-workers, who showed that upon the addition of water/dextran mixtures to FmocFF in DMSO, the storage modulus showed a negative correlation with the viscosity of the water/polymer mixtures.[167] Thordarson's group also found that the ratio of PEG 400/water significantly impacts the properties of the resulting gel. Between concentrations of 0% and 60% (v/v) PEG 400, a gel can be formed, and an increase in the G' values is observed with increasing PEG concentration. However, above concentrations of 60% (v/v) PEG 400, gels could no longer form. It was hypothesised that

this increase in G' and the inability to form gels above 60% (v/v) PEG was the result of macromolecular crowding effects, which provide additional gel stability, resulting in stiffer gels. However, there is an optimal ratio for PEG-to-water interactions, which the authors think could explain why gels do not form above 60% PEG 400. Finally, the group also performed gelation experiments where the order of mixing was changed. They compared gels where the FmocFF was dissolved in the chosen PEG, followed by the addition of water, to those that were first dissolved in basic water before the polymer was added. Rheology showed that when the polymer was added first, the resulting gels were much stronger due to better dissolution of the FmocFF in PEG 400 than water. This work emphasises the importance of controlling experimental conditions when preparing hydrogels, as even the order in which one mixes the components can impact the resulting gels.

1.4 Applications of Hydrogels

There are already many examples of LMWGs used in applications, such as in waste removal,[170] cosmetics,[171] and regenerative medicine.[172] Furthermore, as LMWGs are reversible, they offer the advantage of recyclability and reusability over polymer gels, reducing the need for frequent preparation, synthesis, and acquisition of new materials. These materials also show great versatility, accounting for their vast mechanical properties. A single gelator can also be responsive to multiple stimuli. There are extensive reviews on the applications of LWMGs,[11,173–175] with a few specific examples in the following sections.

1.4.1 3D Printing

Controlled delivery of hydrogels has potential applications in tissue engineering,[176] drug delivery,[177] and optoelectronics.[178] 3D printing can allow for the reproducible, controlled, and automatic delivery of hydrogels without using moulds.[179] The printability of hydrogels is determined by both the properties of solutions and the gelation process. Supramolecular hydrogels are ideal for 3D printing because of their dynamic and reversible self-assembly process.[180] The Adams group previously reported that dipeptide-based LMWG hydrogels formed using a solvent trigger printed better than those formed *via* a pH trigger.[179,181] They showed that when a solvent trigger was used, spherulitic structures formed, which were not as strongly impacted by the shearing process upon printing as the fibrous networks formed by the pH trigger.[179] However, in Chapter 4, we show that by using a polymer additive, we can 3D print pH triggered hydrogels.

Jian *et al.* used two oppositely charged dipeptide LMWGs (Fmoc-YD and Fmoc-YK, Fig. 1.14a) to construct hydrogel scaffolds using layer-by-layer 3D printing (Fig. 1.14b).[180] During printing, *in situ* gelation of the Fmoc-dipeptides occurred *via* electrostatic interactions between the oppositely charged fibres. The mechanical and degradation properties of the scaffold were controlled by changing the composition and concentration of the Fmoc-dipeptides. As such, these materials allowed for the controllable formation, growth, and natural release of uniform tumour spheroids. Furthermore, HepaRG cells showed a more rapid and sustainable proliferation in the 3D-printed hydrogel than in a Petri dish (Fig. 1.14c and d).

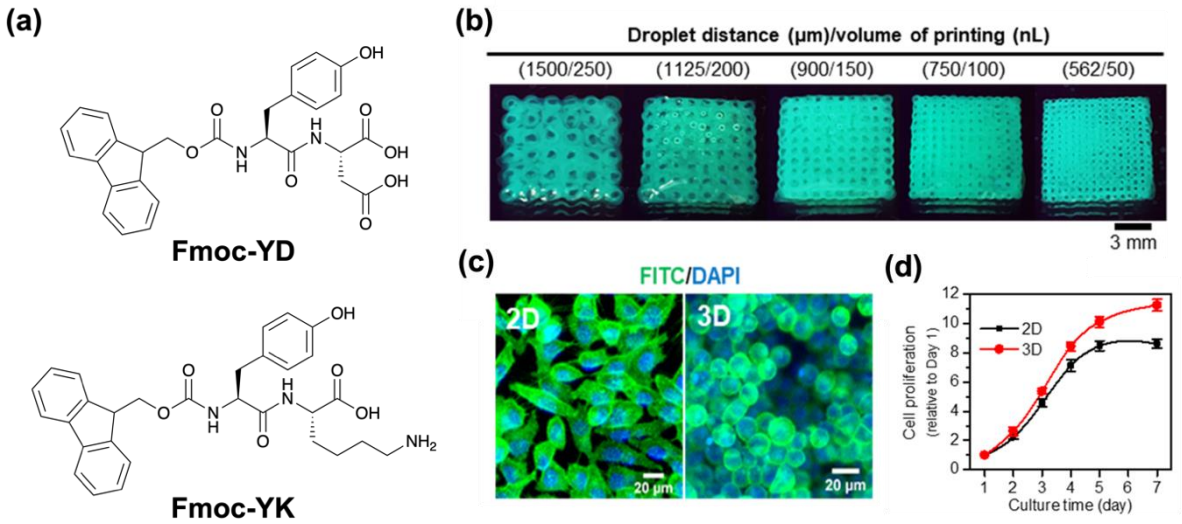

Figure 1.14. (a) Chemical structure of the two Fmoc-dipeptide LMWGs. (b) Fluorescence images of printed hydrogel scaffolds of Fmoc-YD and Fmoc-YK showing different microstructures by changing the droplet distance and volume. (c) Confocal images and (d) cell proliferation curves of HepaRG cells cultured in 2D and 3D cultures. Figure adapted from Reference 180.

1.4.2 Sensors

Gels are highly desirable for use in sensor technologies because of their capacity to undergo gel-sol transitions, which provides a mechanism for detecting analytes.[175,182] One example uses naphthalene diimide (NDI) appended peptide amphiphiles for intracellular pH-sensing.[62] The asymmetric NDI contained two positively and one negatively charged side chains on the peptide amphiphile (Fig. 1.15a), making the hydrogel pH-responsive. Absorption, emission, and circular dichroism spectroscopy showed a drastic increase in aggregation with increasing pH. This behaviour allowed the hydrogel to be used to determine the pH at different cellular locations. When in an alkaline intracellular environment (region

of interest, ROI2, Fig. 1.15b), the probe aggregated strongly, determined by an increase in emission intensity at 500 nm. In comparison, at neutral or lower pH (ROI1, Fig. 1.15b), the aggregation was not as pronounced and resulted in a lower intensity band at 500 nm. Other LMWGs are also capable of sensing. For example, a pyrene-based LMWG has been used as a sensor for insulin concentrations.[183] Furthermore, quinoline-indolin-2-one based hydrogels can sense selected ions in the presence of other ions, showing a selective gel-to-sol transition or colour change.[184]

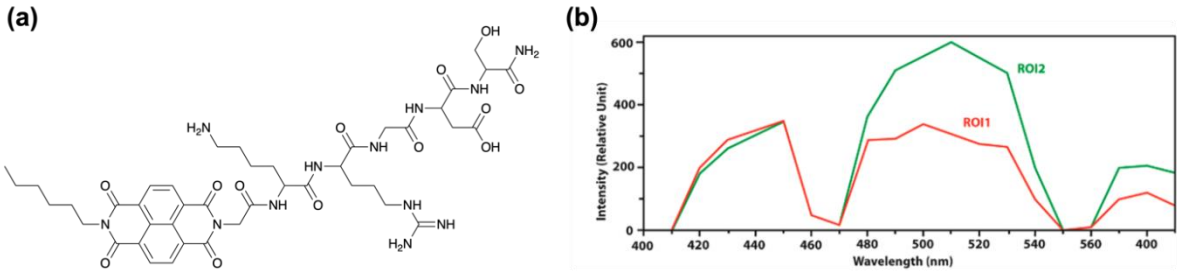

Figure 1.15. (a) Chemical structure of peptide amphiphile-appended NDI. (b) Emission spectra of the hydrogel at region of interest, ROI1 (red) and ROI2 (green), collected at an excitation of 350 nm. Figure adapted from Reference 62.

1.4.3 Optoelectronic Devices

Low molecular weight hydrogels containing π-conjugated components show photo-/electroconductivity, making them excellent candidates in electronic, energy, and optical technologies.[175,185] The performance of these materials depends upon the molecular structure of the gelator, the intermolecular interactions present, and the available charge transfer pathways.[185,186]

Perylene bisimides (PBIs) are an acclaimed example of an electron transporting/accepting organic dye.[187] As PBIs show high electron conductivity and photostability, they are the best non-fullerene n-type semiconductors for application in organic photovoltaic devices. As such, PBIs will be the focus of this thesis. Banerjee and co-workers showed that a tyrosine-appended PBI had semiconducting and photo-switching behaviour.[188] Hydrogels were formed using a heat-cool trigger before drying them between two gold electrodes to form a xerogel. The PBI showed photoconductivity under both visible (filtered UV light) and white light (without filtering UV light) (Fig. 1.16). Furthermore, the sample showed photo-switching behaviour, as the current increased and decreased as soon as the chosen light source was turned on and off, respectively.

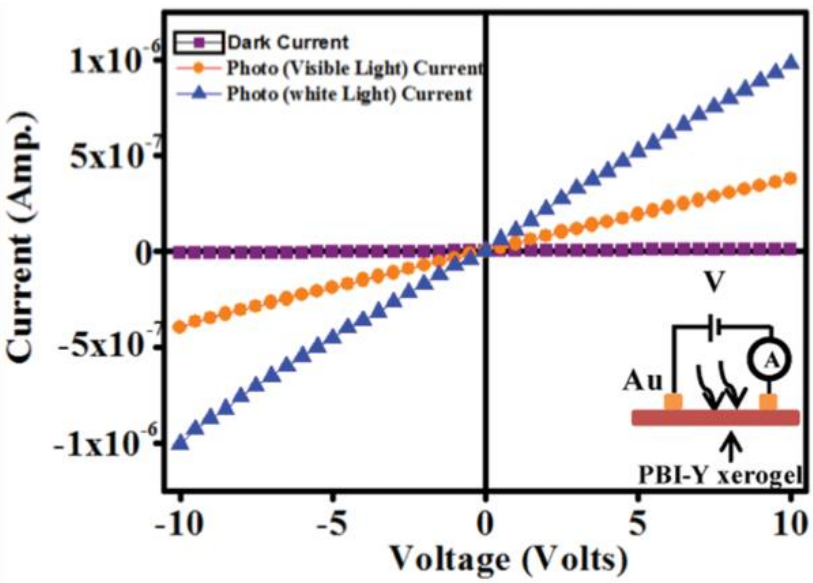

Figure 1.16. *I-V* curves of the PBI xerogel in the dark (purple) and under visible (orange) and white (blue) light. A schematic representation of the layout of the circuit diagram is given as an inset. Figure taken from Reference 188.

1.5 Perylene Bisimides as Low Molecular Weight Gelators

1.5.1 Properties of Perylene Bisimides

PBIs are widely studied functional materials from the rylene family of dyes.[187] Due to their high electron conductivity and photostability, they are the best non-fullerene n-type semiconductors for application in organic photovoltaic devices.[189,190] PBIs are suitable for various applications due to their rigid aromatic perylene scaffold, based on the molecular skeleton of perylene-3,4:9,10-bis(dicarboximide) (Fig. 1.17).[191] Furthermore, their broad UV-vis absorption and thermal stability mean that PBIs are an excellent candidate for light-harvesting materials.[192,193] PBIs can be employed in optoelectronic devices due to the formation of a conductive radical anion.[194–198] Another desirable feature of PBIs is their ability to self-assemble into a range of aggregates in solution.

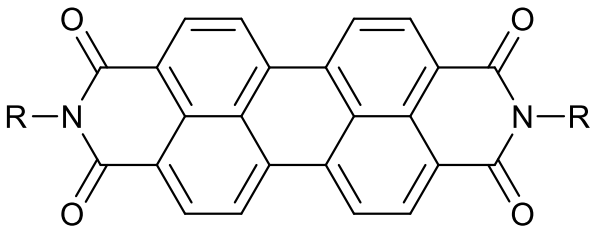

Figure 1.17. General chemical structure of a perylene bisimide with R representing the imide functionalisation.

1.5.2 Self-Assembly of Perylene Bisimides

As a result of their extended quadrupolar π-system, PBIs can self-assemble *via* π-π stacking, even at very low concentrations (<10^{-5} M).[61] This self-assembly results in the formation of aggregates which can, in theory, facilitate exciton and long-range charge transport through the structure.[199] The structure of these aggregates determines the photophysical and photochemical properties of the PBI.[200] Upon aggregation, π-rich systems can form H-type aggregates, J-type aggregates, or a mixture of both (Fig. 1.18).[201–203]

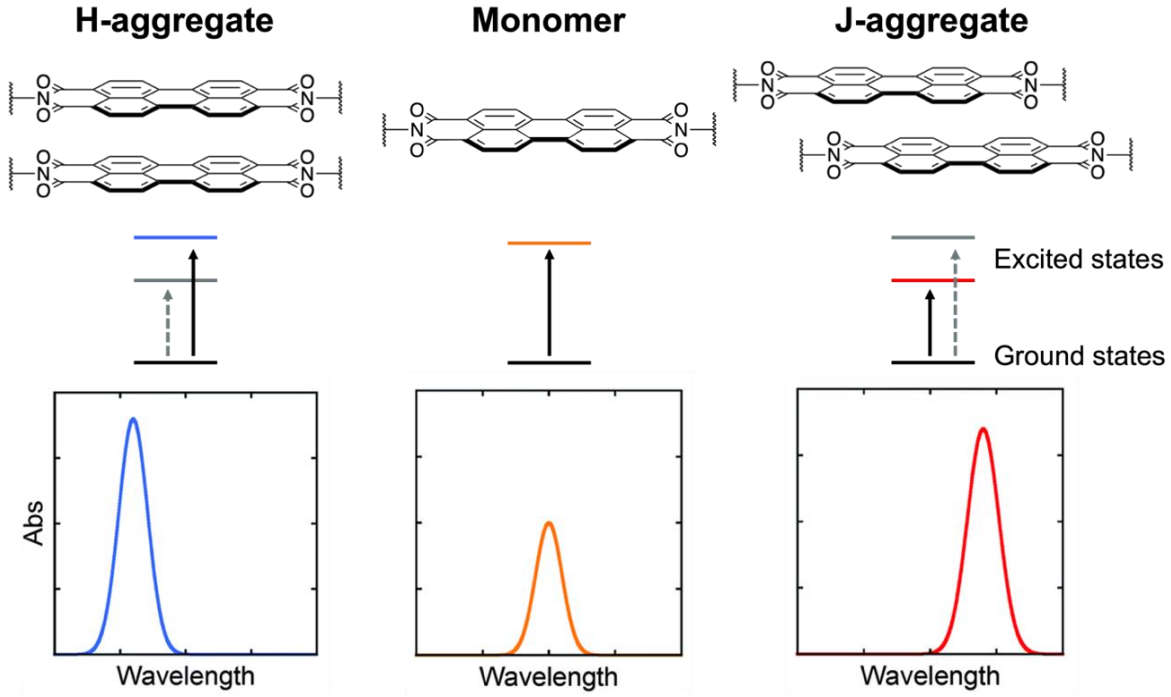

Figure 1.18. Schematic illustrating the stacking of PBI monomers (centre) to produce H-type (left) and J-type (right) aggregates and the corresponding UV-vis absorption spectra. Full arrows depict allowed transitions and dashed arrows represent forbidden ones. Figure adapted from Reference 203.

H-type aggregates are defined by a blue-shifted absorption maximum of the UV-vis spectrum of the isolated chromophore, with molecules being stacked directly on top of each other. In comparison, J-aggregates have a red-shifted absorption maximum, and the molecules are offset with respect to each other.[200] The type of aggregate that forms is crucial as it directly affects the conductivity and optoelectronic properties of the PBI.[200] Controlling the molecular packing of such molecules is difficult, meaning the same PBI can form both H-type or J-type aggregates. Solvents and processing techniques are also influential in determining the hierarchical organisation of PBI aggregates.[204] Water is ideal for self-assembly due to the strong hydrophobic forces formed in the presence of extended

hydrophobic surfaces.[205] However, a disadvantage of most PBIs is that they are insoluble in water. Therefore, supramolecular studies of many PBIs have been limited to organic solvents.[206,207] This solubility can be improved by functionalising at the imide position with an ionisable group, such as an amino acid. Functionalisation can alter aggregation, which in turn affects the electronic properties of the molecule.[142,208,209]

1.5.3 Functionalisation of Perylene Bisimides

Functionalisation of PBIs can occur at the imide, bay, or *ortho* carbon atoms.[189,210] The chosen position will impact the resulting properties in different ways. Imide functionalisation impacts the solubility and the molecular packing and nanostructures.[189,211] However, different imide functional groups have a negligible influence on the redox potential and absorption profiles compared to core substitutions.[212–214] Recently, related perylene *peri*-tetracarbonyl species have gained recognition.[215] These compounds offer the ability to alter the electronic properties as well as significantly influencing solubility and the aggregation behaviour of chromophores into liquid crystals. The Champness group have recently characterised the electronic effects of different carbonyl groups on perylene tetracarbonyl compounds.[215] The study included esters, imides, anhydrides, and their combinations. They found that imide and anhydride groups resulted in enhanced electron-accepting properties, whilst esters made the perylene core more electron-rich. Such research is crucial when designing optoelectronic devices, as different substituents can tune the redox potential, impacting device performance.

Functionalising the bay positions with electron-withdrawing and electron-donating groups can tune such properties.[212,216] However, this can lead to a distortion of the core and impact π-π stacking.[209,214,217,218] The redox and absorption properties can also be altered *via ortho* substitutions.[219–221] Such substitutions do not cause twisting of the perylene core or change the π-π stacking.[222] However, these substitutions are typically carried out under harsher conditions and with a precious metal catalyst.[222,223] Therefore, there is a need to modify the properties of these PBIs and similar LMWGs to increase the number of applications these materials are suitable for without the need to design new gelators.

1.6 Aims of this Thesis

Supramolecular hydrogels continue to attract notable interest with many potential applications. However, there are still significant gaps in understanding these systems and the

correlation between the pre-gel and final gel states. The kinetics of the gelation process play a crucial role in the bulk properties of the hydrogel and present an opportunity to fine-tune these systems to meet the requirements of the chosen application. Therefore, it is possible to use a single gelator for multiple applications. As such, this thesis aims to exemplify some of the methods to modify and control the pre-gel structures of LMWGs before triggering gelation. To do this, we focus on amino acid-appended PBIs in water and use the same gelation trigger throughout. Understanding the pre-gel structures, self-assembly, and gelation across multiple length scales will help to further improve LMWG construction and correlate the micellar structures to the bulk gel properties. Overall, this work aims to provide new opportunities to increase the number of applications these materials are suitable for without the need to design new gelators.

In Chapter 2, we demonstrate how a well-studied amino acid-appended PBI can form different hydrogels with different mechanical and optical properties. This is done by changing the solubility and aggregate morphology through altering the starting pH and the history of the solution before gelling. We use SANS, rheology, ^{1}H NMR spectroscopy, and absorption spectroscopy to examine the effect of starting pH on the gelation kinetics and final gel properties.

In Chapter 3, we exemplify the use of heat-cool cycles as a tool for modulating the self-assembly of three amino acid-appended PBIs. By changing the temperature the solutions are heated to, we show that hydrogels and thin films with differing properties can be prepared. We use SANS, rheology, absorption spectroscopy, and ^{1}H NMR spectroscopy to study the extent of these changes in solution. When these heat-cooled solutions were applied in perovskite solar cells, they show similar power conversion efficiencies to those made from non-heat-processed solutions.

Chapter 4 utilises the non-gelling polymer additive poly(ethylene) oxide to form hydrogels suitable for 3D printing applications. Using rheology and SANS, we aim to better understand the impact printing has on the bulk properties of the hydrogels. We show that when dried down, the resulting xerogels are aligned due to the shear applied during printing, with improved film homogeneity. These materials are also mechanoresponsive, showing an increase in photoresponse upon bending. As such, these hydrogels show promise for applications such as wearable sensors and electronics.

1.7 References

1. L. Thomson and D. J. Adams, in *Chemoresponsive Materials: Smart Materials for Chemical and Biological* Stimulation, Royal Society of Chemistry, Cambridge, 2022, pp. 96–128.

2. R. G. Weiss, *J. Am. Chem. Soc.*, 2014, **136**, 7519–7530.

3. V. K. Praveen, B. Vedhanarayanan, A. Mal, R. K. Mishra and A. Ajayaghosh, *Acc. Chem. Res.*, 2020, **53**, 496–507.

4. M. E. Parente, A. Ochoa Andrade, G. Ares, F. Russo and Á. Jiménez-Kairuz, *Int. J. Cosmet. Sci.*, 2015, **37**, 511–518.

5. Z. Zhang, D. J. Young, Z. Li and X. J. Loh, *Small Methods*, 2019, **3**, 1800270.

6. J. Li, X. Jia and L. Yin, *Food Rev. Int.*, 2021, **37**, 313–372.

7. S. Kimura, M. Yokoya and M. Yamanaka, *Chem. Lett.*, 2021, **50**, 459–466.

8. E. R. Draper and D. J. Adams, in *Supramolecular Nanotechnology: Advanced Design of Self-Assembled Functional Materials*, Wiley, Weinheim, 2023, pp. 619–639.

9. L. A. Estroff and A. D. Hamilton, *Chem. Rev.*, 2004, **104**, 1201–1218.

10. X. Du, J. Zhou, J. Shi and B. Xu, *Chem. Rev.*, 2015, **115**, 13165–13307.

11. E. R. Draper and D. J. Adams, *Chem*, 2017, **3**, 390–410.

12. J. Omar, D. Ponsford, C. A. Dreiss, T. Lee and X. J. Loh, *Chem. Asian J.*, 2022, **17**, e202200081.

13. S. Panja and D. J. Adams, *Chem. Soc. Rev.*, 2021, **50**, 5165–5200.

14. R. K. Mishra, S. Das, B. Vedhanarayanan, G. Das, V. K. Praveen and A. Ajayaghosh, in *Molecular Gels: Structure and Dynamics*, Royal Society of Chemistry, Cambridge, 2018, pp. 190–226.

15. G. Deen and X. Loh, *Gels*, 2018, **4**, 13.

16. P. R. A. Chivers and D. K. Smith, *Nat. Rev. Mater.*, 2019, **4**, 463–478.

17. D. McDowall, B. J. Greeves, R. Clowes, K. McAulay, A. M. Fuentes-Caparrós, L. Thomson, N. Khunti, N. Cowieson, M. C. Nolan, M. Wallace, A. I. Cooper, E. R. Draper, A. J. Cowan and D. J. Adams, *Adv. Energy Mater.*, 2020, **10**, 2002469.

18. A. S. Weingarten, R. V. Kazantsev, L. C. Palmer, M. McClendon, A. R. Koltonow, A. P. S. Samuel, D. J. Kiebala, M. R. Wasielewski and S. I. Stupp, *Nat. Chem.*, 2014, **6**, 964–970.

19. T. Yoshii, S. Onogi, H. Shigemitsu and I. Hamachi, *J. Am. Chem. Soc.*, 2015, **137**, 3360–3365.

20. A. Döring, W. Birnbaum and D. Kuckling, *Chem. Soc. Rev.*, 2013, **42**, 7391–7420.

21. G. L. Eakins, R. Pandey, J. P. Wojciechowski, H. Y. Zheng, J. E. A. Webb, C. Valéry, P. Thordarson, N. O. V. Plank, J. A. Gerrard and J. M. Hodgkiss, *Adv. Funct. Mater.*, 2015, **25**, 5640–5649.

22. J. D. Hartgerink, E. Beniash and S. I. Stupp, *PNAS*, 2002, **99**, 5133–5138.

23. X. Dou and C. Feng, *Adv. Mater.*, 2017, **29**, 1604062.

24. J. A. Foster and J. W. Steed, *Angew. Chem. Int. Ed.*, 2010, **49**, 6718–6724.

25. K. Fan, J. Yang, X. Wang and J. Song, *Soft Matter*, 2014, **10**, 8370–8375.

26. F. Chen, Q. Chen, L. Zhu, Z. Tang, Q. Li, G. Qin, J. Yang, Y. Zhang, B. Ren and J. Zheng, *Chem. Mater.*, 2018, **30**, 1743–1754.

27. D. Giuri, L. J. Marshall, C. Wilson, A. Seddon and D. J. Adams, *Soft Matter*, 2021, **17**, 7221–7226.

28. R. Van Lommel, J. Van Hooste, J. Vandaele, G. Steurs, T. Van der Donck, F. De Proft, S. Rocha, D. Sakellariou, M. Alonso and W. M. De Borggraeve, *Gels*, 2022, **8**, 813.

29. A. K. Patterson and D. K. Smith, *Chem. Comm.*, 2020, **56**, 11046–11049.

30. A. Friggeri, B. L. Feringa and J. van Esch, *J. Controlled Release*, 2004, **97**, 241–248.

31. Z. Yang, G. Liang, L. Wang and B. Xu, *J. Am. Chem. Soc.*, 2006, **128**, 3038–3043.

32. A. N. Shy, J. Li, J. Shi, N. Zhou and B. Xu, *J. Drug Target*, 2020, **28**, 760–765.

33. E. Quigley, J. Johnson, W. Liyanage and B. L. Nilsson, *Soft Matter*, 2020, **16**, 10158–10168.

34. S. Panja and D. J. Adams, *Chem. Eur. J.*, 2021, **27**, 8928–8939.

35. D. Giuri, L. Jurković, S. Fermani, D. Kralj, G. Falini and C. Tomasini, *ACS Appl. Bio. Mater.*, 2019, **2**, 5819–5828.

36. P. Ravarino, D. Giuri and C. Tomasini, *J. Pept. Sci.*, 2023, **29**, e3483.

37. L. Qin, P. Duan, F. Xie, L. Zhang and M. Liu, *Chem. Comm.*, 2013, **49**, 10823–10825.

38. X. Jia, J. Chen, W. Xu, Q. Wang, X. Wei, Y. Ma, F. Chen and G. Zhang, *Sci. Rep.*, 2023, **13**, 6328.

39. C. Colquhoun, E. R. Draper, R. Schweins, M. Marcello, D. Vadukul, L. C. Serpell and D. J. Adams, *Soft Matter*, 2017, **13**, 1914–1919.

40. R. Vegners, I. Shestakova, I. Kalvinsh, R. M. Ezzell and P. A. Janmey, *J. Pept. Sci.*, 1995, **1**, 371–378.

41. Z. Yang, H. Gu, D. Fu, P. Gao, J. K. Lam and B. Xu, *Adv. Mater.*, 2004, **16**, 1440–1444.

42. H. Liu, Z. Lv, K. Ding, X. Liu, L. Yuan, H. Chen and X. Li, *J. Mater. Chem. B*, 2013, **1**, 5550–5556.

43. M. J. Webber, C. J. Newcomb, R. Bitton and S. I. Stupp, *Soft Matter*, 2011, **7**, 9665–9672.

44. K. Thornton, A. M. Smith, C. L. R. Merry and R. V. Ulijn, *Biochem. Soc. Trans.*, 2009, **37**, 660–664.

45. J. Raeburn, G. Pont, L. Chen, Y. Cesbron, R. Lévy and D. J. Adams, *Soft Matter*, 2012, **8**, 1168–1174.

46. L. Chen, J. Raeburn, S. Sutton, D. G. Spiller, J. Williams, J. S. Sharp, P. C. Griffiths, R. K. Heenan, S. M. King, A. Paul, S. Furzeland, D. Atkins and D. J. Adams, *Soft Matter*, 2011, **7**, 9721–9727.

47. A. Aggeli, M. Bell, L. M. Carrick, C. W. G. Fishwick, R. Harding, P. J. Mawer, S. E. Radford, A. E. Strong and N. Boden, *J. Am. Chem. Soc.*, 2003, **125**, 9619–9628.

48. D. J. Adams, M. F. Butler, W. J. Frith, M. Kirkland, L. Mullen and P. Sanderson, *Soft Matter*, 2009, **5**, 1856–1862.

49. D. J. Adams, L. M. Mullen, M. Berta, L. Chen and W. J. Frith, *Soft Matter*, 2010, **6**, 1971–1980.

50. A. Z. Cardoso, A. E. Alvarez Alvarez, B. N. Cattoz, P. C. Griffiths, S. M. King, W. J. Frith and D. J. Adams, *Faraday Discuss*, 2013, **166**, 101–116.

51. G. Ben Messaoud, P. Le Griel, D. Hermida-Merino, S. L. K. W. Roelants, W. Soetaert, C. V. Stevens and N. Baccile, *Chem. Mater.*, 2019, **31**, 4817–4830.

52. L. Chen, T. O. McDonald and D. J. Adams, *RSC Adv.*, 2013, **3**, 8714–8720.

53. W. Ji, C. Yuan, S. Zilberzwige-Tal, R. Xing, P. Chakraborty, K. Tao, S. Gilead, X. Yan and E. Gazit, *ACS Nano*, 2019, **13**, 7300–7309.

54. J. Esch, F. Schoonbeek, M. Loos, E. Marc Veen, R. M. Kellogg and B. L. Feringa, in *Supramolecular Science: Where It Is and Where It Is Going*, Springer Netherlands, Dordrecht, 1999, pp. 233–259.

55. P. Dastidar, *Chem. Soc. Rev.*, 2008, **37**, 2699–2715.

56. D. J. Adams, *J. Am. Chem. Soc.*, 2022, **144**, 11047–11053.

57. G. M. Peters and J. T. Davis, *Chem. Soc. Rev.*, 2016, **45**, 3188–3206.

58. G. Rangel Euzcateguy, C. Parajua-Sejil, P. Marchal, D. Chapron, M.-C. Averlant-Petit, L. Stefan, G. Pickaert and A. Durand, *Polym. Int.*, 2021, **70**, 256–268.

59. R. N. Mitra, D. Das, S. Roy and P. K. Das, *J. Phys. Chem. B*, 2007, **111**, 14107–14113.

60. D. Bordignon, B. Lonetti, C. Coudret, P. Roblin, P. Joseph, L. Malaquin, A. Chalard and J. Fitremann, *J. Colloid Interface Sci.*, 2021, **603**, 333–343.

61. C. L. Smith, L. L. E. Mears, B. J. Greeves, E. R. Draper, J. Doutch, D. J. Adams and A. J. Cowan, *Phys. Chem. Chem. Phys.*, 2019, **21**, 26466–26476.

62. N. Singha, P. Gupta, B. Pramanik, S. Ahmed, A. Dasgupta, A. Ukil and D. Das, *Biomacromolecules*, 2017, **18**, 3630–3641.

63. P. W. J. M. Frederix, G. G. Scott, Y. M. Abul-Haija, D. Kalafatovic, C. G. Pappas, N. Javid, N. T. Hunt, R. V. Ulijn and T. Tuttle, *Nat. Chem.*, 2015, **7**, 30–37.

64. A. K. Patterson, L. H. El-Qarra and D. K. Smith, *Chem. Comm.*, 2022, **58**, 3941–3944.

65. J. K. Gupta, D. J. Adams and N. G. Berry, *Chem. Sci.*, 2016, **7**, 4713–4719.

66. J. Raeburn, A. Zamith Cardoso and D. J. Adams, *Chem. Soc. Rev.*, 2013, **42**, 5143–5156.

67. S. Panettieri and R. V Ulijn, *Curr. Opin. Struct. Biol.*, 2018, **51**, 9–18.

68. E. R. Draper and D. J. Adams, *Langmuir*, 2019, **35**, 6506–6521.

69. G. Ghosh and G. Fernández, *Beilstein J. Org. Chem.*, 2020, **16**, 2017–2025.

70. X. Lu, X. Li, K. Guo, T.-Z. Xie, C. N. Moorefield, C. Wesdemiotis and G. R. Newkome, *J. Am. Chem. Soc.*, 2014, **136**, 18149–18155.

71. V. A. Mallia, P. Terech and R. G. Weiss, *J. Phys. Chem. B*, 2011, **115**, 12401–12414.

72. Y. Xu, S. Fu, F. Liu, H. Yu and J. Gao, *Soft Matter*, 2018, **14**, 8044–8050.

73. L. J. White, C. Wark, L. Croucher, E. R. Draper and J. R. Hiscock, *Chem. Comm.*, 2020, **56**, 9557–9560.

74. R. Chevigny, E. D. Sitsanidis, J. Schirmer, E. Hulkko, P. Myllyperkiö, M. Nissinen and M. Pettersson, *Chem. Eur. J.*, 2023, **29**, e202000155.

75. B. Escuder, M. LLusar and J. F. Miravet, *J. Org. Chem.*, 2006, **71**, 7747–7752.

76. P. Li, C. Malveau, X. X. Zhu and J. D. Wuest, *Langmuir*, 2022, **38**, 5111–5118.

77. M. Wallace, J. A. Iggo and D. J. Adams, *Soft Matter*, 2015, **11**, 7739–7747.

78. S. M. Hashemnejad and S. Kundu, *Langmuir*, 2017, **33**, 7769–7779.

79. B. R. Denzer, R. J. Kulchar, R. B. Huang and J. Patterson, *Gels*, 2021, **7**, 158.

80. D. Adams, *Gels*, 2018, **4**, 32.

81. L. L. E. Mears, E. R. Draper, A. M. Castilla, H. Su, Zhuola, B. Dietrich, M. C. Nolan, G. N. Smith, J. Doutch, S. Rogers, R. Akhtar, H. Cui and D. J. Adams, *Biomacromolecules*, 2017, **18**, 3531–3540.

82. C. Marmorat, A. Arinstein, N. Koifman, Y. Talmon, E. Zussman and M. Rafailovich, *Sci. Rep.*, 2016, **6**, 25495.

83. E. R. Draper and D. J. Adams, *Chem. Soc. Rev.*, 2018, **47**, 3395–3405.

84. J.-B. Guilbaud and A. Saiani, *Chem. Soc. Rev.*, 2011, **40**, 1200–1210.

85. E. R. Draper, B. Dietrich, K. McAulay, C. Brasnett, H. Abdizadeh, I. Patmanidis, S. J. Marrink, H. Su, H. Cui, R. Schweins, A. Seddon and D. J. Adams, *Matter*, 2020, **2**, 764–778.

86. D. McDowall, D. J. Adams and A. M. Seddon, *Soft Matter*, 2022, **18**, 1577–1590.

87. C. J. Gommes, S. Jaksch and H. Frielinghaus, *J. Appl. Crystallogr.*, 2021, **54**, 1832–1843.

88. R. Henderson, *Q. Rev. Biophysics*, 1995, **28**, 171–193.

89. Q. Song, J. Yue, Y. Zhao, J. Zhu, Y. Lin, Q. Zhang, C. Pan, S. Liu, Z. Yang, L. Quan and Y. Wang, *Polymer*, 2022, **245**, 124701.

90. K. McAulay, H. Wang, A. M. Fuentes-Caparrós, L. Thomson, N. Khunti, N. Cowieson, H. Cui, A. Seddon and D. J. Adams, *Langmuir*, 2020, **36**, 8626–8631.

91. H. Endo, *Physica B Condens. Matter*, 2006, **385–386**, 682–684.

92. A. Poirier, P. Le Griel, I. Hoffmann, J. Perez, P. Pernot, J. Fresnais and N. Baccile, *Soft Matter*, 2023, **19**, 378–393.

93. R. I. Randle, A. M. Fuentes-Caparrós, L. P. Cavalcanti, R. Schweins, D. J. Adams and E. R. Draper, *J. Phys. Chem. C*, 2022, **126**, 13427–13432.

94. F. Del Giudice, M. Tassieri, C. Oelschlaeger and A. Q. Shen, *Macromolecules*, 2017, **50**, 2951–2963.

95. K. Almdal, J. Dyre, S. Hvidt and O. Kramer, *Polym. Gels Netw.*, 1993, **1**, 5–17.

96. A. Dawn and H. Kumari, *Chem. Eur. J.*, 2018, **24**, 762–776.

97. C. Yan and D. J. Pochan, *Chem. Soc. Rev.*, 2010, **39**, 3528–3540.

98. P. Dastidar, *Gels*, 2019, **5**, 15.

99. K. Kang, *J. Phys. Conf. Ser.*, 2022, **2152**, 012055.

100. P. Terech and R. G. Weiss, *Chem. Rev.*, 1997, **97**, 3133–3160.

101. V. Lakshminarayanan, C. Chockalingam, E. Mendes and J. H. van Esch, *ChemPhysChem*, 2021, **22**, 2256–2261.

102. S. M. Hashemnejad and S. Kundu, *Langmuir*, 2017, **33**, 7769–7779.

103. K. McAulay, P. A. Ucha, H. Wang, A. M. Fuentes-Caparrós, L. Thomson, O. Maklad, N. Khunti, N. Cowieson, M. Wallace, H. Cui, R. J. Poole, A. Seddon and D. J. Adams, *Chem. Comm.*, 2020, **56**, 4094–4097.

104. A. Arango-Restrepo, J. M. Rubi and D. Barragán, *J. Phys. Chem. B*, 2018, **122**, 4937–4945.

105. S. Panja and D. J. Adams, *Chem. Eur. J.*, 2020, **26**, 6130–6135.

106. S. Panja, K. Boháčová, B. Dietrich and D. J. Adams, *Nanoscale*, 2020, **12**, 12840–12848.

107. J. Wang, K. Liu, R. Xing and X. Yan, *Chem. Soc. Rev.*, 2016, **45**, 5589–5604.

108. F. Tantakitti, J. Boekhoven, X. Wang, R. V. Kazantsev, T. Yu, J. Li, E. Zhuang, R. Zandi, J. H. Ortony, C. J. Newcomb, L. C. Palmer, G. S. Shekhawat, M. O. De La Cruz, G. C. Schatz and S. I. Stupp, *Nat. Mater.*, 2016, **15**, 469–476.

109. Y. Li and Y. Cao, *Chinese J. Polym. Sci.*, 2018, **36**, 366–378.

110. Y. Yan, J. Huang and B. Z. Tang, *Chem. Comm.*, 2016, **52**, 11870–11884.

111. N. A. Dudukovic, B. C. Hudson, A. K. Paravastu and C. F. Zukoski, *Nanoscale*, 2018, **10**, 1508–1516.

112. J. Raeburn, C. Mendoza-Cuenca, B. N. Cattoz, M. A. Little, A. E. Terry, A. Zamith Cardoso, P. C. Griffiths and D. J. Adams, *Soft Matter*, 2015, **11**, 927–935.

113. Z. Huang, T. Jiang, J. Wang, X. Ma and H. Tian, *Angew. Chem. Int. Ed.*, 2021, **60**, 2855–2860.

114. J. S. Foster, J. M. Zurek, N. M. S. Almeida, W. E. Hendriksen, V. A. A. Le Sage, V. Lakshminarayanan, A. L. Thompson, R. Banerjee, R. Eelkema, H. Mulvana, M. J. Paterson, J. H. Van Esch and G. O. Lloyd, *J. Am. Chem. Soc.*, 2015, **137**, 14236–14239.

115. A. Aufderhorst-Roberts, W. J. Frith and A. M. Donald, *Soft Matter*, 2012, **8**, 5940–5946.

116. Xia Chen and S. Thibeault, *2013 35th Annual International Conference of the IEEE Engineering in Medicine and Biology Society (EMBC)*, 2013, 6228–6231.

117. F. E.-T. Heakal and A. E. Elkholy, *J. Mol. Liq.*, 2017, **230**, 395–407.

118. C. A. Dreiss, in *Wormlike Micelles: Advances in Systems, Characterisation and Applications*, Royal Society of Chemistry, Cambridge, 2017.

119. C. A. Dreiss, *Soft Matter*, 2007, **3**, 956–970.

120. D. Ghosh, L. J. Marshall, G. Ciccone, W. Liu, A. Squires, A. Seddon, M. Vassalli and D. J. Adams, *Macromol. Mater. Eng.*, 2023, **308**, 2300082.

121. K. McAulay, B. Dietrich, H. Su, M. T. Scott, S. Rogers, Y. K. Al-Hilaly, H. Cui, L. C. Serpell, A. M. Seddon, E. R. Draper and D. J. Adams, *Chem. Sci.*, 2019, **10**, 7801–7806.

122. K. M. Wolfe, M. Mooney, C. Crep, S. Rondeau-Gagné and G. C. Welch, *Flex. Print. Electron.*, 2022, **7**, 044007.

123. S. Zhang, M. A. Greenfield, A. Mata, L. C. Palmer, R. Bitton, J. R. Mantei, C. Aparicio, M. O. de la Cruz and S. I. Stupp, *Nat. Mater.*, 2010, **9**, 594–601.

124. D. McDowall, M. Walker, M. Vassalli, M. Cantini, N. Khunti, C. J. C. Edwards-Gayle, N. Cowieson and D. J. Adams, *Chem. Comm.*, 2021, **57**, 8782–8785.

125. B. D. Wall, S. R. Diegelmann, S. Zhang, T. J. Dawidczyk, W. L. Wilson, H. E. Katz, H. Mao and J. D. Tovar, *Adv. Mater.*, 2011, **23**, 5009–5014.

126. A. Chalard, L. Vaysse, P. Joseph, L. Malaquin, S. Souleille, B. Lonetti, J.-C. Sol, I. Loubinoux and J. Fitremann, *ACS Appl. Mater. Interfaces*, 2018, **10**, 17004–17017.

127. G. Liu, D. Zhang and C. Feng, *Angew. Chem. Int. Ed.*, 2014, **53**, 7789–7793.

128. E. R. Draper, H. Su, C. Brasnett, R. J. Poole, S. Rogers, H. Cui, A. Seddon and D. J. Adams, *Angew. Chem. Int. Ed.*, 2017, **56**, 10467–10470.

129. E. R. Draper, M. Wallace, R. Schweins, R. J. Poole and D. J. Adams, *Langmuir*, 2017, **33**, 2387–2395.

130. J. H. Yu, S. V. Fridrikh and G. C. Rutledge, *Polymer*, 2006, **47**, 4789–4797.

131. S. Debnath, S. Roy, Y. M. Abul-Haija, P. W. J. M. Frederix, S. M. Ramalhete, A. R. Hirst, N. Javid, N. T. Hunt, S. M. Kelly, J. Angulo, Y. Z. Khimyak and R. V. Ulijn, *Chem. Eur. J.*, 2019, **25**, 7881–7887.

132. C. G. Pappas, Y. M. Abul-Haija, A. Flack, P. W. J. M. Frederix and R. V. Ulijn, *Chem. Commun.*, 2014, **50**, 10630–10633.

133. D. M. Ryan, T. M. Doran, S. B. Anderson and B. L. Nilsson, *Langmuir*, 2011, **27**, 4029–4039.

134. D. M. Ryan, S. B. Anderson and B. L. Nilsson, *Soft Matter*, 2010, **6**, 3220–3231.

135. W. Liyanage and B. L. Nilsson, *Langmuir*, 2016, **32**, 787–799.

136. C. Tang, A. M. Smith, R. F. Collins, R. V. Ulijn and A. Saiani, *Langmuir*, 2009, **25**, 9447–9453.

137. S. Wan, M. Jiang and G. Zhang, *Macromolecules*, 2007, **40**, 5552–5558.

138. S. Panja and D. J. Adams, *Chem. Comm.*, 2019, **55**, 47–50.

139. E. R. Draper, J. J. Walsh, T. O. McDonald, M. A. Zwijnenburg, P. J. Cameron, A. J. Cowan and D. J. Adams, *J. Mater. Chem. C*, 2014, **2**, 5570–5575.

140. M. C. Nolan, J. J. Walsh, L. L. E. Mears, E. R. Draper, M. Wallace, M. Barrow, B. Dietrich, S. M. King, A. J. Cowan and D. J. Adams, *J Mater. Chem. A Mater.*, 2017, **5**, 7555–7563.

141. B. A. K. Kriebisch, C. M. E. Kriebisch, A. M. Bergmann, C. Wanzke, M. Tena-Solsona and J. Boekhoven, *ChemSystemsChem*, 2023, **5**, e20220035.

142. E. R. Draper, L. Wilbraham, D. J. Adams, M. Wallace, R. Schweins and M. A. Zwijnenburg, *Nanoscale*, 2019, **11**, 15917–15928.

143. J. Nanda, A. Biswas and A. Banerjee, *Soft Matter*, 2013, **9**, 4198–4208.

144. R. Pugliese, F. Fontana, A. Marchini and F. Gelain, *Acta Biomater.*, 2018, **66**, 258–271.

145. C. B. Highley, C. B. Rodell and J. A. Burdick, *Adv. Mater.*, 2015, **27**, 5075–5079.

146. L. Latxague, M. A. Ramin, A. Appavoo, P. Berto, M. Maisani, C. Ehret, O. Chassande and P. Barthélémy, *Angew. Chem. Int. Ed.*, 2015, **54**, 4517–4521.

147. K. J. Skilling, B. Kellam, M. Ashford, T. D. Bradshaw and M. Marlow, *Soft Matter*, 2016, **12**, 8950–8957.

148. S. Roy, N. Javid, J. Sefcik, P. J. Halling and R. V. Ulijn, *Langmuir*, 2012, **28**, 16664–16670.

149. K. Aoki, K. Shiraki and T. Hattori, *Phys. Chem. Chem. Phys.*, 2016, **18**, 15060–15069.

150. B. Kang, H. Tang, Z. Zhao and S. Song, *ACS Omega*, 2020, **5**, 6229–6239.

151. Y. Li, T. Zhao, C. Wang, Z. Lin, G. Huang, B. D. Sumer and J. Gao, *Nat. Commun.*, 2016, **7**, 13214.

152. C. Liu, Y. Wang, Y. Gao, Y. Zhang, L. Zhao, B. Xu and L. S. Romsted, *Phys. Chem. Chem. Phys.*, 2019, **21**, 8633–8644.

153. N. Vlachy, M. Drechsler, J.-M. Verbavatz, D. Touraud and W. Kunz, *J. Colloid Interface Sci.*, 2008, **319**, 542–548.

154. G. O. Lloyd and J. W. Steed, *Nat. Chem.*, 2009, **1**, 437–442.

155. A. Klaus, G. J. T. Tiddy, R. Rachel, A. P. Trinh, E. Maurer, D. Touraud and W. Kunz, *Langmuir*, 2011, **27**, 4403–4411.

156. A. M. Hyde, S. L. Zultanski, J. H. Waldman, Y.-L. Zhong, M. Shevlin and F. Peng, *Org. Process Res. Dev.*, 2017, **21**, 1355–1370.

157. M. C. Mañas-Torres, C. Gila-Vilchez, J. A. González-Vera, F. Conejero-Lara, V. Blanco, J. M. Cuerva, M. T. Lopez-Lopez, A. Orte and L. Álvarez de Cienfuegos, *Mater. Chem. Front.*, 2021, **5**, 5452–5462.

158. S. Roy, N. Javid, P. W. J. M. Frederix, D. A. Lamprou, A. J. Urquhart, N. T. Hunt, P. J. Halling and R. V. Ulijn, *Chem. Eur. J.*, 2012, **18**, 11723–11731.

159. H. K. Can and S. Parvizikhosroshahi, *Artif. Cells Nanomed. Biotechnol.*, 2016, **44**, 680–689.

160. J. L. Li, X. Y. Liu, C. S. Strom and J. Y. Xiong, *Adv. Mater.*, 2006, **18**, 2574–2578.

161. J. Li and X. Liu, *Adv. Funct. Mater.*, 2010, **20**, 3196–3216.

162. Y. J. Adhia, T. H. Schloemer, M. T. Perez and A. J. McNeil, *Soft Matter*, 2012, **8**, 430–434.

163. J.-L. Li, B. Yuan, X.-Y. Liu, X.-G. Wang and R.-Y. Wang, *Cryst. Growth Des.*, 2011, **11**, 3227–3234.

164. M. Numata, K. Sugiyasu, T. Kishida, S. Haraguchi, N. Fujita, S. M. Park, Y. J. Yun, B. H. Kim and S. Shinkai, *Org. Biomol. Chem.*, 2008, **6**, 712–718.

165. J.-L. Li and X.-Y. Liu, *J. Phys. Chem. B*, 2009, **113**, 15467–15472.

166. L. Chen, S. Revel, K. Morris, D. G. Spiller, L. C. Serpell and D. J. Adams, *Chem. Comm.*, 2010, **46**, 6738–6740.

167. G. Pont, L. Chen, D. G. Spiller and D. J. Adams, *Soft Matter*, 2012, **8**, 7797–7802.

168. P. Chakraborty, M. Ghosh, L. Schnaider, N. Adadi, W. Ji, D. Bychenko, T. Dvir, L. Adler-Abramovich and E. Gazit, *Macromol. Rapid Commun.*, 2019, **40**, 1900175.

169. Md. M. Hassan, A. D. Martin and P. Thordarson, *J. Mater. Chem. B*, 2015, **3**, 9269–9276.

170. B. O. Okesola and D. K. Smith, *Chem. Soc. Rev.*, 2016, **45**, 4226–4251.

171. A. Á. Toronyi, D. Giuri, S. Martiniakova and C. Tomasini, *Cosmetics*, 2023, **10**, 38.

172. M. A. Elsawy, J. K. Wychowaniec, L. A. Castillo Díaz, A. M. Smith, A. F. Miller and A. Saiani, *Biomacromolecules*, 2022, **23**, 2624–2634.

173. J. Y. C. Lim, Q. Lin, K. Xue and X. J. Loh, *Mater. Today Adv.*, 2019, **3**, 100021.

174. S. Banerjee, R. K. Das and U. Maitra, *J. Mater. Chem.*, 2009, **19**, 6649–6687.

175. D. K. Smith, *Soft Matter*, 2024, **20**, 10–70.

176. F. Andriamiseza, D. Bordignon, B. Payré, L. Vaysse and J. Fitremann, *J. Colloid Interface Sci.*, 2022, **617**, 156–170.

177. Y. Zhou and X. Li, *Chinese Chem. Lett.*, 2017, **28**, 1835–1840.

178. Y. Zhou, M. Layani, S. Wang, P. Hu, Y. Ke, S. Magdassi and Y. Long, *Adv. Funct. Mater.*, 2018, **28**, 1705365.

179. M. C. Nolan, A. M. Fuentes Caparrós, B. Dietrich, M. Barrow, E. R. Cross, M. Bleuel, S. M. King and D. J. Adams, *Soft Matter*, 2017, **13**, 8426–8432.

180. H. Jian, M. Wang, Q. Dong, J. Li, A. Wang, X. Li, P. Ren and S. Bai, *ACS Appl. Mater. Interfaces*, 2019, **11**, 46419–46426.

181. A. M. Fuentes-Caparras, Z. Canales-Galarza, M. Barrow, B. Dietrich, J. Laüger, M. Nemeth, E. R. Draper and D. J. Adams, *Biomacromolecules*, 2021, **22**, 1625–1638.

182. H. Song, S. Ding, M. Zhao and Q. Hu, *Chemosensors*, 2022, **10**, 415.

183. S. Bhuniya and B. H. Kim, *Chem. Comm.*, 2006, 1842–1844.

184. F. Mandegani, H. Zali-Boeini, Z. Khayat and R. Scopelliti, *Talanta*, 2020, **219**, 121237.

185. R. Dong, Y. Pang, Y. Su and X. Zhu, *Biomater. Sci.*, 2015, **3**, 937–954.

186. E. R. Draper, J. R. Lee, M. Wallace, F. Jäckel, A. J. Cowan and D. J. Adams, *Chem. Sci.*, 2016, **7**, 6499–6505.

187. R. S. Moghaddam, E. R. Draper, C. Wilson, H. Heidari and D. J. Adams, 2018, **8**, 34121–34125.

188. S. Roy, D. Kumar Maiti, S. Panigrahi, D. Basak and A. Banerjee, *RSC Adv.*, 2012, **2**, 11053–11060.

189. D. Görl, X. Zhang and F. Würthner, *Angew. Chem. Int. Ed.*, 2012, **51**, 6328–6348.

190. J. Yao, Q. Chen, C. Zhang, Z. Zhang and Y. Li, *SusMat*, 2022, **2**, 243–263.

191. R. K. Dubey and F. Würthner, *Nat. Chem.*, 2023, **15**, 884–884.

192. E. R. Draper, L. J. Archibald, M. C. Nolan, R. Schweins, M. A. Zwijnenburg, S. Sproules and D. J. Adams, *Chem. Eur. J.*, 2018, **24**, 4006–4010.

193. D. Inan, R. K. Dubey, W. F. Jager and F. C. Grozema, *J. Phys. Chem. C*, 2019, **123**, 36–47.

194. Y. Jiao, K. Liu, G. Wang, Y. Wang and X. Zhang, *Chem. Sci.*, 2015, **6**, 3975–3980.

195. D. Schmidt, D. Bialas and F. Würthner, *Angew. Chem. Int. Ed.*, 2015, **54**, 3611–3614.

196. R. O. Marcon and S. Brochsztain, *Langmuir*, 2007, **23**, 11972–11976.

197. E. Shirman, A. Ustinov, N. Ben-Shitrit, H. Weissman, M. A. Iron, R. Cohen and B. Rybtchinski, *J. Phys. Chem. B*, 2008, **112**, 8855–8858.

198. M. A. Iron, R. Cohen and B. Rybtchinski, *J. Phys. Chem. A*, 2011, **115**, 2047–2056.

199. J. J. Walsh, J. R. Lee, E. R. Draper, S. M. King, F. Jäckel, M. A. Zwijnenburg, D. J. Adams and A. J. Cowan, *J. Phys. Chem. C*, 2016, **120**, 18479–18486.

200. E. R. Draper, B. J. Greeves, M. Barrow, R. Schweins, M. A. Zwijnenburg and D. J. Adams, *Chem*, 2017, **2**, 716–731.

201. S. Yagai, T. Seki, T. Karatsu, A. Kitamura and F. Würthner, *Angew. Chem. Int. Ed.*, 2008, **47**, 3367–3371.

202. F. Würthner, C. Thalacker, S. Diele and C. Tschierske, *Chemistry (Easton)*, 2001, **7**, 2245–2253.

203. G. Pescitelli, L. Di Bari and N. Berova, *Chem. Soc. Rev.*, 2014, **43**, 5211–5233.

204. E. Krieg, E. Shirman, H. Weissman, E. Shimoni, S. G. Wolf, I. Pinkas and B. Rybtchinski, *J. Am. Chem. Soc.*, 2009, **131**, 14365–14373.

205. J. E. Anthony, J. S. Brooks, D. L. Eaton and S. R. Parkin, *J. Am. Chem. Soc.*, 2001, **123**, 9482–9483.

206. M. T. Usowicz, M. J. Kelley, K. D. Singer and V. V. Duzhko, *J. Phys. Chem. B*, 2011, **115**, 9703–9709.

207. K. Balakrishnan, A. Datar, T. Naddo, J. Huang, R. Oitker, M. Yen, J. Zhao and L. Zang, *J. Am. Chem. Soc.*, 2006, **128**, 7390–7398.

208. L. Rocard, A. Goujon and P. Hudhomme, *Molecules*, 2020, **25**, 1402.

209. S. L. Haddow, D. J. Ring, H. Bagha, N. Pearce, H. Nowell, A. J. Blake, W. Lewis, J. McMaster and N. R. Champness, *Cryst. Growth Des.*, 2018, **18**, 802–807.

210. Z. Guo, X. Zhang, Y. Wang and Z. Li, *Langmuir*, 2019, **35**, 342–358.

211. F. Würthner, C. R. Saha-Möller, B. Fimmel, S. Ogi, P. Leowanawat and D. Schmidt, *Chem. Rev.*, 2016, 116, 962–1052.

212. C. Huang, S. Barlow and S. R. Marder, *J. Org. Chem.*, 2011, **76**, 2386–2407.

213. R. Renner, B. Mahlmeister, O. Anhalt, M. Stolte and F. Würthner, *Chem. Eur. J.*, 2021, **27**, 11997–12006.

214. A. G. Slater, E. S. Davies, S. P. Argent, W. Lewis, A. J. Blake, J. McMaster and N. R. Champness, *J. Org. Chem.*, 2013, **78**, 2853–2862.

215. N. Pearce, E. S. Davies and N. R. Champness, *Dyes and Pigments*, 2020, **183**, 108735.

216. F. Würthner, P. Osswald, R. Schmidt, T. E. Kaiser, H. Mansikkamäki and M. Könemann, *Org. Lett.*, 2006, **8**, 3765–3768.

217. Á. J. Jiménez, M.-J. Lin, C. Burschka, J. Becker, V. Settels, B. Engels and F. Würthner, *Chem. Sci.*, 2014, **5**, 608–619.

218. P. Osswald and F. Würthner, *J. Am. Chem. Soc.*, 2007, **129**, 14319–14326.

219. J. E. Bullock, M. T. Vagnini, C. Ramanan, D. T. Co, T. M. Wilson, J. W. Dicke, T. J. Marks and M. R. Wasielewski, *J. Phys. Chem. B*, 2010, **114**, 1794–1802.

220. J. Wu, D. He, Y. Wang, F. Su, Z. Guo, J. Lin and H.-J. Zhang, *Org. Lett.*, 2018, **20**, 6117–6120.

221. Y. Fan, K. Ziabrev, S. Zhang, B. Lin, S. Barlow and S. R. Marder, *ACS Omega*, 2017, **2**, 377–385.

222. S. Nakazono, S. Easwaramoorthi, D. Kim, H. Shinokubo and A. Osuka, *Org. Lett.*, 2009, **11**, 5426–5429.

223. S. Nakazono, Y. Imazaki, H. Yoo, J. Yang, T. Sasamori, N. Tokitoh, T. Cédric, H. Kageyama, D. Kim, H. Shinokubo and A. Osuka, *Chem. Eur. J.*, 2009, **15**, 7530–7533.

Chapter 2: Using Solution History to Control Hydrogel Properties of a Perylene Bisimide

This Chapter is adapted from the following publication:

"Using Solution History to Control Hydrogel Properties of a Perylene Bisimide".

R. E. Ginesi, N. R. Murray, R. M. Dalgliesh, J. Doutch and E. R. Draper, *Chem. Eur. J.*, 2023, e202301042.

REG was responsible for the synthesis of the gelator molecule used. Small-angle neutron scattering data were collected by REG and ERD. RMD and JD processed the SANS data. REG fitted the SANS data. REG was responsible for all other methodology, collection of data, and analysis. REG and ERD conceptualised the project. ERD supervised the project. REG and ERD wrote the initial draft of the manuscript, to which all authors contributed for the final publication. All other authors listed above contributed to the paper this Chapter is adapted from, but their work is not shown in this Chapter.

2.1 Introduction

In Chapter 1, we discussed how low molecular weight gelators (LMWGs) can self-assemble to form entangled gelatinous networks.[1–5] The mechanical properties of the final gel depend not only on the molecular structure of the LMWG but also critically on the self-assembly process.[6] Although the literature frequently discusses the importance of gel reproducibility,[7–9] there is usually very little consideration given to the pre-gel solution.

Many groups have reported the presence of self-assembled structures in these LMWG precursor solutions.[10–12] As LMWGs commonly behave as surfactants, micellar aggregates (e.g. spherical, cylindrical, or worm-like micelles) can form in the pre-gel solution phase above the critical micelle concentration and Krafft temperature.[13–16] The chemical structure,[17] concentration,[18,19] and counterions involved in solubilisation of the LMWG are all known to influence the self-assembly of these molecules.[13,20,21] The resulting structures that form will ultimately impact the final properties of the hydrogel upon triggering gelation. External conditions such as temperature,[22] solvent,[23,24] additives,[25,26] and pH[27] can also impact the structures that make up the gel network. Such factors influence morphology by affecting the molecules themselves or changing the kinetics of assembly, which in turn, changes the final aggregated form.

Our group commonly reports on the pH-dependent aggregation of amino acid-appended perylene bisimides (PBIs).[28,29] These PBIs are soluble in water at high pH due to deprotonation of the terminal carboxylic acid groups.[30–33] When the pH decreases below the pK_a value of the gelator, these carboxylic groups become protonated, and a hydrogel can form.[33,34] Such PBIs have two "apparent" pK_a values associated with the pK_a of the self-assembled structures as opposed to the single molecule (we would expect both carboxylic groups to have the same pK_a value at around pH 3-5 in unaggregated systems), giving various aggregated states due to solubility (Fig. 2.1).[35–38] The type of aggregate which forms is crucial as it directly affects the conductivity pathways and optoelectronic properties.[29] For a PBI appended with the amino acid *L*-DOPA (PBI-DOPA), Draper *et al.* could reversibly switch between an H-type and J-type aggregate by adjusting the pH.[29] The type of aggregate initially formed was determined by the equivalents of base (0.1 M NaOH, aq) added during sample preparation. The aggregates displayed different properties, with the J-type aggregates unable to form a gel upon lowering the pH using glucono-δ-lactone (GdL).

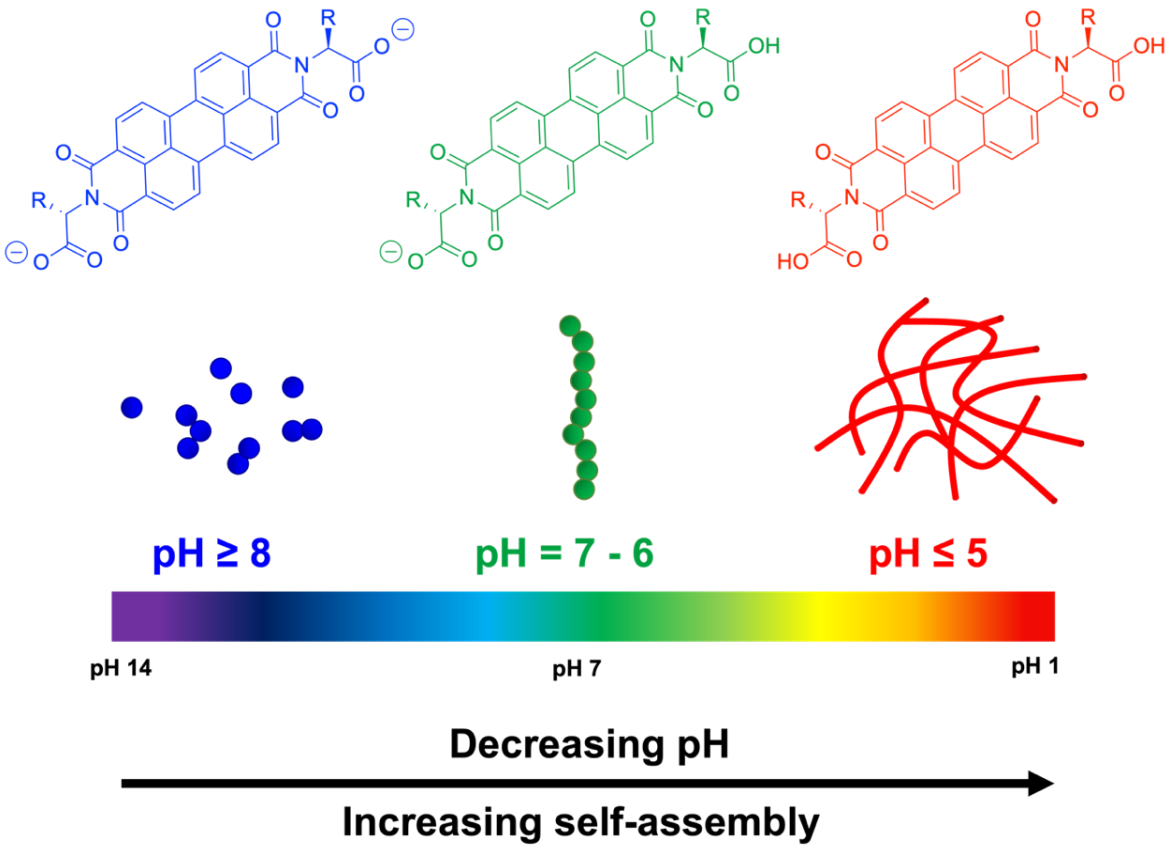

Figure 2.1. Cartoon showing PBI molecules forming different aggregates with changing pH due to various extents of deprotonation of **PBI-R** (**R** = amino acid sidechain).

For pH-triggered gels, there are many examples of tuning the gelation kinetics to form gels with different properties. Lakshminarayanan *et al.* investigated how changing the gelation kinetics impacted the final gel properties of a dipeptide gelator (dibenzoyl-*L*-cystine).[39] To alter this kinetic process, they used different concentrations of GdL to change the rate of acidification. They found that faster GdL hydrolysis (*i.e.*, using a higher concentration of GdL) resulted in weaker gels with microstructural inhomogeneities. Such results have also been seen with Fmoc-dipeptide gels.[40]

Similarly, the Baccile group have also used kinetic control to modify the mechanical properties of stearic acid sophorolipid-based hydrogels.[27] The kinetics were altered by changing the pH-trigger, using either hydrochloric acid (HCl) or GdL. When HCl was used, weak gels were formed due to the promotion of fibre branching. The GdL-triggered gels showed little to no branching, forming stronger hydrogels. Similar differences due to the mode of pH decrease have been observed by Adams *et al*. However, they did not observe an impact on the final gel properties, which were instead affected by the final pH of the hydrogel.[34,41,42]

Currently, whether the initial pH plays a role in the bulk properties of the gel is not as well understood.[27] Singh *et al.* studied the self-assembly and gelation of a 9-fluorenylmethyloxycarboxnyl (Fmoc) derivative of 3-nitrotyrosine (3-NT, FNT) in different phosphate buffer solutions ranging from pH 5-8.5.[43] This molecule was chosen as the phenolic hydroxyl group is highly sensitive to pH due to the electron-withdrawing nitro group of the FNT molecule. The gelation kinetics were dependent on the pH of the buffer, with higher pH buffers taking longer to gel, which impacted gel stiffness. Scanning electron microscopy (SEM) and transmission electron microscopy (TEM) showed that all gels formed nanofibres. However, the fibres were smaller and less overlapped for the gels formed at lower pHs (pH 5 and 6). However, this article does not provide much detail into how the solutions were prepared.

Commonly in the literature, different mechanical properties are achieved using different gelation triggers.[41] Often, these assembly conditions may not be suitable for the final applications. For example, high temperatures and solvents such as DMSO can be detrimental to cells, making them unsuitable for use as cell growth media.[44,45] However, we hypothesise that by simply changing the conditions of the pre-gel solution, one can use the same gelation trigger to form gels with different mechanical properties. The advantage of this is that a reproducible gelation trigger, such as GdL,[7] can be used, and the properties precisely fine-tuned to suit the chosen application. This reproducibility is crucial in most applications, especially for device fabrication.

In this chapter, we aim to investigate the effect of changing the pre-gel solution pH (and thus the pre-aggregated starting form) on the gelation kinetics and final gel properties of an amino acid-appended PBI. We show that the molecular packing and aggregation state can be tuned by changing the pre-gelation pH, which results in hydrogels with different bulk properties, thus reducing the need to design a new LWMG from scratch.

2.2. Results and Discussion

We focus here on **PBI-A** (Fig. 2.2), a well-studied LMWG within the group, with interesting photoelectric behaviour due to the formation of a radical anion on exposure to UV light.[36,46–48] We investigate two starting pHs: pH 9, where the molecules are more soluble, and pH 6, which is between the two "apparent" pK_a values of this gelator (6.8 and 5.3, Fig. A.1.1, Appendix). As the pK_a indicates the pH at which these structures change,[35,49] we can expect

the structures formed at these two pHs to be different. Therefore, we can investigate the impact this change in aggregation has on the bulk properties of the resulting hydrogels.

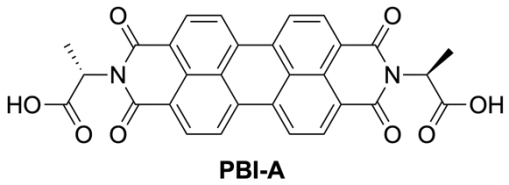

PBI-A

Figure 2.2. Structure of **PBI-A** used in this chapter.

PBI-A was synthesised as described in Section 2.4.1. Stock solutions of the gelator were prepared at a concentration of 5 mg/mL, adding either 1 or 2 equivalents of NaOH (0.1 M, aq) to give solutions with an initial pH of 6 and 9, respectively. Homogenous hydrogels were formed by adding GdL. As discussed in Chapter 1, GdL hydrolyses slowly to gluconic acid, resulting in a slow and uniform change in pH throughout the system.[7,50–52] 7.5 mg/mL and 10 mg/mL of GdL were used for solutions starting at pH 6 and 9, respectively, to give a gel with a final pH of 3.2. By controlling the final pH of the gel, we could correlate any observed differences to the gelation kinetics rather than the pH of the gel.

2.2.1 Differences in Aggregation – Solution Phase

First, we determined whether there were any differences in aggregation in the solutions at the different pHs using UV-visible (UV-vis) absorption spectroscopy. PBIs have distinct absorption bands at 490 and 540 nm, attributed to the 0-0 and 0-1 vibronic bands of the S_0-S_1 transitions.[33,37,46,53] The intensity, resolution, and shift of the absorbance bands depend on the environment around the aromatic core, allowing UV-vis absorption spectroscopy to be used to study aggregation processes.[37] The absorbance spectra at pH 6 and 9 showed a shoulder at 470 nm and two distinct absorbances at 490 and 540 nm (Fig. 2.3a). As there is no shift in the absorbance wavelengths with changing pH, we infer no drastic structural changes occur. However, the difference in the ratios of the absorbances at 490 and 540 nm suggests a difference in molecular packing of the aggregates for each pH.[54,55] The ratios of the peaks are 0.90:0.64 and 0.79:0.67 (490:540 nm) for pH 6 and 9, respectively. Such behaviour has also been reported in amino acid-appended naphthalene diimides (NDIs).[56] At pH 6, the spectrum is broader, and the peaks are less defined, suggesting that these solutions are more aggregated.[57] At pH 6, we expect the molecules to be fully protonated and less charged, increasing the fibre-fibre interactions and reducing any electrostatic repulsion which may be influencing the aggregates at higher pH.[38] Differences were also

observed in the fluorescence data, with pH 6 and 9 solutions having different ratios in the emission spectra and pH 6 being slightly more fluorescent than pH 9 (Fig. 2.3b).

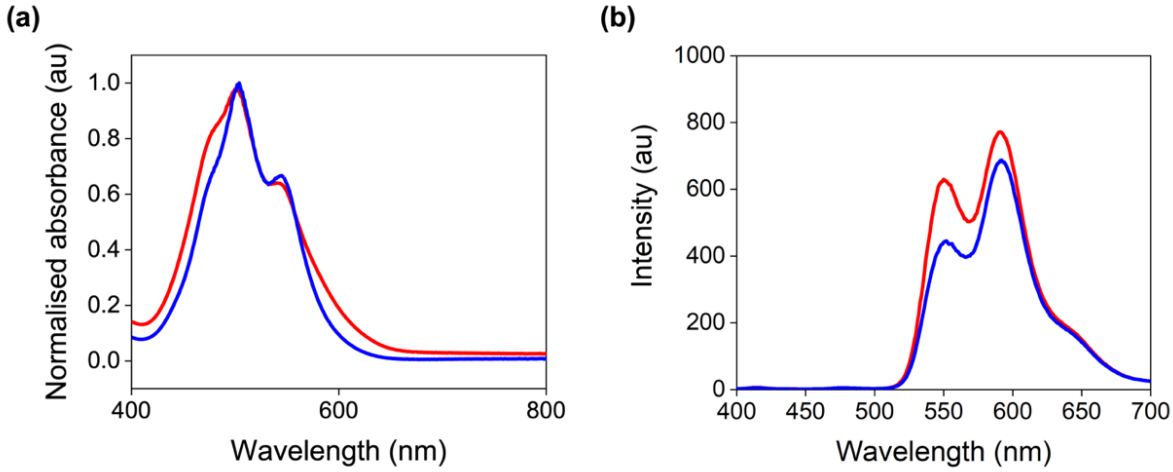

Figure 2.3. (a) UV-vis absorption spectra of **PBI-A** solutions at pH 6 (red) and pH 9 (blue). Data is normalised to the highest absorption of each spectrum. (b) Fluorescence spectra of **PBI-A** solutions at pH 6 (red) and pH 9 (blue). Fluorescence spectra were collected at an excitation of 365 nm and a gelator concentration of 0.05 mg/mL to minimise quenching of the fluorescence.

This difference in aggregation was also observed in the dynamic viscosity measurements (Fig. 2.4). Shear-thinning behaviour was observed at pH 6, indicating the presence of worm-like micelles or fibrous-type structures.[15,29,58,59] The decrease in viscosity upon increasing the shear rate is due to the alignment of these structures and the fibres interacting less with each other.[60] This behaviour was not observed at pH 9, which had a viscosity close to that of water, which we have previously reported.[53] Such results suggest that the **PBI-A** molecules were more dispersed or not forming persistent aggregates in solution, which was further suggested by the viscosity at low shear. Differences in the 1D structures' morphology, length, or abundance will result in a difference in the viscosity at low shear. The increase in viscosity at low shear at pH 6 further suggests these solutions are more aggregated, in agreement with the UV-vis data.

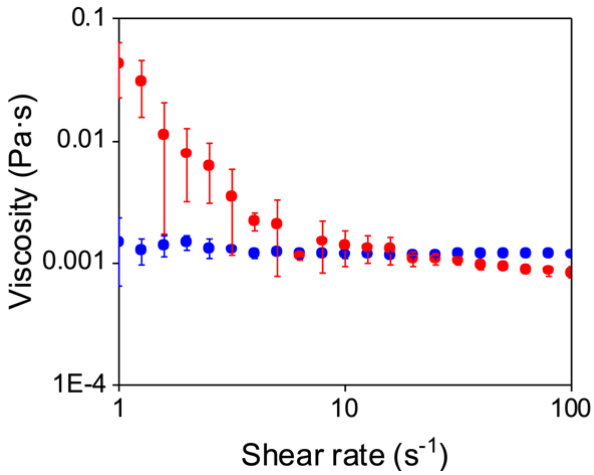

Figure 2.4. Dynamic viscosity of **PBI-A** solutions at pH 6 (red) and pH 9 (blue).

To investigate the aggregation further, small-angle neutron scattering (SANS) was used. As discussed in Chapter 1, SANS can determine the fibre-level assembly of LMWGs and fit to mathematical models to determine information about the length, radius, and flexibility of the fibres.[52] Typically, amino-acid appended PBI systems have been modelled using various cylindrical or spherical models.[29,46,61] As samples are prepared in deuterated solvents, pD is used rather than pH. Solutions at pD 9 could not be fit to a suitable model, suggesting the presence of either poorly scattering structures or non-persistent aggregates (Fig. 2.5),[62] correlating with the UV-vis and viscosity data. In comparison, the scattering at pD 6 showed aggregates had formed, which could be best fit to a flexible elliptical cylinder combined with a power law to consider the scattering at low Q. Such data are comparable with those previously reported by our group for **PBI-A**.[46] The fit depicts flexible elliptical cylindrical fibres with a radius of 43 Å and a Kuhn length of 179 Å (Table 2.1). The length of the cylinders is outside of the Q range of this technique (greater than 100 nm) and so cannot be reliably fitted.[52,63,64]

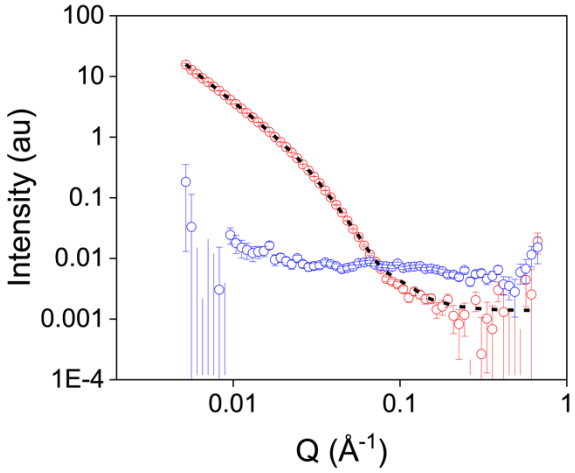

Figure 2.5. Small-angle neutron scattering patterns from **PBI-A** solutions at pD 6 (red) and pD 9 (blue). Open circles show the data and black dashed lines represent the fit.

Table 2.1. Tabulated parameters of the SANS model fit for a **PBI-A** solution at pD 6.

Flexible Elliptical Cylinder + Power Law	**Value**	**Error**
Background (cm^{-1})	0.007	
Cylinder scale	1.8153×10^{-4}	4.3214×10^{-6}
Length (Å)	2484	502
Kuhn length (Å)	179	5.2
Radius (Å)	42.7	0.5
Axis ratio	2.3	0.04
Power law scale	3.2971×10^{-6}	3.1231×10^{-7}
Power law	2.8	0.02
χ^2	2.5789	

2.2.1 Differences in Aggregation – Gel Phase

We wanted to see whether these differences in aggregation would impact the properties of the resulting hydrogels. Gelation was induced by adding the appropriate amount of GdL. UV-vis absorption spectroscopy showed significant differences in the molecular packing within the gels formed from the two starting pHs (Fig. 2.6). Both gels gave spectra that were broader than those for the corresponding solutions, which is due to the gels being denser and more assembled. Furthermore, there is a change in the ratio of absorbance for the 0-0 and 0-1 vibronic bands of the S_0-S_1 transitions compared to the solutions. This change in ratio is expected since the molecular packing changes as the fibres entangle and form a gel network.[65] Again, we see a difference in the broadness of the two spectra, showing a difference in aggregation between the two gels. However, the spectra of both gels undergo a hypsochromic shift, suggesting the formation of H-type aggregates upon gelation.[33] This shift is more significant in gels formed from solutions starting at pH 9 (referred to as Gel-1) than those starting at pH 6 (referred to as Gel-2).

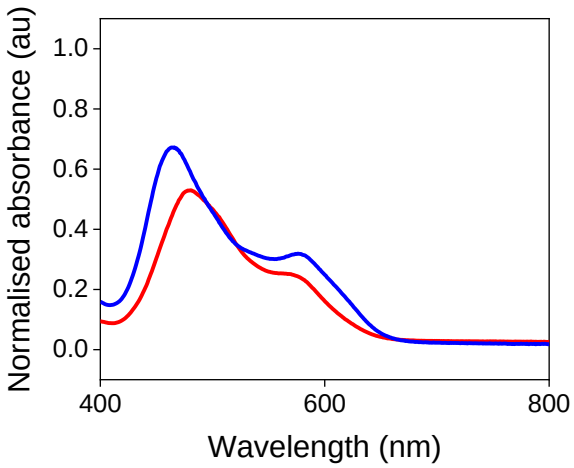

Figure 2.6. UV-vis absorption data of **PBI-A** Gel-1 (blue) and Gel-2 (red). Data is normalised to the highest absorption of each spectrum.

Rheological strain sweeps showed that both gels had a single yield point (Fig. 2.7), suggesting that they have one dominating factor controlling the mechanical properties. However, the gel strength and stiffness were influenced by the starting pH. Gel-1 was stiffer than Gel-2 (G′ values at 0.1% strain of 600 Pa and 170 Pa for Gel-1 and Gel-2, respectively). Furthermore, Gel-2 was stronger, with a higher yield point of 12.6%, compared to 3.2% for Gel-1. This difference in strength suggests that the way the fibres entangle and interact with each other may have changed or that different types of fibres are present within the gels.

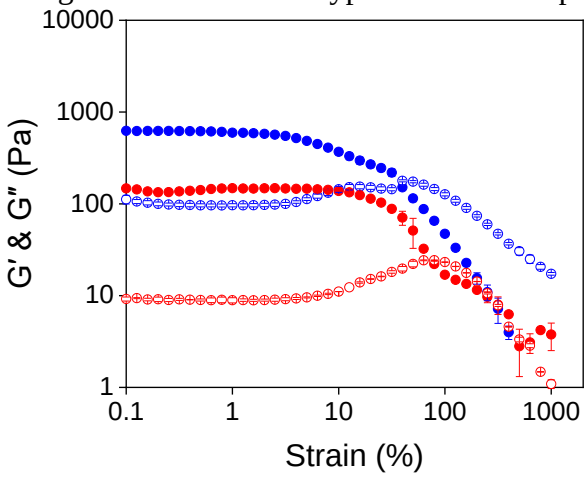

Figure 2.7. Strain sweeps of **PBI-A** Gel-1 (blue) and Gel-2 (red). Closed circles represent G′ and open circles represent G″. Data shown are averaged data for triplicate runs, with error bars representing standard deviation.

As the rheological data suggested differences in the fibres within the different gels, we again used SANS to probe the gel structures. The scattering data for Gel-1 fit to an elliptical cylinder with a power law (Fig. 2.8b). The radius of the fibres was 61 Å (Table 2.2). In

comparison, the data for Gel-2 best fit to a flexible elliptical cylinder with a power law (Fig. 2.8a) and a radius of 35 Å (Table 2.3), suggesting that smaller aggregates are present in this gel. The power law is very similar for both samples, meaning that the larger length scale structures and networks are similar. Therefore, any changes in the scattering are due to the fibres themselves. The SANS data clearly demonstrate the differences in the two gels formed and further explain the rheological data. The increase in stiffness of Gel-1 could be due to the formation of elliptical cylindrical fibres,[66] which are more rigid than the flexible elliptical fibres found in Gel-2. Furthermore, the increase in strength of Gel-2 can also be explained by the scattering data. The increased flexibility of the fibres in these gels may allow the gel to withstand higher stress as the fibres have more freedom of movement, which facilitates yielding under the force applied without breaking.[67]

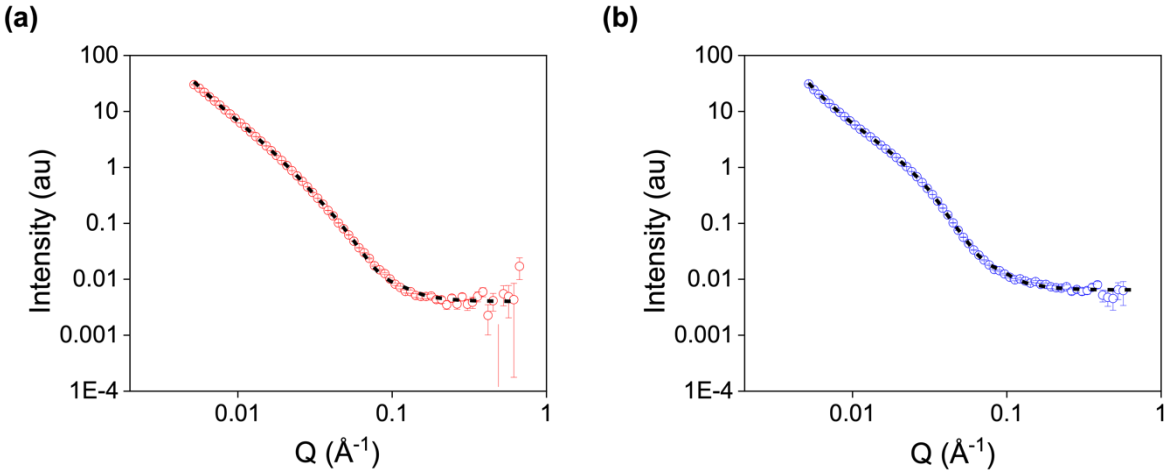

Figure 2.8. Small-angle neutron scattering of **PBI-A** (a) Gel-2 and (b) Gel-1. Open circles show the data and black dashed lines represent the fits.

Table 2.2. Parameters of the SANS model fit for **PBI-A** Gel-1.

Elliptical Cylinder + Power Law	**Value**	**Error**
Background (cm^{-1})	0.007	
Cylinder scale	7.5974×10^{-4}	8.7217×10^{-6}
Length (Å)	328	4
Radius (Å)	60.9	0.3
Axis ratio	1.9	0.02
Power law scale	4.8562×10^{-6}	2.8229×10^{-7}
Power law	2.90	0.01
χ^2	3.5974	

Table 2.3. Parameters of the SANS model fit for **PBI-A** Gel-2.

Flexible Elliptical Cylinder + Power Law	**Value**	**Error**
Background (cm^{-1})	0.07	
Cylinder scale	2.2163×10^{-4}	2.0519×10^{-6}
Length (Å)	2484	502
Kuhn length (Å)	112.6	8.4
Radius (Å)	34.5	0.8
Axis ratio	2.8	0.05
Power law scale	6.3390×10^{-6}	5.0770×10^{-7}
Power law	2.84	0.02
χ^2	3.4305	

2.2.3 Difference in Kinetics

We hypothesised that the differences in the rheological and structural properties of the gels were due to different gelation kinetics since the final pH of the gels was the same. In theory, Gel-1 would have more open freedom in the structures they can form upon gelation, whereas at pH 6, the structures are "locked in", limiting the possibility of different aggregates upon its gelation. The controlled reproducible hydrolysis of GdL allows the gelation to be followed using numerous techniques, provided that the temperature and concentration are accurately controlled.[7] As previously discussed, for gelation to occur, the pH must be below the pK_a of the chosen gelator.[68] At the pK_a value, half of the carboxylic acid moieties of the PBI are protonated. As a result of the hydrophobic effect, the gelator molecules begin to stack on top of each other to develop fibres and eventually form a gel.[69] Therefore, the stages of gelation can be observed by monitoring the pH change over time. Furthermore, rheological time sweeps can show the evolution of the storage modulus (G′) and the loss modulus (G″) with time. ^{1}H NMR spectroscopy can also determine whether the fibres are self-assembled. When the molecules are assembled, they become NMR-invisible as they are unable to diffuse.[70] From the spectra collected, the percent assembly is calculated by following the progressive disappearance of a signal from the gelator.[71] For **PBI-A**, the methyl signal of the alanine was chosen to avoid interference from the signals of the GdL. The reproducibility of the GdL hydrolysis allows for the NMR, rheological, and pH data to

be correlated and provides a detailed insight into what occurs during the gelation period (Fig. 2.9).

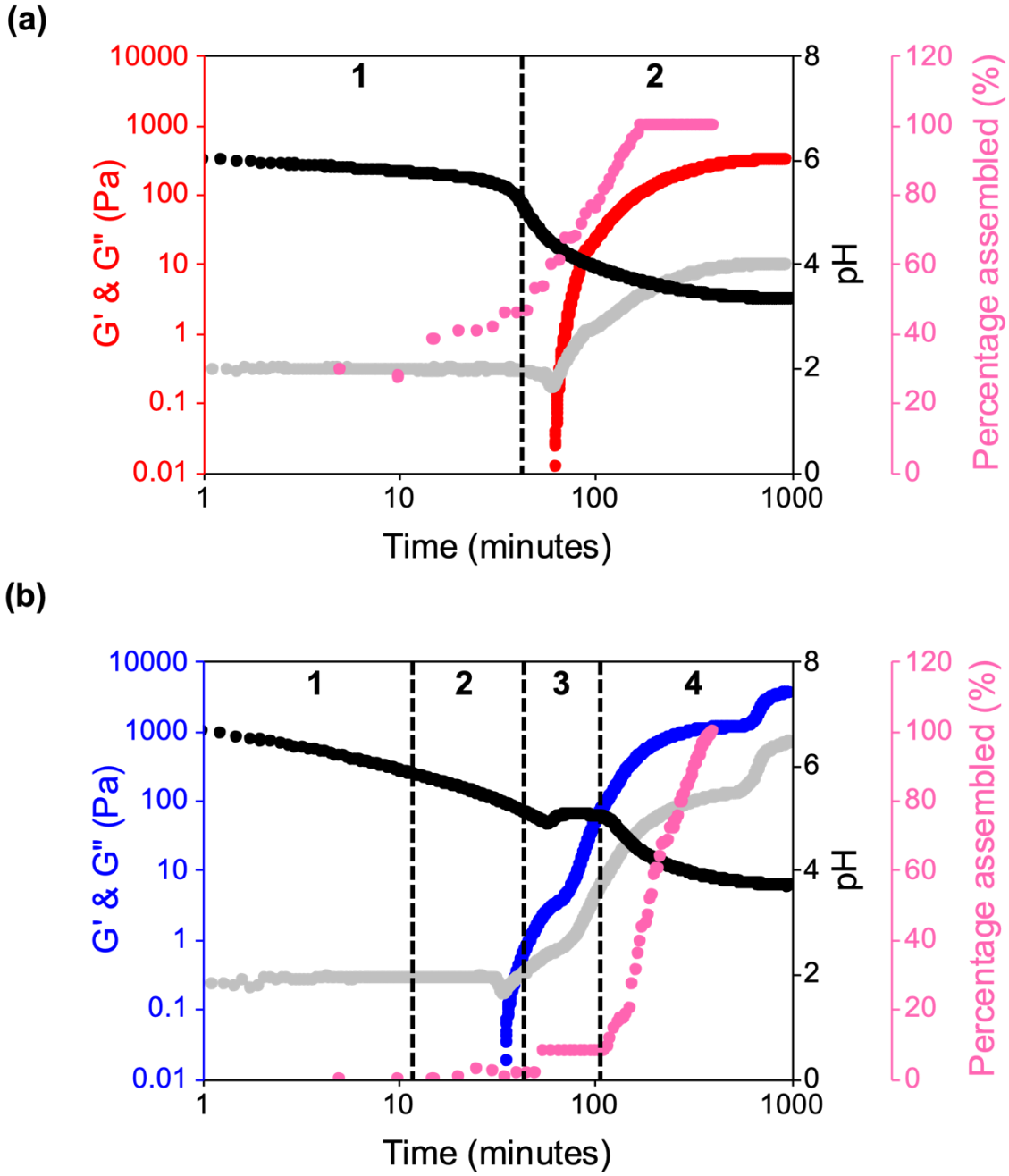

Figure 2.9. Plots showing the evolution of the gel networks starting at a pH of (a) 6 and (b) 9. The graph shows the development of G′ (in red for a starting pH of 6 and blue for a starting pH of 9) and G″ (grey) with time and change in pH (black) and percentage assembly (pink).

Rheology, pH, and ^{1}H NMR data all showed clear differences in the self-assembly process depending on the starting pH. Initially, we thought this process would be the same irrespective of pH but would happen quicker when starting at pH 6, as the **PBI-A** has already started to assemble. There are examples which show that changing the rate of hydrolysis,

and therefore the speed of gelation, can influence the final gel properties.[40] However, instead we found that when starting at pH 9, there are three stages of self-assembly, represented by the three plateaus in G′ and G″ (Fig. 2.9b). In comparison, when starting at pH 6, the gelation is a single continuous process (Fig. 2.9a).

Upon addition of GdL to a solution of **PBI-A** starting at pH 9, the percentage assembly is low (Zone 1, Fig. 2.9b). This is also seen in the rheological data, where G″ is greater than G′ (which is too low to be recorded), showing that the sample is liquid and self-assembly of the molecule has not yet occurred. After 35 minutes (Zone 2, Fig. 2.9b), G′ starts to increase, and the pH is below 5.34, which is the first "apparent" pK_a of **PBI-A**. At 75 minutes (Zone 3, Fig. 2.9b), there is an increase in pH before the pH and percentage assembly plateau. The increase and level in pH could be due to the structures rearranging, causing buffering.[49,72,73] The pH then begins to decrease again after 118 minutes (Zone 4, Fig. 2.9b), causing an increase in the percentage of molecules assembled. The percentage assembly reaches 100% before the final plateau in G′ and G″. Such results indicate that the structures in solution may be elongating or thickening to entangle, which we have previously observed with other amino acid-appended PBIs.[28] The ^{1}H NMR data also further suggest that the gelation process is continuous when starting at pH 6, as the percentage assembly continuously increases over time (Fig. 2.9a). The percentage assembly is also 20% at the beginning of the experiment (Zone 1, Fig. 2.9a), confirming the presence of pre-assembled structures before gelation has been triggered. The rheological, pH, and ^{1}H NMR data all suggest a more complex explanation than simply a change in the rate of gelation and suggest that the differences in the gel properties are due to the structures present in solution determining the gelation pathway.[74]

2.2.4 Impact of pH-Switching

We next wanted to investigate whether we could switch between the two differently aggregated states by adjusting the pH from pH 6 to 9 (referred to as pH 9*) or from pH 9 to 6 (referred to as pH 6*). To switch between the singly deprotonated species found at pH 6 and the doubly deprotonated species found at pH 9, 1 equivalent of NaOH (0.1 M, aq) was added. Similarly, to go from the doubly to singly deprotonated **PBI-A**, 1 equivalent of HCl (0.1 M, aq) was added. To form the hydrogels, the same concentrations of GdL were added as previously described (Fig. 2.10).

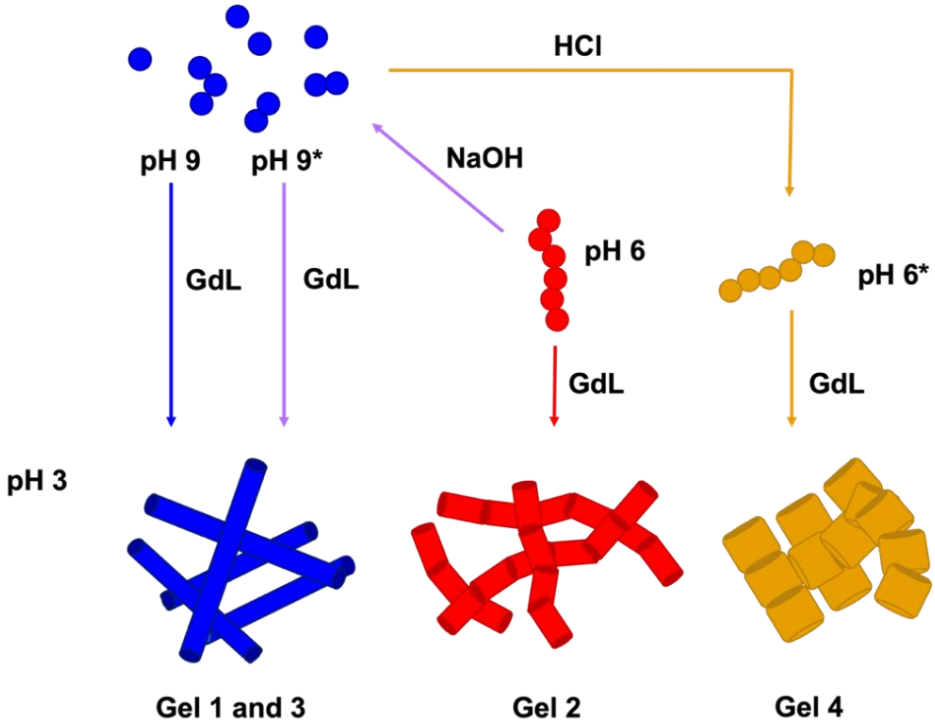

Figure 2.10. Cartoon illustrating how the different pathways to form aggregates and gels directly influence the network and gel properties.

The resulting gels showed a single yield point, as observed in the previous gels (Fig. 2.11). The gels formed from solutions at high pH showed similarities despite the solutions being prepared differently (Fig. 2.11b). The stiffness of the gels is almost identical (G′ values at 0.1% strain of 623 Pa for Gel-2 and 540 Pa for gels formed from solutions at pH 9*, referred to as Gel-3, respectively). Such results can be ascribed to the increased solubility at high pH, meaning the structures are not "locked in". Therefore, when the pH is lowered with GdL, the solutions follow the same kinetic pathway. In comparison, the gels formed at the lower pH showed significant differences in the stiffness of the gels, with the pH 6* solution producing stiffer gels (Fig. 2.11a). To ensure this increase was not the result of NaCl formed upon adding 1 eq of HCl, strain sweeps of gels formed from solutions at pH 6 with 1 eq of NaCl (0.1 M, aq) added were also run (Fig. A.1.14, Appendix), which showed that the salt did not impact the gel properties. A possible explanation for this increase in stiffness (G′ values at 0.1% strain of 150 Pa for Gel-2 and 2800 Pa for gels formed from solutions at pH 6*, referred to as Gel-4) could be due to differences in solubility. At a higher pH, the PBI is more dispersed in solution. However, at a lower pH, more self-assembled structures have started to form. When the samples are prepared with 2 equivalents of NaOH and an equivalent of HCl is added, the high initial solubility may allow different self-assembled

structures to form as the pH decreases. Furthermore, the samples prepared by lowering the pH using HCl have a process history very different from that of the samples prepared with only 1 equivalent of base to begin with. Therefore, the solutions do not pass through the same structural intermediates due to differences in kinetics and give different gels.

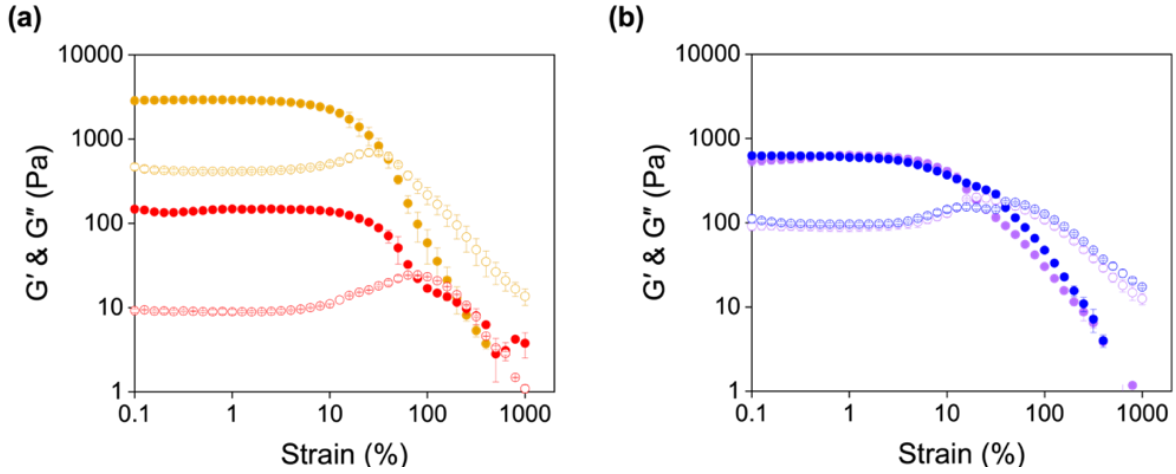

Figure 2.11. Strain sweeps of **PBI-A** gels formed from solutions starting at (a) pH 6 and (b) pH 9. Blue data is for Gel-1, red data is for Gel-2, purple data is for Gel-3, and orange data is for Gel-4. Closed circles represent G′ and open circles represent G″. Data shown are averaged data for triplicate runs, with error bars representing standard deviation.

The absorption spectra for pH 9 and 9* solutions showed nearly identical molecular packing (Fig. 2.12a). These results support the hypothesis that no structures are "locked in" at high pH. Therefore, raising the pH results in the same structures despite the differences in how the pH was changed, as there are limited possibilities available due to the solubility. However, the SANS data for the pH 9* solutions could be fit to a power-law alone, suggesting ill-defined, large structures are present (Fig. 2.12b and Table 2.4). Furthermore, there are differences in the intensity of the scattering data at low Q. Scattering at low Q is derived from larger structures, and thus, an increase in scattering intensity at pH 9* would be associated with an increased population of large self-assembled structures.[46] In comparison, a lower intensity suggests that at pH 9, there are small, or more solvated, aggregates present.[56] The corresponding gels showed similarities in the shape of the absorption spectra, but the intensities of the peaks were different (Fig. 2.12c). The scattering data for Gel-3 fit to a power law with a value of 2.21 (Fig. 2.12d and Table 2.5). This value is lower than that used in the elliptical cylinder and power law model for Gel-1. This decrease in power law suggests a porous structure but on too large a length scale to be captured by SANS.

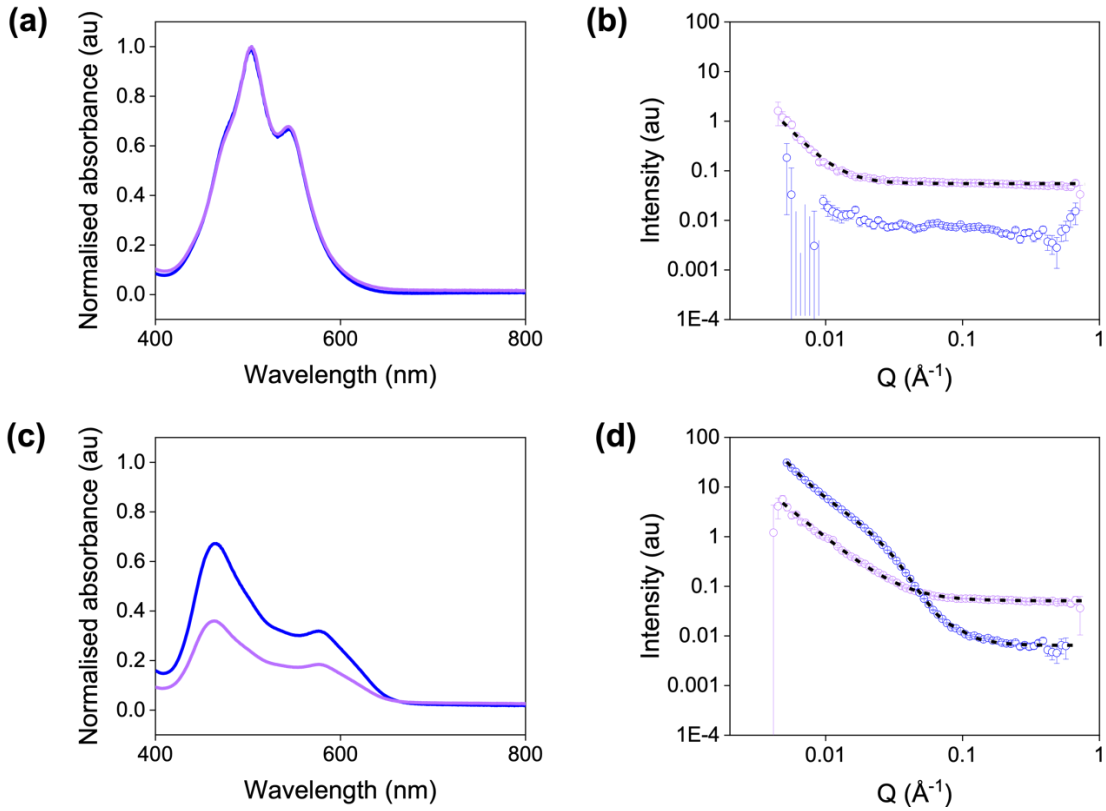

Figure 2.12. (a) UV-vis absorption spectra and (b) scattering data of **PBI-A** solutions at pH 9 (blue) and pH 9* (purple). (c) UV-vis absorption spectra and (d) scattering data of **PBI-A** Gel-1 (blue) and Gel-3 (purple). Open circles show the data and black dashed lines represent the fit for (b) and (d). For (a) and (c), the data is normalised to the highest absorption of each spectrum.

Table 2.4. Parameters of the SANS model fit for a **PBI-A** solution at pD 9*.

Power Law	**Value**	**Error**
Background (cm^{-1})	0.05	
Power law scale	1.1931×10^{-7}	4.1349×10^{-9}
Power law	2.90	0.03
χ^2	10.191	

Table 2.5. Parameters of the SANS model fit for **PBI-A** Gel-3.

Power Law	**Value**	**Error**
Background (cm^{-1})	0.05	
Power law scale	3.3286×10^{-5}	2.1034×10^{-6}
Power law	2.21	0.02
χ^2	2.5182	

In comparison, there were differences in the absorption spectra of the two differently prepared singly deprotonated solutions (Fig. 2.13a). The 490:540 nm peak ratios were different (0.89:0.64 and 0.94:0.74 for the pH 6 and 6* samples, respectively), further suggesting differences in the starting structures present. Furthermore, pH 6* had a broader absorption, suggesting these solutions were more aggregated. The scattering data revealed that these solutions fit to a power law of 3.4 (Fig. 2.13b and Table 2.6). These structural differences resulted in differences in the UV-vis spectra of the corresponding gels (Fig. 2.13c). SANS of Gel-4 fit to a flexible elliptical cylinder, as for Gel-2 (Fig. 2.13d and Table 2.7). However, the fibres were much more tape-like in Gel-4. Such planar tape-like structures have been reported to form in molecules containing amide motifs capable of hydrogen bonding.[75] It was hypothesised that these more tape-like structures can pack closer together, which could explain the higher stiffness observed in the rheological data (Fig. 2.11).

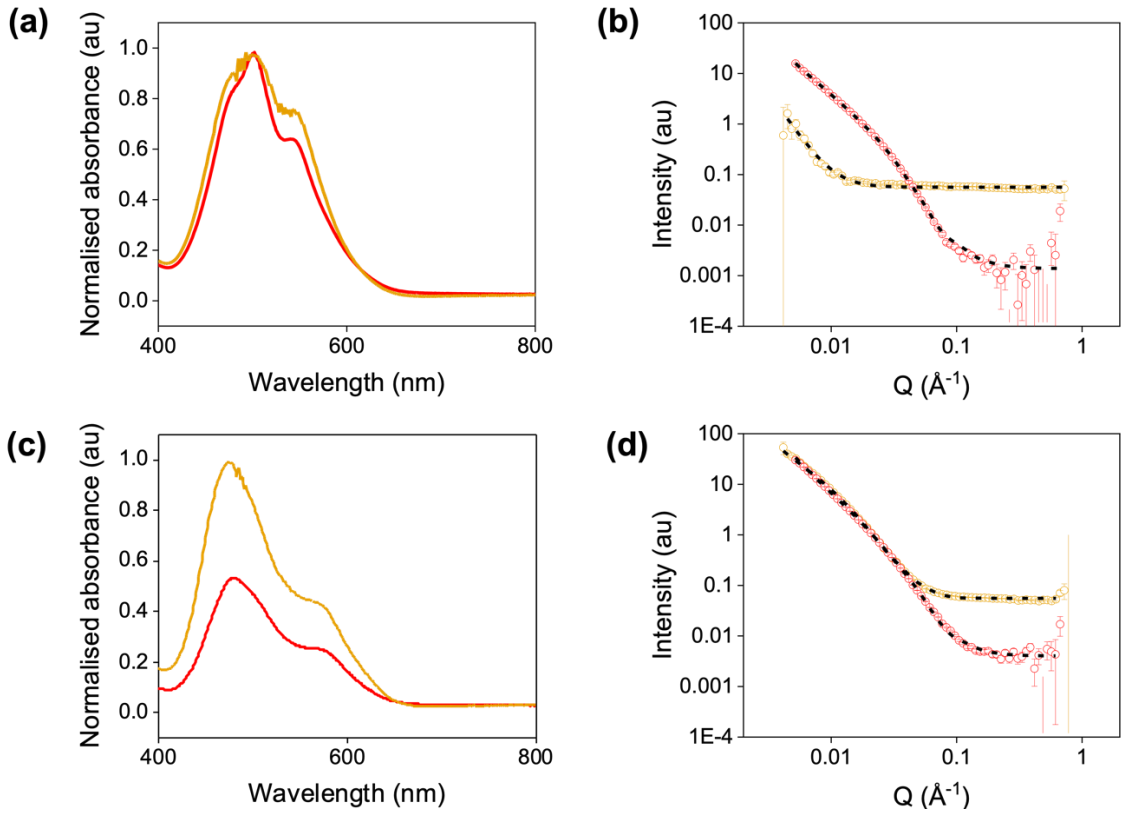

Figure 2.13. (a) UV-vis absorption spectra and (b) scattering data of **PBI-A** solutions at pH 6 (red) and pH 6* (orange). (c) UV-vis absorption spectra and (d) scattering data of **PBI-A** Gel-2 (red) and Gel-4 (orange). Open circles show the data and black dashed lines represent the fit for (b) and (d). For (a) and (c), the data is normalised to the highest absorption of each spectrum.

Table 2.6. Parameters of the SANS model fit for a **PBI-A** solution at pD 6*.

Power Law	**Value**	**Error**
Background (cm^{-1})	0.05	
Power law scale	8.3993×10^{-9}	1.000×10^{-11}
Power law	3.44	0.7
χ^2	10.443	

Table 2.7. Parameters of the SANS model fit for **PBI-A** Gel-4. A dash represents no fitting error available.

Flexible Elliptical Cylinder	**Value**	**Error**
Background (cm^{-1})	0.005	
Cylinder scale	1.7459×10^{-4}	6.1590×10^{-6}
Length (Å)	1000	-
Kuhn length (Å)	69.5	2.9
Radius (Å)	28.7	0.4
Axis ratio	5.33	0.1
χ^2	9.3703	

Monitoring the development of G′ and G″ over time for pH 6* and pH 9* solutions, there is again a multi-stage development in the moduli (Fig. 2.14). Furthermore, for pH 9* solutions, both G′ and G″ are seen at the start of the experiment (Fig. 2.14b), confirming the presence of pre-assembled structures compared to the gelation profile of solutions starting at pH 9 (Fig. 2.9b). The gelation profiles are different for all four solutions, showing the importance of sample history. The data further highlight that the aggregates present in solution before triggering gelation heavily influence the kinetics of this process, which in turn impacts the final mechanical properties of the gel.

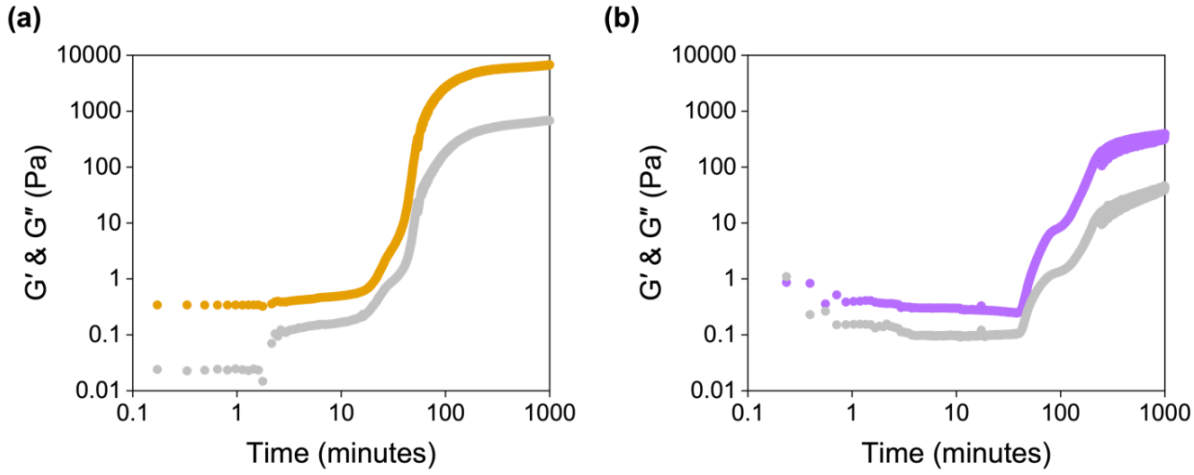

Figure 2.14. Plots showing the evolution of the gel networks for solutions of **PBI-A** at (a) pH 6* and (b) pH 9*. The graphs show the development of G′ (in orange for pH 6* and purple for pH 9*) and G″ (grey) with time.

2.3 Conclusions

In this Chapter, we aim to show the importance of the sample history of the solutions on the resulting gels whilst also highlighting the importance of sample preparation before triggering gelation. We can access three distinct gels with widely different mechanical properties simply by changing the pH at which we start the gelation process and how we get to the pre-assembled structures in solution. These differences in the gels have large consequences on the suitability of the gels for certain applications.

At high pH, the PBI molecules are more soluble and form less defined structures in solution. Therefore, at this pH, the gelation kinetics are likely to be very similar and form the same gel. Upon addition of GdL, pH 9 solutions form gels with more rigid cylindrical fibres. At pH 6, the molecules are already assembled, and lowering the pH gives more flexible gel networks and fibres.

We also find that one cannot change between the different aggregated states if these self-assembled structures are already pre-formed, and this can be exploited to again give gels with different mechanical properties. We show that the gels formed from the two different aggregated states at pH 6 had more than an order of magnitude in difference in their stiffness, with solutions formed at pH 6* giving thicker, flatter fibres.

The results shown here provide an opportunity to precisely control the morphology of the gel networks to suit the chosen application without the need to design and synthesise new materials. Such control could be valuable in cell culturing and tissue engineering, for example, where the morphology of the scaffolds can impact cell proliferation and differentiation.[76–78] This work highlights the importance of controlling the pH of solutions before gelation but also presents the opportunity to access multiple morphologies from a single gelator simply by changing how we prepare the solution.

2.4 Experimental

2.4.1 Synthetic Procedures

Perylene-3,4-9,10-tetracarboxylic dianhydride (PTCDA) was purchased from Sigma-Aldrich. L-alanine and imidazole were purchased from Fluorochem. All commercial reagents were used as received. Distilled water was used throughout. NaOD was purchased from Sigma-Aldrich as a 40 wt% solution in D_2O and diluted with D_2O to provide a 0.1 M solution.

2.4.1.1 Synthesis of PBI-A

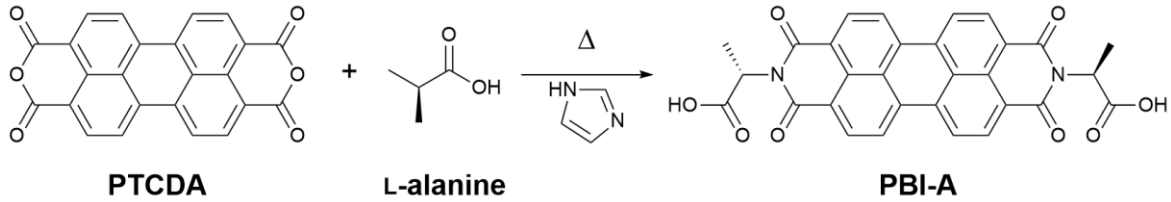

Figure 2.15. Synthesis of **PBI-A**.

PTCDA (2.00 g, 5.1 mmol), L-alanine (0.91 g, 10.2 mmol) and imidazole (3.47 g, 51.0 mmol) were added to a 100 mL Schlenk flask and sealed with a rubber septum. The reagents were purged with nitrogen for 15 minutes whilst mixing thoroughly at room temperature. The mixture was then heated to 120°C for 5 hours with magnetic stirring under nitrogen. The temperature was reduced to 90°C, and deionised water (50 mL) was added. The solution was left to stir for 1 hour and then cooled to room temperature. Once cooled, the solution was filtered through filter paper under gravity to remove any unreacted PTCDA. The filtrate was collected, and the pH was lowered to below pH 4 with 2 M HCl (50 mL), triggering precipitation of the PBI. The precipitate was collected by vacuum filtration, washed with 2

M HCl (60 mL) and then thoroughly with deionised water (60 mL) until a neutral pH was achieved. The resulting solid was dried under vacuum. The solid was then extracted in refluxing 2 M HCl (50 mL) for 5 hours. The solids were collected by vacuum filtration whilst hot and washed three times with 2 M HCl (10 mL) and then with deionised water until a neutral pH was achieved. The product was dried by lyophilisation overnight to yield **PBI-A** as a blood-red solid (2.50 g, 91% yield). The compound was characterised by ^{1}H and ^{13}C NMR, and HRMS.

^{1}H NMR (500 MHz, DMSO-d_6, 25°C): δ (ppm) = 12.70 (2H, br s, COOH), 8.34 (4H, t, J = 8.4 Hz, ArH), 8.20 (4H, t, J = 7 Hz, ArH), 5.59 (2H, q, J = 6.9 Hz, CH*), 1.68 (6H, d, J = 6.5 Hz, CH_3). ^{13}C NMR (125 MHz, DMSO-d_6, 25°C): δ (ppm) = 171.7 (COOH), 163.3 (C=O), 135.7, 130.6, 127.4, 122.7, 117,7 and 116.7 (perylene core), 52.3 (CH*), 15.2 (CH_3). HRMS (ESI) m/z, nominal mass calculated for $[C_{30}H_{18}N_2O_8+H]^+$: 535.4800. Found $[C_{30}H_{18}N_2O_8+H]^+$: 535.1136 .

2.4.1 Experimental Procedures

2.4.2.1 Freeze-Dryer

Synthetic products were dried by lyophilisation. Solids were neutralised by washing with deionised water and filtering until the filtrate was no longer acidic (determined using universal indicator paper (Merck Life Sciences)). Solids were then frozen in a freezer to approximately -18°C and freeze dried using an Alpha 2-4 LSCbasic freeze-dryer (Martin Christ).

2.4.2.2 Nuclear Magnetic Resonance (NMR) Spectroscopy

NMR measurements were carried out on a Bruker UltraShield™ 500 MHz spectrometer to characterise the synthesis of **PBI-A**. Solids were dissolved in DMSO-d_6. The spectrometer operates at 500 MHz for ^{1}H NMR and 101 MHz for ^{13}C NMR spectroscopy.

2.4.2.3 High-Resolution Mass Spectrometry (HRMS)

Measurements were carried out using a Bruker microTOFq mass spectrometer using electrospray ionisation (ESI) coupled to a time-of-flight analyser. The instrument is accurate to <5 ppm. Samples were run in ethanol by the University of Glasgow mass spectrometry service.

2.4.2.4 Preparation of PBI-A Solutions

All solutions were prepared to a concentration of 5 mg/mL by dispersing **PBI-A** in deionised water and adding either two molar equivalents or one molar equivalent of sodium hydroxide (0.1 M, aqueous). The solutions were agitated on a MX-T6-S tube roller (SCILOGEX) overnight until all the gelator had dissolved.

2.4.2.5 Preparation of pH-Switched Solutions

To switch a solution from 1 molar equivalent to 2 molar equivalents of NaOH, 1 molar equivalent of NaOH (0.1 M, aqueous) was added, and the sample was mixed on a stirrer plate at 1000 rpm for 10 minutes. To switch a solution from 2 molar equivalents to 1 molar equivalent of NaOH, 1 molar equivalent of HCl (0.1 M, aqueous) was added, and the sample was mixed for 10 minutes on a stirrer plate at 1000 rpm.

2.4.2.6 Preparation of PBI Hydrogels

A pH-switch method was used to form the hydrogels. Solutions were prepared as above. 2 mL of solution was transferred to a 7 mL Sterilin vial containing a pre-weighed amount of glucono-δ-lactone (GdL) and gently shaken three times. The sample was then left to stand overnight to allow gelation to occur. For solutions with a starting pH of 6, 7.5 mg/mL of GdL was used, and 10 mg/mL of GdL was used for solutions with a starting pH of 9. A simple inversion test was performed to indicate whether gel formation had been successful. If the sample was stable to inversion, rheological measurements were taken.

2.4.2.7 pH Measurements

pH measurements were recorded with an FC200 pH probe (HANNA instruments) with a 6 mm x 10 mm conical tip at 25°C. The stated accuracy of the pH measurement is $\pm$ 0.1.

2.4.2.8 UV-Vis Absorption Spectroscopy

Solution UV-vis absorption data were obtained on an Agilent Cary 60 UV-vis spectrophotometer in 0.1 mm quartz cuvettes. Gel samples were made by the pH switch method: an appropriate amount of GdL was added to 2 mL gelator solution in a 7 mL Sterilin vial and gently shaken three times. An aliquot of the solution was then transferred to a 0.1 mm cuvette and tightly wrapped in parafilm to prevent the gel from drying out. Samples were then left overnight to gel.

2.4.2.9 Fluorescence Spectroscopy

Fluorescence spectra were collected using an Agilent Cary Eclipse fluorescence spectrophotometer in the Welch lab (University of Calgary). The samples were prepared, diluted to a concentration of 0.05 mg/mL using deionised water, and transferred into 10.0 mm quartz cuvettes. Emission and excitation spectra were recorded with slit widths of 10 nm at a scan rate of 600 nm/min. Emission spectra were collected between 700 and 200 nm, exciting at 365 nm.

2.4.2.10 Rheological Measurements

Dynamic rheological and viscosity measurements were performed with Anton Paar Physica MCR101 and MCR301 rheometers. A cup-and-vane measuring system was used for strain and frequency sweeps, a cone-and-plate measuring system for viscosity measurements, and a parallel plate measuring system for time sweeps. For strain and frequency tests, 2 mL of gels were prepared in 7 mL Sterilin vials and left for 16 hours at room temperature before measurements were taken. For viscosity measurements, **PBI-A** solutions were prepared as previously discussed. For time sweeps, the gels were prepared in a vial and quickly transferred onto the bottom plate. The temperature was maintained at 25°C during all measurements using a water bath. All measurements were recorded in triplicate.

Strain Sweeps

Strain sweeps were performed over a range of 0.1% to 1000% with a frequency of 10 rad/s. The critical strain was quoted at the point where the storage modulus (G′) began to become non-linear and ultimately crossed over the loss modulus (G″), consequently causing the gel to break down.

Frequency Sweeps

Frequency sweeps were performed from 1 rad/s to 100 rad/s under a strain of 0.1%. The shear moduli (G′ and G″) were quoted at 10 rad/s. The measurements were performed within the viscoelastic region where G′ and G″ were independent of strain amplitude.

Viscosity Measurements

Viscosity measurements were performed with a 75 mm cone (angle = 1.000°) and a plate gap of 0.1 mm. 2 mL solutions were poured onto the plate for the measurement. The viscosity was measured under a rotational shear rate from 1 to 100 s^{-1}.

Time Sweeps

Time sweeps were performed with a 50 mm sandblasted plate and a plate gap of 0.8 mm. Tests were performed at an angular frequency of 10 rad/s and with a strain of 0.1%. Mineral oil was carefully added around the circumference of the top plate to prevent the sample from drying out.

2.4.2.11 SANS

SANS measurements were performed using the Larmor and SANS2D instruments (ISIS, Rutherford Appleton Laboratory, Didcot, UK) under experiment numbers RB2210011 and RB2220192, respectively. Measurements were performed using a wavelength band of 0.9 to 13 Å to access a Q range of 0.004 to 0.7 $Å^{-1}$. Solutions and gels were measured in 2 mm path length UV spectrophotometer quartz cuvettes (Hellma). These were placed in a temperature-controlled sample rack during the measurements. Measurements were run at 25°C. Solutions were prepared as described above, but in D_2O and NaOD (0.1 M). Gels formed using GdL were prepared in Sterilin vials and quickly transferred to the cuvettes before being placed on the rack.

The data were reduced to 1D scattering curves of intensity vs. Q using the facility-provided software. The electronic background was subtracted, the full detector images for all data were normalised, and scattering from the empty cell was subtracted. The scattering from D_2O was also measured and subtracted from the data using the Mantid software package installed inside the ISIS virtual machines, IDAaaS.[79] The instrument-independent data were then fitted to the models discussed in the text using the SasView software package (version 5.0.4).[80] The scattering length density (SLD) of each material was calculated using the National Institute of Standards and Technology's neutron activation and scattering calculator.[81] The SLD of D_2O was calculated to be 6.393 x 10^{-6} $Å^{-2}$, and the SLD of **PBI-A** was calculated to be 3.445 x 10^{-6} $Å^{-2.}$ All data fit best to a cylindrical model combined with a power law. The best fit was determined as the one which overlapped well to the data and had the lowest χ^2 value. Errors were calculated by the SASView fitting software as a function of the error bars of the experimental data and the chosen model.

2.4.2.12 "Apparent" pK_a Titrations

An FC200 pH probe (HANNA instruments) with a 6 mm x 10 mm conical tip was used for pK_a titrations. The "apparent" pK_a values of **PBI-A** were determined by the addition of

aliquots of 0.1 M aqueous hydrochloric acid. The pH was recorded after each aliquot addition once a stable pH was maintained. To prevent gel formation, the solutions were gently stirred using a magnetic stirrer. For pH titrations using GdL, the appropriate amount of GdL was added to a 2 mL sample in a Sterilin vial and the pH recorded overnight. The temperature was maintained at 25°C using a water bath. The plateaus in the pH data are indicative of the "apparent" pK_a values for the gelator. "Apparent" here refers to a change in aggregation which causes a plateau in the pH data brought about by the protonation of the carboxyl groups.

2.4.2.13 ^{1}H NMR Kinetics

^{1}H NMR spectra were measured using a Bruker UltraShield™ 500 MHz spectrometer at 25°C. Spectra were analysed using Bruker Topspin 4.1.0 software. Solutions were prepared as described above in D_2O (as opposed to H_2O) and 0.1 M NaOD (as opposed to NaOH). MeOH (2 μL) was then added as an internal standard. For the time-zero measurements (t_0), a ^{1}H NMR spectrum of 1 mL of the stock solution was recorded. 2 mL of the gelator solution was then mixed with GdL in a Sterilin vial, and 1 mL was directly loaded into an NMR tube to gel. Due to experimental limitations, there was a 10-minute delay between loading of the sample into the spectrometer and the first measurement. During the gelation period, spectra were recorded every 5 minutes until the protons on the methyl group of the **PBI-A** were no longer detectable. The methyl protons of **PBI-A** were then integrated and compared to the integration value for the **PBI-A** methyl peak in the t_0 spectrum. When assembled, PBIs become NMR-invisible as they cannot diffuse,[70] which can be used to calculate the percentage unassembled. From this, the percentage assembled was calculated and plotted against time.

2.5 References

1. E. R. Draper and D. J. Adams, *Chem*, 2017, **3**, 390–410.

2. J. Omar, D. Ponsford, C. A. Dreiss, T. Lee and X. J. Loh, *Chem. Asian J.*, 2022, **17**, e202200081.

3. X. Du, J. Zhou, J. Shi and B. Xu, *Chem. Rev.*, 2015, **115**, 13165–13307.

4. R. G. Weiss, *J. Am. Chem. Soc.*, 2014, **136**, 7519–7530.

5. L. A. Estroff and A. D. Hamilton, *Chem. Rev.*, 2004, **104**, 1201–1218.

6. J. Raeburn, A. Zamith Cardoso and D. J. Adams, *Chem. Soc. Rev.*, 2013, **42**, 5143–5156.

7. D. J. Adams, M. F. Butler, W. J. Frith, M. Kirkland, L. Mullen and P. Sanderson, *Soft Matter*, 2009, **5**, 1856–1862.

8. C. Rizzo, P. Cancemi, L. Mattiello, S. Marullo and F. D'Anna, *ACS Appl. Mater. Interfaces*, 2020, **12**, 48442–48457.

9. Y. Lyu and H. S. Azevedo, *Molecules*, 2021, **26**, 873.

10. E. R. Draper and D. J. Adams, *Langmuir*, 2019, **35**, 6506–6521.

11. R. V. Ulijn and A. M. Smith, *Chem. Soc. Rev.*, 2008, **37**, 664–675.

12. J. Rodon Fores, M. Criado-Gonzalez, M. Schmutz, C. Blanck, P. Schaaf, F. Boulmedais and L. Jierry, *Chem. Sci.*, 2019, **10**, 4761–4766.

13. D. Ghosh, L. J. Marshall, G. Ciccone, W. Liu, A. Squires, A. Seddon, M. Vassalli and D. J. Adams, *Macromol. Mater. Eng.*, 2023, **308**, 2300082.

14. C. A. Dreiss, in *Wormlike Micelles: Advances in Systems, Characterisation and Applications*, Royal Society of Chemistry, Cambridge, 2017.

15. C. A. Dreiss, *Soft Matter*, 2007, **3**, 956-970.

16. F. E.-T. Heakal and A. E. Elkholy, *J. Mol. Liq.*, 2017, **230**, 395–407.

17. Y. Li, Y. Sun, M. Qin, Y. Cao and W. Wang, *Nanoscale*, 2015, **7**, 5638–5642.

18. C. Jian, N. Tao, L. Xu, M. Liu, X. Huang, W. Gao and H. Wu, *ACS Sustain. Chem. Eng.*, 2019, **7**, 11062–11068.

19. Q. Yu, M. Fan, D. Li, Z. Song, M. Cai, F. Zhou and W. Liu, *ACS Appl. Mater. Interfaces*, 2014, **6**, 15783–15794.

20. K. McAulay, P. A. Ucha, H. Wang, A. M. Fuentes-Caparrós, L. Thomson, O. Maklad, N. Khunti, N. Cowieson, M. Wallace, H. Cui, R. J. Poole, A. Seddon and D. J. Adams, *Chem. Comm.*, 2020, **56**, 4094–4097.

21. L. Thomson, D. McDowall, L. Marshall, O. Marshall, H. Ng, W. J. A. Homer, D. Ghosh, W. Liu, A. M. Squires, E. Theodosiou, P. D. Topham, L. C. Serpell, R. J. Poole, A. Seddon and D. J. Adams, *ACS Nano*, 2022, **16**, 20497–20509.

22. L. Chen, S. Revel, K. Morris, L. C. Serpell and D. J. Adams, *Langmuir*, 2010, **26**, 13466–13471.

23. J. Raeburn, C. Mendoza-Cuenca, B. N. Cattoz, M. A. Little, A. E. Terry, A. Zamith Cardoso, P. C. Griffiths and D. J. Adams, *Soft Matter*, 2015, **11**, 927–935.

24. K. Rosińska, M. Bartniak, A. Wierzbicka, A. Sobczyk-Guzenda and D. Bociaga, *J. Biomed. Mater. Res. B Appl. Biomater.*, 2023, **111**, 314–330.

25. C. C. Piras, P. G. Genever and D. K. Smith, *Mater. Adv.*, 2022, **3**, 7966–7975.

26. D. J. Cornwell and D. K. Smith, *Mater. Horiz.*, 2015, **2**, 279–293.

27. G. Ben Messaoud, P. Le Griel, D. Hermida-Merino, S. L. K. W. Roelants, W. Soetaert, C. V. Stevens and N. Baccile, *Chem. Mater.*, 2019, **31**, 4817–4830.

28. J. G. Egan, G. Brodie, D. McDowall, A. J. Smith, C. J. C. Edwards-Gayle and E. R. Draper, *Mater. Adv.*, 2021, **2**, 5248–5253.

29. E. R. Draper, B. J. Greeves, M. Barrow, R. Schweins, M. A. Zwijnenburg and D. J. Adams, *Chem*, 2017, **2**, 716–731.

30. F. Würthner, C. R. Saha-Möller, B. Fimmel, S. Ogi, P. Leowanawat and D. Schmidt, *Chem. Rev.*, 2016, **116**, 962–1052.

31. S. Roy, D. Kumar Maiti, S. Panigrahi, D. Basak and A. Banerjee, *RSC Adv.*, 2012, **2**, 11053–11060.

32. C. Chen, K. Wang, L. Gu and H. Li, *RSC Adv.*, 2017, **7**, 42685–42689.

33. D. Görl, X. Zhang and F. Würthner, *Angew. Chem. Int. Ed.*, 2012, **51**, 6328–6348.

34. L. Chen, K. Morris, A. Laybourn, D. Elias, M. R. Hicks, A. Rodger, L. Serpell and D. J. Adams, *Langmuir*, 2010, **26**, 5232–5242.

35. C. Tang, A. M. Smith, R. F. Collins, R. V. Ulijn and A. Saiani, *Langmuir*, 2009, **25**, 9447–9453.

36. E. R. Draper, J. J. Walsh, T. O. McDonald, M. A. Zwijnenburg, P. J. Cameron, A. J. Cowan and D. J. Adams, *J. Mater. Chem. C*, 2014, **2**, 5570–5575.

37. M. C. Nolan, J. J. Walsh, L. L. E. Mears, E. R. Draper, M. Wallace, M. Barrow, B. Dietrich, S. M. King, A. J. Cowan and D. J. Adams, *J. Mater. Chem. A Mater.*, 2017, **5**, 7555–7563.

38. B. A. K. Kriebisch, C. M. E. Kriebisch, A. M. Bergmann, C. Wanzke, M. Tena-Solsona and J. Boekhoven, *ChemSystemsChem*, 2023, **5**, e202200035.

39. V. Lakshminarayanan, C. Chockalingam, E. Mendes and J. H. van Esch, *ChemPhysChem*, 2021, **22**, 2256–2261.

40. A. Z. Cardoso, A. E. Alvarez Alvarez, B. N. Cattoz, P. C. Griffiths, S. M. King, W. J. Frith and D. J. Adams, *Faraday Discuss*, 2013, **166**, 101–116.

41. C. Colquhoun, E. R. Draper, R. Schweins, M. Marcello, D. Vadukul, L. C. Serpell and D. J. Adams, *Soft Matter*, 2017, **13**, 1914–1919.

42. E. K. Johnson, D. J. Adams and P. J. Cameron, *J. Am. Chem. Soc.*, 2010, **132**, 5130–5136.

43. P. Singh, S. Misra, A. Das, S. Roy, P. Datta, G. Bhattacharjee, B. Satpati and J. Nanda, *ACS Appl. Bio. Mater.*, 2019, **2**, 4881–4891.

44. X. Du, J. Zhou, J. Shi and B. Xu, *Chem. Rev.*, 2015, **115**, 13165–13307.

45. Xia Chen and S. Thibeault, in *2013 35th Annual International Conference of the IEEE Engineering in Medicine and Biology Society (EMBC)*, IEEE, 2013, pp. 6228–6231.

46. D. McDowall, B. J. Greeves, R. Clowes, K. McAulay, A. M. Fuentes-Caparrós, L. Thomson, N. Khunti, N. Cowieson, M. C. Nolan, M. Wallace, A. I. Cooper, E. R. Draper, A. J. Cowan and D. J. Adams, *Adv. Energy Mater.*, 2020, **10**, 2002469.

47. J. Cameron, D. J. Adams, P. J. Skabara and E. R. Draper, *J. Mater. Chem. C Mater.*, 2022, **10**, 3944–3950.

48. L. Thomson, R. E. Ginesi, D. D. Osborne, E. R. Draper and D. J. Adams, *Chem. Eur. J.*, 2023, **29**, e202300663.

49. D. J. Adams, L. M. Mullen, M. Berta, L. Chen and W. J. Frith, *Soft Matter*, 2010, **6**, 1971–1980.

50. Y. Pocker and Edmond. Green, *J. Am. Chem. Soc.*, 1973, **95**, 113–119.

51. E. R. Draper, M. Wallace, R. Schweins, R. J. Poole and D. J. Adams, *Langmuir*, 2017, **33**, 2387–2395.

52. E. R. Draper, B. Dietrich, K. McAulay, C. Brasnett, H. Abdizadeh, I. Patmanidis, S. J. Marrink, H. Su, H. Cui, R. Schweins, A. Seddon and D. J. Adams, *Matter*, 2020, **2**, 764–778.

53. E. R. Draper, L. J. Archibald, M. C. Nolan, R. Schweins, M. A. Zwijnenburg, S. Sproules and D. J. Adams, *Chem. Eur. J.*, 2018, **24**, 4006–4010.

54. D. Görl and F. Würthner, *Angew. Chem. Int. Ed.*, 2016, **55**, 12094–12098.

55. E. R. Draper, L. Wilbraham, D. J. Adams, M. Wallace, R. Schweins and M. A. Zwijnenburg, *Nanoscale*, 2019, **11**, 15917–15928.

56. R. I. Randle, L. Cavalcanti, S. Sproules and E. R. Draper, *Mater. Adv.*, 2022, **3**, 3326–3331.

57. P.-A. Plötz, S. P. Polyutov, S. D. Ivanov, F. Fennel, S. Wolter, T. Niehaus, Z. Xie, S. Lochbrunner, F. Würthner and O. Kühn, *Phys. Chem. Chem. Phys.*, 2016, **18**, 25110–25119.

58. E. R. Draper, H. Su, C. Brasnett, R. J. Poole, S. Rogers, H. Cui, A. Seddon and D. J. Adams, *Angew. Chem. Int. Ed.*, 2017, **56**, 10467–10470.

59. A. Z. Cardoso, L. L. E. Mears, B. N. Cattoz, P. C. Griffiths, R. Schweins and D. J. Adams, *Soft Matter*, 2016, **12**, 3612–3621.

60. L. Chen, G. Pont, K. Morris, G. Lotze, A. Squires, L. C. Serpell and D. J. Adams, *Chem. Comm.*, 2011, **47**, 12071–12073.

61. M. C. Nolan, J. J. Walsh, L. L. E. Mears, E. R. Draper, M. Wallace, M. Barrow, B. Dietrich, S. M. King, A. J. Cowan and D. J. Adams, *J. Mater. Chem. A Mater.*, 2017, **5**, 7555–7563.

62. D. McDowall, D. J. Adams and A. M. Seddon, *Soft Matter*, 2022, **18**, 1577–1590.

63. K. McAulay, L. Thomson, L. Porcar, R. Schweins, N. Mahmoudi, D. J. Adams and E. R. Draper, *Organic Materials*, 2020, **2**, 108–115.

64. K. McAulay, H. Wang, A. M. Fuentes-Caparrós, L. Thomson, N. Khunti, N. Cowieson, H. Cui, A. Seddon and D. J. Adams, *Langmuir*, 2020, **36**, 8626–8631.

65. S. Ramachandran, J. Trewhella, Y. Tseng and Y. B. Yu, *Chem. Mater.*, 2006, **18**, 6157–6162.

66. P. Chakraborty, M. Ghosh, L. Schnaider, N. Adadi, W. Ji, D. Bychenko, T. Dvir, L. Adler-Abramovich and E. Gazit, *Macromol. Rapid. Commun.*, 2019, **40**, 1900175.

67. J. Douglas, *Gels*, 2018, **4**, 19.

68. E. R. Cross and D. J. Adams, *Soft Matter*, 2019, **15**, 1522–1528.

69. E. R. Draper and D. J. Adams, *Langmuir*, 2019, **35**, 6506–6521.

70. J. Raeburn, B. Alston, J. Kroeger, T. O. McDonald, J. R. Howse, P. J. Cameron and D. J. Adams, *Mater. Horiz.*, 2014, **1**, 241–246.

71. A. M. Castilla, E. R. Draper, M. C. Nolan, C. Brasnett, A. Seddon, L. L. E. Mears, N. Cowieson and D. J. Adams, *Sci. Rep.*, 2017, **7**, 8380.

72. E. R. Draper, O. O. Mykhaylyk and D. J. Adams, *Chem. Commun.*, 2016, **52**, 6934–6937.

73. C. Tang, R. V. Ulijn and A. Saiani, *Langmuir*, 2011, **27**, 14438–14449.

74. J. H. van Esch, R. Klajn and S. Otto, *Chem. Soc. Rev.*, 2017, **46**, 5474–5475.

75. J. C. Macdonald and G. M. Whitesides, *Chem. Rev.* , 1994, **94**, 2383–2420.

76. A. J. Rufaihah, S. Cheyyatraivendran, M. D. M. Mazlan, K. Lim, M. S. K. Chong, C. N. Z. Mattar, J. K. Y. Chan, T. Kofidis and D. Seliktar, *Front. Physiol.*, 2018, **9**, 1555.

77. W. Wang, G. Caetano, W. Ambler, J. Blaker, M. Frade, P. Mandal, C. Diver and P. Bártolo, *Materials*, 2016, **9**, 992.

78. L. Ghasemi-Mobarakeh, *World J. Stem. Cells*, 2015, **7**, 728–744.

79. O. Arnold, J. C. Bilheux, J. M. Borreguero, A. Buts, S. I. Campbell, L. Chapon, M. Doucet, N. Draper, R. F. Leal, M. A. Gigg, V. E. Lynch, A. Markvardsen, D. J. Mikkelson, R. L. Mikkelson, R. Miller, K. Palmen, P. Parker, G. Passos, T. G. Perring, P. F. Peterson, S. Ren, M. A. Reuter, A. T. Savici, J. W. Taylor, R. J. Taylor, R. Tolchenov, W. Zhou and J. Zikovsky, *Nucl. Instrum. Methods Phys. Res.*, 2014, **764**, 156–166.

80. https://www.sasview.org/.

81. https://www.ncnr.nist.gov/resources/activation/.

Chapter 3: The Impact of Heat-Cool Processing on the Behaviour and Properties of Perylene Bisimides

This Chapter is adapted from the following publication:

"The impact of heat-cool processing on the behaviour and properties of perylene bisimides"

R. E. Ginesi, F. Angus, B. Vella, J. Doutch, P. Docampo, and E. R. Draper, manuscript in preparation.

REG was responsible for the synthesis of the gelators used. Small-angle neutron scattering data were collected by REG and ERD. JD processed the SANS data. REG fitted the SANS data. FA made the perovskite devices. BV synthesised the precursor salts for the perovskite devices. REG was responsible for all other methodology, collection of data, and analysis. REG and ERD conceptualised the project. ERD supervised the project. REG and ERD wrote the initial draft of the manuscript, to which all authors contributed for the final publication.

3.1 Introduction

As discussed in Chapter 1, using heat-cool cycles is another method for tuning the properties of pre-gel LMWG solutions. LMWGs based on small π-conjugated molecules have become a promising semiconductor material in organic electronic devices.[1] Such materials have the advantage that they can be lightweight and flexible, allowing them to be integrated onto large-area flexible substrates using processing techniques such as slot-die coating,[2,3] and screen printing.[4,5] This flexibility is highly desirable due to the growing demand for wearable and flexible "smart" electronics.[6–9] Regardless of the application, care must be taken when processing these materials to ensure robustness and durability.[10,11]

During device fabrication, the film processing technique requires the solution to be heated to remove the solvent, such as in doctor blading,[12,13] or to turn it into a vapour to coat the substrate, such as in thermal evaporation.[14] This heating is commonly used with more "green" solvents (*i.e.*, more environmentally friendly solvents made from renewable resources which have a lower toxicity and are biodegradable).[15] There have been many studies on how thermal annealing alters the morphology and conductivity of thin films.[16–18] However, the effect such heating has on the structures present in the solution phase is rarely considered, despite the arrangement of these molecules commonly influencing the film morphology and, thus, its electronic properties.[19–21]

PBIs are commonly used in optoelectronic devices and light-harvesting.[22–26] When appended with amino acids, these PBIs are soluble in water at high pH due to deprotonation of the terminal carboxylic acids.[27] By lowering the pH towards the "apparent" pK_a values of the molecule (around pH 6), more self-assembled structures start to form, such as worm-like micelles. This aggregation is dependent on the assembly conditions,[28–30] allowing us to access otherwise energetically unattainable structures and architectures simply by changing how we prepare the solution.[21,30–32] However, it can be difficult to predict how the structures in the solution phase will impact the electronic properties of the resulting films. Therefore, by studying the factors that can alter self-assembly, we can fine-tune our systems for improved functional material design.

When PBIs and similar molecules are heated, it increases their solubility, making them more dispersed in solution. For example, Wolfe *et al.* have shown, using temperature-dependent ^{1}H NMR, that increasing the temperature of an N-annulated perylene tetraester (PTEN-H)

decreased the aggregation in solution due to reduced intermolecular interactions.[33] Therefore, because these molecules are molecularly dissolved, they may assemble differently upon cooling. As such, both the temperature the solution is heated to and the cooling rate will influence the kinetics, which could alter the structures that form after cooling (Fig. 3.1).

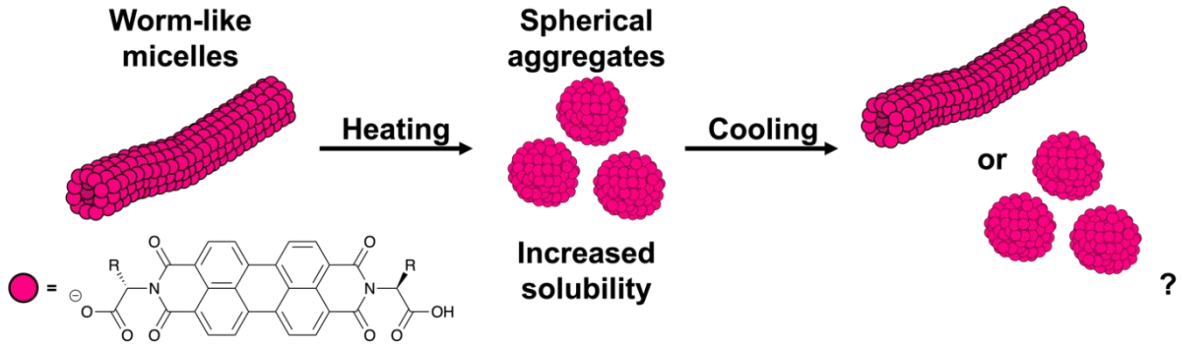

Figure 3.1. Cartoon and chemical structure of **PBI-R** (**R** = amino acid sidechain) showing the possible outcomes of assembly during a heat-cool cycle.

The strengths of the non-covalent interactions that control the self-assembly have different temperature dependencies.[34] As such, it should be possible to tune the assembly pathways and the consequent nanostructures by altering the thermal history. Avinash and Govindaraju showed that heating an isoleucine methyl ester-appended PBI resulted in conformational modifications in the isoleucine sidechain, which were not reversible upon cooling.[35] Instead, cooling resulted in random aggregation. These random aggregates were reversible only upon the addition of thermally untreated aggregates of the isoleucine methyl ester-appended PBI. The behaviour of this system could be used as a simplified model to understand protein folding and refolding.

The molecular organisation of these systems is directly related to the pathways involved in the supramolecular assembly process. Commonly, multiple pathways compete for the same building block, known as pathway complexity.[36–39] Seo *et al*. investigated the temperature-controlled pathway complexity of PBIs functionalised with diacetylene chains (PDI-DA).[40] They showed that the self-assembly process of PDI-DA involved three different aggregation pathways that led to the formation of thermodynamically favoured nanofibres and kinetically favoured nanosheets and nanoparticles. The type of aggregation was directed by synergistic H-bonding interactions, with nanosheets and nanoparticles originating from H-aggregates and nanofibres forming from J-aggregates. Similar behaviour has also been reported by the Würthner group.[41] The PDI-DA fibres also displayed reversible thermochromism (Fig. 3.2)

upon heating and cooling from red (heating) to purple (cooling).[40] This chromatic reversibility was due to switching between J-aggregates and H-aggregates.

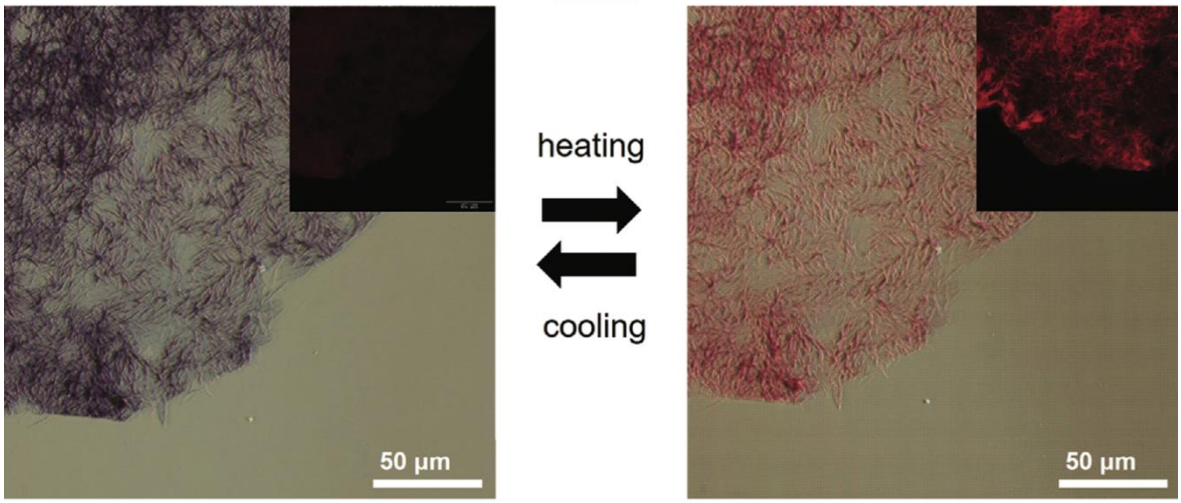

Figure 3.2. Optical and fluorescence (insets) microscope images (λ_{ex}= 520-560 nm) of PDI-DA fibres on a glass substrate during a heat-cool cycle. Figure adapted from Reference 40.

Understanding and controlling the structures present in pre-gel solutions containing micellar aggregates is crucial for designing functional materials. As discussed in Chapter 1, such control must be considered across multiple length scales. In this chapter, we aim to investigate the effect of heating and cooling cycles on the aggregation of amino acid-appended PBIs. We examine how the aggregation of these solutions is changed using a heat-cool cycle and the impact this has on the applications of the resulting thin films and hydrogels. We show that the temperature the solution is heated to and the kinetics of the cooling stage both result in films and gels with different bulk properties, allowing us to access multiple self-assembled states from the same molecule.

3.2 Results and Discussion

In this chapter, we chose three different amino acid-appended PBIs: **PBI-A**, **PBI-L**, and **PBI-Y** (Fig. 3.3). These PBIs were chosen due to the contrast in the size of their amino acid sidechains, which would influence their molecular packing. Furthermore, it has been shown that these PBIs show differences in their photoconductive properties when applied as interlayers in organic photovoltaic devices.[42] Therefore, we were interested in seeing how the heat-cool processing would affect the photoconductivity of the resulting films.

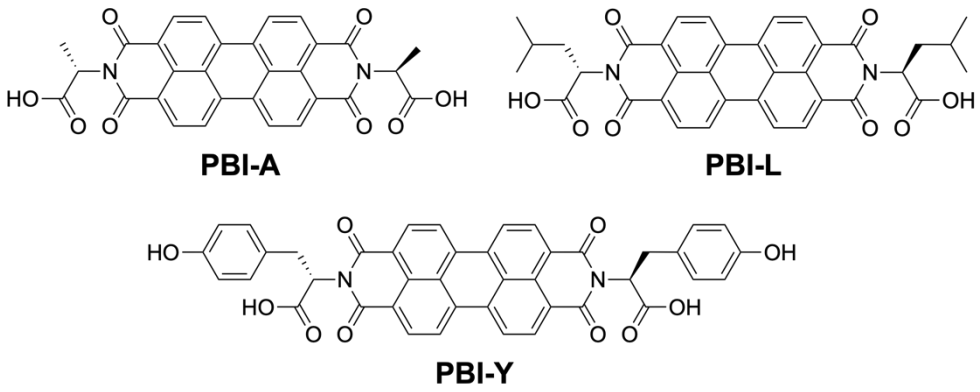

Figure 3.3. Structures of **PBI-A**, **PBI-L**, and **PBI-Y** used in this chapter.

All PBIs were synthesised as described in Sections 2.4.1 and 3.4.1. Stock solutions of the PBIs were prepared at a concentration of 5 mg/mL, adding an equivalent of NaOH (0.1 M, aq) to give solutions with a pH of 6. These PBIs all form worm-like micelles at pH 6,[29,30,43,44] which has previously been reported as a prerequisite for heat-induced changes in similar LMWGs.[45] The suspensions were allowed to stir overnight to ensure homogenous dispersion of the gelator.

3.2.1 Impact of Heat-Cool Processing on PBI Solutions

To investigate the effect of heat-cool cycles on the assembled structures, the viscosity was measured under a constant shear whilst increasing and decreasing the temperature (Fig. 3.4). A maximum temperature of 70°C was chosen as this is the temperature commonly used when preparing thin films using a doctor blade.[46,47] A minimum of 25°C was used as this is typically accepted as room temperature. For all PBIs, as the solution was heated from 25°C to 70°C, the viscosity decreased to that of water alone, suggesting a change in structure. Such thermo-thinning (*i.e.*, a viscosity decrease with increasing temperature) is commonly observed in worm-like micelles.[48] Upon cooling from 70°C, the viscosity increased and resulted in samples more viscous than the initial solution, suggesting that these changes were not reversible. Such behaviour has been previously observed with a similar LMWG, 2NapFF.[45] This increase in viscosity was most apparent for **PBI-A** (Fig. 3.4a), with **PBI-L** (Fig. 3.4b) and **PBI-Y** (Fig. 3.4c) showing similar increases in viscosity. Such results suggest that **PBI-A** is more process-dependent than the other two PBIs. To ensure that this increase in viscosity was not due to the applied shear, the same shear rate was applied for 10 minutes to samples kept at room temperature, which showed very little change in viscosity during this time (Fig. A.2.1- A.2.3, Appendix). Since this change in viscosity was minimal

compared to the heat-cool data, it confirms that the heating and cooling processes are impacting the solutions rather than an ageing effect under shear.

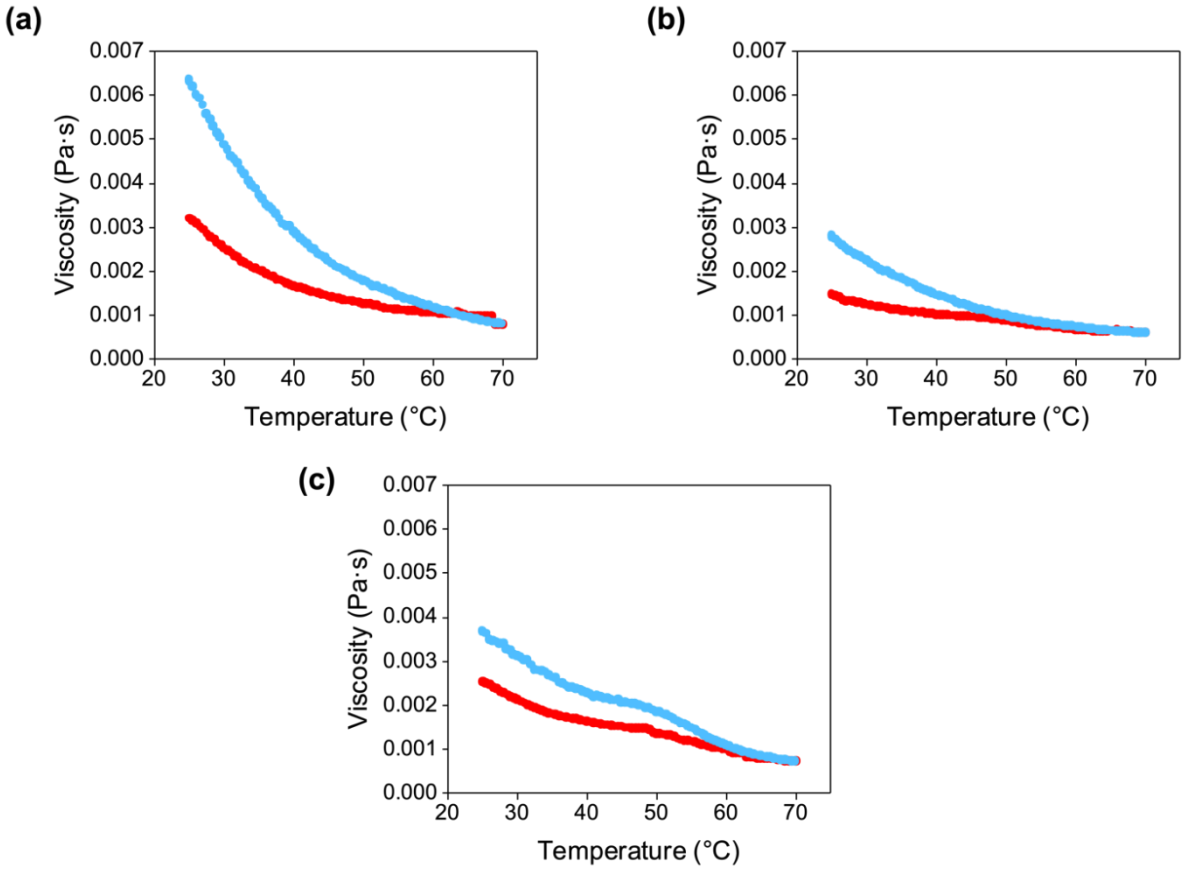

Figure 3.4. Change in viscosity with temperature of (a) **PBI-A**, (b) **PBI-L**, and (c) **PBI-Y** at a shear rate of 10 s^{-1} and heating and cooling rates of 0.5°C/min. The temperature was maintained at 70°C for two minutes before cooling. Red data represent the heating cycle, and blue data represent the cooling cycle.

As the constant shear measurements suggested that **PBI-A** was more process-dependent than **PBI-L** and **PBI-Y**, we measured the change in viscosity upon applying three consecutive heat-cool cycles (Fig. 3.5). If the final viscosity was similar upon each heat-cool cycle, this would suggest that the structures were reversible. For **PBI-L** and **PBI-Y**, there were minimal changes in final viscosities upon the heating and cooling cycles (Fig. 3.5b and 3.5c, respectively). In comparison, each heat-cool cycle gives a different final viscosity upon cooling for **PBI-A** (Fig. 3.5a), further suggesting it is more process-dependent. It is possible that heating **PBI-A** results in the disassembly of the self-assembled structures, and upon re-cooling, the structures reassemble in a more thermodynamically favourable fashion.[49] However, the micelles formed by **PBI-L** and **PBI-Y** may not be as susceptible to heating

and cooling, which could explain the more subtle temperature-dependent behaviour (Fig 3.4 and Fig. 3.5).

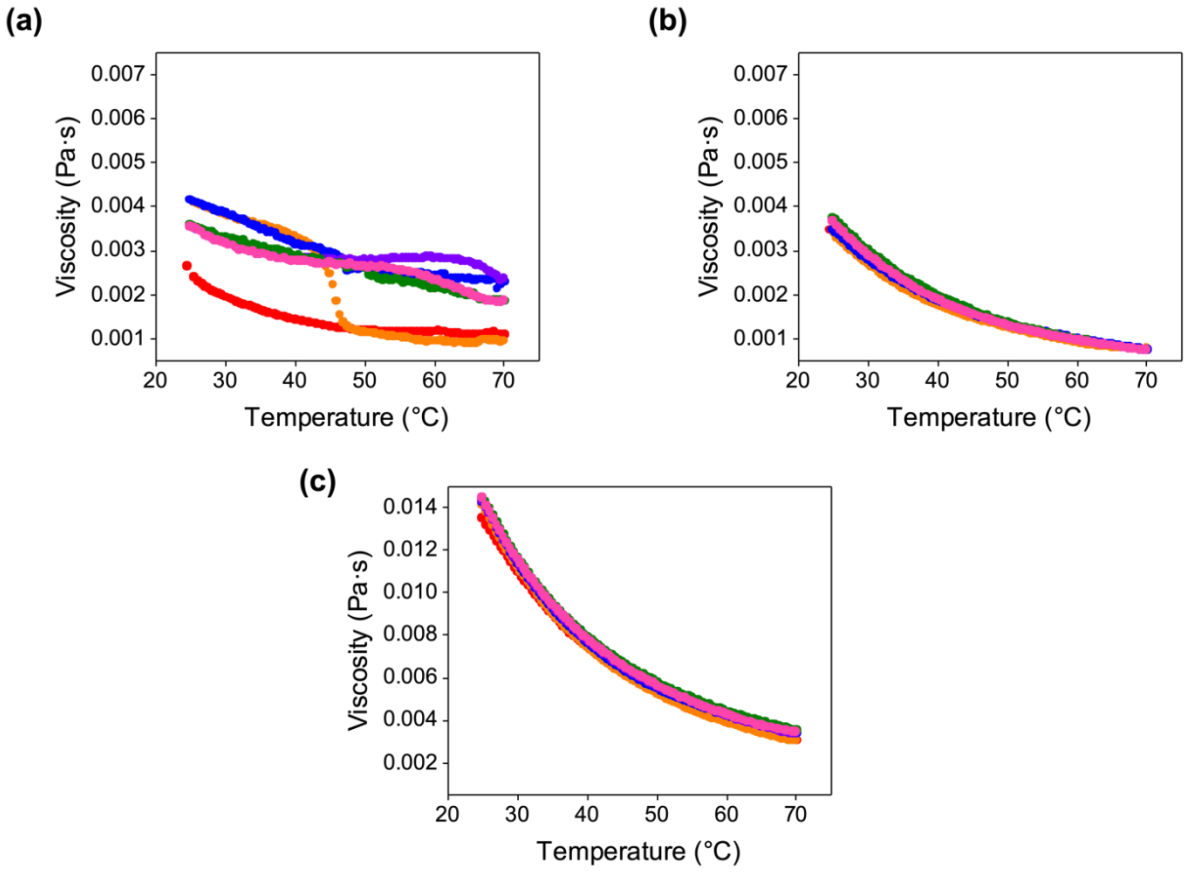

Figure 3.5. Change in viscosity with temperature of (a) **PBI-A**, (b) **PBI-L**, and (c) **PBI-Y** at a shear rate of 10 s^{-1} and heating and cooling rates of 0.5°C/min over three consecutive heat-cool cycles. The temperature was maintained at 70°C for two minutes after each heating cycle before cooling. Red, blue, and green data are heating cycles 1, 2, and 3, respectively. Orange, purple, and pink data are cooling cycles 1, 2, and 3, respectively.

To further understand the influence of the heat-cool cycles, the dynamic viscosity was measured at 25°C after heating to various temperatures (Fig. 3.6). Before heat-cooling, all PBIs showed shear-thinning, suggesting the presence of worm-like micelles.[30,45,50,51] There was a noticeable increase in viscosity as the size of the sidechain of the amino acid increased, with **PBI-Y** being the most viscous at room temperature (Fig. 3.6c). This increase in viscosity could be due to the larger phenyl rings of **PBI-Y** experiencing more steric hindrance due to their proximity as they align under shear. For **PBI-A** and **PBI-L**, we again found that the viscosity at high shear of the cooled solution increased with increasing heating temperature (Fig. 3.6a and 3.6b, respectively). This increase in final viscosity was not observed with **PBI-Y** until the heating temperature was 60°C or 70°C, with lower heating

temperatures showing lower final viscosities than the initial non-heat-cooled samples (Fig. 3.6c). For **PBI-A**, samples kept at 25°C and those heated to 30°C and then cooled to 25°C displayed shear-thinning behaviour (Fig. 3.6a). However, at heating temperatures greater than 50°C, this behaviour was not seen upon cooling. This lack of shear thinning but increase in viscosity suggests spherical aggregates may be present. For **PBI-L**, all samples showed shear-thinning, but this behaviour was less apparent at temperatures greater than 50°C (Fig. 3.6b). In comparison, this lack of shear-thinning in **PBI-Y** was not observed until the heating temperature was 60°C. These results highlight that each PBI behaves differently after a heat-cool cycle.

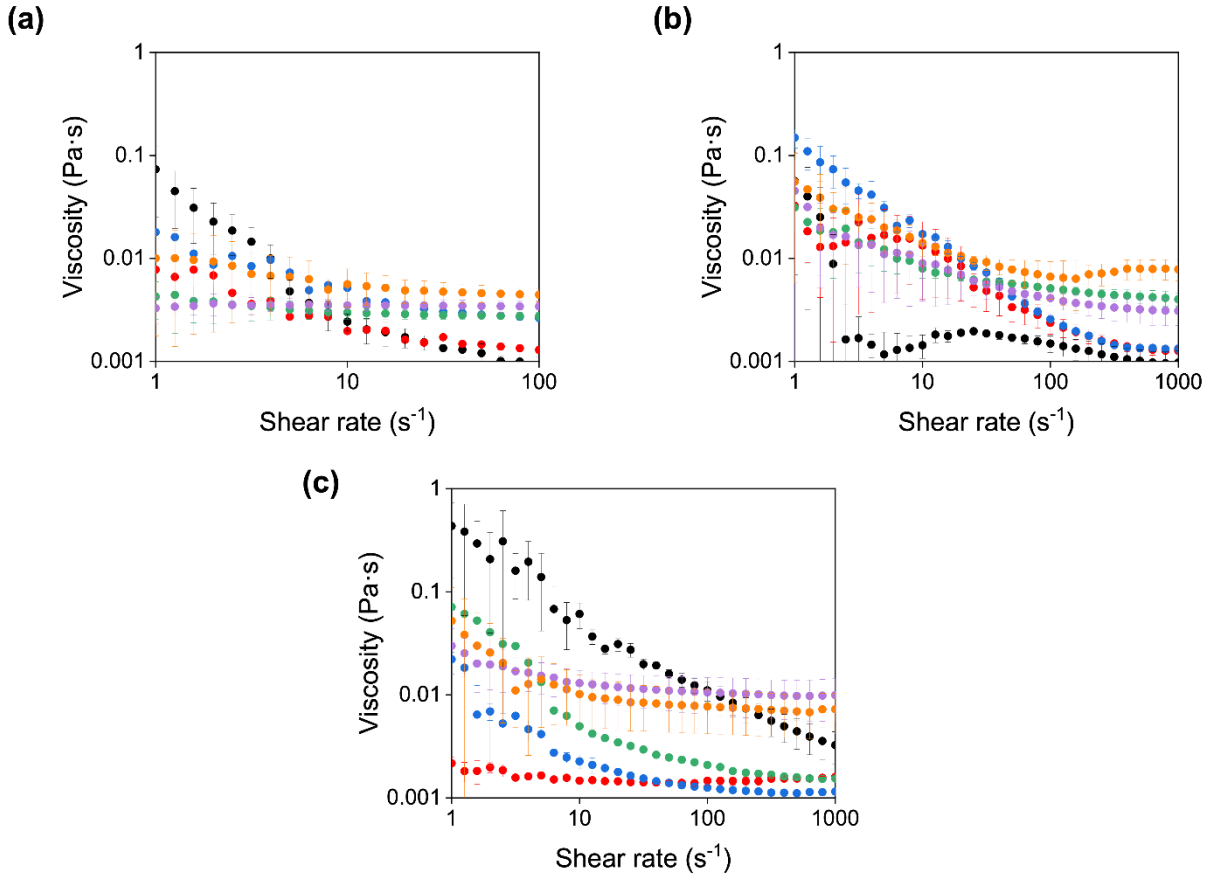

Figure 3.6. Dynamic viscosity of (a) **PBI-A**, (b) **PBI-L**, and (c) **PBI-Y** at 25°C (black) and solutions heated to 30°C (red), 40°C (blue), 50°C (green), 60°C (purple), and 70°C (orange) and re-cooling to 25°C before measurements. Data shown are averaged data for triplicate runs, with error bars representing standard deviation.

To understand the change in rheological behaviour, we used SANS to assess any morphological changes at the fibre level (Fig. 3.7). At 25°C, **PBI-A** solutions fit best to a flexible elliptical cylinder combined with a power law, with a radius of 56 Å and a Kuhn length of 120 Å (Fig. 3.7a and Table 3.1). Samples heated to 70°C (*in situ*) still fit best to a

flexible elliptical cylinder model and power law (Fig. 3.7b and Table 3.1). However, these fibres had an increased radius and Kuhn length (63 Å and 250 Å, respectively), suggesting thicker and more rigid fibrous structures. Such results show that heating **PBI-A** solutions results in structural changes to the fibres, which was not apparent from the viscosity data alone. After a heat-cool cycle from 70°C, the data now fit a combined flexible elliptical cylinder and sphere model (Fig. 3.7c and Table 3.2), explaining the increase in viscosity and lack of shear thinning observed in the rheological data. Compared to the heated solution, the Kuhn length of the heat-cooled fibres decreased (190 Å compared to 250 Å for the heated solution), as did the radius (56 Å vs. 63 Å). Furthermore, the Kuhn length of the heat-cooled solution is greater than that of the non-heat-cooled solution (190 Å and 125 Å for heat-cooled and non-heat-cooled samples, respectively), but the radius remains at 56 Å. This behaviour is different to that previously observed for 2NapFF, which also showed an increase in Kuhn length but a decrease in the radius, attributed to partial dehydration of the fibrous core.[45]

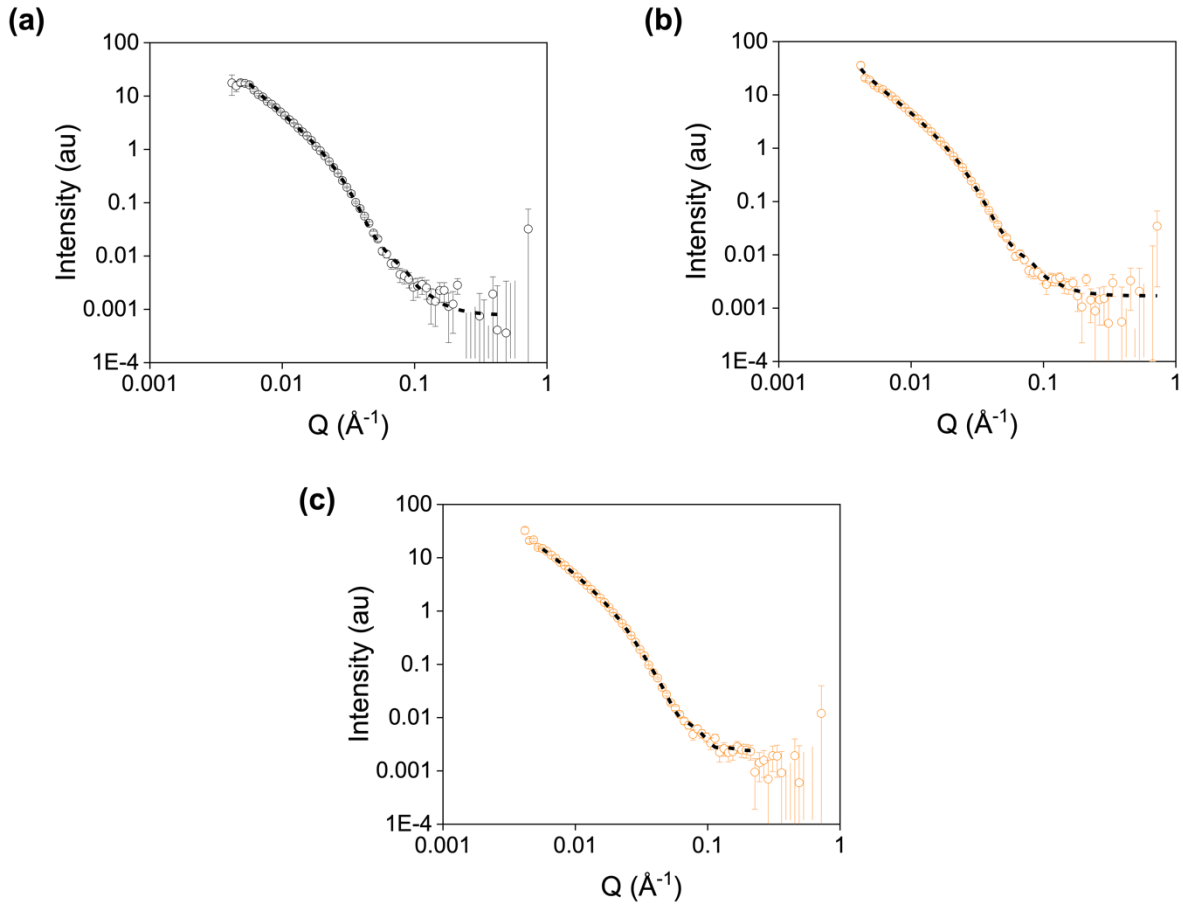

Figure 3.7. Small-angle neutron scattering patterns from **PBI-A** solutions at (a) 25°C, (b) 70°C, and (c) heat-cooled from 70°C.

Table 3.1. Tabulated parameters of the SANS model fits for a **PBI-A** solution at 25°C and those heated to various temperatures.

Heating temperature (°C)	**25**	**30**	**50**	**70**
Model	Flexible elliptical cylinder + power law	Flexible elliptical cylinder + power law	Flexible elliptical cylinder + power law	Flexible elliptical cylinder + power law
Background (cm^{-1})	0.001	0.001	0.001	0.001
Cylinder scale	$2.0000\times10^{-4} \pm 4.1903\times10^{-5}$	$5.4386\times10^{-4} \pm 1.1589\times10^{-5}$	$2.0825\times10^{-4} \pm 4.8646\times10^{-6}$	$1.1701\times10^{-4} \pm 1.1368\times10^{-5}$
Length (Å)	1160 ± 160	1250 ± 90	890 ± 65	1000 ± 100
Kuhn length (Å)	120 ± 0.1	125 ± 0.8	139 ± 2.1	250 ± 3.4
Radius (Å)	56.3 ± 0.3	55.5 ± 1.2	53.9 ± 2.9	62.5 ± 0.2
Axis ratio	1.80 ± 0.02	1.93 ± 0.2	2.09 ± 0.2	1.83 ± 0.08
Power law scale	$3.2971\times10^{-6} \pm 3.1231\times10^{-7}$	$1.8939\times10^{-6} \pm 3.0612\times10^{-7}$	$1.5842\times10^{-5} \pm 1.5569\times10^{-7}$	$2.3322\times10^{-6} \pm 3.5973\times10^{-7}$
Power law	2.88 ± 0.03	2.99 ± 0.03	2.81 ± 0.02	2.92 ± 0.03
χ^2	5.3400	1.0742	1.1337	1.2236

Table 3.2. Tabulated parameters of the SANS model fits for a **PBI-A** solution at 25°C and those heated to various temperatures and cooled back to 25°C before measurements.

Heating temperature (°C)	**25**	**30**	**50**	**70**
Model	Flexible elliptical cylinder + power law	Elliptical cylinder + power law	Flexible elliptical cylinder + sphere	Flexible elliptical cylinder + sphere
Background (cm^{-1})	0.001	0.001	0.001	0.001
Cylinder scale	$2.0000\times10^{-4} \pm 4.1903\times10^{-5}$	$5.9020\times10^{-4} \pm 2.5484\times10^{-5}$	$6.8148\times10^{-4} \pm 6.3857\times10^{-6}$	$2.7464\times10^{-4} \pm 5.4442\times10^{-6}$
Length (Å)	1160 ± 160	500 ± 23	1000 ± 150	1000 ± 50
Kuhn length (Å)	120 ± 0.1	N/A	165.1 ± 4.0	190 ± 0.2
Radius (Å)	56.3 ± 0.3	59.6 ± 1.0	74.2 ± 0.2	62.5 ± 0.2
Axis ratio	1.80 ± 0.02	2.68 ± 0.1	4.69 ± 0.5	2.22 ± 0.06
Sphere scale	N/A	N/A	$9.1241 \times 10^{-5} \pm 3.2978 \times 10^{-5}$	$7.056 \times 10^{-4} \pm 1.1258 \times 10^{-5}$
Sphere radius (Å)	N/A	N/A	25.1 ± 3.7	38.1 ± 1.5
Power law scale	$3.2971\times10^{-6} \pm 3.1231\times10^{-7}$	$2.9093\times10^{-7} \pm 1.5959\times10^{-8}$	N/A	N/A
Power law	2.88 ± 0.03	3.35 ± 0.1	N/A	N/A
χ^2	5.3400	1.2924	1.3962	1.4916

The scattering data of **PBI-A** with other heating temperatures showed that the Kuhn length increased with increasing temperature, whilst the radius remained within error (Table 3.1).

Such results suggest that heating changes the flexibility of the fibres. The scattering at different temperatures was similar at low Q, indicating that heating did not cause any network changes (Fig. 3.8a). All the heat-cooled samples fit the combined flexible elliptical cylinder and sphere model (Fig. A.2.7 and A.2.8, Appendix and Table 3.2), again in agreement with the rheological data. Comparing the heated samples to those that had undergone a heat-cool cycle, the heat-cooled samples had larger Kuhn lengths and/or radii than their heated counterparts (Fig. 3.8b and 3.8c). However, this trend was not observed at 70°C (Fig. 3.8d). These results highlight the importance of the heating temperature, as a change of 5-10°C can cause a large structural change.

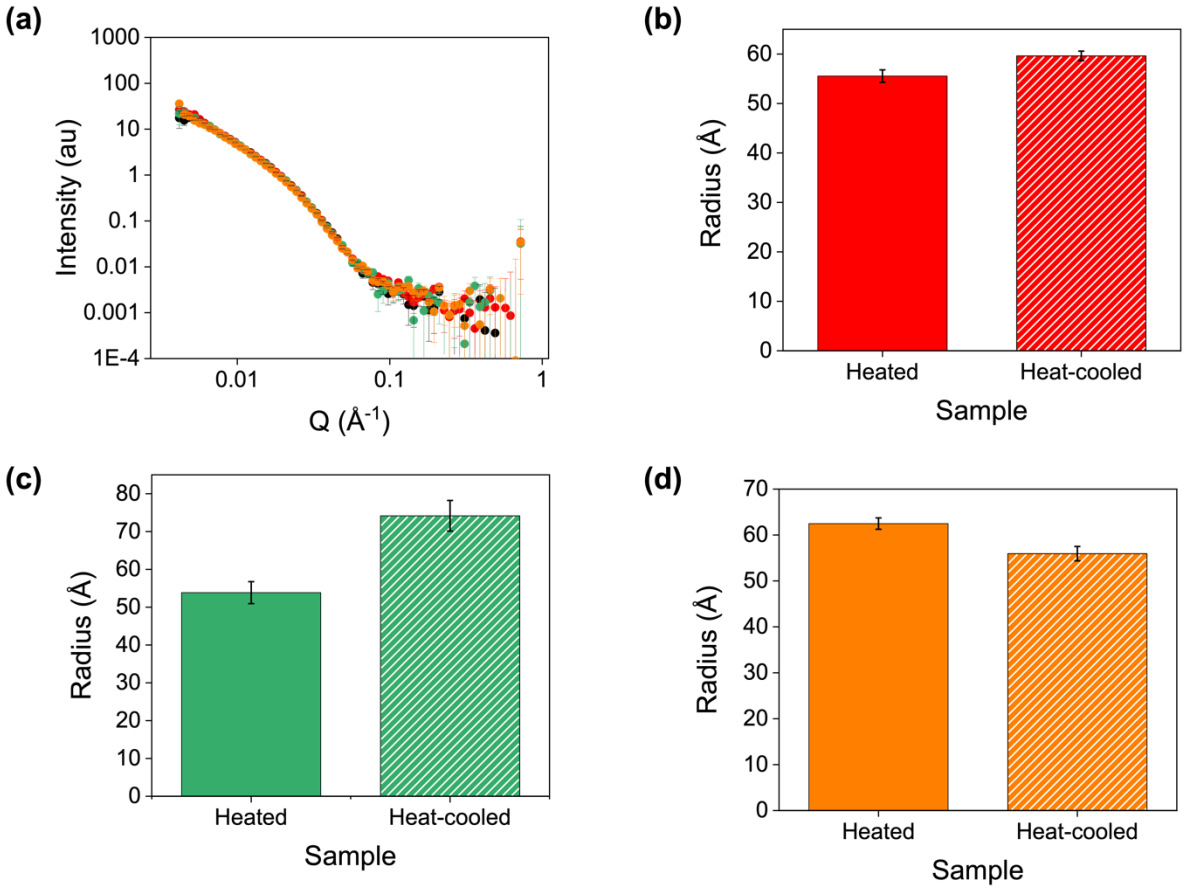

Figure 3.8. (a) Small-angle neutron scattering patterns from **PBI-A** solutions at 25°C (black), 30°C (red), 50°C (green), and 70°C (orange). (b)-(d) Comparison of the radius of **PBI-A** solutions heated (solid colour) and heat-cooled (dashed lines), with heating temperatures of (b) 30°C, (c) 50°C, and (d) 70°C.

At 25°C, **PBI-L** fit best to a sphere with power law model (Fig. 3.9a and Table 3.3), with a radius of 62 Å, in agreement with previous reports.[52,53] The sphere model is attributed to small aggregates that have not yet assembled into large fibrous structures. Samples heated from 30-50°C (*in situ*) all fit best to a sphere and power law model (Fig. A.2.9 and A.2.10,

Appendix and Table 3.3). Samples heated to 70°C (*in situ*) fit best to a combined elliptical cylinder and power law model (Fig. 3.9b and Table 3.3), indicating increased aggregation of the nanostructures. Upon cooling from 70°C to 25°C, the data again fit best to a sphere and power law model (Fig. 3.9c and Table 3.4) with a slight increase in the radius (66 Å), further suggesting that **PBI-L** is less process-dependent than **PBI-A**. For **PBI-L**, all the heat-cooled samples with different heating temperatures fit to a combined sphere and power law model (Fig. A.2.11 and A.2.12, Appendix, Fig. 3.9c and Table 3.4), except for that heated to 50°C and cooled to 25°C (Fig. A.2.12, Appendix and Table 3.4), which instead fit to a combined model of an elliptical cylinder and power law. Such results again highlight the importance of the heating temperature, which can impact each PBI differently.

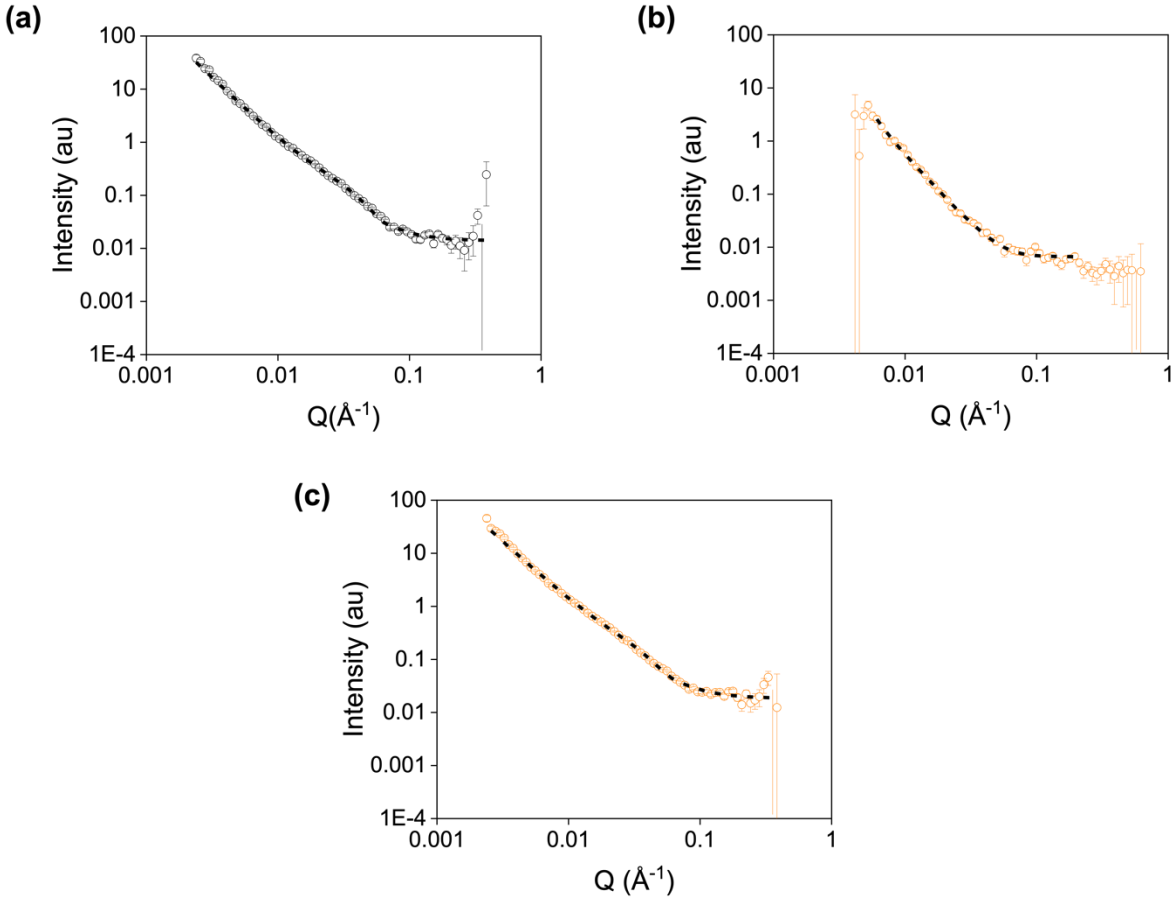

Figure 3.9. Small-angle neutron scattering patterns from **PBI-L** solutions at (a) 25°C, (b) 70°C, and (c) heat-cooled from 70°C.

Table 3.3. Tabulated parameters of the SANS model fits for a **PBI-L** solution at 25°C and those heated to various temperatures.

Heating temperature (°C)	**25**	**30**	**50**	**70**
Model	Sphere + power law	Power law	Sphere + power law	Elliptical cylinder + power law
Background (cm^{-1})	0.001	0.001	0.001	0.001
Cylinder scale	N/A	N/A	N/A	$5.1042 \times 10^{-5} \pm 3.8997 \times 10^{-6}$
Length (Å)	N/A	N/A	N/A	350 ± 90
Radius (Å)	N/A	N/A	N/A	22.9 ± 0.3
Axis ratio	N/A	N/A	N/A	4.10 ± 0.08
Sphere scale	$1.0980 \times 10^{-4} \pm 6.4336 \times 10^{-6}$	N/A	$9.6393 \times 10^{-5} \pm 2.1129 \times 10^{-6}$	N/A
Sphere radius (Å)	62.0 ± 0.2	N/A	21.0 ± 1.9	N/A
Power law scale	$2.9644 \times 10^{-5} \pm 3.1780 \times 10^{-6}$	$6.2956 \times 10^{-7} \pm 1.8464 \times 10^{-9}$	$1.3933 \times 10^{-7} \pm 6.2711 \times 10^{-9}$	$1.9884 \times 10^{-8} \pm 1.5745 \times 10^{-9}$
Power law	2.28 ± 0.02	2.83 ± 0.07	3.15 ± 0.06	3.62 ± 0.04
χ^2	2.1655	1.4050	1.0041	1.1401

Table 3.4. Tabulated parameters of the SANS model fits for a **PBI-L** solution at 25°C and those heated to various temperatures and cooled back to 25°C before measurements.

Heating temperature (°C)	**25**	**30**	**50**	**70**
Model	Sphere + power law	Sphere + power law	Elliptical cylinder + power law	Sphere + power law
Background (cm^{-1})	0.001	0.001	0.001	0.001
Cylinder scale	N/A	N/A	$3.2275 \times 10^{-4} \pm 3.0392 \times 10^{-5}$	N/A
Length (Å)	N/A	N/A	1000 ± 70	N/A
Radius (Å)	N/A	N/A	23.9 ± 0.2	N/A
Axis ratio	N/A	N/A	2.84 ± 0.4	N/A
Sphere scale	$1.0980 \times 10^{-4} \pm 6.4336 \times 10^{-6}$	$1.2491 \times 10^{-4} \pm 7.4188 \times 10^{-6}$	N/A	$9.5320 \times 10^{-5} \pm 7.2215 \times 10^{-6}$
Sphere radius (Å)	62.0 ± 0.2	58.1 ± 0.1	N/A	65.6 ± 1.3
Power law scale	$2.9644 \times 10^{-5} \pm 3.1780 \times 10^{-6}$	$3.1739 \times 10^{-5} \pm 2.5023 \times 10^{-6}$	$2.7070 \times 10^{-6} \pm 8.2457 \times 10^{-7}$	$5.5250 \times 10^{-5} \pm 5.3869 \times 10^{-6}$
Power law	2.28 ± 0.02	2.30 ± 0.02	2.71 ± 0.06	2.18 ± 0.02
χ^2	2.1655	2.6734	1.1741	2.5813

At 25°C, **PBI-Y** fit to a sphere and power law model with a radius of 137 Å (Fig. 3.10a and Table 3.5). This much larger spherical radius could be due to the increase in the size of the tyrosine amino acid sidechain, which may prevent the molecules from stacking as close

together as **PBI-A** and **PBI-L** can. As **PBI-Y** is heated (*in situ*), solutions at all heating temperatures best fit to a sphere and power law model (Fig. A.2.13 and A.2.14, Appendix and Table 3.5), with the radii of the spheres increasing with increasing heating temperature. As with **PBI-L**, solutions of **PBI-Y** heated to 30°C and cooled to 25°C best fit to a combined sphere and power law model (Fig. A.2.15, Appendix and Table 3.6). However, when heated to 50°C and cooled to 25°C, the data now fit to a combined elliptical cylinder and sphere model (Fig. A.2.16, Appendix and Table 3.6). When heated to 70C° and cooled to 25°C, the data fit to an elliptical cylinder and power law model (Fig. 3.10c and Table 3.6), similar to **PBI-L**. It is evident that both the heating temperature and PBI influence the fibre structure. As such, this can be exploited in the development of hydrogels, as it should impact their gelation route and final bulk properties. Similarly, these structures will dry down to form thin films with potentially different properties.

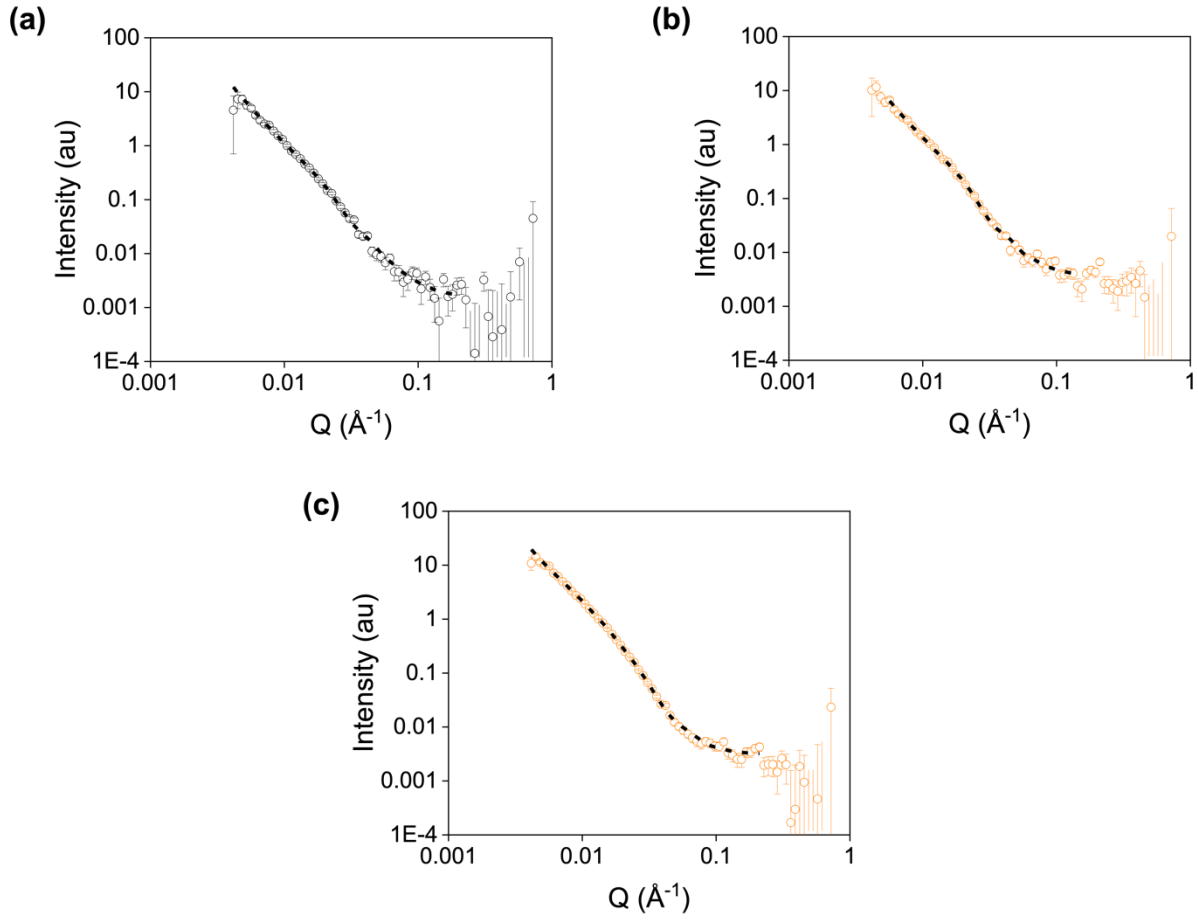

Figure 3.10. Small-angle neutron scattering patterns from **PBI-Y** solutions at (a) 25°C, (b) 70°C, and (c) heat-cooled from 70°C.

Table 3.5. Tabulated parameters of the SANS model fits for a **PBI-Y** solution at 25°C and those heated to various temperatures.

Heating temperature (°C)	**25**	**30**	**50**	**70**
Model	Sphere + power law	Sphere + power law	Sphere + power law	Sphere + power law
Background (cm^{-1})	0.001	0.001	0.001	0.001
Sphere scale	$2.6054\times10^{-5} \pm 3.5407\times10^{-6}$	$4.4695\times10^{-5} \pm 3.9434\times 10^{-6}$	$3.8556\times10^{-5} \pm 3.7789\times10^{-6}$	$3.3982\times10^{-5} \pm 2.4299\times10^{-6}$
Sphere radius (Å)	137.0 ± 5.3	98.4 ± 2.9	138.5 ± 4.2	142.2 ± 3.2
Power law scale	$2.1920\times10^{-6} \pm 3.9978\times10^{-7}$	$4.4433\times10^{-7} \pm 1.3326\times10^{-8}$	$1.8635\times10^{-6} \pm 2.8448\times10^{-7}$	$6.3609\times10^{-6} \pm 9.9632\times10^{-8}$
Power law	2.80 ± 0.04	3.20 ± 0.04	2.90 ± 0.03	3.07 ± 0.03
χ^2	1.0429	1.8750	1.1212	1.7569

Table 3.6. Tabulated parameters of the SANS model fits for a **PBI-Y** solution at 25°C and those heated to various temperatures and cooled back to 25°C before measurements.

Heating temperature (°C)	**25**	**30**	**50**	**70**
Model	Sphere + power law	Sphere + power law	Elliptical cylinder + sphere	Elliptical cylinder + power law
Background (cm^{-1})	0.001	0.001	0.001	0.001
Cylinder scale	N/A	N/A	$2.2208\times10^{-4} \pm 3.9495\times10^{-6}$	$1.4718\times10^{-5} \pm 8.8333\times10^{-6}$
Length (Å)	N/A	N/A	1011 ± 77	697 ± 68
Radius (Å)	N/A	N/A	97.3 ± 1.9	74.3 ± 2.0
Axis ratio	N/A	N/A	4.3 ± 0.3	2.9 ± 0.2
Sphere scale	$2.6054\times10^{-5} \pm 3.5407\times10^{-6}$	$3.1812\times10^{-5} \pm 1.6623\times10^{-6}$	$8.2343\times10^{-5} \pm 3.6758\times10^{-6}$	N/A
Sphere radius (Å)	137.0 ± 5.3	131.8 ± 2.5	67.7 ± 2.1	N/A
Power law scale	$2.1920\times10^{-6} \pm 3.9978\times10^{-7}$	$1.6053\times10^{-6} \pm 2.2433\times10^{-7}$	N/A	$8.0597\times10^{-6} \pm 2.0098\times10^{-7}$
Power law	2.80 ± 0.04	2.84 ± 0.02	N/A	3.03 ± 0.05
χ^2	1.0429	1.4586	1.6900	1.3590

The molecular packing and aggregation of the PBI solutions are critical parameters in the conductivity of the resulting films.[10,21] Therefore, UV-vis absorption spectra were recorded upon changing the temperature (Fig. 3.11 and Fig. A.2.17- A.2.22, Appendix). The peak ratio of the 490 and 540 nm peaks (attributed to the 0-0 and 0-1 vibronic bands of the S_0-S_1 transitions) increases with increasing temperature and decreases with decreasing temperature. A high 0-0/0-1 ratio is indicative of high PBI solubility and less aggregation, while a lower ratio indicates greater aggregation, which is typical for charged species in

water.[54] For all PBIs, the absorption did not revert to the original absorption of the non-heat-cooled samples upon cooling, in agreement with the viscosity and SANS data. This change in peak intensity is most intense for **PBI-Y** (Fig. 3.11f), with aggregates becoming more J-like upon heat-cooling.

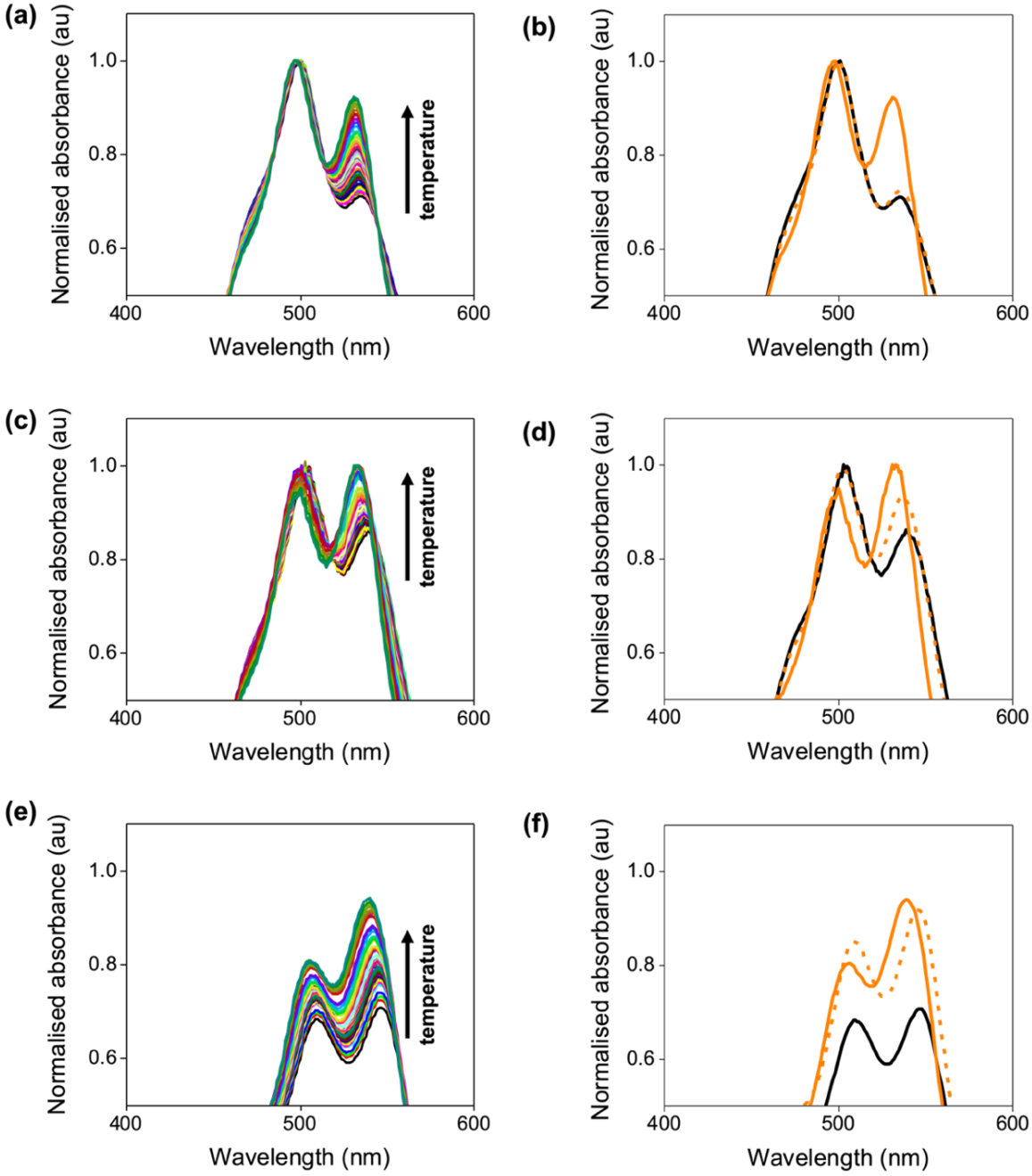

Figure 3.11. (a), (c), and (e): normalised UV-vis absorption spectra with increasing temperature, highlighting the S_0-S_1 changes. The temperature range was 25-70°C, with the increase in temperature shown by the black arrow. (b), (d) and (f): normalised UV-vis absorption spectra of solutions that are non-heat-cooled (black), heated to 70°C (orange), and heat-cooled from 70°C (orange dashed). (a) and (b) are **PBI-A**, (c) and (d) are **PBI-L**, and (e) and (f) are **PBI-Y**. Data are normalised to the highest absorption of each spectrum.

As discussed in Chapter 1, there is a link between the micellar aggregates and "apparent" pK_a values.[55] Furthermore, it is known that pK_a values can shift drastically in protein and peptide-self-assembly, particularly in hydrophobic environments.[56] Therefore, the "apparent" pK_a values were determined for heated and heat-cooled solutions for various heating temperatures (Fig. 3.12 and Table 3.7). The results show that the "apparent" pK_a values of the PBIs differed depending on the heating temperature chosen. For all PBIs, two "apparent" pK_a values were observed at 25°C despite only two identical ionisable groups being present. It has been previously hypothesised, from time-resolved small-angle neutron scattering, that this is due to structural transitions with decreasing pH.[57] For the heated solutions, all PBIs showed a decrease in both "apparent" pK_a values compared to those at 25°C (Fig. 3.12a, 3.12c, and 3.12f). Hydrogen bonding between molecules can lead to an increase in "apparent" pK_a values.[58] Therefore, this decrease in "apparent" pK_a with increasing temperature suggests that interactions between the PBI molecules are reduced at higher temperatures.[59] For the heat-cooled samples, the values did not revert to the initial 25°C ones. Such results suggest that a structural transition occurs when the PBIs are heated, which is not reversible upon cooling, in agreement with the viscosity measurements under shear (Fig. 3.4).

Table 3.7. Tabulated "apparent" pK_a values of **PBI-A**, **PBI-L**, and **PBI-Y** solutions heated to various temperatures and solutions heated to various temperatures and then cooled to 25°C before measurements.

Heating temperature (°C)	**25**	**30**	**40**	**50**	**60**	**70**
PBI-A	6.80, 5.30	6.64, 5.20	6.45, 5.40	5.45	6.94, 5.15	6.70, 5.55
PBI-L	7.70, 5.58	6.28, 5.60	6.72, 5.69	6.80, 5.45	6.33, 5.87	6.22, 5.53
PBI-Y	7.44, 6.78	4.67	5.43, 4.87	6.37, 4.30	7.52, 4.77	7.68, 4.90
Heating temperature (°C)	**25**	**30 Heat-cooled**	**40 Heat-cooled**	**50 Heat-cooled**	**60 Heat-cooled**	**70 Heat-cooled**
PBI-A	6.80, 5.30	6.83, 5.82	6.25, 5.60	6.23, 5.19	6.86, 5.25	5,88, 5.27
PBI-L	7.70, 5.58	6.74, 5.63	6.06, 5.56	6.85, 5.53	6.25, 5.53	6.53, 5.51
PBI-Y	7.44, 6.78	5.55	6.57, 5.17	6.34, 4.83	6.12, 5.05	5.00

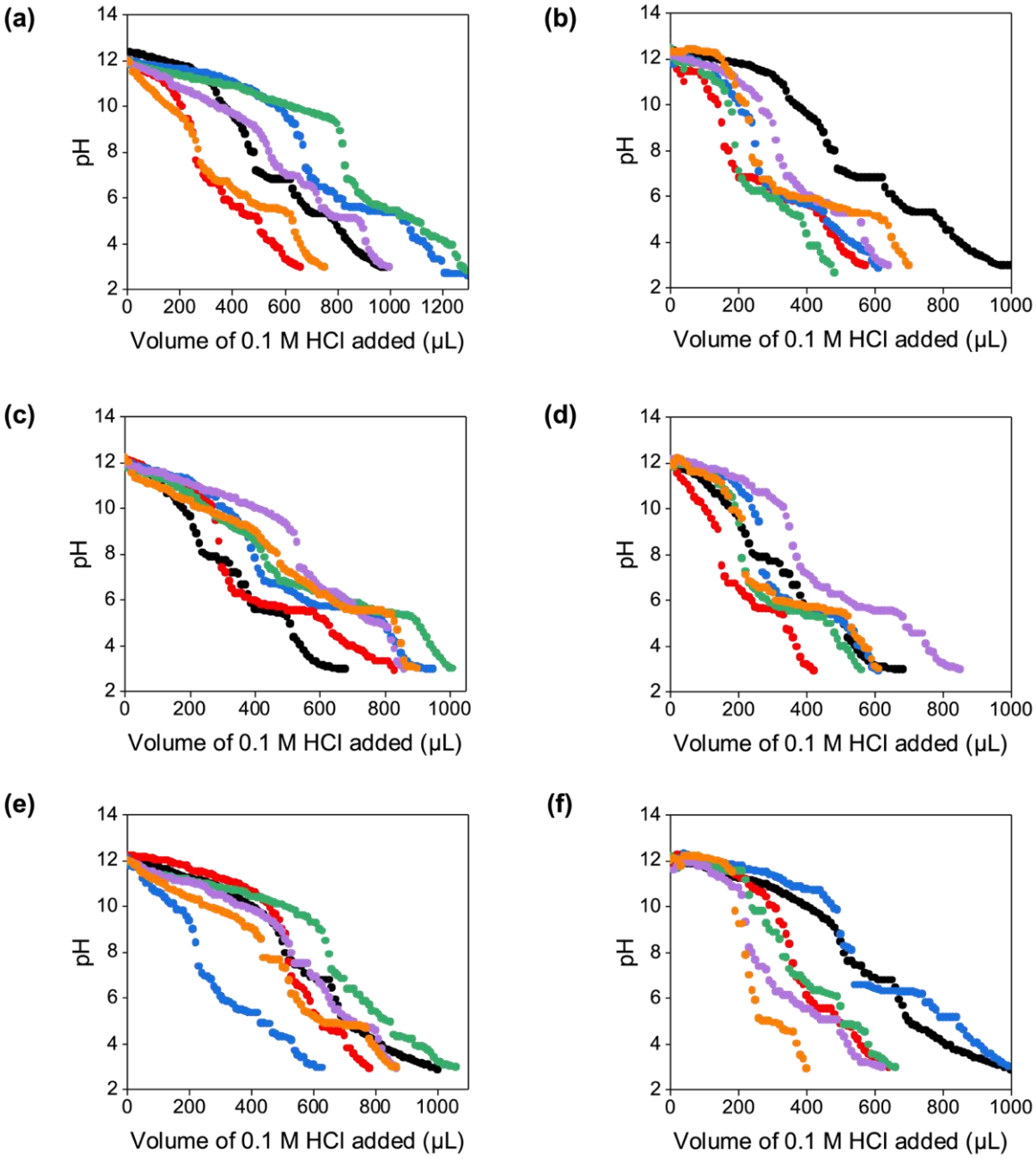

Figure 3.12. "Apparent" pK_a titrations of (a) and (b) **PBI-A**, (c) and (d) **PBI-L**, and (e) and (f) **PBI-Y** with (a), (c), and (e) heated, and (b), (d), and (f) heat-cooled solutions. Titrations were recorded at 25°C (black) and with heating temperatures of 30°C (red), 40°C (blue), 50°C (green), 60°C (purple), and 70°C (orange).

The solubility of a molecule across a range of temperatures can be monitored using the integrations of ^{1}H NMR spectra. Therefore, ^{1}H NMR spectroscopy was used to gain further insight into the impact of heating and cooling (Fig. 3.13 and Table 3.8). For all PBIs, the peaks are broad and poorly resolved at 25°C due to their aggregation.[45] Upon heating, the resolution and the integral of the methyl signal of the alanine increased for **PBI-A** (integral

of methanol:**PBI-A** = 3.33 at 25°C compared to 3.52 at 70°C, Fig. 3.13a and 3.13b). This increase in sharpness/integral suggests the molecule is soluble and freely tumbling in solution. Such behaviour was less apparent for **PBI-L** (Fig. 3.13c and 3.13d) and **PBI-Y** (Fig. 3.13e and 3.13f), further suggesting that **PBI-A** is more process-dependent. There was a shift in peak position after heating for all PBIs, which became more apparent at heating temperatures greater than 40°C. This change in chemical shift was due to the deshielding effect. As the PBI samples are cooled back to 25°C, the peaks move back upfield to the same chemical shift as that before heating. The UV-vis absorption and ^{1}H NMR data suggest that the heat-cool cycle leads to changes in the packing of the PBI molecules as opposed to the formation of new chemical structures or degradation of the materials upon heating. The nature of these changes remains to be addressed, and as such, future work should use theoretical studies and computational simulations to further understand the changes in packing with temperature.

Table 3.8. Tabulated proton integrals of **PBI-A**, **PBI-L**, and **PBI-Y** solutions heated to various temperatures and solutions heated to various temperatures and cooled to 25°C. The integrals represent the CH_3 protons of the alanine and leucine, and the CH_2 protons of the tyrosine sidechains. Integrals are calculated in reference to a methanol standard.

Heating temperature (°C)	**25**	**30**	**40**	**50**	**60**	**70**
PBI-A	3.33	3.43	3.40	3.43	3.55	3.52
PBI-L	2.91	3.12	4.92	3.22	4.15	5.96
PBI-Y	1.39	1.36	1.44	1.38	1.54	2.72
Heating temperature (°C)	**25**	**30 Heat-cooled**	**40 Heat-cooled**	**50 Heat-cooled**	**60 Heat-cooled**	**70 Heat-cooled**
PBI-A	3.33	3.43	3.32	3.34	3.41	3.35
PBI-L	2.91	2.99	4.89	3.63	4.17	6.61
PBI-Y	1.39	1.39	1.36	1.38	1.33	1.81

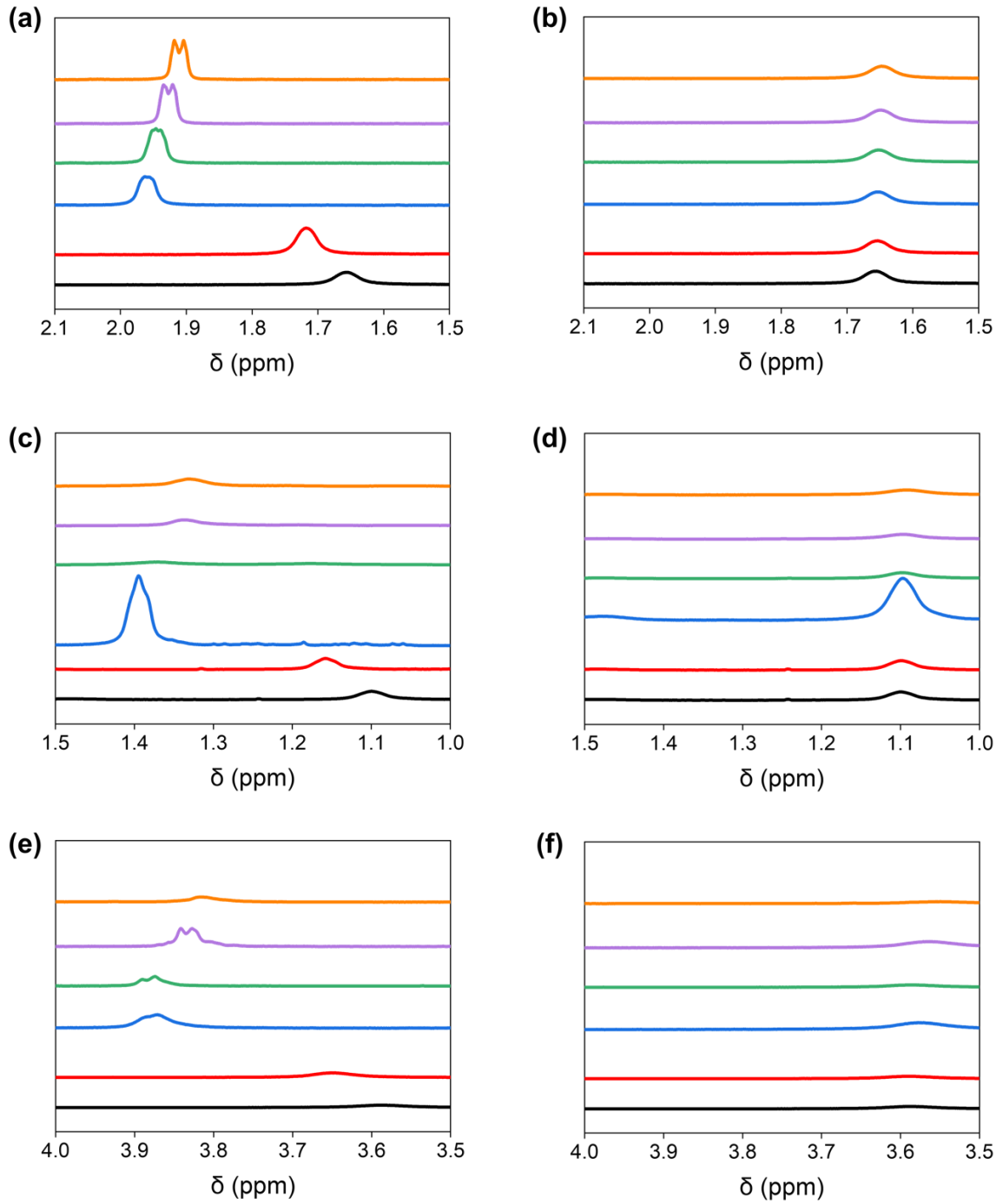

Figure 3.13. Partial ^{1}H NMR spectra for solutions of (a) and (b) **PBI-A**, (c) and (d) **PBI-L**, and (e) and (f) **PBI-Y** after being (a), (c) and (e) heated, and (b), (d) and (f) heat-cooled. The peaks shown represent the CH_3 protons of the alanine and leucine, and the CH_2 protons of the tyrosine sidechains at 25°C (black) and heating temperatures of 30°C (red), 40°C (blue), 50°C (green), 60°C (purple), and 70°C (orange).

3.2.2 Impact of Heat-Cool Processing on PBI Thin Films

As there had been such a large change in the aggregated structures, the photoresponse of these materials was investigated. Current-voltage (IV) plots were collected on films formed

from solutions kept at 25°C and the heat-cooled processed solutions (Fig. 3.14). The films were tested in the dark and after irradiation with 365 nm light for 1 minute to generate the radical anion.[10,29,44] All films maintained electrical continuity during the measurements, with currents less than or equal to 2 μA at +4 V, as previously reported upon irradiation.[10] Due to organic films being prepared and tested under different conditions, and also more typically tested as multi-layered devices rather than as an individual component, it is difficult to compare the photoresponse of these materials to those in the literature. However, as these materials show photoconductivity without any additional layers, we hope the results here show they are promising materials for optoelectronic devices. The heat-cool processing significantly altered the photoresponse, with the extent of this depending on the chosen PBI. For **PBI-A**, the non-heat-cooled samples showed the largest response and films formed from the heat-cooled solutions showed a significant decrease in current (Fig. 3.14a). However, this decrease was not proportional to the increase in temperature. This decrease in conductivity may be due to the formation of spherical aggregates, as observed in the SANS data, which do not form a continuous pathway for the electrons to move between the electrodes. Again, small changes in the heating temperature showed drastic changes in behaviour, with the difference between films cast from a solution at 25°C and a solution heated to 30°C and cooled to 25°C before casting showing the biggest difference. Similar behaviour was also observed for **PBI-Y** films (Fig. 3.14c). However, the photoresponse of **PBI-L** films showed an increase in current when the solutions were heat-cooled before casting (Fig. 3.14b). A possible explanation could be that the increased solubility of **PBI-L** upon heating causes more continuous films to form when dried down. Cross-polarised optical microscopy images (Fig. A.2.30, Appendix) showed that solutions kept at 25°C did not give continuous films (Fig. A.2.30a) with the film continuity increasing with increasing heating temperature (Fig. A.2.30b-f, Appendix). However, all **PBI-L** films did not adsorb well onto the glass, which could explain their poor photoresponse.

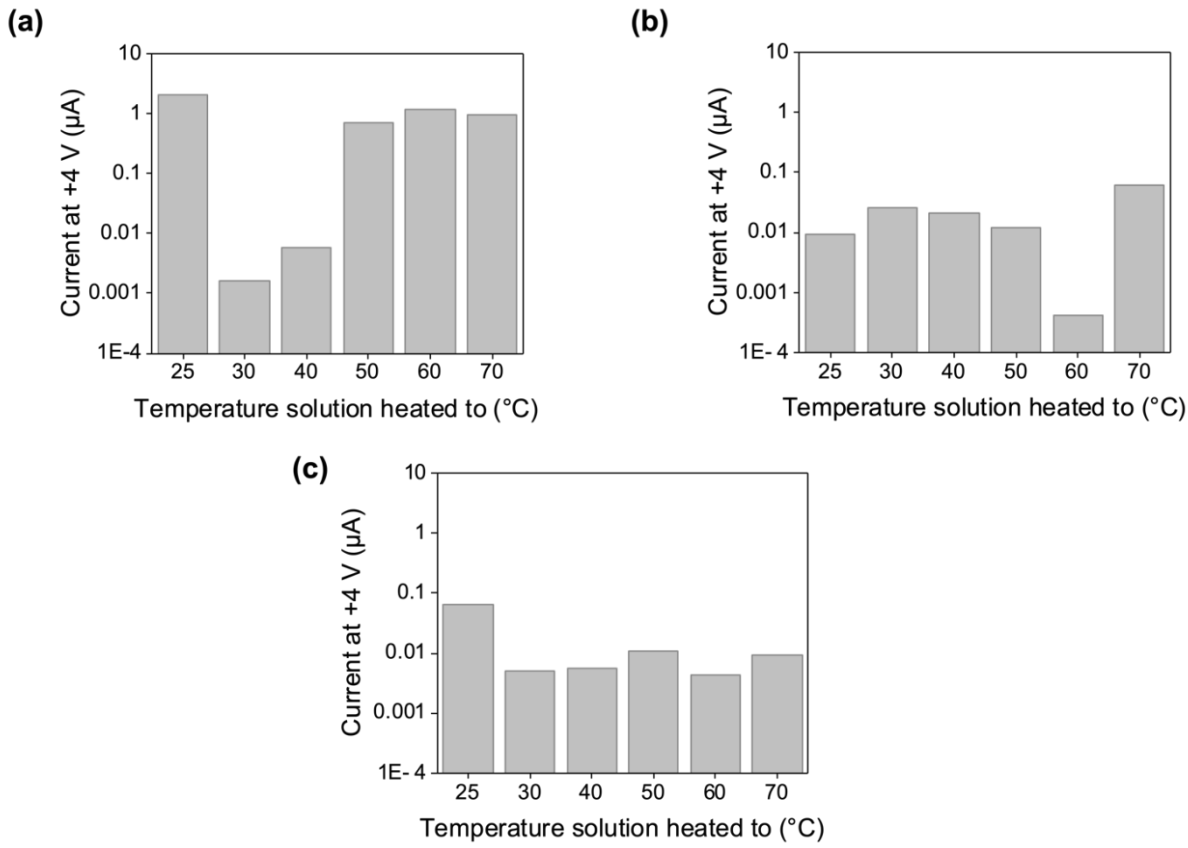

Figure 3.14. Current quoted at +4 V of (a) **PBI-A**, (b) **PBI-L**, and (c) **PBI-Y** films after irradiation for 1 minute with a 365 nm LED light source.

Nanoindentation was used to give further insight into the bulk properties of the PBI films. Nanoindentation has become a common method to characterise the mechanical properties of hydrogels and thin films.[60–63] During the experiment, the nanoindenter tip is lowered onto the sample surface at a constant speed.[64] The force necessary to indent the surface is measured, and the data are outputted as a force-distance curve. By fitting to an appropriate mathematical model, parameters such as the Young's modulus can be calculated. Here, nanoindentation measurements were carried out using a Berkovich indenter tip, using suggested parameters for "hard" materials (materials with an elastic modulus greater than 10 GPa). The average modulus of indentation (E_{IT}) and indentation hardness (H_{IT}) values for each PBI film are shown in Fig. 3.15. The E_{IT} describes the elastic surface behaviour of the film during the indentation, while the H_{IT} is the material's resistance to permanent deformation.[65]

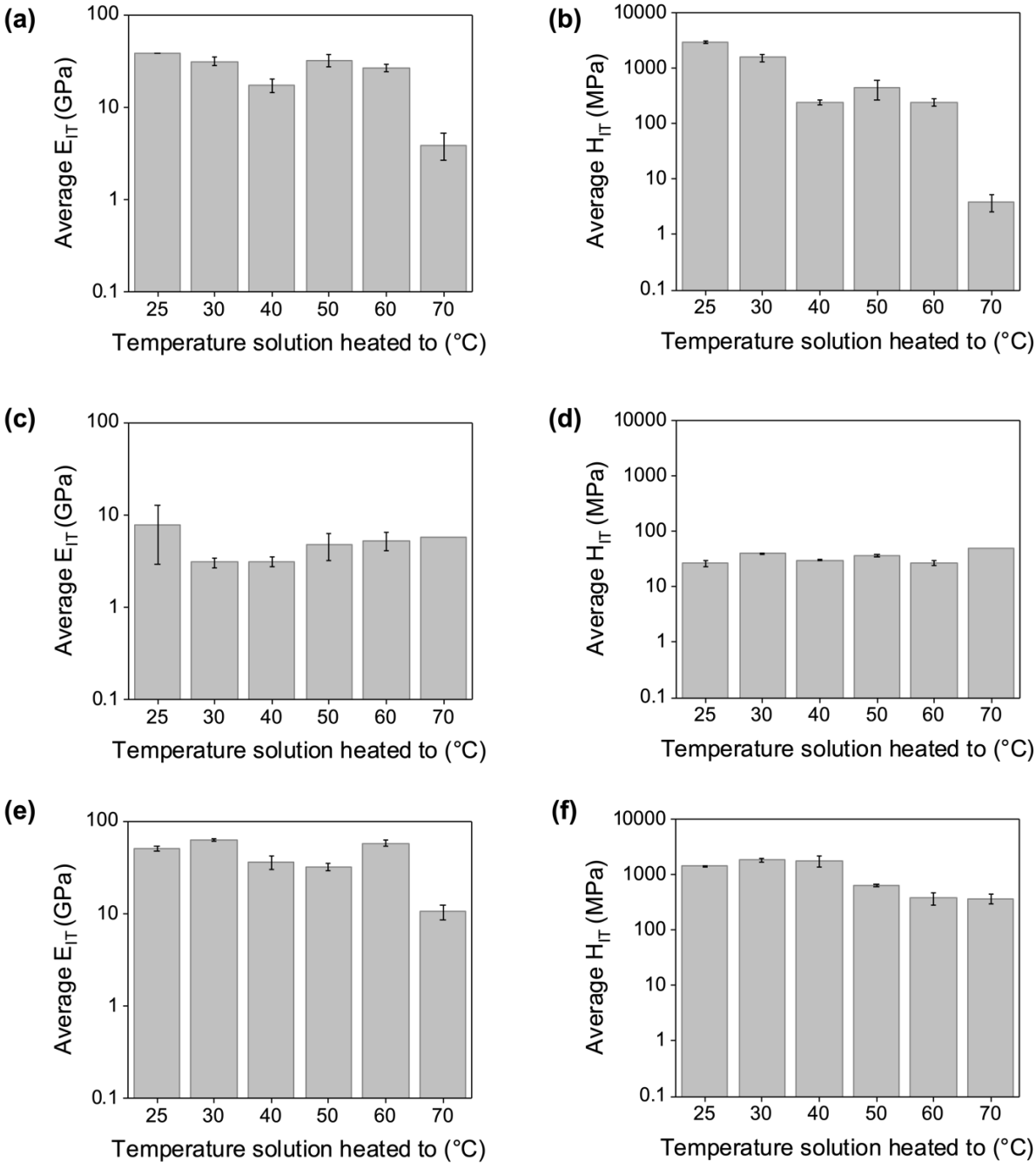

Figure 3.15. The average (a), (c), and (e) E_{IT} and (b), (d), and (f) H_{IT} of PBI thin films formed from heat-cooled solutions. (a) and (b) are **PBI-A**, (c) and (d) are **PBI-L**, and (e) and (f) are **PBI-Y**. Measurements were run in triplicate, with bars representing standard deviation.

The E_{IT} and H_{IT} values for **PBI-A** films formed from non-heat-cooled solutions are 37 GPa and 2950 MPa, respectively (Fig. 3.15a and 3.15b). The E_{IT} (Fig. 3.15a, 3.15c, and 3.15e) and H_{IT} (Fig. 3.15b, 3.15d, and 3.15f) values are smaller for films formed from heat-cooled processed samples. However, as with the photoconductivity, a definitive trend was not

observed. Furthermore, the E_{IT} and H_{IT} values for films formed from solutions heated to 70°C had significantly decreased, suggesting that these films are instead now classified as "soft" materials (E_{IT} and H_{IT} values of 3.9 GPa and 4.1 MPa, respectively). The E_{IT} values for films from heat-cooled **PBI-L** solutions were smaller than that of a film of a solution at 25°C (Fig. 3.15c). However, the H_{IT} values showed variations for the various heating temperatures (Fig. 3.15d), which again did not follow a definitive trend. As with **PBI-L**, **PBI-Y** showed variations in E_{IT} and H_{IT} values, which were not dependent on temperature (Fig. 3.15e and 3.15f). Again, the E_{IT} and H_{IT} values for films formed from solutions heated to 60 and 70°C had significantly decreased, suggesting that these films were also "soft" materials. These results suggest that the bulk mechanical properties of the film do not always correlate with its electronic properties. Although a direct link between bulk film properties and conductivity could not be obtained, these results highlight that heating and cooling solutions impact the properties of the film.

As the photoconductivity and nanoindentation measurements had shown differences in the properties of the thin films, we wanted to see if this would impede their performance when used in devices. Hybrid metal halide perovskites have attracted significant interest as they can be easily prepared and exhibit exceptional optoelectronic characteristics.[66] In this device architecture, the perovskite absorber is positioned between two selective charge extraction layers, which facilitates the transfer of charges to the electrodes.[67] The most commonly used organic hole transporting materials (HTM) are 2,2',7,7'-tetrakis-(*N*,*N*-di-4-methoxyphenylamino)-9,9'-spirobifluorene (Spiro-OMeTAD) and polytriarylamines (PTAAs). However, such materials require multi-step, costly synthetic procedures involving metal-catalysed cross-coupling reactions, harsh reaction conditions, and extensive purification.[67] As such, replacing such materials with PBIs could reduce the total device cost. **PBI-A** was chosen since it showed the greatest photoresponse upon irradiation (Fig. 3.14).

The photovoltaic performance of **PBI-A** as an HTM was studied in planar methylammonium lead iodide ($MAPbI_3$) perovskite solar cells (fluorinated tin oxide (FTO)/SnO_2/$MaPbI_3$/**PBI-A**/Au, Fig. 3.16a). Devices were fabricated and tested by Fraser Angus (University of Glasgow). The performance of devices made from **PBI-A** solutions at 25°C and solutions heat-cooled from 70°C were compared (Fig. 3.16b and Table 3.9). Reference devices using SnO_2 only gave a power conversion efficiency (PCE) value of 17.6%, consistent with the literature.[68] Use of an SnO_2/**PBI-A** HTM layer gave a lower PCE of 9.37% for the solution

at 25°C and induced a large amount of charge recombination, reducing the rate at which the current is extracted from the device. Furthermore, the short circuit current density (J_{SC}) was 18.88 mA/cm^2 for devices made with **PBI-A** solutions kept at 25°C and 19.89 mA/cm^2 for devices made with the heat-cooled solutions. The decrease in the open-circuit voltage (V_{OC}) of the **PBI-A**-based devices compared to that of SnO_2 only was postulated to be due to the **PBI-A** layer being coloured, thus reducing incident light in the bulk of the perovskite. Overall, these proof-of-concept perovskite devices demonstrate subtle differences in the non-heat-cooled and heat-cooled PBI solutions. However, further testing is required to determine the extent of these differences. Furthermore, different perovskite device architectures could also be tested to further improve the device metrics.

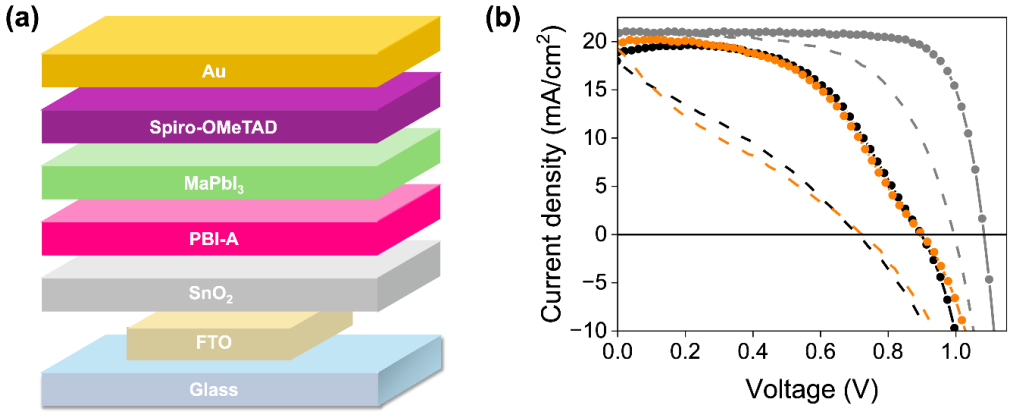

Figure 3.16. (a) Cartoon of the device architecture used. (b) *J-V* curves collected under AM 1.5 simulated sunlight of the champion devices of SnO_2 only (grey), SnO_2/**PBI-A** solutions at 25°C (black), and SnO_2/**PBI-A** solutions heat-cooled from 70°C (orange). The photovoltaic parameters are taken from the *J-V* curves. Circles and lines represent the reverse voltage sweep, and dashed lines represent the forward voltage sweep.

Table 3.9. Summary of photovoltaic device metrics of the perovskite devices.

Device	V_{OC} (V)	J_{sc} (mA/cm^2)	FF	PCE (%)
Reference SnO_2	1.083	20.88	0.78	17.60
PBI-A (Non-heat-cooled)	0.897	18.88	0.55	9.37
PBI-A (Heat-cooled)	0.899	19.89	0.51	9.07

3.2.3 Impact of Heat-Cool Processing on PBI Hydrogels

As we had changed the pre-gel aggregation state using heat-cool cycles, we hypothesised that this would change the properties of the resulting hydrogels. Gelation was induced by adding the appropriate amount of GdL (Table A.2.1, Appendix) to give gels with a final pH of 3.2. We believed that if we controlled the cooling rate of our solutions, this could change

the kinetic pathway of the self-assembly process that occurs during cooling, allowing us to form different types of aggregates. Therefore, GdL was added to solutions cooled on the benchtop (uncontrolled cooling rates), and solutions cooled inside an Anton Paar MCR301 rheometer (controlled cooling rates).

Rheological strain sweeps showed that the stiffness of the gels was influenced by heat-cool cycles. For **PBI-A** (Fig. 3.17), gels formed from heat-cooled solutions were stiffer than the corresponding gels from solutions at 25°C (G′ values at 1% strain of 148 Pa and 208 Pa for gels formed from solutions at 25°C, and solutions heated to 70°C and cooled to 25°C with a controlled cooling rate, respectively). Furthermore, the stiffness of the gels increased with increasing heating temperature. Such differences in stiffness could be due to an increase in solubility of the **PBI-A** molecules with increasing temperature. This increase in solubility may allow different self-assembled structures to form as the temperature drops, impacting the final gel network formed upon lowering the pH. The cooling rate also changed the stiffness of the gels, with gels formed from solutions with an uncontrolled cooling rate being stiffer than the corresponding gels formed from solutions with a controlled cooling rate. However, all gels had the same yield point of 12.6%, suggesting that the way the types of fibres present or the way they entangle and interact with each other was the same.

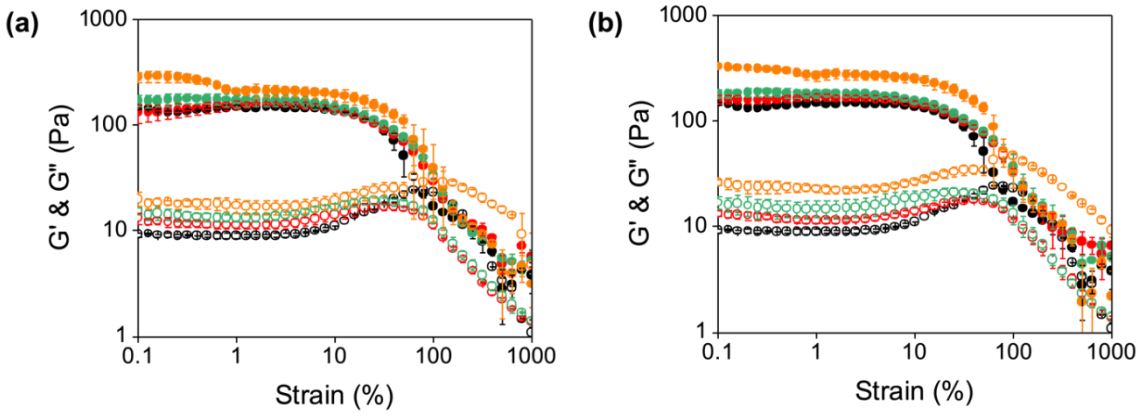

Figure 3.17. Strain sweeps of **PBI-A** gels formed from solutions at 25°C (black) and those heated to 30°C (red), 50°C (green), and 70°C (orange) and cooled to 25°C with (a) controlled and (b) uncontrolled cooling rates before triggering gelation. Closed circles represent G′ and open circles represent G″. Data shown are averaged data for triplicate runs, with error bars representing standard deviation.

For **PBI-L** gels (Fig. 3.18), the gels formed from heat-cooled solutions were again stiffer than the gels formed from solutions kept at 25°C (G′ values at 1% strain of 83 Pa and 115 Pa for gels formed from solutions at 25°C and solutions heated to 70°C and cooled to 25°C

with a controlled cooling rate, respectively). However, no trend was observed between the heating temperature and the stiffness of the gels. These results suggest that the temperature the solution is heated to causes structural differences, which may be apparent in the final gels. Again, differences in the stiffness were seen for the different cooling rates. However, unlike **PBI-A**, **PBI-L** gels were stiffer when the solutions were cooled with a controlled cooling rate. Such results further emphasise that the heat-cool cycles affect each PBI differently. All gels had the same yield point of 8%, suggesting that the heat-cool cycles did not impact the fibres that formed.

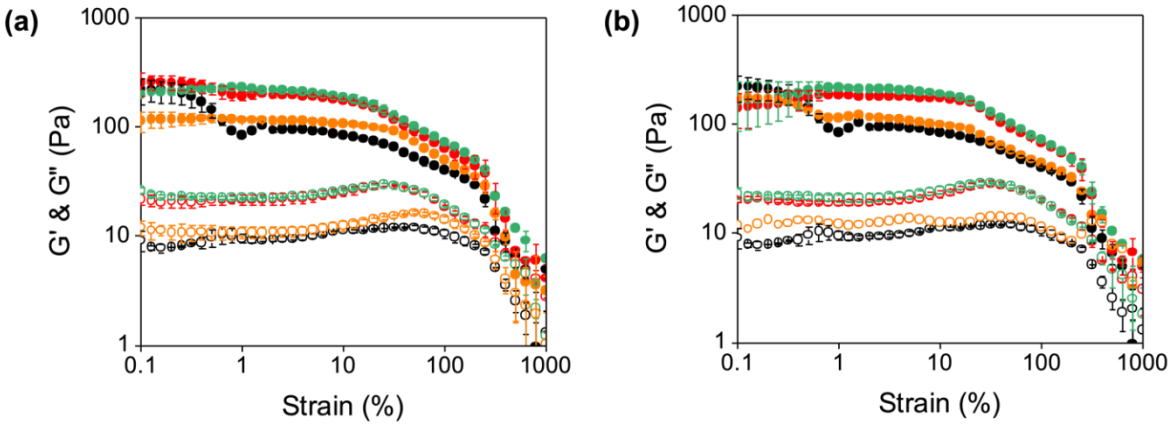

Figure 3.18. Strain sweeps of **PBI-L** gels formed from solutions at 25°C (black) and those heated to 30°C (red), 50°C (green), and 70°C (orange) and cooled to 25°C with (a) controlled and (b) uncontrolled cooling rates before triggering gelation. Closed circles represent G′ and open circles represent G″. Data shown are averaged data for triplicate runs, with error bars representing standard deviation.

The gels formed from **PBI-Y** solutions heated to 70°C with a controlled cooling rate were stiffer than gels formed from solutions kept at 25°C (Fig. 3.19). This increase in stiffness could again be due to the increased solubility as the temperature increases. Contrarily, gels formed from solutions heated to 30°C and 50°C with controlled cooling rates showed a decrease in stiffness compared to gels formed from solutions at 25°C. When the cooling rate was not controlled, an opposite trend in gel stiffness was observed, with the gels formed from solutions heated to 70°C being significantly less stiff than the gels formed from solutions at 25°C. These results reiterate that the kinetics of cooling influence the self-assembled structures formed upon cooling, which influences the final gel properties. However, the formation of hydrogels from heat-cooled **PBI-L** and **PBI-Y** solutions was not always successful. As such, only **PBI-A** hydrogels were investigated further.

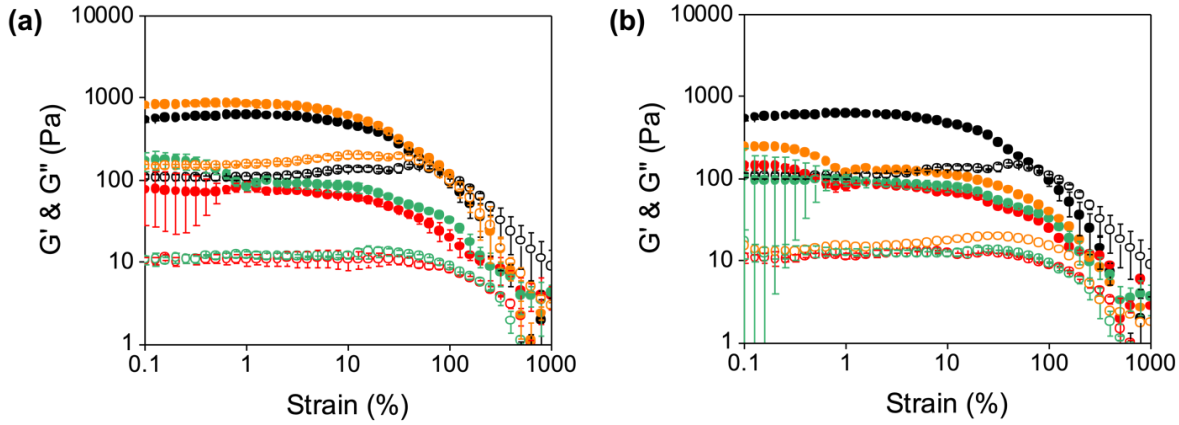

Figure 3.19. Strain sweeps of **PBI-Y** gels formed from solutions at 25°C (black) and those heated to 30°C (red), 50°C (green), and 70°C (orange) and cooled to 25°C with (a) controlled and (b) uncontrolled cooling rates before triggering gelation. Closed circles represent G′ and open circles represent G″. Data shown are averaged data for triplicate runs, with error bars representing standard deviation.

SANS was used to probe the gel structures to help understand the observed differences in the gel stiffness from the rheological data. For **PBI-A**, the scattering data of the gels formed from solutions at 25°C fit to a flexible elliptical cylinder with a power law (Fig. 3.20). In comparison, the gels formed from the heat-cooled solutions all fit to an elliptical cylinder with a power law. Such elliptical cylinders are more rigid than the flexible elliptical cylinders, which could explain the increase in stiffness.[69] The scattering data for the gels formed from solutions with controlled and uncontrolled cooling rates were very similar, with very subtle changes at low Q. Such results suggest that differences in the gels are due to the tertiary structures present rather than in the primary and secondary structures.

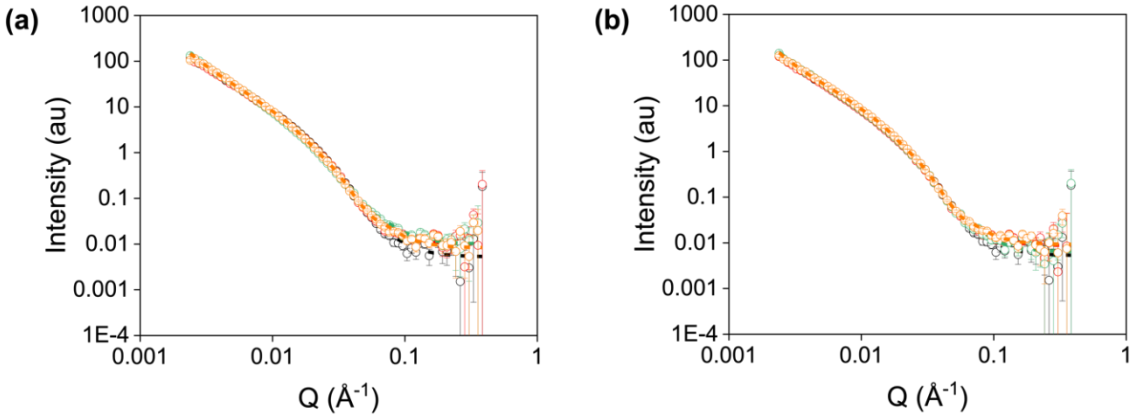

Figure 3.20. Small-angle neutron scattering of **PBI-A** gels formed from solutions heated to various temperatures and cooled to 25°C with (a) controlled and (b) uncontrolled cooling rates. Gels were formed from solutions at 25°C (black) and solutions heated to 30°C (red), 50°C (green), and 70°C (orange) and cooled to 25°C before triggering gelation.

Table 3.10. Tabulated parameters of the SANS model fits for hydrogels formed from **PBI-A** solutions at 25°C and after heating to various temperature and cooling to 25°C with controlled cooling rates.

Heating temperature (°C)	**25**	**30**	**50**	**70**
Model	Flexible elliptical cylinder + power law	Elliptical cylinder + power law	Elliptical cylinder + power law	Elliptical cylinder + power law
Background (cm^{-1})	0.001	0.001	0.001	0.01
Cylinder scale	$8.6752\times10^{-5} \pm 3.6134\times10^{-6}$	$1.0063\times10^{-3} \pm 2.5397\times10^{-5}$	$7.3446\times10^{-4} \pm 1.8723\times10^{-5}$	$9.2045\times10^{-4} \pm 2.1566\times10^{-5}$
Length (Å)	739 ± 1.0	828 ± 34	712 ± 19	829 ± 22
Kuhn length (Å)	73.8 ± 3.4	N/A	N/A	N/A
Radius (Å)	51.1 ± 0.3	58.1 ± 0.7	64.5 ± 0.9	61.6 ± 0.7
Axis ratio	8.01 ± 0.6	3.2 ± 0.07	3.2 ± 0.08	3.1 ± 0.07
Power law scale	$7.5295\times10^{-6} \pm 1.9743\times10^{-7}$	$6.5922\times10^{-6} \pm 1.3212\times10^{-7}$	$1.5842\times 10^{-5} \pm 1.5569\times10^{-7}$	$9.8561\times10^{-6} \pm 1.3486\times10^{-7}$
Power law	2.71 ± 0.04	2.70 ± 0.04	2.60 ± 0.02	2.70 ± 0.02
χ^2	1.5545	3.4694	2.1788	3.3012

Table 3.11. Tabulated parameters of the SANS model fits for hydrogels formed from **PBI-A** solutions at 25°C and after heating to various temperature and cooling to 25°C with uncontrolled cooling rates.

Heating temperature (°C)	**25**	**30**	**50**	**70**
Model	Flexible elliptical cylinder + power law	Elliptical cylinder + power law	Elliptical cylinder + power law	Elliptical cylinder + power law
Background (cm^{-1})	0.001	0.001	0.01	0.001
Cylinder scale	$8.6752\times10^{-5} \pm 3.6134\times10^{-6}$	$1.0270\times10^{-3} \pm 2.6592\times10^{-5}$	$1.0119\times10^{-3} \pm 2.4395\times10^{-5}$	$1.0699\times10^{-3} \pm 2.3712\times10^{-5}$
Length (Å)	739 ± 1.0	790 ± 21	833 ± 34	762 ± 17
Kuhn length (Å)	73.8 ± 3.4	N/A	N/A	N/A
Radius (Å)	51.1 ± 0.3	57.4 ± 0.7	58.8 ± 0.7	60.2 ± 0.6
Axis ratio	8.01 ± 0.6	3.4 ± 0.07	3.3 ± 0.07	3.2 ± 0.06
Power law scale	$7.5295\times10^{-6} \pm 1.9743\times10^{-7}$	$5.3530\times10^{-6} \pm 1.1768\times10^{-7}$	$7.4931\times10^{-6} \pm 1.3262\times10^{-7}$	$6.5769\times10^{-6} \pm 1.1685\times10^{-7}$
Power law	2.71 ± 0.04	2.80 ± 0.04	2.70 ± 0.03	2.80 ± 0.03
χ^2	1.5545	2.8343	3.1045	3.3937

As in Chapter 2, we believed the increase in solubility upon heating would increase the number of possible structures which could form upon gelation. Furthermore, when the kinetics of the cooling stage are altered, this could potentially change the kinetics of the structural change from the spherical aggregates formed upon heating to the more fibrous structures formed upon cooling, again allowing different gels to form. Therefore, rheological time-sweeps were run to monitor the gelation of **PBI-A** solutions heat-cooled to various heating temperatures with controlled and uncontrolled cooling rates (Fig. 3.21). Compared to the solution kept at 25°C, all heat-cooled solutions showed G′ at the start of the experiment, indicating the presence of pre-assembled structures. The gelation profiles are different for the different heating temperatures, showing the importance of sample history. Furthermore, there is a large difference in the gelation process for corresponding solutions with controlled and uncontrolled cooling rates, emphasizing that different self-assembly kinetic pathways can be accessed by changing how the solutions are heated and cooled.

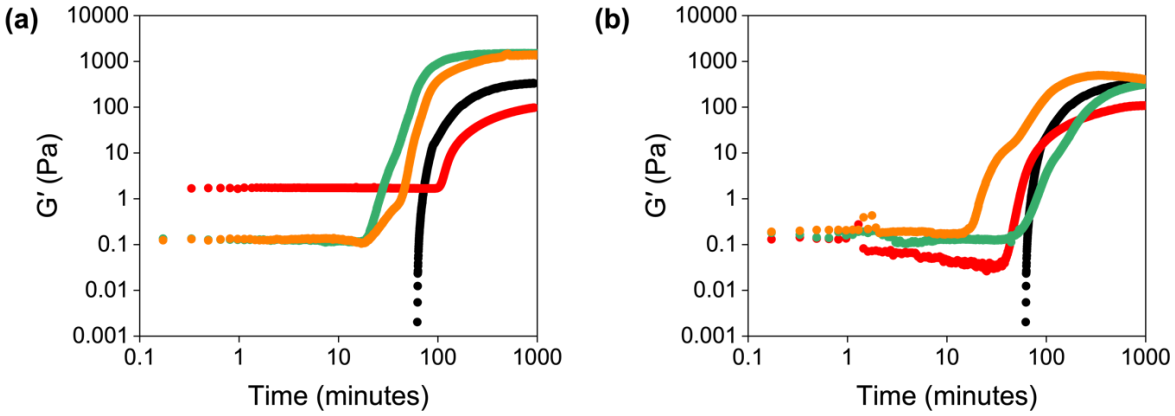

Figure 3.21. Plots showing the evolution of G′ with time for **PBI-A** solutions at 25°C and solutions heated to 30°C (red), 50°C (green), and 70°C (orange) and cooled to 25°C with (a) controlled and (b) uncontrolled cooling rates.

3.3 Conclusions

In this chapter, we demonstrate the importance of temperature during sample preparation or thermal evaporation techniques when preparing thin films. By altering the temperature at which the solution is heated, we can access various pre-made structures in the solution. This change in temperature affects the solubility, consequently influencing the properties of the thin films and hydrogels made from these heat-cooled solutions. It was observed that even a minor temperature decrease of 5°C was sufficient to alter the photoconductivity of the films. Such sensitivity to temperature fluctuations may contribute to the variability seen in devices fabricated from organic materials.

The challenge arising from this shift in aggregation during a heat-cool cycle is that the characteristics observed in the solution phase may not align with those in the gel or solid state. Such discrepancies make it challenging to determine the optimal temperature when preparing materials suited for a specific application. For example, **PBI-A** films heat-cooled from 70°C showed a decrease in photoresponse compared to 25°C, whereas **PBI-L** had an increased photoresponse when heat-cooled from 70°C. Furthermore, each PBI showed a different trend in hydrogel stiffness when comparing gels formed from non-heat-cooled solutions to those that had been heat-cooled. Therefore, this work emphasises the importance of controlling experimental conditions during sample preparation, especially during different times of the year when there are fluctuations in ambient workplace temperature.

3.4 Experimental

3.4.1 Synthetic Procedures

Perylene-3,4-9,10-tetracarboxylic dianhydride (PTCDA) was purchased from Sigma-Aldrich. L-alanine, L-leucine, L-tyrosine, and imidazole were purchased from Fluorochem. All commercial reagents were used as received. Distilled water was used throughout. NaOD was purchased from Sigma-Aldrich as a 40 wt% solution in D_2O and diluted with D_2O to provide a 0.1 M solution.

PBI-A, **PBI-L**, and **PBI-Y** were synthesised using the experimental procedure for **PBI-A** described in Section 2.4.1.1.

PBI-L: ^{1}H NMR (500 MHz, DMSO-d_6, 25°C): δ (ppm) = 8.30 (8H, m, ArH), 5.58 (2H, t, J = 4 Hz, CH*), 2.11 (4H, m, CH_2), 1.66 (2H, m, CH_2), 1.00 (6H, t, J = 4.8 Hz, CH_3), 0.97 (6H, t, J = 5.6 Hz, CH_3). ^{13}C NMR (125 MHz, DMSO-d_6, 25°C): δ (ppm) = 170.5 (COOH), 161.9 (C=O), 133.3, 133.2, 130.5, 130.4, 127.8, 127.8, 124.7, 123.1, 123.0, 121.7, 121.7 (perylene core), 51.4 (CH*), 37.7 (CH_2), 24.8 (CH), 22.3 and 21.7 ((CH_3)$_2$). HRMS (ESI) m/z, nominal mass calculated for $[C_{36}H_{30}N_2O_8+H]^+$: 619.6400. Found $[C_{36}H_{30}N_2O_8+H]^+$: 619.2074.

PBI-Y: ^{1}H NMR (500 MHz, DMSO-d_6, 25°C): δ (ppm) = 13.03 (2H, br s, COOH), 9.08 (2H, br s, OH), 8.26 (8H, br s, Ar H), 7.05 (4H, d, J = 10 Hz, Ar H), 6.56 (4H, J = 10 Hz, Ar H), 5.92 (2H, dd, J = 10 Hz, 5 Hz, CH*), 3.53-3.40 (4H, m, CH_2). ^{13}C NMR (125 MHz,

DMSO-d_6, 25°C): δ (ppm) = 170.9 (COOH), 162.1 (C=O), 155.9 (aromatic C-OH), 133.1, 130.8, 128.0, 127.9, 124.7, 122.8 (perylene core), 133.1, 127.8, 115.0 (aromatic C), 54.1 (CH), 33.5 (CH_2). HRMS (ESI) m/z, nominal mass calculated for $[C_{42}H_{26}N_2O_{10}+H]^+$: 719.6700. Found $[C_{42}H_{26}N_2O_{10}+H]^+$: 719.1657.

3.4.2 Experimental Procedures

3.4.2.1 Preparation of PBI Solutions

Solutions were prepared at a concentration of 5 mg/mL by dispersing the appropriate PBI in deionised water and adding one equivalent of sodium hydroxide (0.1 M, aqueous). The solutions were agitated overnight on a MX-T6-S tube roller (SCILOGEX) until all the gelator had visibly dissolved. If required, the pH of the solution was adjusted using sodium hydroxide (0.1 M, aqueous) to pH 6 to give the singly deprotonated PBI.

3.4.2.2 pH Measurements

pH measurements were recorded on an FC200 pH probe (HANNA instruments) with a 6 mm x 10 mm conical tip at 25°C. The stated accuracy of the pH measurements is ± 0.1.

3.4.2.3 Heating Methods

For the samples for quantitative measurements, solutions were heated in an oil bath fitted with a temperature probe to the required temperature. The temperature of the solution is quoted, not that of the oil bath. 2 mL of solution was heated in a sealed 7 mL Sterilin vial, using a temperature probe to measure the temperature of a “sacrificial” solution. Once at the desired temperature, the solution was maintained at this temperature for 5 minutes. For heat-cooled solutions, the samples were then removed from the oil bath and allowed to cool to room temperature, again monitoring the temperature of a "sacrificial” solution using a temperature probe.

3.4.2.4 Preparation of PBI Hydrogels

A pH-switch method was used to form the hydrogels. Solutions were prepared as described above. 6 mL of solution was then transferred to a 7 mL aluminium cup and heated to the chosen temperature using an Anton Paar MRC301 rheometer. A heating rate of 0.5°C/min was used. Once at this temperature, the solution was maintained at the chosen temperature for 5 minutes. For uncontrolled cooling rates, the samples were taken out of the rheometer and allowed to cool on the bench. For controlled cooling rates, the samples were cooled

inside the rheometer at a cooling rate of 0.5°C/min. Once cooled, 2 mL of solution was transferred to a 7 mL Sterilin vial containing a pre-weighed amount of GdL (Table A.2.1, Appendix) and gently shaken three times. The sample was then left to stand overnight to allow gelation to occur. A simple inversion test was performed to indicate whether gelation had been successful. If the sample was stable to inversion, then rheological measurements were taken.

3.4.2.5 Rheological Measurements

Dynamic rheological and viscosity measurements were performed with an Anton Paar Physica MCR301 rheometer. A cup-and-vane measuring system was used for strain and frequency sweeps, a cone-and-plate measuring system for viscosity measurements, and a parallel plate measuring system for time sweeps. For strain and frequency tests, 2 mL of gel were prepared in 7 mL Sterilin vials and left for 16 hours at room temperature before measurements were taken. For viscosity measurements, solutions were prepared as described above. For time sweeps, the gels were prepared in a vial and quickly transferred onto the bottom plate. The temperature was maintained at 25°C during all measurements using a water circulator bath. All measurements were recorded in triplicate.

Constant Shear

A constant shear of 10 s^{-1} was applied to the samples. 2 mL of solution was poured onto the plate for measurements. Mineral oil was carefully added around the circumference of the top plate to prevent the sample from drying out. Data were first collected on samples kept at room temperature, with the viscosity recorded every minute over a period of 10 minutes to ensure that changes in viscosity were not the result of the applied shear. The samples were then heated from 25°C to 70°C at a rate of 0.5°C/min, recording the viscosity at every 1°C. The samples were then held at 70°C for 5 minutes before cooling back to 25°C at a rate of 0.5°C/min, again recording the viscosity at every 1°C. For reproducibility experiments, a sample was heated to 70°C and cooled to 25°C over three consecutive cycles.

Viscosity

Viscosity measurements were performed using a 75 mm cone (angle = 1.000°) and plate. 2 mL of solution was poured onto the plate for measurement. Mineral oil was carefully added around the circumference of the top plate to prevent the sample from drying out. The viscosity was measured under a rotational shear rate from 0.1 to 100 s^{-1}. The temperature

was maintained during all measurements by using a water circulator bath. To measure the effect of heating and cooling, the sample was heated on the plate to the desired temperature at a heating rate of 0.5°C/min. The sample was maintained at the chosen temperature for 5 minutes. After this time, the solution was cooled to 25°C at a cooling rate of 0.5°C/min, and the viscosity was measured after an equilibration period of 5 minutes.

Strain Sweeps

Strain sweeps were performed over a range of 0.1% to 1000% with a frequency of 10 rad/s. The critical strain (yield point) was quoted at the point where G′ became non-linear and ultimately crossed over G″ (flow point), causing the gel to break down.

Frequency Sweeps

Frequency sweeps were performed from 1 rad/s to 100 rad/s under a strain of 0.1%. G′ and G″ were quoted at 10 rad/s. The measurements were performed within the viscoelastic region where G′ and G″ were independent of strain amplitude.

Time Sweeps

Time sweeps were performed with a 50 mm sandblasted plate and a plate gap of 0.8 mm. Tests were performed at an angular frequency of 10 rad/s and with a strain of 0.1%. Mineral oil was carefully added around the circumference of the top plate to prevent the sample from drying out.

3.4.2.6 SANS

SANS measurements were performed using the SANS2D instrument (ISIS Rutherford Appleton Laboratory, Didcot, UK) under experiments RB2220189 and RB2310028. Measurements were performed using a wavelength band of 0.9 to 13 Å to access a Q range of 0.004 to 0.7 $Å^{-1}$. Solutions were measured in 2 mm path length UV spectrophotometer quartz cuvettes (Hellma). These were placed in a temperature-controlled sample rack during the measurements. For heated solutions, samples were heated directly in the beamline, recording the scattering data for a period of 30 minutes every 1.5 hours. For heat-cooled solutions, samples were prepared offline in a water bath as described above. Solutions were prepared as described above, but in D_2O and NaOD (0.1 M).

The data were reduced to 1D scattering curves of intensity vs. Q using the facility-provided software. The electronic background was subtracted, the full detector images for all data were normalised, and the scattering from the empty cell was subtracted. The scattering from D_2O was also measured and subtracted from the data using the Mantid software package installed inside the ISIS virtual machines, IDAaaS.[70] The instrument-independent data were then fitted to the models discussed in the text using the SasView software package (version 5.0.4).[71] The scattering length density of each material was calculated using the National Institute of Standards and Technology's neutron activation and scattering calculator.[72] The SLD of D_2O was calculated to be 6.393 x 10^{-6} Å^{-2}. The SLD of **PBI-A** was calculated to be 3.445 x 10^{-6} Å^{-2}. The SLD of **PBI-L** was calculated to be 2.901 x 10^{-6} Å^{-2}. The SLD of **PBI-Y** was calculated to be 3.361 x 10^{-6} Å^{-2}. All data best fit cylindrical models or combined cylindrical and sphere models. The best fit was determined as the one which overlapped well with the data and had the lowest χ^2 value. Errors were calculated by the SASView fitting software as a function of the error bars of the experimental data and the chosen model.

3.4.2.7 UV-vis Absorption Spectroscopy

UV-vis absorption data were obtained on a Cary 60 UV-vis spectrophotometer (Agilent Technologies). For heat-cooled and heated samples, the samples were prepared as described above. For the temperature sweeps, samples were prepared as described above and diluted with deionised water to give a final concentration of 0.025 mg/mL. The diluted samples were then transferred into a 1 x 1 cm quartz cuvette. Samples were heated and cooled using a Cary Single Cell Peltier Accessory (Agilent Technologies). The temperature was maintained during all measurements by using a water circulator bath. To ensure even distribution of heat throughout the sample, a stirrer bar was used during heating and cooling. UV-vis absorption spectra were recorded over a heating and cooling cycle between 25 and 70°C at a rate of 1°C/min, with a spectrum recorded at each temperature increment.

3.4.2.8 "Apparent" pK_a Titrations

An FC200 pH probe (HANNA instruments|) with a 6 mm x 10 mm conical tip was used for pK_a titrations. The "apparent" pK_a of each PBI was determined by the addition of aliquots of 0.1 M aqueous hydrochloric acid. The pH was recorded after each aliquot addition once a stable pH was maintained. To prevent gel formation, the solutions were gently stirred using a magnetic stirrer. For heated titrations, samples were heated in an oil bath fitted with a temperature probe to the required temperature. The temperature of the solution is quoted,

not that of the oil bath. For heat-cooled titrations, the samples were prepared as described above and the titration was performed in a water bath maintained at 25°C.

3.4.2.9 ^{1}H NMR Spectroscopy

^{1}H NMR spectra were measured using a Bruker UltraShield™ 500 MHz spectrometer. Spectra were analysed using Bruker Topspin 4.1.0 software. Solutions were prepared as described above in D_2O and 0.1 M NaOD. MeOH (2 μL) was then added as an internal standard. Samples were heated in the spectrometer to the desired temperature. The sample was then held at the chosen temperature for 5 minutes before cooling back to 25°C. Spectra were recorded at 25°C, after the 5-minute time interval at the desired heating temperature, and once cooled back to 25°C.

3.4.2.10 Thin Film Preparation

Thin films were prepared on a glass microscope slide (Thermo Scientific) by dropping 10 μL of the required solution inside a 3 x 3 mm mask and leaving to air dry (average lab temperature 23.4°C and average lab humidity 31%). Once dried, the mask was removed to produce a 3 x 3 mm square. Two silver electrodes were made from silver paste (Agar Scientific, Acheson Silver Electrodag, 1415), ensuring that full contact was made to opposite sides of the sample square. Two copper wires were attached to the glass slide *via* the silver electrodes. More silver paste was then applied and left to dry to ensure good contact between the silver and copper wires. Epoxy resin glue (Araldite) was then placed over the silver electrodes, to prevent oxidation of the silver, and to secure the copper wires. Samples were left to dry in air overnight.

3.4.2.11 Photoconductivity Measurements

Photoconductivity measurements were performed with a Palmsens4 potentiostat using a two-electrode set-up. Linear sweep measurements were recorded from -4 V to +4 V at a scan rate of 0.05 V/s. Thin films were prepared as described above. The counter and reference electrodes were connected to one copper wire, and the working electrode was attached to the other. Dark measurements were performed in a Faraday cage in air. The samples were then irradiated with a 365 nm LED (RS Components Ltd) placed 1 cm from the sample for one minute before another linear sweep measurement was taken. The distance from the LED to the sample was adjusted so that an optical power probe (Thorlabs PM100D with S120VC

sensor) placed at the same distance as the sample registered 20 mW of incident power. All samples were recorded in triplicate.

3.4.2.12 Nanoindentation Measurements

Nanoindentation measurements were carried out on a Step 700 Surface Testing Platform (UNHT^3, Anton Paar) using a Berkovich indenter tip. Linear loading was applied with a maximum load of 3000 μN, a loading and unloading rate of 2000 N/min, with a pause of 5 seconds. The constant force was set at 150 μN, with an approach distance of 7500 nm, and an approach and retract speed of 500 and 2 nm/min. Prior to each measurement, an adjust depth offset measurement was taken to correctly setup the depth sensor measurement range to eliminate any issues due to film surface inhomogeneities. Each measurement was performed in triplicate, using a simple matrix, where three points in the film were measured with a gap of 1 mm from each other to prevent any surface deformation from the previous indent affecting the next measurement. For each new triplicate, a different area of the film was chosen to again avoid influence from the previous indentation.

3.4.2.13 Synthesis of Precursor Salts for Perovskite Devices

The precursor salts were synthesised by Benjamin Vella (University of Glasgow). To prepare the methylammonium (MAI) crystals, methylamine (40% wt. in H_2O, 79.1 mL, 913.7 mmol) and hydriodic acid (without stabilisers, 55% wt. in H_2O, 50 mL, 365.5 mmol) were added to a round bottom flask containing ethanol (300 mL) and stirred overnight, resulting in a colourless solution. A white crystalline solid was obtained by rotary evaporation. The crude product was washed with diethyl ether, then recrystallised three times from dry ethanol, washing with diethyl ether after each procedure to yield white crystals of the pure product (19.152 g, 33%).

3.4.2.14 Preparation of Solutions for Perovskite Devices

PBI-A solutions were prepared by Rebecca Ginesi as described above. All other solutions were prepared by Fraser Angus (University of Glasgow). To make the SnO_2 nanoparticles, 2 mL of 15% tin (IV) oxide nanoparticle colloidal dispersion was diluted with 2 mL of deionised water. To make the methylammonium lead iodide (MAPI) solution, 750 mg PbI_2 and 260 mg MAI were dissolved in a 4:1 (v:v) *N*-*N*-dimethylformamide (DMF):dimethylsulfoxide (DMSO) mixed solvent at 70°C and filtered through a 0.2 μm polytetrafluoroethylene (PTFE) filter. The Spiro-OMeTad solution was prepared by

dissolving 90 mg of Spiro-OMeTad in 1 mL of chlorobenzene. After filtering, the solution was doped with 23 μL of Li-TFSI salt solution (520 mg/mL in acetonitrile), 5 μL of FK209 salt solution (180 mg/mL in acetonitrile), and 35.5 μL of *tert*-butyl pyridine.

3.4.2.15 Perovskite Solar Cell Device Fabrication

Perovskite solar cells were prepared and tested by Fraser Angus (University of Glasgow). Fluorine-doped tin oxide (FTO) glass was cleaned sequentially using Hellmanex III, deionised water, acetone, ethanol, and deionised water. The glass was then treated with UV-ozone plasma for 15 minutes.

The SnO_2 layer was deposited by spin-coating 220 μL of nanoparticle solution at 4000 rpm for 30 seconds and annealed at 150°C for 30 minutes. The **PBI-A** layers were deposited by spin-coating 50 μL of precursor solution at 4000 rpm for 40 seconds and annealed at 100°C for 10 minutes. The substrates were then transferred into a nitrogen-containing glovebox for further processing. The $MAPbI_3$ perovskite layer was then deposited by spin-coating 50 μL of precursor solution during a two-step spin-coating process (1000 rpm for 10 seconds, followed by 5000 rpm for 30 seconds). Films were annealed at 100°C for 15 minutes to yield high quality black perovskites. The Spiro-OMeTAD layer was deposited by spin-coating 50 μL of precursor solution at 4000 rpm for 30 seconds. Finally, a 50 nm layer of gold was thermally evaporated on top to complete the device stack.

3.4.2.16 Perovskite Solar Cell Testing

The devices were measured in a home-built set-up,[67] using a white LED calibrated to a reference AM 1.5G solar simulator.

3.5 References

1. A. Mateo-Alonso, *Chem. Mater.*, 2023, **35**, 1467–1469.
2. M. R. Niazi, R. Munir, R. M. D'Souza, T. L. Kelly and G. C. Welch, *ACS Appl. Mater. Interfaces*, 2022, **14**, 57055–57063.
3. A. Sandström, H. F. Dam, F. C. Krebs and L. Edman, *Nat. Commun.*, 2012, **3**, 1002.
4. C. Liu, C. Xiao, C. Xie and W. Li, *Nano Energy*, 2021, **89**, 106399.
5. C. Chen, C. Ran, Q. Yao, J. Wang, C. Guo, L. Gu, H. Han, X. Wang, L. Chao, Y. Xia and Y. Chen, *Adv. Sci.*, 2023, 2303992.
6. M. Stoppa and A. Chiolerio, *Sensors*, 2014, **14**, 11957–11992.
7. J. Singh, in *Smart Electronic Materials*, Cambridge University Press, Cambridge, 2005.
8. M. Ghahremani Honarvar and M. Latifi, *J. Text. Inst.*, 2017, **108**, 631–652.
9. G. Wang, C. Hou and H. Wang, Eds., in *Flexible and Wearable Electronics for Smart Clothing*, Wiley, USA, 2020.
10. V. Adams, J. Cameron, M. Wallace and E. R. Draper, *Chem. Eur. J.*, 2020, **26**, 9879–9882.
11. V. Zardetto, T. M. Brown, A. Reale and A. Di Carlo, *J. Polym. Sci. B Polym. Phys.*, 2011, **49**, 638–648.
12. S. Hong, B. Park, C. Balamurugan, J. Lee and S. Kwon, *Heliyon*, 2023, **9**, e18209.
13. A. Agrawal, S. A. Siddiqui, A. Soni, K. Khandelwal and G. D. Sharma, *Solar Energy*, 2021, **226**, 9–19.
14. D. M. Taylor, *Semicond. Sci. Technol.*, 2015, **30**, 054002.
15. C. Capello, U. Fischer and K. Hungerbühler, *Green Chem.*, 2007, **9**, 927–934.
16. B. Qiu, Z. Chen, S. Qin, J. Yao, W. Huang, L. Meng, H. Zhu, Y. Yang, Z. G. Zhang and Y. Li, *Adv. Mater.*, 2020, **32**, 1908373.
17. Z. Yi, W. Ni, Q. Zhang, M. Li, B. Kan, X. Wan and Y. Chen, *J. Mater. Chem. C*, 2014, **2**, 7247–7255.
18. Y. Liu, J. Zhang, C. Tian, Y. Shen, T. Wang, H. Zhang, C. He, D. Qiu, Y. Shi and Z. Wei, *Adv. Funct. Mater.*, 2023. **33**, 2300778.
19. Z. Chen, B. Fimmel and F. Würthner, *Org. Biomol. Chem.*, 2012, **10**, 5845–5855.
20. D. P. Ostrowski, L. A. Lytwak, M. L. Mejia, K. J. Stevenson, B. J. Holliday and D. A. Vanden Bout, *ACS Nano*, 2012, **6**, 5507–5513.
21. E. R. Draper, L. J. Archibald, M. C. Nolan, R. Schweins, M. A. Zwijnenburg, S. Sproules and D. J. Adams, *Chem. Eur. J.*, 2018, **24**, 4006–4010.

22. E. R. Draper and D. J. Adams, *Chem*, 2017, **3**, 390–410.

23. S. S. Babu, V. K. Praveen and A. Ajayaghosh, *Chem. Rev.*, 2014, **114**, 1973–2129.

24. E. R. Draper and D. J. Adams, *Chem. Comm.*, 2016, **52**, 8196–8206.

25. F. Würthner, C. R. Saha-Möller, B. Fimmel, S. Ogi, P. Leowanawat and D. Schmidt, *Chem. Rev.*, 2016, **116**, 962–1052.

26. Y. Li, X. Zhang and D. Liu, *J. Photochem. Photobiol. C Photochem. Rev.*, 2021, **48**, 100436.

27. D. Görl, X. Zhang and F. Würthner, *Angew. Chem. Int. Ed.*, 2012, **51**, 6328–6348.

28. E. R. Draper, L. Wilbraham, D. J. Adams, M. Wallace, R. Schweins and M. A. Zwijnenburg, *Nanoscale*, 2019, **11**, 15917–15928.

29. A. M. Castilla, E. R. Draper, M. C. Nolan, C. Brasnett, A. Seddon, L. L. E. Mears, N. Cowieson and D. J. Adams, *Sci. Rep.*, 2017, **7**, 8380.

30. E. R. Draper, B. J. Greeves, M. Barrow, R. Schweins, M. A. Zwijnenburg and D. J. Adams, *Chem*, 2017, **2**, 716–731.

31. R. I. Randle, L. Cavalcanti, S. Sproules and E. R. Draper, *Mater. Adv.*, 2022, **3**, 3326–3331.

32. C. L. Smith, L. L. E. Mears, B. J. Greeves, E. R. Draper, J. Doutch, D. J. Adams and A. J. Cowan, *Phys. Chem. Chem. Phys.*, 2019, **21**, 26466–26476.

33. K. M. Wolfe, M. Mooney, C. Crep, S. Rondeau-Gagné and G. C. Welch, *Flex. Print. Electron.*, 2022, **7**, 044007.

34. S. Debnath, S. Roy, Y. M. Abul-Haija, P. W. J. M. Frederix, S. M. Ramalhete, A. R. Hirst, N. Javid, N. T. Hunt, S. M. Kelly, J. Angulo, Y. Z. Khimyak and R. V. Ulijn, *Chem. Eur. J.*, 2019, **25**, 7881–7887.

35. M. B. Avinash and T. Govindaraju, *J. Phys. Chem. Lett.*, 2013, **4**, 583–588.

36. J. Rottler and M. Müller, *ACS Nano*, 2020, **14**, 13986–13994.

37. M. F. J. Mabesoone, A. J. Markvoort, M. Banno, T. Yamaguchi, F. Helmich, Y. Naito, E. Yashima, A. R. A. Palmans and E. W. Meijer, *J. Am. Chem. Soc.*, 2018, **140**, 7810–7819.

38. P. A. Korevaar, T. F. A. de Greef and E. W. Meijer, *Chem. Mater.*, 2014, **26**, 576–586.

39. E. E. Greciano, B. Matarranz and L. Sánchez, *Angew. Chem. Int. Ed.*, 2018, **57**, 4697–4701.

40. J. Seo, M. I. Khazi, K. Bae and J. Kim, *Small*, 2023, **19**, 2206428.

41. W. Wagner, M. Wehner, V. Stepanenko, S. Ogi and F. Würthner, *Angew. Chem. Int. Ed.*, 2017, **56**, 16008–16012.

42. J. Cameron, D. J. Adams, P. J. Skabara and E. R. Draper, *J. Mater. Chem. C Mater.*, 2022, **10**, 3944–3950.

43. E. R. Draper, M. Wallace, D. Honecker and D. J. Adams, *Chem. Comm.*, 2018, **54**, 10977–10980.

44. E. R. Draper, J. J. Walsh, T. O. McDonald, M. A. Zwijnenburg, P. J. Cameron, A. J. Cowan and D. J. Adams, *J. Mater. Chem. C*, 2014, **2**, 5570–5575.

45. E. R. Draper, H. Su, C. Brasnett, R. J. Poole, S. Rogers, H. Cui, A. Seddon and D. J. Adams, *Angew. Chem. Int. Ed.*, 2017, **56**, 10467–10470.

46. L. Zhang, H. Zhao, B. Lin, J. Yuan, X. Xu, J. Wu, K. Zhou, X. Guo, M. Zhang and W. Ma, *J. Mater. Chem. A Mater.*, 2019, **7**, 22265–22273.

47. R. Ramos-Hernández, F. D. Calvo, E. Pérez-Gutiérrez and M. J. Percino, *Thin Solid Films*, 2023, **771**, 139787.

48. Y. Feng, Z. Chu and C. A. Dreiss, in *Stimulus-responsive Wormlike Micelles*, Royal Society of Chemistry, Cambridge, 2017, pp. 121–170.

49. S. Roy, N. Javid, J. Sefcik, P. J. Halling and R. V. Ulijn, *Langmuir*, 2012, **28**, 16664–16670.

50. C. A. Dreiss, *Soft Matter*, 2007, **3**, 956–970.

51. A. Z. Cardoso, L. L. E. Mears, B. N. Cattoz, P. C. Griffiths, R. Schweins and D. J. Adams, *Soft Matter*, 2016, **12**, 3612–3621.

52. J. G. Egan, G. Brodie, D. McDowall, A. J. Smith, C. J. C. Edwards-Gayle and E. R. Draper, *Mater. Adv.*, 2021, **2**, 5248–5253.

53. D. McDowall, B. J. Greeves, R. Clowes, K. McAulay, A. M. Fuentes-Caparrós, L. Thomson, N. Khunti, N. Cowieson, M. C. Nolan, M. Wallace, A. I. Cooper, E. R. Draper, A. J. Cowan and D. J. Adams, *Adv. Energy Mater.*, 2020, **10**, 2002469.

54. E. Shirman, A. Ustinov, N. Ben-Shitrit, H. Weissman, M. A. Iron, R. Cohen and B. Rybtchinski, *J. Phys. Chem. B*, 2008, **112**, 8855–8858.

55. K. McAulay, P. A. Ucha, H. Wang, A. M. Fuentes-Caparrós, L. Thomson, O. Maklad, N. Khunti, N. Cowieson, M. Wallace, H. Cui, R. J. Poole, A. Seddon and D. J. Adams, *Chem. Comm.*, 2020, **56**, 4094–4097.

56. C. Tang, A. M. Smith, R. F. Collins, R. V. Ulijn and A. Saiani, *Langmuir*, 2009, **25**, 9447–9453.

57. E. R. Draper, B. Dietrich, K. McAulay, C. Brasnett, H. Abdizadeh, I. Patmanidis, S. J. Marrink, H. Su, H. Cui, R. Schweins, A. Seddon and D. J. Adams, *Matter*, 2020, **2**, 764–778.

58. S. Mafé, V. García-Morales and P. Ramírez, *Chem. Phys.*, 2004, **296**, 29–35.

59. L. Chen, S. Revel, K. Morris, L. C. Serpell and D. J. Adams, *Langmuir*, 2010, **26**, 13466–13471.

60. B. Yang, M. Lledos, R. Akhtar, G. Ciccone, L. Jiang, E. Russo, S. Rajput, C. Jin, M. G. F. Angelereou, T. Arnold, J. Rawle, M. Vassalli, M. Marlow, D. J. Adams and M. Zelzer, *Chem. Sci.*, 2021, **12**, 14260–14269.

61. L. J. Marshall, M. Wallace, N. Mahmoudi, G. Ciccone, C. Wilson, M. Vassalli and D. J. Adams, *Adv. Mater.*, 2023, **35**, 2211277.

62. B. A. Latella, B. K. Gan, C. J. Barbé and D. J. Cassidy, *J. Mater. Res.*, 2008, **23**, 2357–2365.

63. G. M. Pharr and W. C. Oliver, *MRS Bull.*, 1992, **17**, 28–33.

64. T. Xia, W. Liu and L. Yang, *J. Biomed. Mater. Res. A*, 2017, **105**, 1799–1812.

65. L. Lorenz, T. Chudoba, S. Makowski, M. Zawischa, F. Schaller and V. Weihnacht, *J. Mater. Sci.*, 2021, **56**, 18740–18748.

66. N. J. Jeon, J. H. Noh, Y. C. Kim, W. S. Yang, S. Ryu and S. Il Seok, *Nat. Mater.*, 2014, **13**, 897–903.

67. M. L. Petrus, K. Schutt, M. T. Sirtl, E. M. Hutter, A. C. Closs, J. M. Ball, J. C. Bijleveld, A. Petrozza, T. Bein, T. J. Dingemans, T. J. Savenije, H. Snaith and P. Docampo, *Adv. Energy Mater.*, 2018, **8**, 1801605.

68. W. Ke, G. Fang, Q. Liu, L. Xiong, P. Qin, H. Tao, J. Wang, H. Lei, B. Li, J. Wan, G. Yang and Y. Yan, *J. Am. Chem. Soc.*, 2015, **137**, 6730–6733.

69. P. Chakraborty, M. Ghosh, L. Schnaider, N. Adadi, W. Ji, D. Bychenko, T. Dvir, L. Adler-Abramovich and E. Gazit, *Macromol. Rapid Commun.*, 2019, **40**, 1900175.

70. O. Arnold, J. C. Bilheux, J. M. Borreguero, A. Buts, S. I. Campbell, L. Chapon, M. Doucet, N. Draper, R. F. Leal, M. A. Gigg, V. E. Lynch, A. Markvardsen, D. J. Mikkelson, R. L. Mikkelson, R. Miller, K. Palmen, P. Parker, G. Passos, T. G. Perring, P. F. Peterson, S. Ren, M. A. Reuter, A. T. Savici, J. W. Taylor, R. J. Taylor, R. Tolchenov, W. Zhou and J. Zikovsky, *Nucl. Instrum. Methods Phys. Res.*, 2014, **764**, 156–166.

71. https://www.sasview.org/.

72. https://www.ncnr.nist.gov/resources/activation/.

Chapter 4: Using Polymer Additives to 3D Print Perylene Bisimide Hydrogels

4.1 Introduction

Printable hydrogels are gaining interest in all fields, from precision medicine to optoelectronics.[1–3] During 3D printing, a material (also sometimes referred to as an ink) is continuously deposited in a layer-by-layer manner.[4] As such, 3D printing allows for the preparation of more complex shapes and fine structures and is more precise and less time-consuming than using moulds.[2,3,5] The extrusion of polymer- and peptide-based hydrogels has been well reported.[6,7] Typically, these materials are expelled as pre-gel solutions that undergo gelation post-printing *via* a gelation trigger, such as exposure to cross-linking agents,[8] temperature change,[9] or UV photocuring.[10] However, polymer gels are limited by their irreversibility and lack of shear thinning properties.[4] Furthermore, some cross-linking agents used to trigger gelation can be toxic.[11] 3D printing of LMWGs is still scarcely described in the literature, with many LMWGs requiring an additive to improve their printability. Unlike chemical gels, some supramolecular gels can be formed before printing,[2,12] allowing the properties of the final printed material to be pre-defined.[2,13] However, this requires that the material be printable and that its properties do not change (or at least recover) upon printing.

There are many different types of 3D printing currently available to suit various materials (Fig. 4.1). The type of printing method chosen depends on the properties of the hydrogel.[14] Inkjet printing delivers small droplets of ink (1-100 picolitres, 10-50 μm diameter) onto the chosen substrate. The two most used types of inkjet printing are piezoelectric and thermal inkjet printing. Piezoelectric printing requires piezoelectric crystals to produce acoustic waves which force the liquid in small volumes through the nozzle,[15] whilst thermal inkjet printing produces pulses of pressure by vaporising the ink around a heating element, expelling the ink out from the printing head.[14] Inkjet printing has been previously used to pattern hydrogels to resemble body tissue.[16] In extrusion printing, the ink is typically extruded from a syringe as larger hydrogel filaments (approximately 150-300 μm in diameter) onto the substrate. This extrusion can either be done pneumatically or mechanically. In pneumatic deposition, it is possible to adjust the air pressure, allowing a wide range of ink types and viscosities to be used. Extrusion-printed hydrogels have a variety of potential applications, including tissue engineering and drug delivery.[17] In laser-assisted printing, a pulsed laser beam is focused and scanned over a donor substrate coated with an absorbing layer (e.g. gold or titanium) and the ink.[14] The focal point of the laser causes local evaporation of the absorbing layer, and the ink is delivered to the target in droplet form.[18]

Among the different 3D printing methods, extrusion-based printing is the most common method due to its ease of use, low cost, and ability to be adapted to suit specific needs.[2,19]

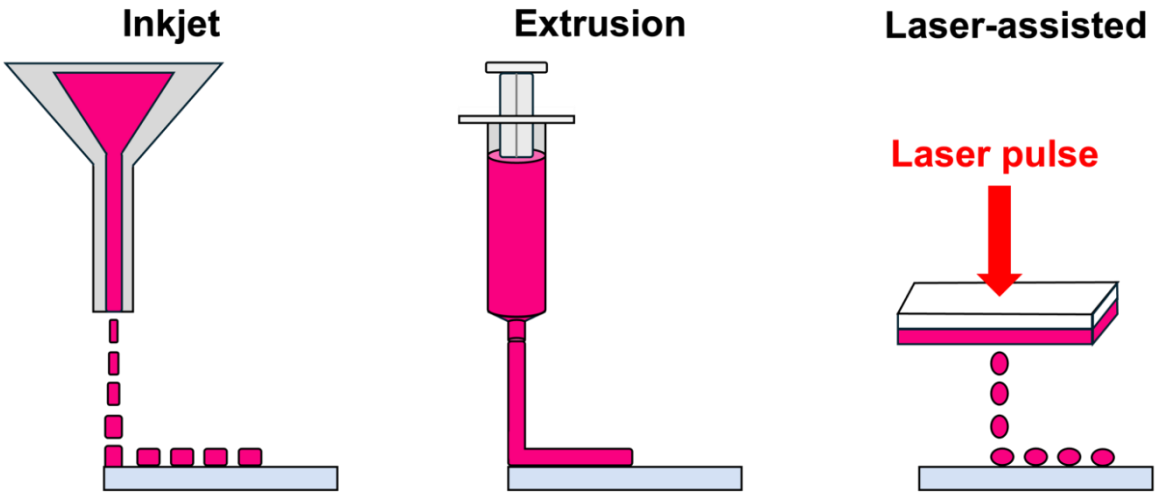

Figure 4.1. Cartoon showing the different types of 3D printing methods.

For hydrogels to be used in extrusion printing, it is crucial to understand the printability of the precursor gel.[20] The printability is related to the behaviour of the material whilst being sheared during extrusion (known as extrudability) and its performance and stability post-printing (denoted by shape fidelity). The rheological properties of the hydrogel are the physiochemical parameters that have the greatest influence on its behaviour throughout the 3D printing process (Fig. 4.2).[21,22] The material's viscosity and shear-thinning properties will determine how easily it flows through the syringe nozzle and impact its ability to maintain its shape after extrusion. The thixotropy of the gel is another crucial parameter that determines the suitability of hydrogels for printing. Thixotropy is the steady decrease in viscosity over time for a constant applied shear stress, followed by a gradual recovery when this stress is removed.[23] In extrusion printing, shear-thinning relates to the ease of extrusion and the shape preservation of the gel as it is printed. When the material moves through the syringe nozzle, its viscosity is reduced due to the large increase in applied shear causing shear-thinning. Thus, a quick recovery time is a desirable property of the hydrogel.[20] Currently, most reported examples of hydrogels suitable for printing have been discovered through serendipity.[2] Therefore, the link between the microstructure of the gel network and its printability is poorly understood. In the literature, the suitability of a hydrogel for 3D printing is commonly assessed by characterising its mechanical properties before printing, with little, if any, rheological measurements done post-printing.[24] It is assumed that the mechanical properties of the printed gels are unaffected by the printing process, which seems unlikely due to the processes involved. This lack of analysis is likely due to the difficulty in

carrying out such characterisations. However, such information is crucial to determine the types of applications these materials are suitable for. For example, to determine the suitability of printed gels for organic electronics (a field commonly described as a potential application in 3D printing-based literature), it is important to understand how printing would impact the bulk properties and conductivity of the resulting gels.

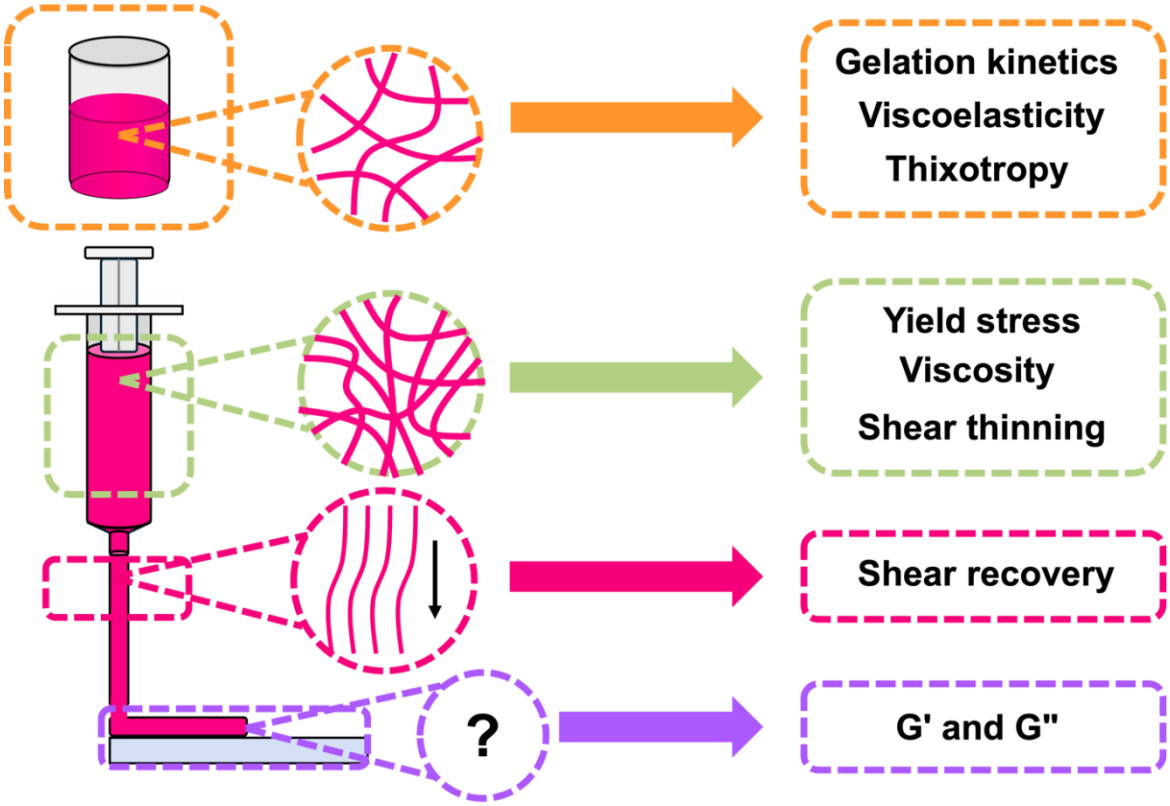

Figure 4.2. Cartoon showing how printing can impact the properties of gels and the types of rheological characterisations that are important during the different stages of the printing process.

Fabrication of anisotropic materials is highly desirable in organic electronics as it can allow for greater control of the orientation of fibres and the direction of conductivity. The structures should also have suitable exciton diffusion lengths and spatial arrangement and distribution of the self-assembled fibres. Such parameters need to be controlled over the length scale of the device.[25] Many methods of alignment exist, such as spin-coating,[26,27] magnetic alignment,[28] and doctor blading.[29] Draper *et al.* previously showed that magnetic fields could be used to create highly aligned and directionally dependent films.[28] However, using an NMR magnet was not always reproducible due to fluctuations in temperature and humidity impacting the evaporation rates. Such reproducibility was improved by using an MRI magnet in a temperature- and humidity-controlled environment. Using NMR or MRI magnets is an expensive way to make aligned films. A much cheaper method is spin-coating

or doctor blading, but these can be wasteful and difficult to control.[28] Furthermore, using such techniques on low-viscosity, water-based solutions is typically unsuccessful due to the water being unable to evaporate quickly enough. Therefore, there is a need to create aligned fibres of water-based materials without using large magnets or wasteful coating techniques.

Another desirable property of organic electronic devices is flexibility due to their potential for use in wearable electronics.[30,31] Flexibility can describe the bendability, resilience, or stretchability of a material.[32] Such properties are highly sought after in applications such as robotic skin and wearable biological sensors.[33,34] For robotic skin, the material must be able to sense pH, moisture and temperature, which is not possible with metal-based or Si-based electronics.[30] Furthermore, crystalline materials are typically brittle, meaning they have limited applications in flexible electronics. Although most self-assembled small molecules are amorphous, they can form monodisperse, flexible fibres. The Draper group have previously shown mechanoresponsive films can be made from amino acid-appended perylene bisimides.[30] Three PBIs functionalised with L-alanine, L-phenylalanine, and L-histidine (**PBI-A**, **PBI-F**, and **PBI-H**, respectively) were investigated. Upon drying, **PBI-F** films produced very little current due to the formation of cracks, and thus were not suitable for further testing. The photoconductivity of **PBI-A** and **PBI-H** films was tested under various degrees of bending. After bending, **PBI-H** films showed small cracks, which disrupted electrical continuity and prevented conductivity. By contrast, **PBI-A** films did not show cracking initially and maintained electrical continuity during the measurements. However, these films showed a decrease in current with increasing bending angle. Furthermore, after 20 bending cycles, cracks began to form on these films. These cracks did not appear to have any impact on the films' resistance.

This chapter aims to create aligned and flexible materials by 3D printing amino acid-appended PBI/polymer-based hydrogels. Crucially, we utilise both rheology and SANS to characterise the properties of the gels before, during, and after printing to understand the impact of the printing process and its impact on the bulk properties. The electrochemical properties of the hydrogels before and after printing are also examined to determine the suitability of these materials for optoelectronic devices. Finally, we aim to show that these gels can be dried to form homogenous, flexible, and aligned materials using nanoindentation, profilometry, electrochemical techniques, and microscopy.

4.2 Results and Discussion

Due to previous work in the group, **PBI-A** (Fig. 4.3) was chosen because it can form mechanoresponsive films.[30] Furthermore, **PBI-**A has been used in Chapters 2 and 3, highlighting the versatility of a single gelator simply by changing the pre-gel conditions. However, PBI hydrogels are typically soft, which may lead to fragile architectures upon printing.[35,36] Many groups have shown that using polymer additives can modulate the properties of supramolecular hydrogels, such as making them stronger.[37–40] Regarding organic electronics, blending with polymers should improve the flexibility of the resulting films.[41] Therefore, a non-gelling polymer additive was added to create **PBI-A**/polymer blends. Initially, three polymers were tested: poly(ethylene) glycol (**PEG**, average M_n = 950 – 1050), poly(vinyl) alcohol (**PVA**, average M_n = 9000 – 10000), and poly(ethylene) oxide (**PEO**, average M_n = 500,000). However, hydrogels formed with **PEG** were too soft (Tables A.3.1 and A.3.2, Appendix). Contrarily, hydrogels formed from **PVA** blends were deemed too stiff to print (Tables A.3.1 and A.3.2, Appendix). Therefore, **PEO** (Fig. 4.3) was chosen for the blends. The blend composition was altered by adjusting the percentage volume of the PBI and polymer (which in this chapter will be quoted as ratios of **PBI-A**/**polymer**). PBIs act as surfactants, meaning their aggregation state is likely dependent on concentration.[42] As such, the final concentration of both **PBI-A** and **PEO** in each blend was maintained at 5 mg/mL. Stock solutions of **PBI-A** and **PEO** were made at concentrations of 20 mg/mL, 10 mg/mL, or 6.66 mg/mL. Therefore, any differences in the blends would be due to the volumes of the **PBI-A** and polymer in each blend and the aggregates formed when mixing the single components. Rheological time sweeps showed the gelation process was different for **PBI-A** alone and for each blend (Figures A.3.1 – A.3.7, Appendix), suggesting that both the polymer and the blend composition impact gel formation.

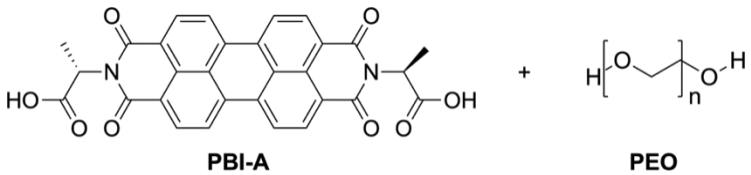

Figure 4.3. Structures of **PBI-A** and **PEO** used in this chapter.

4.2.1 Optimisation of 3D Printing Conditions

As previously discussed, to be suitable for extrusion-based 3D printing, a gel should exhibit thixotropy.[20] At high shear rates, the gel should be able to easily flow through the syringe nozzle. As the material is deposited on the substrate, its viscoelastic effects become

important, and the kinetic energy applied during extrusion is converted into elastic energy and/or dissipated.[43] Therefore, the recovery properties of the **PBI-A/PEO** hydrogels were measured using rheology (Fig. A.3.8 – Fig. A.3.15, Appendix) A high shear rate (300%) was applied for 60 seconds to disrupt the equilibrated state of the gel, and hence break the gel network. The recovery of G′ and G″ was subsequently measured at a low shear rate (0.5%) for 200 seconds (Fig. 4.4). Five cycles of high and low shear were applied, constantly measuring G′ and G″.

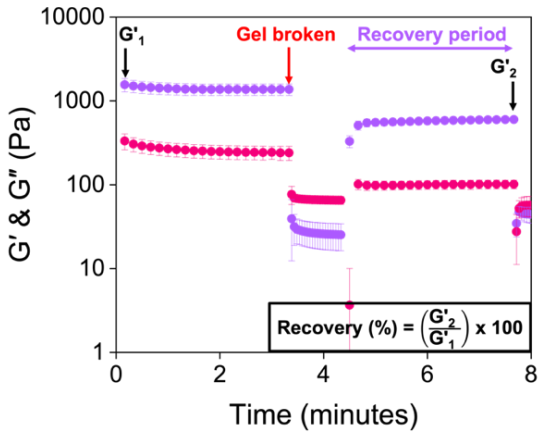

Figure 4.4. Exemplar recovery test data, highlighting when the gel is broken and the recovery period. The equation to calculate the percentage recovery is also given as an inset.

The initial G′ and the percentage recovery of G′ of each blend are shown in Fig. 4.5. Hydrogels were formed from blends with initial pHs of 6 (Fig. 4.5a) and 9 (Fig. 4.5b) since, as discussed in Chapter 2, these pHs were found to give gels with different properties. Hydrogels formed from **PBI-A** alone showed low recovery (26% and 7% for gels formed from **PBI-A** solutions with an initial pH of 6 and 9, respectively), suggesting that the polymer additive improves the thixotropic properties of the multicomponent hydrogel.

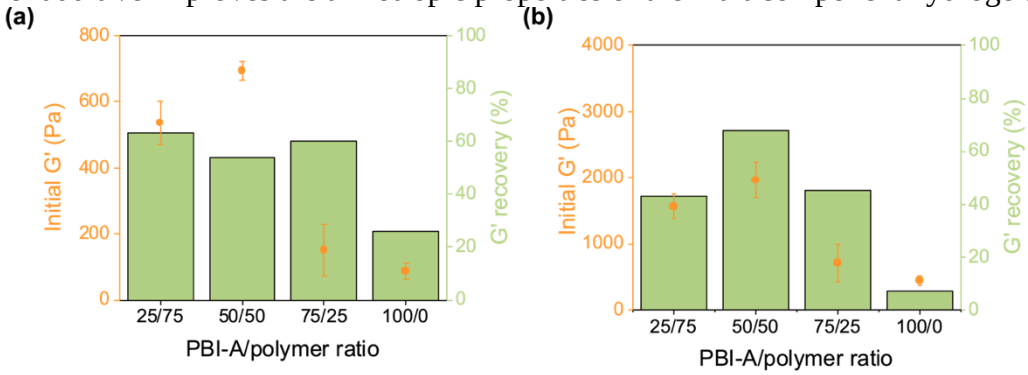

Figure 4.5 Rheological recovery tests of hydrogels from different **PBI-A/PEO** blends at an initial pH of (a) 6 and (b) 9. The initial G′ (*i.e.*, the G′ value at t=0) is shown as orange circles. Data shown are averaged data for triplicate runs, with error bars representing standard deviation. The percentage recovery (green columns) is the ratios of the average G′ after each restoration with the original G′.

After determining the recoverability on the rheometer, the hydrogel blends were then all printed in 6 cm lines to correlate the recovery data to their printability (Fig. A.3.16, Appendix). The shear rate at which a gel is extruded through the nozzle of the syringe can be calculated for a Newtonian fluid using Equation 1, where γ is the shear rate (in s^{-1}), V is the volume of the extruded gel (in m^3), r is the radius of the nozzle (in m), and t is the time taken to extrude the volume of the gel (in s). It is important to clearly identify the shear rate applied during extrusion to implement the same conditions when measuring the rheological properties of the gels.[44] Furthermore, the shear stress at any point within a sheared gel is determined by the value of the shear rate.[22] Therefore, such information is critical to judge a material's printability, printing resolution, and ink integrity.[43] The automation of the 3D printer allowed for precise control over the flow rate of the gel during extrusion, and Equation 1 was used to calculate the shear rate for all prints.

$$Shear\ rate, \gamma = \frac{4V}{\pi r^3 t} \qquad \text{(Equation 1)}$$

The 3D printer has various parameters which can be optimised (such as the volume of the gel extruded, the extrusion speed, the height of the nozzle from the printing bed, and the translational speed of the extruder relative to the print bed).[2,45] Each parameter was systematically changed and optimised by printing a line of 6 cm. The optimal value for the given parameter was that which gave the thinnest continuous line (examples given in Fig. 4.6, Fig. A.3.17, and Fig. A.3.18., Appendix). A hydrogel of **PBI-A** only was also printed (Fig. 4.6a), with the gel completely breaking upon extrusion. These results suggest that the polymer is a prerequisite for creating thixotropic hydrogels suitable for printing continuous lines. The final optimal printing parameters are shown in Table 4.1.

Table 4.1. Optimal parameters for printing **Printed Gel-1** as shown in Fig. 4.6c.

Printing parameter	Value
Total volume (μL)	1000
Volumetric rate (μL/cm)	166
Nozzle speed above bed (mm/min)	9408
Nozzle height from print bed (mm)	3
Time taken to print a 6 cm line (s)	0.38
Shear rate (s^{-1})	2500

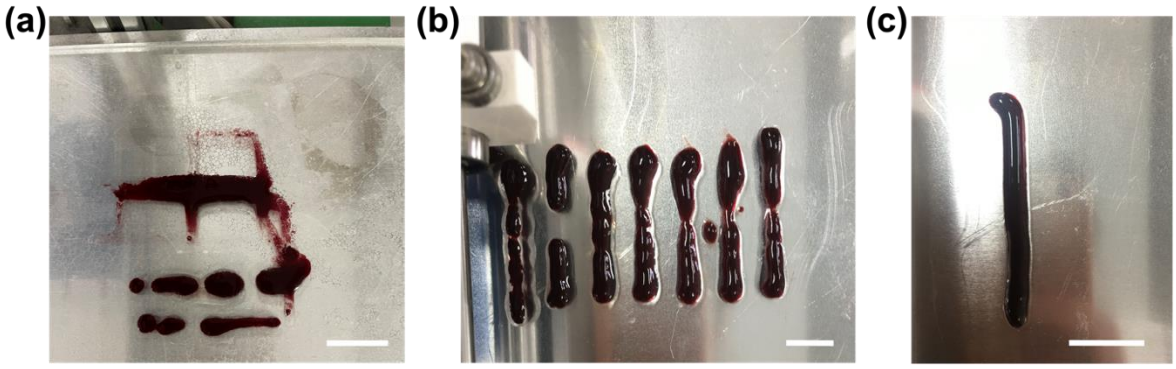

Figure 4.6. Photographs of (a) control **PBI-A** hydrogels printed at a total volume of 1000 μL, a nozzle height above the print bed of 3 mm, a nozzle speed relative to the print bed of 9408 mm/min, and a printed line length of 6 cm. (b) **Printed Gel-1** printed at a total volume of 1000 μL, a nozzle height of 3 mm from the print bed and, from left to right, nozzle speeds relative to the print bed of 4704, 7056, 9408, 14112, 18816, and 28224 mm/min. (c) Final optimised printed gel. Scale bars represent 2 cm.

Gels formed from the **PBI-A**/**PEO** 75/25 blend with an initial pH of 6 were liquid-like upon printing (Fig. A.3.16c, Appendix) despite having a recovery of 60% (Fig. 4.5a). Furthermore, the gels formed from the **PBI-A**/**PEO** 50/50 blend with a starting pH of 9 gave the highest recoveries (68%, Fig. 4.5b), but when they were printed, they showed gaps in the lines (Fig. A.3.16e, Appendix). Such results emphasize that recovery tests alone are not enough to determine the printability of a hydrogel, despite this being a commonly used proof of concept in the literature. From this preliminary screening, we chose to print hydrogels from the **PBI-A**/**PEO** 25/75 blend with an initial pH of 9, as these gels gave the thinnest continuous lines when printed (Fig. A.3.16d, Appendix). In this chapter, this blend will be referred to as **Gel-1** or **Printed Gel-1** for simplicity.

As the properties of hydrogels can be concentration dependent,[46,47] the impact of changing the concentration of **PBI-A** and **PEO** in the blend on their printability was also investigated. The concentration of **PBI-A** or **PEO** was altered to 10, 15 or 20 mg/mL, whilst the second component of the blend remained at 5 mg/mL. 6 cm lines were printed using the optimised conditions described in Table 4.1. Increasing the **PBI-A** concentration caused the gels to become more globular and inhomogeneous (Fig. A.3.19, Appendix); in comparison, a higher **PEO** concentration caused the gels to become more liquid-like, with thicker lines formed (Fig. A.3.20, Appendix). Rheological strain sweeps showed the gel stiffness increased with increasing **PBI-A** content (Fig. 4.7a). This increase in stiffness may cause the printer to exert

more strain to extrude the gels, resulting in the gels breaking completely upon printing. In comparison, the **PEO** concentration caused little variation in the gel stiffness (Fig. 4.7b). Such results are unsurprising, considering that **PBI-A** is the only gelator present in the blend. The strength of the gels was also impacted by the concentrations of the two components in the hydrogel (Fig. A.3.21, Fig. A.3.22, Table A.3.6, and Table A.3.7, Appendix). Such results highlight the effect of the rheological properties on the quality of the printed hydrogels, as even slight changes in strength or stiffness can impact the shape retention and consistency of the gels upon extrusion.

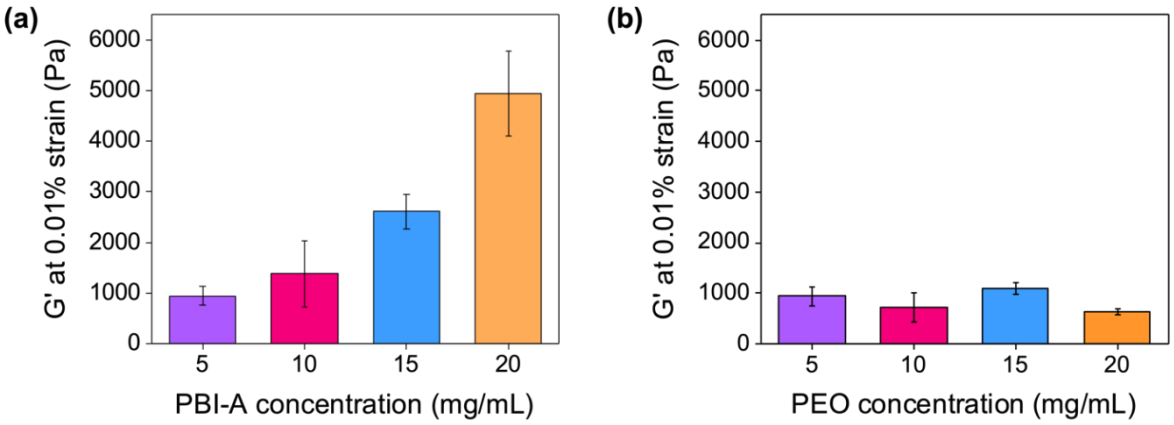

Figure 4.7. G′ values quoted at 0.01% strain with increasing (a) **PBI-A** and (b) **PEO** concentration in the **Gel-1** blend. Data shown are averaged data for triplicate runs, with error bars representing standard deviation.

4.2.2 Using Rheology to Understand the Printing Process

As previously mentioned, rheology can be used to study the effects of applied shear on the restoration kinetics of the gel. Although recovery tests can inform one about the printability of hydrogels, they are not representative of the extrusion process. Therefore, to mimic the shear applied during printing, the hydrogel was exposed to 2500 s^{-1} (as calculated using Equation 1) for one second. G′ and G″ were then monitored over time (Fig. 4.8). Both G′ and G″ initially dropped in value, which could be due to slight slippage during the shearing process. After 1 minute, the moduli were the same value as those for the pre-sheared gel. The gels continued to show a stepwise increase in G′ over time. However, the gel was only slightly different to the original pre-sheared sample (G′ values of 10,800 and 12,800 Pa for the pre-sheared and sheared samples, respectively) and suggests that the gels are not broken upon extrusion. However, it should be emphasized that such measurements are not fully representative of the type of shear found inside a syringe during extrusion.

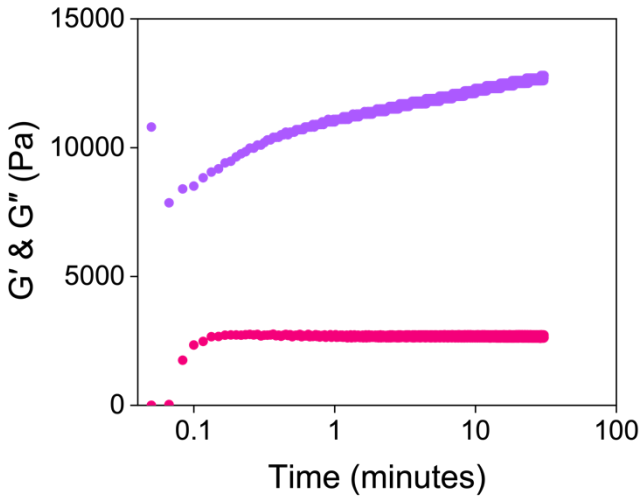

Figure 4.8. Restoration of G′ (purple) and G″ (pink) as a function of time after shearing **Gel-1** at 2500 s^{-1} for 1 second.

Since the gels were formed in 3.5 mL syringes and left to gel overnight, we hypothesised that pre-compression of the gel could potentially occur inside the syringe, leading to the strengthening of the network.[2] It has previously been reported that compression of gels resulted in non-reversible changes to the networks of similar LMWGs.[48] Therefore, a compression sweep was carried out where the gap distance of the measuring system was lowered from a position of 1.8 mm by 5 μm/s for 5 minutes. After this time, the measuring system was lifted back to 1.8 mm and a strain sweep was immediately run (Fig. 4.9). Compressed gels were stiffer, as shown by an increase in G′ (G′ values at 0.01% strain of 1,380 Pa and 31,200 Pa before and after compression, respectively), in agreement with previous data on similar pH-triggered gels.[2,48] However, the compressed gels were significantly weaker than non-compressed gels, represented by the small linear viscoelastic region, differing from previous reports. The yield points of the gels were 3.2% and 0.02% before and after compression, respectively. This change in strength suggests that the fibres may interact and entangle differently or that different types of fibres are formed upon compression. However, another possible explanation could be that as the strain sweeps were performed immediately after applying compression, the gels did not have time to fully recover.

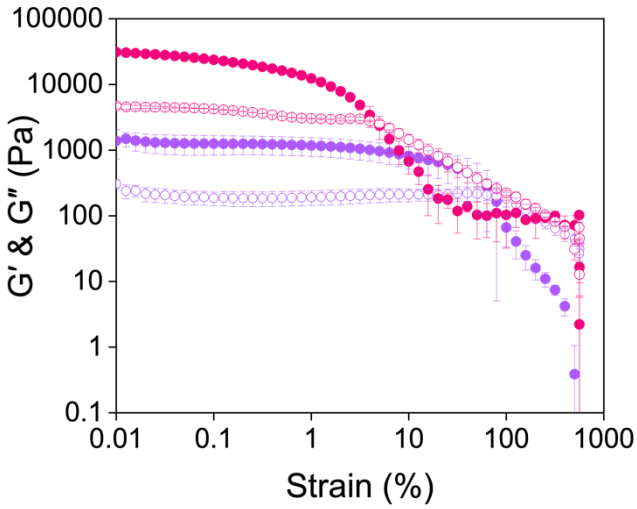

Figure 4.9. Strain sweeps of **Gel-1** before (purple) and after (pink) compression. Closed circles represent G′ and open circles represent G″. Data shown are averaged data for triplicate runs, with error bars representing standard deviation.

Next, kinetic measurements were performed under different normal forces, F, measuring the development in G′ and G″ over time (Fig. 4.10a) to mimic the force experienced in the syringe. The G′ values of the hydrogels at 1000 minutes increased with increasing normal force applied (Fig. 4.10b), indicating that the gels were becoming stiffer. However, the development of the moduli was similar irrespective of the force, suggesting that the gels all undergo the same self-assembly process. Such results suggest that compression of the gels strengthens the network, which may result in a gradient effect in the printing results if one is printing large volumes of gel from a single syringe.

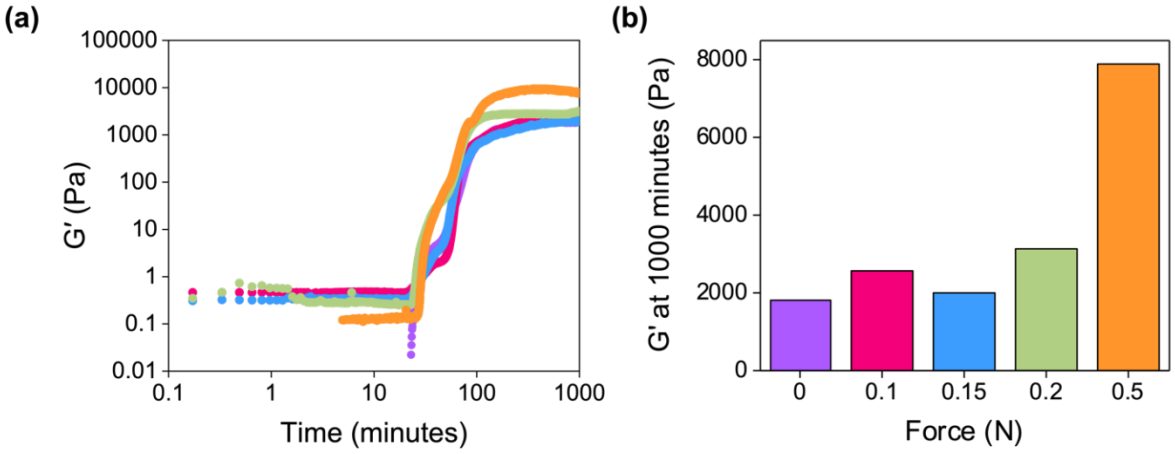

Figure. 4.10. (a) Development of G′ during the gelation of **Gel-1** under a normal force of 0 N (purple), 0.10 N (pink), 0.15 N (blue), 0.20 N (green), and 0.50 N (orange). Measurements were performed under a strain of 0.5%, a frequency of 10 rad/s, and at 25°C. (b) G′ comparison after 1000 minutes as a function of normal force.

To determine whether there was a gradient effect on the gels formed at different depths of the syringe (Fig. 4.11a), strain sweeps were conducted on slices of gels from the same syringe (Fig. 4.11b). Gels were again formed in 3.5 mL syringes with the nozzle removed. The gels were then sliced in half to compare the rheological properties of the gel formed at the top and bottom of the syringe (Fig. 4.11c). The value of G′ nearly doubled when comparing the gel from the bottom of the syringe to that from the top (G′ values at 0.1% strain of 440 Pa and 240 Pa for the bottom and top of the syringe, respectively). Furthermore, both gels had the same yield point of 1.6%. The linear viscoelastic region for both gels showed slight fluctuations in G′ values, which could be the result of loading artefacts from placing the sample on the rheometer plate. Comparing these results to the data given in Fig. 4.9 would suggest that the force applied by the gel's own weight in the syringe is minimal, giving more homogenous gels. However, such results may not be observed when using larger syringes, which require greater volumes of the gel.

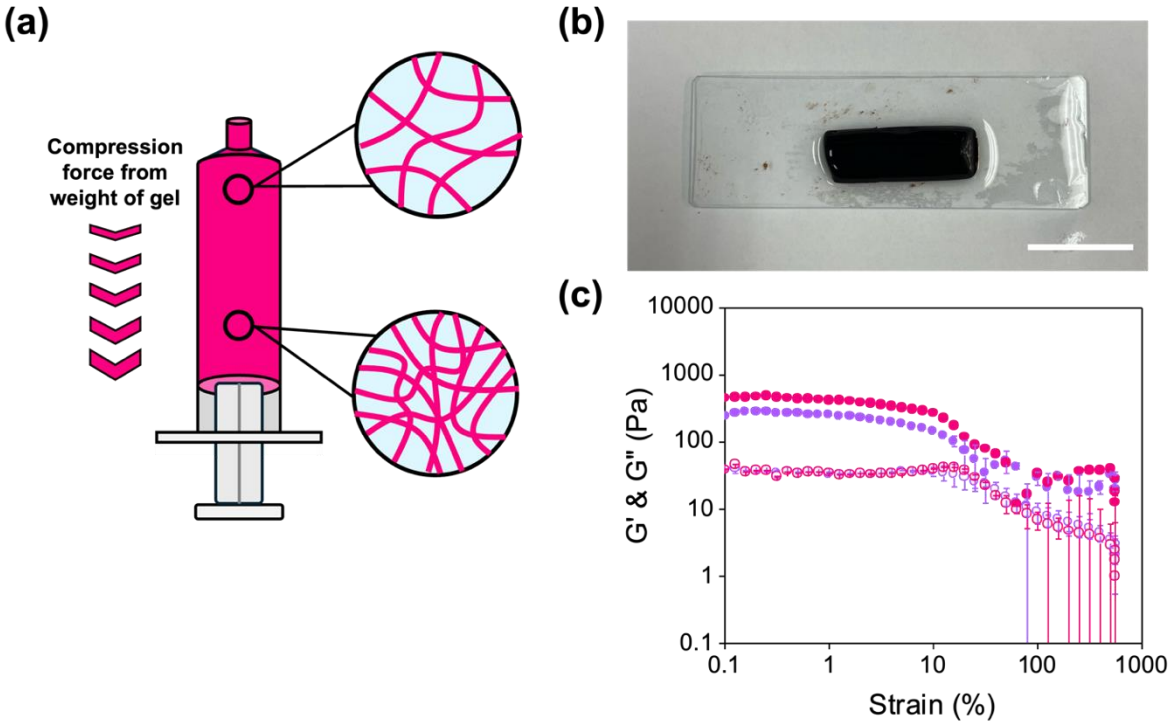

Figure 4.11. (a) Cartoon representing the hypothesised compression happening inside the syringe. (b) Photograph of a slice of **Gel-1** gelled inside a syringe. Scale bar represents 2 cm. (c) Strain sweeps of syringe gels formed at the top (purple) and bottom (pink) of the syringe. Closed circles represent G′, and open circles represent G″. Data shown are averaged data for triplicate runs, with error bars representing standard deviation.

4.2.3 Characterisation of 3D Printed Hydrogels

As previously discussed, characterisation of printed hydrogels is scarce in the literature. One method is to print the gels into moulds and measure the rheological properties with a parallel plate (PP) geometry.[2] The PP geometry is widely used for sample thicknesses between 0.5 and 2.0 mm.[24,49–51] However, such measurements are typically performed on the top of the bulk sample, which may cause compressional stress during loading and measurements,[52] as shown in the previous experiment testing applied force on the gels (Fig. 4.9). Furthermore, the shear rate is not constant across the geometry, being higher at the outer edges.[24] The shear stress applied depends on the contact area between the sample and geometry and is higher with smaller PP geometries. Slippage can also occur, which can cause large errors after the critical strain. Although vane geometries are less commonly used, they are more effective for performing rheology on soft materials, which could be susceptible to pre-shear caused during sample loading. Furthermore, the vane can penetrate the sample without destroying the overall structure. Gels were therefore printed directly into Sterilin vials and rheology was performed using the cup-and-vane measuring system.

Printed gels were stiffer than the corresponding non-printed gels (Fig. 4.12, G′ values at 0.01% strain of 12550 Pa and 1380 Pa for printed and non-printed gels, respectively), which is at odds with results previously reported for similar LMWGs.[24,53] Furthermore, the non-extruded gels were stronger, with a higher yield point (2.5% compared to 0.1% for the extruded gels). These changes in rheological properties could be due to the shear applied when the gels are extruded, or compression caused by the syringe plunger during extrusion altering the fibres or gel network. It is also possible that the energy dissipated in the system when sheared is causing an increase in gel stiffness.[54]

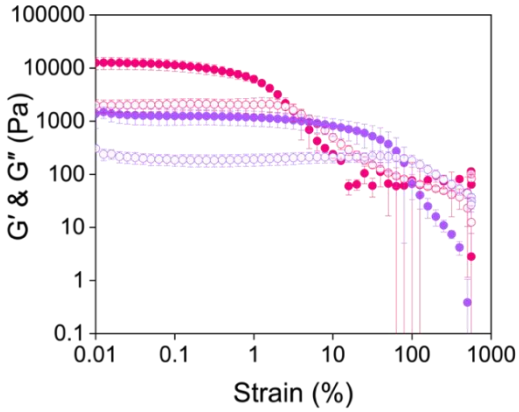

Figure 4.12. Strain sweeps of **Gel-1** (purple) and **Printed Gel-1** (pink). Closed circles represent G′ and open circles represent G″. Data shown are averaged data for triplicate runs, with error bars representing standard deviation.

To understand what was happening to the fibre-level assembly upon printing, SANS was used to probe the gel structures before and after printing (Fig. 4.13 and Tables 4.2 and 4.3). The scattering data fit to an elliptical cylinder with a power law before and after printing. The scattering intensity at low Q ($0.002 < Q < 0.01$) increased upon extrusion, suggesting an increase in the number of large self-assembled structures and loss of homogeneity after printing. Furthermore, the axis ratio significantly increases for printed hydrogels (5.2 versus 1.8 for printed and non-printed gels, respectively). An increase in axis ratio indicates that the fibres are more compact or tape-like in the printed gels,[55,56] and could explain the increase in stiffness observed in the rheological data (Fig. 4.12). One explanation could be that the extrusion process pushes the fibres into a more continuous network, and the compression causes them to elongate.

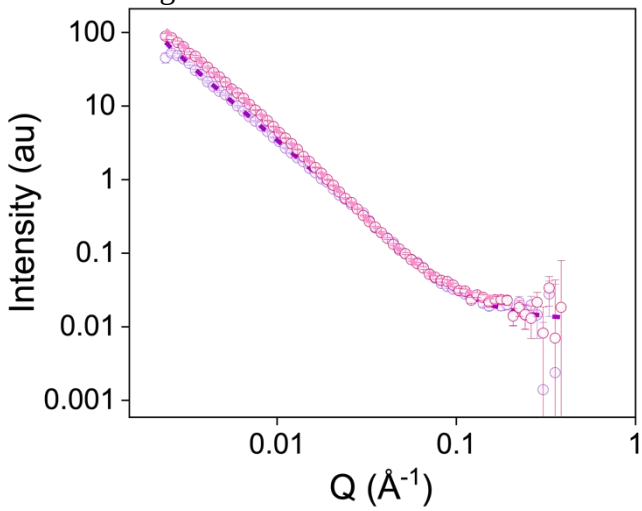

Figure 4.13. Small-angle neutron scattering patterns for **Gel-1** (purple) and **Printed Gel-1** (pink). Open circles show the data and dashed lines represent the fit.

Table 4.2. Tabulated parameters of the SANS model fit for **Gel-1**.

Elliptical Cylinder + Power Law	**Value**	**Error**
Background (cm^{-1})	0.01	
Cylinder scale	5.5860×10^{-5}	4.7674×10^{-6}
Length (Å)	600	215
Radius (Å)	50.0	1.8
Axis ratio	1.8	0.1
Power law scale	1.2938×10^{-4}	7.0703×10^{-6}
Power law	2.2	0.01
χ^2	1.6043	

Table 4.3. Tabulated parameters of the SANS model fit for **Printed Gel-1**.

Elliptical Cylinder + Power Law	**Value**	**Error**
Background (cm^{-1})	0.01	
Cylinder scale	1.1227×10^{-4}	7.4941×10^{-6}
Length (Å)	448	46
Radius (Å)	55.0	2.3
Axis ratio	5.2	0.4
Power law scale	7.1350×10^{-5}	3.7335×10^{-6}
Power law	2.3	0.01
χ^2	1.2917	

For the printed gels to be suitable for applications (such as optoelectronic devices), the gels should be homogenous along the printing axis. Therefore, cavitation rheology was utilised to measure the critical pressure at different points along the printed gel (Fig. 4.14). This technique is a form of microrheology which utilises the cavitation effect to probe the localised mechanical properties of a material.[57] Cavitation rheology has the advantage that it can be conducted on gels of any shape in their native environment.[58,59] Briefly, the method involves growing a cavity at the tip of a needle and quantifying a critical pressure of mechanical instability (Fig. 4.14a).[60] The pressure at which this instability occurs is directly related to the modulus of the material, meaning cavitation rheology can easily probe the homogeneities of the gel. The critical pressure was measured in 0.5 cm increments along the length of the printed gel, with a control experiment performed in a Sterilin vial (Fig. 4.14b). The critical pressure was identical at points 1.0 and 1.5 cm along the printing axis (22 Pa for 1.0 and 1.5 cm, respectively) and was slightly lower (16 Pa) 0.5 cm along the gel. This decrease in pressure could be due to this section of gel being from the top of the syringe, so it is not as compressed as the gel from the middle and bottom of the syringe, in agreement with the rheology data.

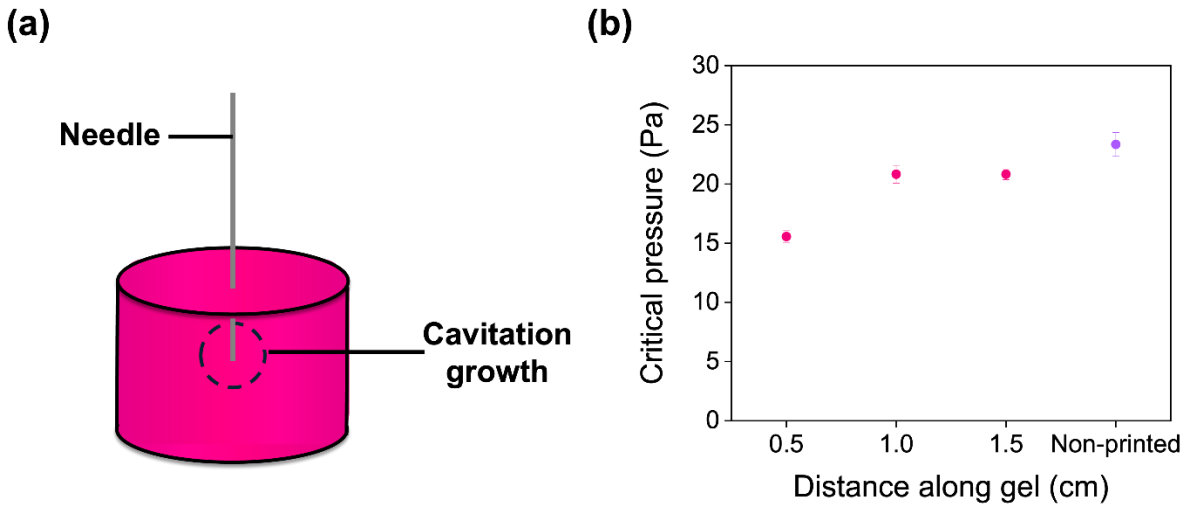

Figure 4.14. (a) Cartoon showing the basic idea of cavitation rheology. (b) Cavitation rheology of **Gel-1** (purple) and **Printed Gel-1** (pink). Data shown are averaged data for triplicate runs, with error bars representing standard deviation.

Cyclic voltammetry (CV) was used to determine if the printing process impacted the reduction potential of the gel (Fig. 4.15) in a two-electrode window cell set-up (Section 4.4.1.9). Gels were either prepared in or printed directly onto the fluorine-doped Sn oxide (FTO) glass (as described in more detail in Section 4.4.18). The reduction potentials were -0.12 V and -0.10 V for non-printed and printed gels, respectively. The shapes of the CV voltammograms for non-printed and printed gels were significantly different. There are two possible explanations for this change. The shape of the CV waveform changes depending on how electrons move through the system. Furthermore, as structures become larger, they should become less efficient at electron transfer due to a change in the available surface area. Therefore, the differences in the CV waveforms could be due to differences in the micellar structures and/or nanostructures caused upon extrusion. The second explanation could be related to how the samples were prepared in the FTO window set-up. For the non-printed gels, gelation occurred *in-situ* directly on the FTO glass. In comparison, the printed gels were prepared in a syringe and printed onto the FTO glass. Therefore, there may be poorer contact between the glass and printed gel, which could explain the less defined peaks and curve. As NaCl was used as the electrolyte, strain sweeps of gels with 1 equivalent of NaCl were also measured (Fig. A.3.26, Appendix), showing that the salt did not impact the properties of the gel.

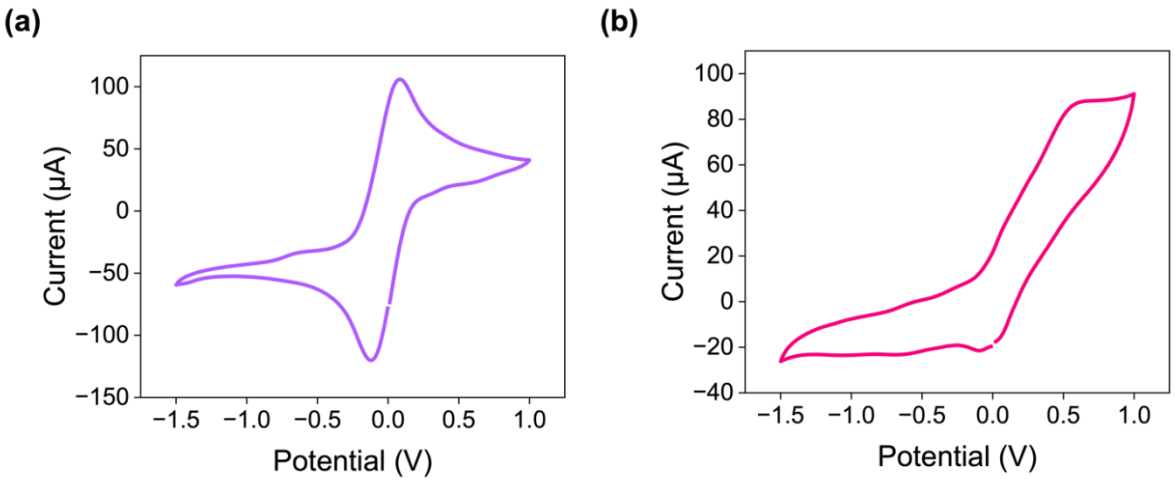

Figure 4.15. Cyclic voltammograms of (a) **Gel-1** and (b) **Printed Gel-1** using 0.1 M NaCl electrolyte solution with a scan rate of 0.05 V/s.

4.2.4 Characterisation of 3D Printed Xerogels

Previously, amino acid-appended PBIs have been used to form photoconductive xerogels.[25,61] Such xerogels are formed by drying the gel in air and at room temperature until the water is removed. This method maintains the fibrous network but removes the solvent, causing the structure to collapse. Printed gels were dried to form xerogels and imaged using cross-polarised optical microscopy to investigate how printing impacted the xerogel morphology (Fig. 4.16). Gels were printed in 6 cm lines (Fig. 4.16b) and left to dry in air overnight (average lab temperature 23.5°C and 48% humidity). These gels were compared to xerogels drop cast in a 0.5 x 6 cm mould (Fig. 4.16a). The printed gels showed alignment, which is promising if these materials are to be used in optoelectronic devices. Aligned fibres facilitate electron transport, as the path is shorter, reducing the chance of charge recombination.[62] These results suggest that the alignment caused by the shear applied during printing remains after drying, which can sometimes be lost when using doctor blading or spin-coating of water-based materials. In comparison, the xerogels formed by drop-casting showed no alignment.

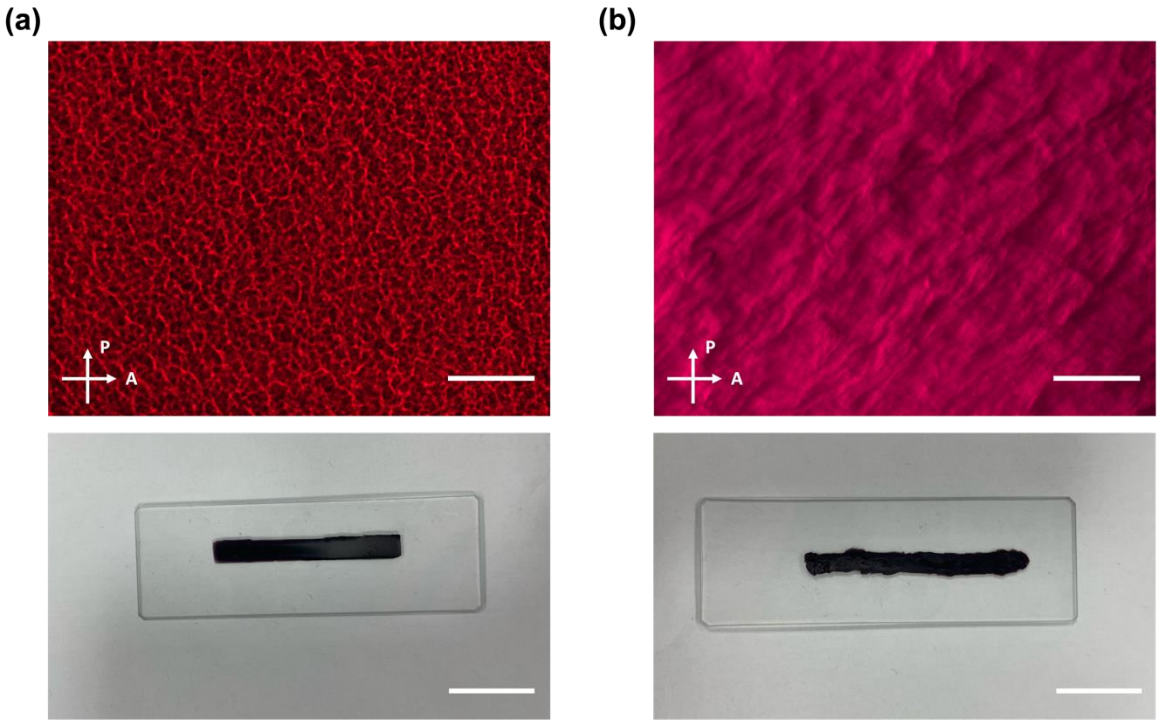

Figure 4.16. Cross-polarised optical microscope images (top) and photographs (bottom) of dried down (a) **Gel-1** and (b) **Printed Gel-1** hydrogels. Scale bars represent 100 μm for optical microscope images and 2 cm for photographs.

As the cavitation rheology suggested that the gels were homogenous along the printing axis, profilometry was performed on the xerogels to ensure this homogeneity was preserved upon drying (Table 4.4 and Figure A.3.28, Appendix). It is important that the sample thickness is consistent across the gel to ensure the photoresponse is the same. If the films are too thick this could prevent light penetration through the gel. Profilometry works like atomic force microscopy in which a cantilever is dragged across the sample's surface to measure the difference in height.[63] Again, the thickness was measured 0.5, 1.0, and 1.5 cm along the printing direction, with very subtle differences between the thickness (thicknesses ranging between 16.60 and 16.85 μm, Table 4.4). Such results agree with the cavitation rheology data (Fig. 4.14).

Table 4.4. Tabulated thickness of the **Printed Gel-1** xerogel along the printing axis.

Distance along gel (cm)	Thickness (μm)
0.5	16.76
1.0	16.83
1.5	16.61

To further test the bulk properties of the xerogels, nanoindentation was used. Such measurements were performed using a Berkovich indenter tip, using suggested parameters for "soft" materials (materials with an elastic modulus less than 10 GPa). As with the cavitation rheology and profilometry measurements, points were measured 0.5, 1.0, and 1.5 cm along the printing direction. The E_{IT} values were very similar along the printing axis (Fig. 4.17a), in agreement with the profilometry measurements. There were some variations in the H_{IT} values at the top and bottom of the xerogels (Fig. 4.17b), which again could be due to slight compression inside the syringe. Nanoindentation was also attempted on drop-casted xerogels to determine if printing impacted the elasticity or hardness. However, no measurements could be taken due to the inhomogeneity of these xerogels and the presence of cracks (Fig. A.3.30, Appendix).

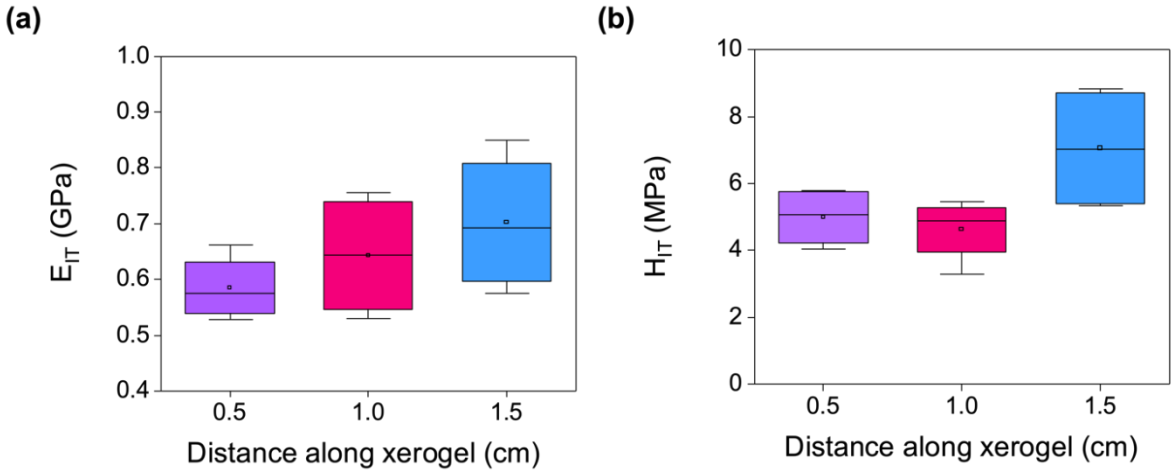

Figure 4.17. The average (a) E_{IT} and (b) H_{IT} of **Printed Gel-1** xerogels along the printing axis. Measurements were run in triplicate, with error bars representing standard deviation.

To test the flexibility of the printed xerogels, the **PBI-A/PEO** hydrogels were printed onto PVC sheets to allow for bending of the substrate. Previous work on **PBI-A** has shown that there is no difference in the adsorption of the material on glass compared to plastic.[30] Chronoamperometry measurements were collected under various bending angles (Fig. 4.18a). The length of plastic used for each printed xerogel was the same to ensure each film had the same radius of curvature upon bending. The measurement of the effect of the degree of curvature on the resistance of the films was conducted under constant irradiation with a 365 nm LED. From previous EPR and UV-vis absorption measurements on amino acid-appended PBIs, it was assumed the sample was saturated with radical anion, meaning any changes in current would be due to bending.[30,42] The films were bent to a maximum bending angle of 70° and straightened back to 0° whilst continuously measuring the current

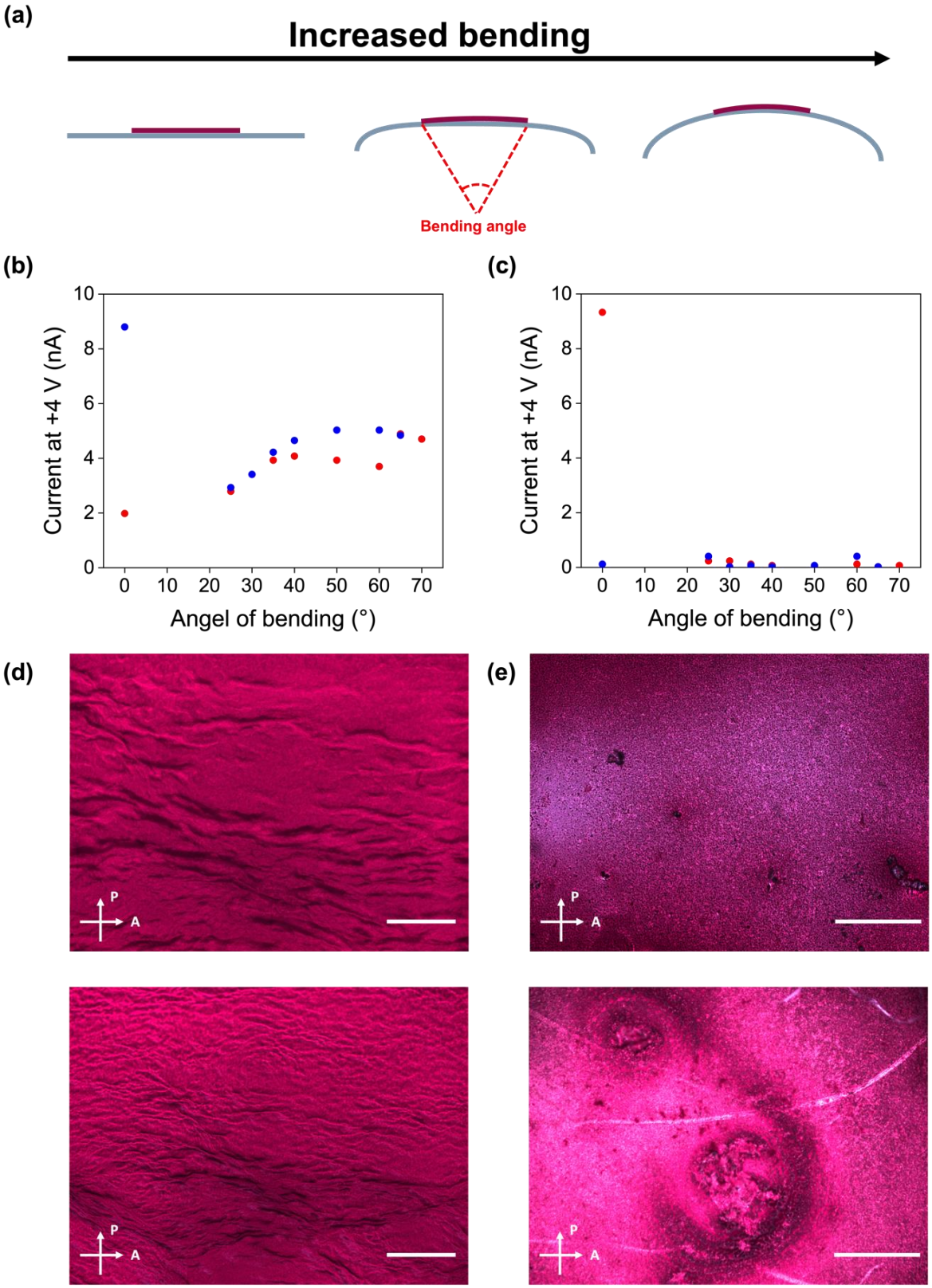

Figure 4.18. (a) Cartoon showing the films being bent and the radius of curvature. (b) and (c) Current at +4 V whilst bending (blue) and straightening (red) (b) **Printed Gel-1** and (c) **PBI-A** xerogels. (d) and (e) Cross polarised optical microscope images of (d) **Printed Gel-1** and (e) **PBI-A** xerogels before (top) and after (bottom) bending. Scale bars represent 100 μm.

The **Printed Gel-1** xerogels maintained electrical continuity during the measurements. Bending the films increased the current, whilst straightening the films decreased the current. However, once straight, the current produced was greater than the original value. Furthermore, the xerogels did not show cracking under the microscope after bending (Fig. 4.18d). Xerogels of **PBI-A** alone showed a large decrease in current upon bending (Fig. 4.18b), which did not recover upon straightening. Inspection of these xerogels under the microscope showed that cracks formed after bending (Fig. 4.18e). Such results suggest that the polymer and alignment caused by printing could aid in the xerogels' response to bending. The aligned fibres of the **Printed Gel-1** xerogels could act like layers that can slide over each other, stretching the film on bending and creating longer pathways for the current and thus increasing the resistivity.[30,64] Moreover, the more uniform surface of the **Printed Gel-1** xerogels could be less prone to cracking with bending.[30,65] Similar results have been observed with macroscopically aligned fibrous PBIs, which showed improved mechanical properties and flexibility compared to isotropic or non-fibrous films.[66]

4.3 Conclusions

In this work, we aim to control the pre-gel and final gel structures of **PBI-A** LMWGs *via* the addition of the non-gelling polymer **PEO**. By controlling the self-assembly process, structures, and resulting properties of these **PBI-A**/polymer blends, we hope to reduce the need to design new gelators. We can print the **PBI-A**/polymer hydrogels to create continuous printed lines, which has not previously been reported for similar pH-triggered hydrogels. We show that the properties of the printed gels are highly influenced by the extrusion process, which presents another method to tailor these materials to suit the chosen application. Upon drying, these hydrogels form aligned and flexible materials, which are reversibly mechanoresponsive with a photoresponse functional to the radius of the film's curvature. Such responses could be suitable for wearable sensors and electronics.

We also emphasise the importance of proper characterisation during all stages of the printing process across multiple length scales to understand the impact of the printing process on these materials. We demonstrate that rheological recovery tests, the most used technique to suggest a material's printability, are not always sufficient when put into practice. Therefore, we hope the work presented here may act as an aid in the characterisation of new materials made using 3D printing.

4.4 Experimental

PBI-A was synthesised as discussed in Section 2.4.1. All commercial reagents were used as received. Distilled water was used throughout. PEO (average M_n = 500,000) was purchased from Sigma-Aldrich. NaOD was purchased from Sigma-Aldrich as a 40 wt% solution in D_2O and diluted with D_2O to provide a 0.1 M solution.

4.4.1 Experimental Procedures

4.4.1.1 Preparation of PBI-A/PEO Blends

Solutions of **PBI-A** and **PEO** were made separately in deionised water at concentrations of 6.66 mg/mL, 10 mg/mL, and 20 mg/mL. For **PBI-A** solutions, an equimolar equivalent of sodium hydroxide (0.1 M, aqueous) was added. The solutions were agitated on a MX-T6-S tube roller (SCILOGEX) overnight until all the gelator had dissolved. The **PBI-A** solution was then adjusted to pH 9 using NaOH (1 M, aqueous). For 25:75 (v/v) blends, 2.5 mL of **PBI-A** (20 mg/mL) and 7.5 mL of **PEO** (6.66 mg/mL) were combined. For 50:50 (v/v) blends, 5 mL of **PBI-A** (10 mg/mL) and 5 mL of **PEO** (10 mg/mL) were added. For 75:25 (v/v) blends, 7.5 mL of **PBI-A** (6.66 mg/mL) and 2.5 mL of **PEO** (20 mg/mL) were added. The blends were left to mix overnight.

4.4.1.2 pH Measurements

An FC200 pH probe from HANNA instruments with a 6 mm x 10 mm conical tip was used for pH measurements at 25°C. The stated accuracy of the pH measurement is $\pm$ 0.1.

4.4.1.3 Preparation of PBI-A/PEO Hydrogels

A pH-switch method was used to form the hydrogels. Solutions and blends were prepared as above. For non-printed hydrogels, 2 mL of solution was transferred to a 7 mL Sterilin vial containing a pre-weighed amount of glucono-δ-lactone (GdL) and gently shaken three times. The sample was left to stand overnight to allow gelation to occur. For printed hydrogels, 2 mL of solution was transferred to a 7 mL Sterilin vial containing a pre-weighed amount of GdL and gently shaken three times. The mixture was quickly transferred to a 3.5 mL syringe, and the syringe nozzle was tightly wrapped in parafilm to prevent the gel from drying out. Syringes were stood vertically on their plungers and left overnight to gel (Fig. 4.19).

Figure 4.19. Photograph of **Gel-1** formed inside a 3.5 mL syringe. Scale bar represents 2 cm.

4.4.1.4 3D Printing

Gels were prepared in 3.5 mL syringes as described above. A 3D printer (RepRap Ormerod 1, Fig. 4.20) was modified and repurposed for gel printing by Dr Bart Dietrich (University of Glasgow).[2] The inner diameter of the 3.5 mL syringe nozzles used for extrusion was 2.2 mm. To print a 6 cm gel line at a shear rate of 2500 s^{-1} and a rate of extrusion of 166 µL/cm, the speed of the printer head was 9408 mm/min, raised 3 mm above the printing bed.

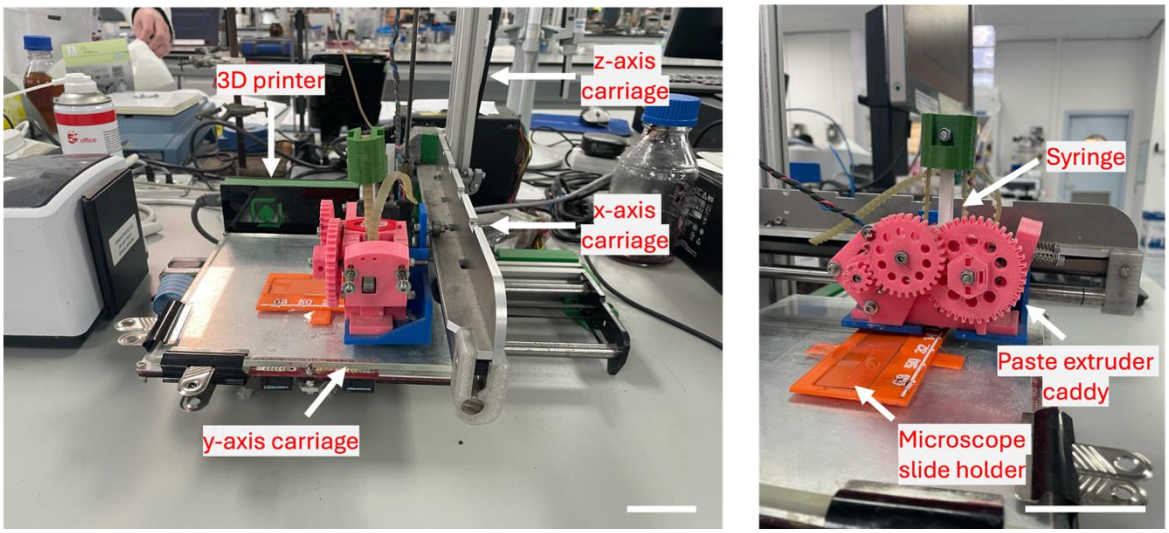

Figure 4.20. 3D printing experimental set-up. Scale bars represent 6 cm.

4.4.1.5 Rheology

Dynamic rheological measurements were performed with an Anton Paar Physica MCR301 rheometer. A cup-and-vane measuring system was used for recovery tests and strain sweeps, and a parallel plate measuring system for compression sweeps and time sweeps. Gels were prepared as described above. Printed gels were printed directly into Sterilin vials (Fig. 4.21). The temperature was maintained at 25°C during all measurements using a water bath. All measurements were recorded in triplicate.

Figure 4.21. Photograph of **Printed Gel-1** in a Sterilin vial. Scale bar represents 2 cm.

Recovery Tests

For recovery tests, a constant frequency of 10 rad/s and strain of 0.5% were first applied for 200 seconds, followed by a strain of 300% for 60 seconds to destroy the gel. Restoration of G′ and G″ were monitored in the subsequent time sweep (with a frequency of 10 rad/s and a strain of 0.5%) for 200 seconds. The shear-recovery cycles were performed 5 times. The percentage recovery was calculated by dividing the average G′ after each restoration by the original G′.

Recovery After Extrusion

A parallel plate geometry (diameter of plate = 12.5 mm) was used for the constant shear and recovery measurements. As the parallel plate is not compatible with the cup measuring system, a 3D printed holder was used to secure the Sterilin vial in place (Fig. 4.22). To mimic printing through a syringe, a constant shear of 2500 s^{-1} was applied to the sample for 1

second. After this time, G′ and G″ were measured at an angular frequency of 10 rad/s and with a strain of 0.5% for 30 minutes.

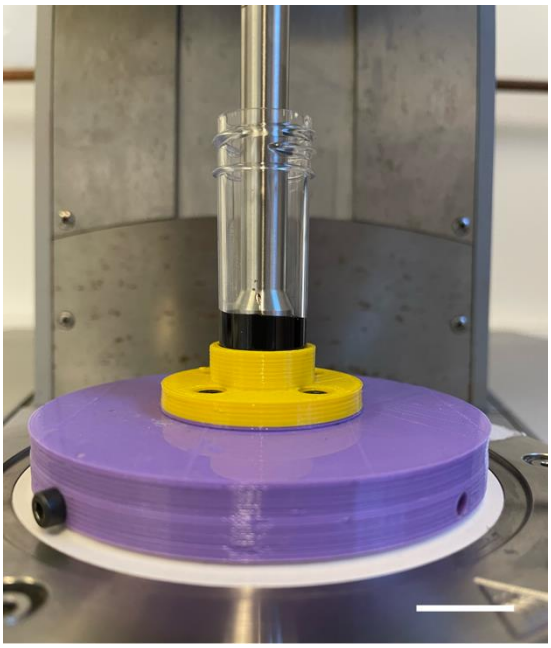

Figure 4.22. 3D printed Sterilin vial holder used for parallel plate geometry. Scale bar represents 2 cm.

Strain Sweeps

Strain sweeps were performed over a range of 0.1% to 1000% with a frequency of 10 rad/s. The critical strain (yield point) was quoted where G′ departed from linearity and ultimately crossed over G″ (flow point), causing the gel to break down.

Frequency Sweeps

Frequency sweeps were performed from 1 rad/s to 100 rad/s under a strain of 0.1%. G′ and G″ were quoted at 10 rad/s. The measurements were performed within the viscoelastic region where G′ and G″ were independent of strain amplitude.

Compression Sweeps

Compression sweeps were performed at a constant strain of 0.5% and a constant frequency of 10 rad/s. The gap distance was decreased from a position of 1.8 mm at a constant rate of 5 μm/s for 5 minutes. After this time, the parallel plate was raised back to a gap distance of 1.8 mm and a strain or frequency sweep measurements were performed.

Time Sweeps Under Compression

Time sweeps were performed with a 50 mm sandblasted plate and a plate gap of 0.8 mm. Tests were performed at an angular frequency of 10 rad/s and with a strain of 0.5%. The normal force was set at either 0, 0.1, 0.15, 0.2, or 0.5 N. Mineral oil was carefully added around the circumference of the top plate to prevent the sample from drying out.

4.4.1.6 SANS

SANS measurements were performed using the SANS2D instrument (ISIS, Rutherford Appleton Laboratory, Didcot, UK) under experiment number RB2310032. Measurements were performed using a wavelength band of 0.9 to 13 Å to access a Q range of 0.004 to 0.7 $Å^{-1}$. Solutions and gels were measured in 2 mm path length UV spectrophotometer quartz cuvettes (Hellma). These were placed in a temperature-controlled sample rack during the measurements. Measurements were run at 25°C. Solutions were prepared as described above, but in D_2O and NaOD (0.1 M). For non-printed gels, the pre-gel solutions were added to Sterilin vials with the appropriate amount of GdL, shaken three times, and quickly transferred to the cuvettes before leaving to gel overnight. For printed gels, gels were prepared in 3.5 mL syringes and left to gel overnight, with syringes stood vertically on their plungers. These gels were then transferred into the cuvette before being placed on the rack.

The data were reduced to 1D scattering curves of intensity vs. Q using the facility-provided software. The electronic background was subtracted, the full detector images for all data were normalised, and the scattering from the empty cell was subtracted. The scattering from D_2O was also measured and subtracted from the data using the Mantid software package installed inside the ISIS virtual machines, IDAaaS.[67] The instrument-independent data were then fitted to the models discussed in the text using the SasView software package (version 5.0.4).[68] The scattering length density (SLD) of each material was calculated using the National Institute of Standards and Technology's neutron activation and scattering calculator.[69] The SLD of D_2O was calculated to be 6.393×10^{-6} $Å^{-2}$, the SLD of **PBI-A** was calculated to be 3.445×10^{-6} $Å^{-2}$, and the SLD of **PEO** was calculated to be 1.122×10^{-6} $Å^{-2}$. The SLD of the **PBI-A/PEO** blend was calculated to be 1.70275×10^{-6} $Å^{-2}$. All data fit best to a cylindrical model combined with a power law. The best fit was determined as the one which overlapped well with the data and had the lowest χ^2 value. Errors were calculated by the SASView fitting software as a function of the error bars of the experimental data and the chosen model.

4.4.1.7 Cavitation Rheology

Cavitation experiments were performed using a custom-built cavitation rheometer (Dr Bart Dietrich, University of Glasgow). The setup involves a syringe pump (World Precision Instruments Aladdin, AL-1000), a 50 mL syringe (BD Plastipak™), a needle of inner diameter 0.41 mm (Fisher Scientific, Hamilton™ Kel-F Hub Blunt Point Needle with Luer-lock attachment), the custom-made Cavitation Rheology Analyser Box (CRAB), a conductivity probe circuit for accurate homing of the 3D printer platform z-axis, a modified 3D printer platform for needle positioning, and a computer with "PuTTY" software to control the 3D printer platform and record pressure data from the CRAB.[58,70] All these components were connected using plastic tubing and plastic adapters to allow air to be pushed through the system and create pressure (Fig. 4.23). CRAB pressure readings were calibrated using a commercial manometer before measurements were recorded. Hydrogels were printed on glass microscope slides (Thermo Scientific). For printed gels, measurements were taken 0.5, 1.0, and 1.5 cm along the length of the printed gel lines. The needle was homed to the surface of the slide, raised above the sample, and then lowered into the sample to a height of 0.5 mm above the slide surface to ensure constant sample depth between the slide and needle. This eliminated any issues due to inhomogeneities in the gel surface. The syringe pump was then turned on, with a pump rate of 0.4 mL/min. The experiment was finished after a drop in pressure was recorded. All measurements were carried out in triplicate.

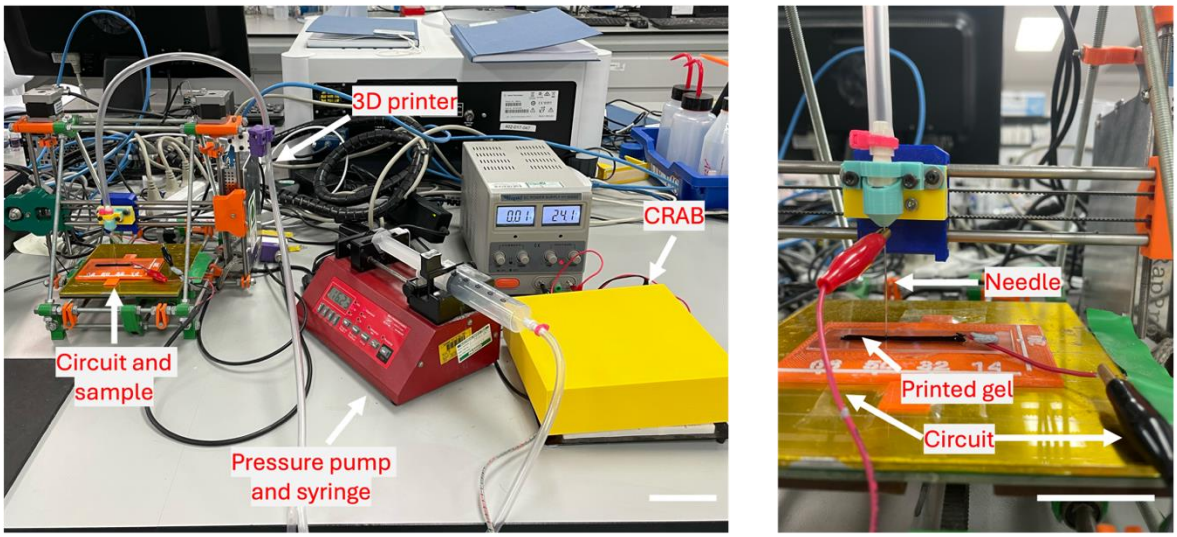

Figure 4.23. Cavitation rheology experimental set-up. Scale bars represent 6 cm.

4.4.1.8 FTO Windows

FTO-coated glass (50 x 50 x 2.2 mm, TEC 7, surface resistivity ~7 Ω/sq, Sigma Aldrich) was cleaned by submerging in detergent and deionised water, acetone, and isopropanol, respectively, with ultrasonication for 15 minutes in each solvent. Gloves were used throughout to prevent fingerprints on the glass. Gels were prepared as described above but using a 0.1 M NaCl background electrolyte (10% 0.1 M NaCl, aq). Gels were formed or printed in an O-ring with a diameter of 30 mm between two pieces of FTO-coated glass facing inwards and held in place with bulldog clips. Copper tape was placed on opposite ends of the top and bottom pieces of glass as working and counter electrodes (Fig. 4.24).

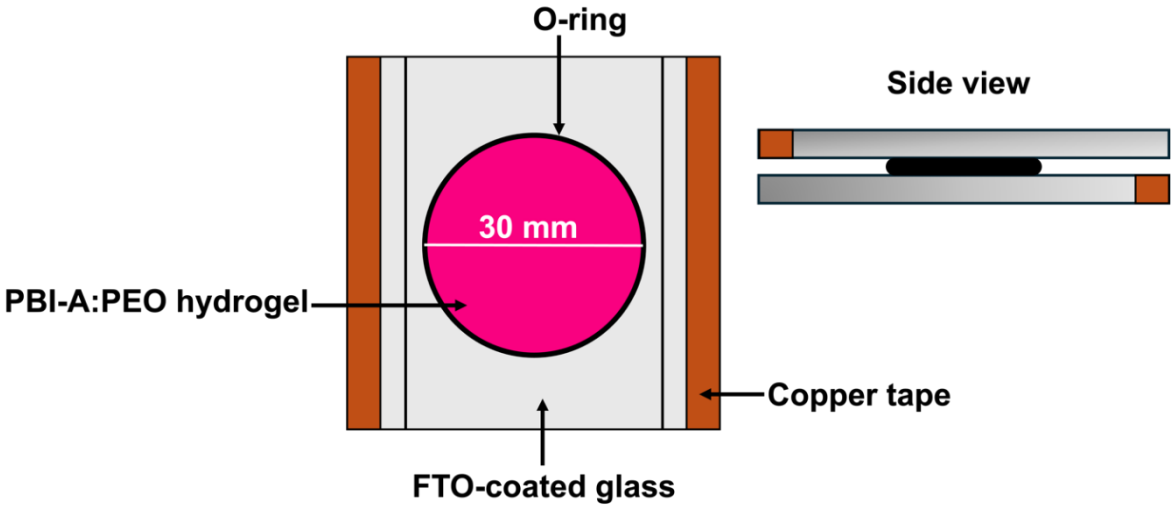

Figure 4.24. Cartoon of the FTO glass set-up described above.

4.4.1.9 Cyclic Voltammetry

Cyclic voltammetry measurements were performed with a Palmsens4 potentiostat. Samples were prepared in the FTO-coated glass assembly as described above. All data were collected using a two-electrode set-up. Therefore, values cannot be stated in reference to a known value. Thus, CVs were carried out using a solution of 10 mg/mL hydroquinone dissolved in water with 10% 0.1 M NaCl in the same set-up (Fig. 2.25). Such data is tabulated in Table A.3.9, Appendix. For **Gel-1** and **Printed Gel-1**, the potential was scanned from +1.0 V to -1.5 V at a scan rate of 0.05 V/s, and measurements were carried out in triplicate. The clearest of the three scans was used for analysis.

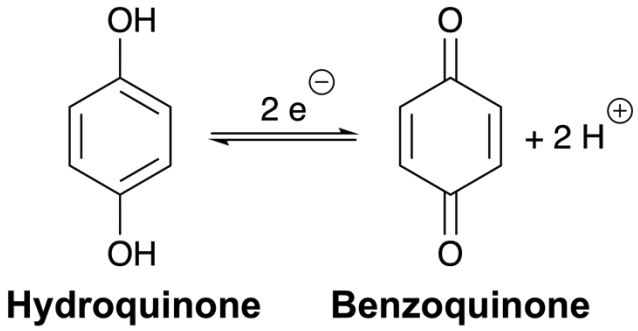

Figure 4.25. The redox reaction of hydroquinone/benzoquinone used as a control.

4.4.1.10 Xerogel Formation

For printed xerogels, a 6 cm gel line was printed as described above onto a glass microscope slide (Thermo Scientific) and left to dry in air overnight (average lab temperature 23.4°C and average lab humidity 31%). For non-printed xerogels, 2 mL of the **PBI-A/PEO** blend was transferred to a 7 mL Sterilin vial containing a pre-weighed amount of GdL and gently shaken three times. 10 μL of the solution was drop cast inside a 3 x 3 mm mask and left to air dry overnight.

4.4.1.11 Optical Microscopy

Cross-polarised light optical images were collected using a Nikon Eclipse LV100 microscope with a Nikon Plan ELWD 50x/0.60 or x10 lens attached to an Infinity2-1C camera. No post-processing was applied to the images.

4.4.1.12 Profilometry

Printed xerogels were prepared as described above. The film thickness was estimated using an Alpha-Step® D-500 Stylus Profiler (KLA Instruments). Measurements were taken 0.5, 1.0, and 1.5 cm along the length of the printed xerogel lines, along the direction of printing.

4.4.1.13 Nanoindentation

Xerogels were prepared as described above. Nanoindentation measurements were carried out on a Step 700 Surface Testing Platform (UNHT^3, Anton Paar) using a Berkovich indenter tip. Linear loading was applied, with a maximum load of 1000 μN, a loading and unloading rate of 2000 μN/min, and a pause of 60 seconds. The constant force was set at 150 μN, with an approach distance of 7500 nm and an approach and retract speed of 5000 and 2 nm/min, respectively. Prior to each measurement, an adjust depth offset measurement was taken to correctly set up the depth sensor measurement range to eliminate any issues due to film

surface inhomogeneities. Measurements were taken 0.5, 1.0, and 1.5 cm along the length of the xerogel, along the direction of printing. Each measurement was performed in triplicate, using a simple matrix where three points in the film were measured with a gap of 1 mm from each other to prevent any surface deformation from the previous indent affecting the next measurement. For each new triplicate, a different area of the film was chosen to again avoid influence from the previous indentation.

4.4.1.14 Flexibility Tests

Xerogels were prepared by drop casting or printing onto A4 Universal Inkjet Transparency Film (Haber Crafts), cut into 5.5 cm x 2.5 cm rectangles, and drying in air. Two silver electrodes were made from silver paste (Agar Scientific, Acheson Silver Electrodag 1415), ensuring proper contact was made to opposite sides of the sample square. Two pieces of copper tape (RS components) were then attached to the silver electrodes to allow connection to the potentiostat.

Flexibility tests were performed by Rebecca Ginesi (University of Glasgow) and Tom Jacquin (University of Glasgow). The xerogels were tested by clamping them on a custom-made motorised moving stage (Fig. 4.26).[71] Chronoamperometric measurements were simultaneously performed using a PalmsSens4 potentiostat and a custom-made data acquisition unit, which collected both the current produced and displacement of the stage from the starting point. Before each test, the films were irradiated for 5 minutes with a 365 nm LED light (LZ1-10UV00, LED Engin), placed 1 cm away from the sample. The distance from the LED to the sample was adjusted so that an optical power probe (Thorlabs PM100D with S120VC sensor) placed at the same distance as the sample registered 20 mW of incident power. The stage was moved 4 cm away from the starting point in increments of 0.5 cm. The film was held at each position for 1 minute, and the current measured. The stage was then moved back to the initial starting point, again in 0.5 cm increments for 1 minute, and again the current was measured at each position. Tracing the film outline in digital side view photographs of the film allowed ImageJ software to calculate the bending angle.

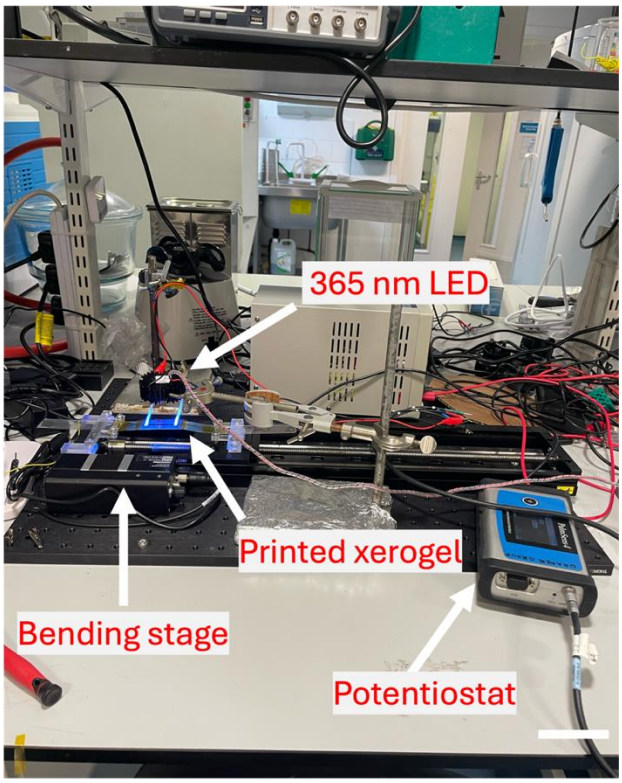

Figure 4.26. Bending experimental set-up. Scale bar represents 12 cm

4.5 References

1. M. E. Prendergast and J. A. Burdick, *Adv. Mater.*, 2020, **32**, 1902516.
2. M. C. Nolan, A. M. Fuentes Caparrós, B. Dietrich, M. Barrow, E. R. Cross, M. Bleuel, S. M. King and D. J. Adams, *Soft Matter*, 2017, **13**, 8426–8432.
3. C. Liu, N. Xu, Q. Zong, J. Yu and P. Zhang, *Colloid Interface Sci. Commun.*, 2021, **44**, 100498.
4. J. Omar, D. Ponsford, C. A. Dreiss, T. Lee and X. J. Loh, *Chem. Asian J.*, 2022, **17**, e202200081.
5. A. Chalard, M. Mauduit, S. Souleille, P. Joseph, L. Malaquin and J. Fitremann, *Addit. Manuf.*, 2020, **32**, 101162.
6. F. Puza and K. Lienkamp, *Adv. Funct. Mater.*, 2022, **32**, 2205345.
7. J. Li, R. Xing, S. Bai and X. Yan, *Soft Matter*, 2019, **15**, 1704–1715.
8. L. Shi, H. Carstensen, K. Hölzl, M. Lunzer, H. Li, J. Hilborn, A. Ovsianikov and D. A. Ossipov, *Chem. Mater.*, 2017, **29**, 5816–5823.
9. R. Suntornnond, J. An and C. K. Chua, *Macromol. Mater. Eng.*, 2017, **302**, 1600266.
10. L. Ouyang, C. B. Highley, C. B. Rodell, W. Sun and J. A. Burdick, *ACS Biomater. Sci. Eng.*, 2016, **2**, 1743–1751.
11. P. Sapuła, K. Bialik-Wąs and K. Malarz, *Pharmaceutics*, 2023, **15**, 253.
12. H. H. Susapto, D. Alhattab, S. Abdelrahman, Z. Khan, S. Alshehri, K. Kahin, R. Ge, M. Moretti, A.-H. Emwas and C. A. E. Hauser, *Nano Lett.*, 2021, **21**, 2719–2729.
13. M. J. S. Hill and D. J. Adams, *Soft Matter*, 2022, **18**, 5960–5965.
14. K. Hölzl, S. Lin, L. Tytgat, S. Van Vlierberghe, L. Gu and A. Ovsianikov, *Biofabrication*, 2016, **8**, 032002.
15. M. A. Shah, D.-G. Lee, B.-Y. Lee and S. Hur, *IEEE Access*, 2021, **9**, 140079–140102.
16. A. Negro, T. Cherbuin and M. P. Lutolf, *Sci. Rep.*, 2018, **8**, 17099.
17. A. Agrawal and C. M. Hussain, *Gels*, 2023, **9**, 960.
18. J. Li, M. Chen, X. Fan and H. Zhou, *J. Transl. Med.*, 2016, **14**, 271.
19. T. D. Ngo, A. Kashani, G. Imbalzano, K T. Q. Nguyen, D. Hui, *Composites Part B*, 2018, **143**, 172–196.
20. M. Champeau, D. A. Heinze, T. N. Viana, E. R. de Souza, A. C. Chinellato and S. Titotto, *Adv. Funct. Mater.*, 2020, **30**, 1910606.
21. A. Schwab, R. Levato, M. D'Este, S. Piluso, D. Eglin and J. Malda, *Chem. Rev.*, 2020, **120**, 11028–11055.

22. H. Herrada-Manchón, M. A. Fernández and E. Aguilar, *Gels*, 2023, **9**, 517.

23. C. H. Lee, V. Moturi and Y. Lee, *J. Control. Release*, 2009, **136**, 88–98.

24. A. M. Fuentes-Caparras, Z. Canales-Galarza, M. Barrow, B. Dietrich, J. Laüger, M. Nemeth, E. R. Draper and D. J. Adams, *Biomacromolecules*, 2021, **22**, 1625–1638.

25. E. R. Draper, J. R. Lee, M. Wallace, F. Jäckel, A. J. Cowan and D. J. Adams, *Chem. Sci.*, 2016, **7**, 6499–6505.

26. C. R. Harding, J. Cann, A. Laventure, M. Sadeghianlemraski, M. Abd-Ellah, K. R. Rao, B. S. Gelfand, H. Aziz, L. Kaake, C. Risko and G. C. Welch, *Mater. Horiz.*, 2020, **7**, 2959–2969.

27. M. Sadeghianlemraski, C. R. Harding, G. C. Welch and H. Aziz, *ACS Appl. Energy Mater.*, 2020, **3**, 11655–11665.

28. E. R. Draper, M. Wallace, D. Honecker and D. J. Adams, *Chem. Comm.*, 2018, **54**, 10977–10980.

29. X. Guo, H. Li, Y. Han, Y. Yang, Q. Luo, C.-Q. Ma and J. Yang, *Org. Electron.*, 2020, **82**, 105725.

30. V. Adams, J. Cameron, M. Wallace and E. R. Draper, *Chem. Eur. J.*, 2020, **26**, 9879–9882.

31. M. Stoppa and A. Chiolerio, *Sensors*, 2014, **14**, 11957–11992.

32. J. Singh, in *Smart Electronic Materials*, Cambridge University Press, Cambridge, 2005.

33. A. Kalkal, S. Kumar, P. Kumar, R. Pradhan, M. Willander, G. Packirisamy, S. Kumar and B. D. Malhotra, *Addit. Manuf.*, 2021, **46**, 102088.

34. A. Shamirian, H. Samareh Afsari, A. Hassan, L. W. Miller and P. T. Snee, *ACS Sens.*, 2016, **1**, 1244–1250.

35. F. Andriamiseza, D. Bordignon, B. Payré, L. Vaysse and J. Fitremann, *J. Colloid Interface Sci.*, 2022, **617**, 156–170.

36. E. R. Draper, B. J. Greeves, M. Barrow, R. Schweins, M. A. Zwijnenburg and D. J. Adams, *Chem*, 2017, **2**, 716–731.

37. G. Pont, L. Chen, D. G. Spiller and D. J. Adams, *Soft Matter*, 2012, **8**, 7797–7802.

38. K. Hanabusa, A. Itoh, M. Kimura and H. Shirai, *Chem. Lett.*, 1999, **28**, 767–768.

39. Y. J. Adhia, T. H. Schloemer, M. T. Perez and A. J. McNeil, *Soft Matter*, 2012, **8**, 430–434.

40. B. Adhikari and A. Banerjee, *Soft Matter*, 2011, **7**, 9259–9266.

41. M. Supur, A. Yurtsever and Ü. Akbey, *RSC Adv.*, 2015, **5**, 64240–64246.

42. E. R. Draper, L. J. Archibald, M. C. Nolan, R. Schweins, M. A. Zwijnenburg, S. Sproules and D. J. Adams, *Chem. Eur. J.*, 2018, **24**, 4006–4010.

43. M. Bercea, *Molecules*, 2023, **28**, 2766.

44. H. Lopez Hernandez, J. W. Souza and E. A. Appel, *Macromol. Biosci.*, 2021, **21**, 2000295.

45. S. Kyle, Z. M. Jessop, A. Al-Sabah and I. S. Whitaker, *Adv. Healthc. Mater.*, 2017, **6**, 1700264.

46. G. Ghosh and G. Fernández, *Beilstein J. Org. Chem.*, 2020, **16**, 2017–2025.

47. X. Lu, X. Li, K. Guo, T.-Z. Xie, C. N. Moorefield, C. Wesdemiotis and G. R. Newkome, *J. Am. Chem. Soc.*, 2014, **136**, 18149–18155.

48. D. J. Adams, L. M. Mullen, M. Berta, L. Chen and W. J. Frith, *Soft Matter*, 2010, **6**, 1971–1980.

49. R. Akhtar, E. R. Draper, D. J. Adams and J. Hay, *J. Mater. Res.*, 2018, **33**, 873–883.

50. E. V. Alakpa, V. Jayawarna, A. Lampel, K. V. Burgess, C. C. West, S. C. J. Bakker, S. Roy, N. Javid, S. Fleming, D. A. Lamprou, J. Yang, A. Miller, A. J. Urquhart, P. W. J. M. Frederix, N. T. Hunt, B. Péault, R. V. Ulijn and M. J. Dalby, *Chem*, 2016, **1**, 298–319.

51. M. G. T. A. Rutten, L. Rijns and P. Y. W. Dankers, *J. Polym. Sci.*, 2024, **62**, 155–164.

52. R. Ferraro, S. Guido, S. Caserta and M. Tassieri, *Soft Matter*, 2023, **19**, 2053–2057.

53. M. J. S. Hill and D. J. Adams, *Soft Matter*, 2022, **18**, 5960–5965.

54. Y. Li, C. Zhu, Y. Dong and D. Liu, *Polymer*, 2020, **210**, 122993.

55. T. A. Welsh, J. G. Egan, B. Dietrich, N. Rafferty, R. E. Ginesi, J. Doutch, R. Schweins and E. R. Draper, *J. Phys. Mater.*, 2024, **7**, 015004.

56. C. Patterson, B. Dietrich, C. Wilson, A. R. Mount and D. J. Adams, *Soft Matter*, 2022, **18**, 1064–1070.

57. M. J. S. Hill, A. M. Fuentes-Caparrós and D. J. Adams, *Biomacromolecules*, 2023, **24**, 4253–4262.

58. A. M. Fuentes-Caparrós, B. Dietrich, L. Thomson, C. Chauveau and D. J. Adams, *Soft Matter*, 2019, **15**, 6340–6347.

59. J. A. Zimberlin, J. J. McManus and A. J. Crosby, *Soft Matter*, 2010, **6**, 3632–3635.

60. J. A. Zimberlin, N. Sanabria-DeLong, G. N. Tew and A. J. Crosby, *Soft Matter*, 2007, **3**, 763–767 .

61. A. M. Castilla, E. R. Draper, M. C. Nolan, C. Brasnett, A. Seddon, L. L. E. Mears, N. Cowieson and D. J. Adams, *Sci. Rep.*, 2017, **7**, 8380.

62. M. Janani, P. Srikrishnarka, S. V. Nair and A. S. Nair, *J. Mater. Chem. A Mater.*, 2015, **3**, 17914–17938.

63. L. Mei and G. Guan, *Nano TransMed*, 2023, **2**, e9130017.

64. M. Gunda, P. Kumar and M. Katiyar, *Crit. Rev. Solid State Mater. Sci.*, 2017, **42**, 129–152.

65. P. J. Withers and H. K. D. H. Bhadeshia, *Mater. Sci. Technol.*, 2001, **17**, 355–365.

66. P. Im, D.-G. Kang, D.-Y. Kim, Y.-J. Choi, W.-J. Yoon, M.-H. Lee, I.-H. Lee, C.-R. Lee and K.-U. Jeong, *ACS Appl. Mater. Interfaces*, 2016, **8**, 762–771.

67. O. Arnold, J. C. Bilheux, J. M. Borreguero, A. Buts, S. I. Campbell, L. Chapon, M. Doucet, N. Draper, R. F. Leal, M. A. Gigg, V. E. Lynch, A. Markvardsen, D. J. Mikkelson, R. L. Mikkelson, R. Miller, K. Palmen, P. Parker, G. Passos, T. G. Perring, P. F. Peterson, S. Ren, M. A. Reuter, A. T. Savici, J. W. Taylor, R. J. Taylor, R. Tolchenov, W. Zhou and J. Zikovsky, *Nucl. Instrum. Methods Phys. Res.*, 2014, **764**, 156–166.

68. https://www.sasview.org/.

69. https://www.ncnr.nist.gov/resources/activation/.

70. L. Thomson, R. Schweins, E. R. Draper and D. J. Adams, *Macromol. Rapid Commun.*, 2020, **41**, 2000093.

71. M. Nankali, N. M. Nouri, M. Navidbakhsh, N. Geran Malek, M. A. Amindehghan, A. Montazeri Shahtoori, M. Karimi and M. Amjadi, *J. Mater. Chem. C Mater.*, 2020, **8**, 6185–6195.

Chapter 5: Conclusions and Future Work

Conclusions and Future Work

Supramolecular hydrogels show great promise in several potential applications owing to their ease of synthesis and tuneable properties. However, there are still significant gaps in our understanding of these systems. Currently, the link between the chemical structure of LMWGs, the structures present in the solution and gel phases, and how these relate to the final hydrogel properties is poorly understood. Research in this area focuses on creating hydrogels with different properties by changing the gelation trigger or synthesising new molecules. Furthermore, processing when forming these gels is an often overlooked issue. In this thesis, we have examined the link between LMWG pre-gel structures and the overall bulk properties across multiple length scales in both the solution and gel phases. Understanding this connection will allow for a more systematic approach to acquiring materials with desired properties, which is currently lacking in this field.

Throughout this thesis, we have focussed on changing the pre-gel precursor solution using different pre-processing methods. However, we stress that differences in gel properties are likely due to changes in the kinetics during the gelation process. How the kinetics are changed depends on the pre-processing conditions. Using pH and heat-cool cycles changes the solubility of the gelator, and thus, the kinetics. In comparison, non-interacting polymer additives only interfere with the kinetics due to potential steric effects. We have probed the behaviour of these systems at multiple length scales, from their molecular level-interactions, the self-assembled structures within the gel network, and the bulk material properties of the systems. Additionally, we have investigated the systems throughout the gelation process, spanning their behaviour before gelation, during self-assembly, and into the gel phase.

In Chapter 2, we report the significance of the sample history in solution. By adjusting the pH at which gelation begins and manipulating the pre-assembled structures in solution, we can produce three distinct gels with vastly different mechanical properties. These variations in gel characteristics have profound implications for their suitability in specific applications. Small-angle neutron scattering, UV-vis absorption spectroscopy, and rheology showed that the starting pH significantly impacts the nanostructures' morphology, which is translated into the gel phase. Such differences in aggregation directly influence the gelation kinetics. Furthermore, we show that transitioning between different solution-phase aggregated states from pH 9 to pH 6 is not possible if these self-assembled structures are already pre-formed, further enabling the formation of gels with distinct properties. We demonstrate a method for

changing the gel properties without using triggers that could be damaging to cells. As such, future work would involve determining the suitability of these materials for applications such as cell culturing and tissue engineering.

Heating is commonly used to increase the solubility of materials in a solution or during coating techniques, such as doctor blading, to remove solvents when preparing films for devices. However, the impact of these heating processes on the final properties of the material is rarely discussed or even examined. In Chapter 3, we demonstrate how heat-cool cycles can regulate the self-assembly of three amino acid-appended PBIs. By adjusting the temperatures to which the solutions are heated, we illustrate the preparation of hydrogels and thin films with different properties. We can access multiple pre-assembled structures in solution simply by changing the heating temperature, which changes the solubility and impacts the properties of the resulting thin films made from these heat-cooled solutions. All samples showed that a temperature change of as little as 5°C was enough to change the electronic properties of the films. This work could explain variability in devices prepared from organics, as they are so sensitive to small changes in temperature before being cast. The difficulties that arise from this change in aggregation upon a heat-cool cycle is that the properties observed in the solution phase do not necessarily correspond to the properties of the solid state, making it difficult to predict which temperature to choose when preparing materials for the given application. As such, further work should use theoretical studies and computational predictions to address the changes in packing with temperature and correlate these to the observed bulk properties.

Finally, in Chapter 4, we successfully show that we can 3D print perylene bisimide hydrogels through the incorporation of the non-gelling polymer poly(ethylene) oxide. One of the main issues with 3D printing is the difficulty in characterising these gels after printing. Therefore, we developed a series of rheological methods to characterise these materials before, during, and after printing. We illustrate that while rheological recovery tests are commonly relied upon to gauge a material's printability, they may not always provide comprehensive and accurate insights for practical applications. Hence, we aim for this research to serve as a valuable tool in characterising novel materials fabricated *via* 3D printing. Additionally, we show that the properties of the printed gels are significantly affected by the extrusion process, presenting another method to tailor these materials to suit the chosen application. Upon drying, aligned and flexible xerogels are formed, exhibiting reversible

mechanoresponsiveness with the photoresponse being a function of the bending angle. We hope that through the work undertaken in this chapter, we have provided advances to the field of 3D printing of LMWGs, as well as showing the versatility of this fabrication technique.

The challenges that arise from adjusting the process of assembly is that it can be difficult to know where to begin, as there are no guiding principles for which method will give the desired properties in the end material. How a material is impacted by the different pre-processing methods discussed throughout this thesis is dependent on each system. As we have shown, many factors must be considered and controlled when preparing materials for a given application. However, such control is not always applied in academic labs. Therefore, future work should also focus on studies into why gelation has occurred to help better understand the relationship between the pre-gel and final gel states. A deeper understanding of this complex process will allow us to further improve prediction models to correlate the micellar structures to the bulk gel properties. Such understanding will result in significant advances in areas such as organic electronics and regenerative medicine.

In conclusion, we have examined the link between LMWG pre-gel structures and overall bulk properties over multiple length scales in both the solution and gel phase. Overall, the work in this thesis provides new opportunities to increase the number of applications these materials are suitable for without the need to design new gelators.

Chapter 6: Appendix

A.1 Chapter 2 Appendix

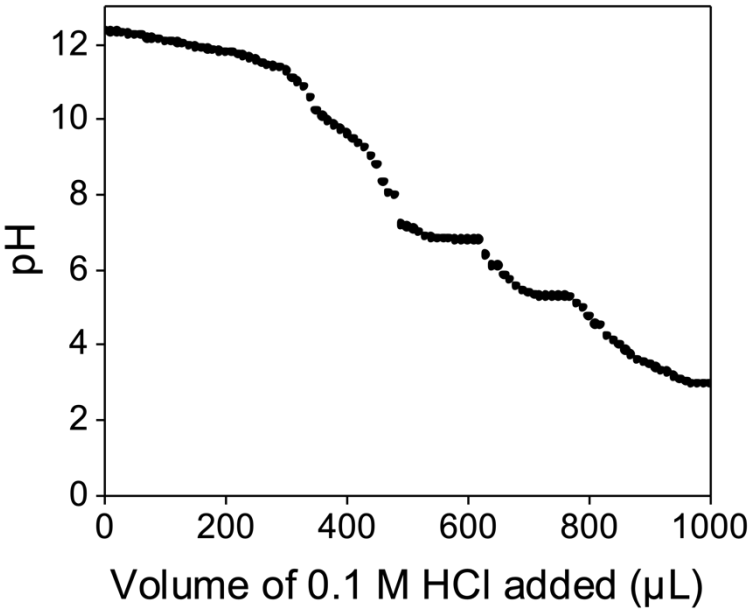

Figure A.1.1. "Apparent" pK_a curve for **PBI-A** upon the addition of 0.1 M HCl (aq).

Table A.1.1. Concentrations of glucono-δ-lactone required to form hydrogels from **PBI-A** solutions with different equivalents of 0.1 M NaOH (aq) with a final pH of approximately 3.2. pH data shown are averaged data for triplicate samples, with errors representing standard deviation.

Gel	**GdL concentration (mg/mL)**	**Average pH**
1	7.5	3.22 ± 0.010
2	10	3.27 ± 0.005
3	10	3.20 ± 0.020
4	7.5	3.19 ± 0.005

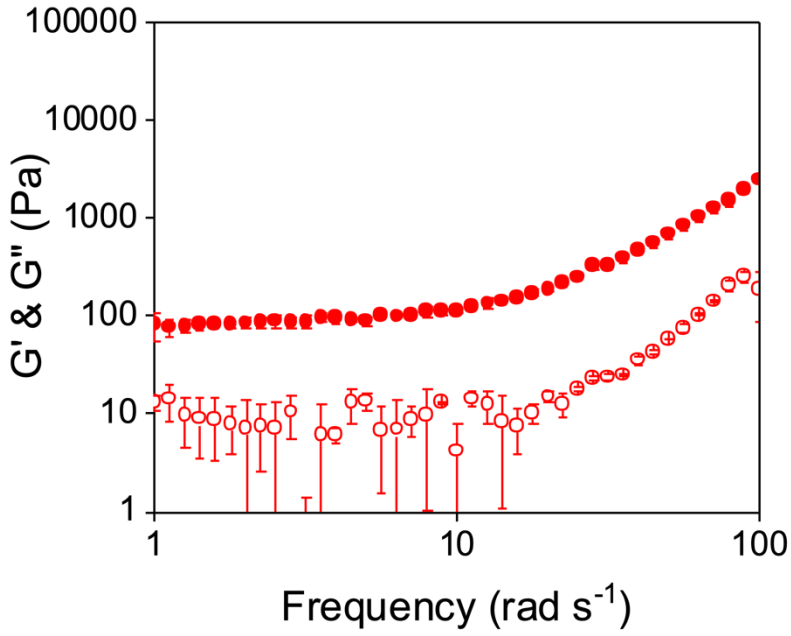

Figure A.1.2. Frequency sweep of gels formed from a solution of **PBI-A** starting at pH 6 (Gel-2). Closed circles represent G′ and open circles represent G″. Frequency sweeps were performed at 0.1% strain at 25°C. Data shown are averaged data for triplicate runs, with error bars representing standard deviation.

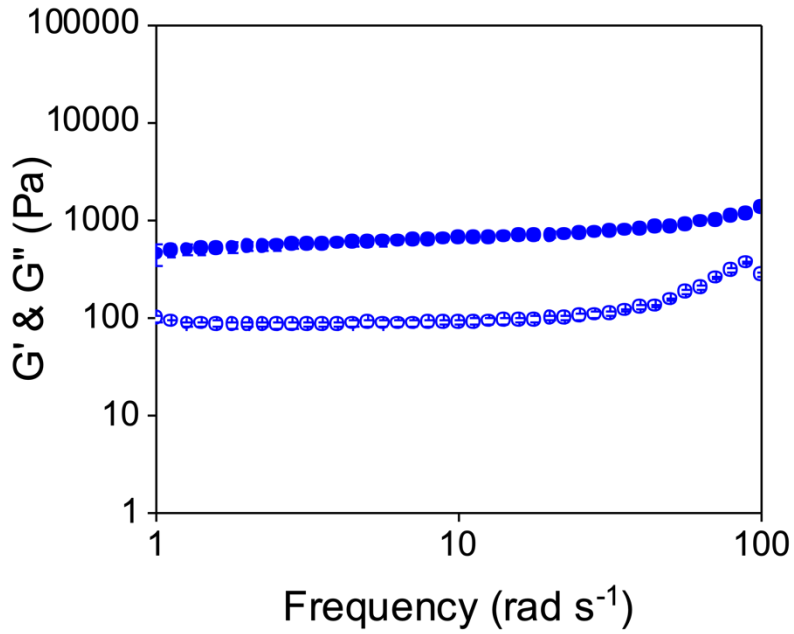

Figure A.1.3. Frequency sweep of gels formed from a solution of **PBI-A** starting at pH 9 (Gel-1). Closed circles represent G′ and open circles represent G″. Frequency sweeps were performed at 0.1% strain at 25°C. Data shown are averaged data for triplicate runs, with error bars representing standard deviation.

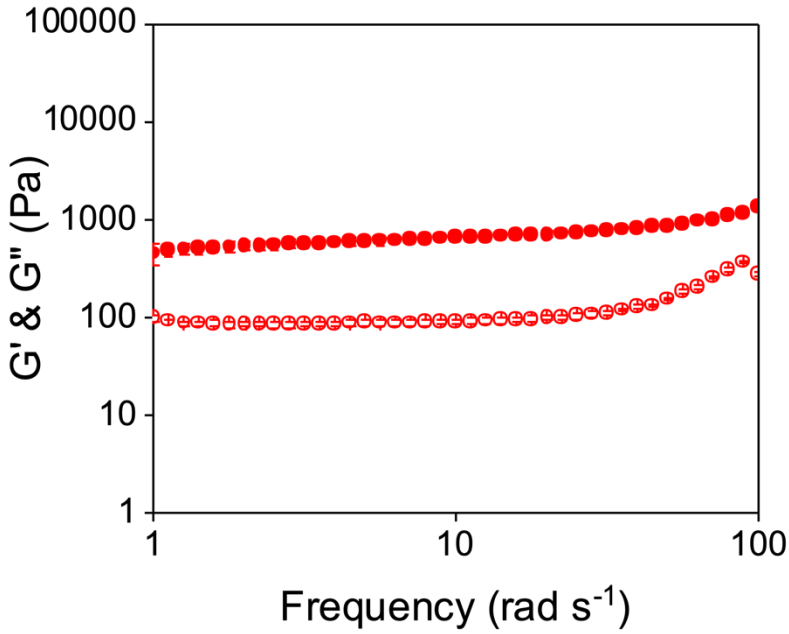

Figure A.1.4. Frequency sweep of gels formed from a solution of **PBI-A** starting at pD 6 (Gel-2). Closed circles represent G′ and open circles represent G″. Frequency sweeps were performed at 0.1% strain at 25°C. Data shown are averaged data for triplicate runs, with error bars representing standard deviation.

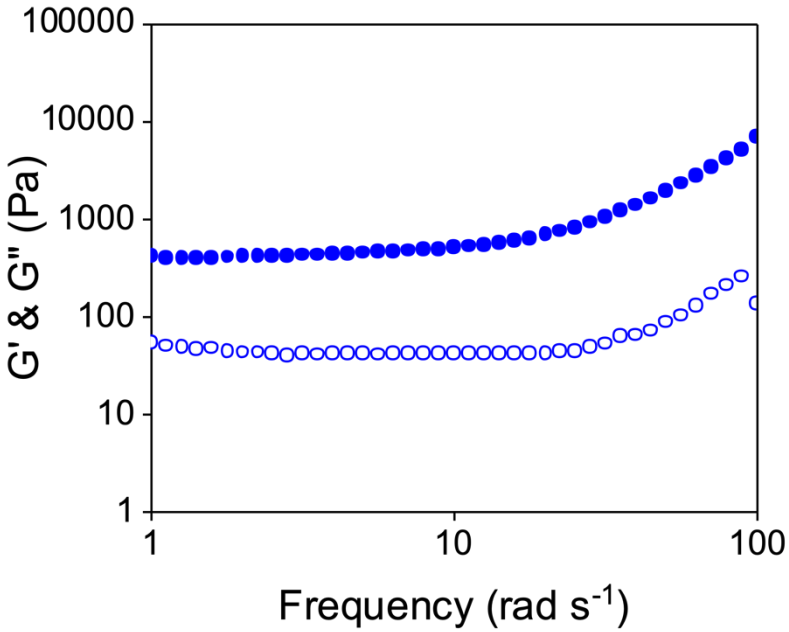

Figure A.1.5. Frequency sweep of gels formed from a solution of **PBI-A** starting at pD 9 (Gel-1). Closed circles represent G′ and open circles represent G″. Frequency sweeps were performed at 0.1% strain at 25°C. Data shown are averaged data for triplicate runs of the samples, with error bars representing standard deviation.

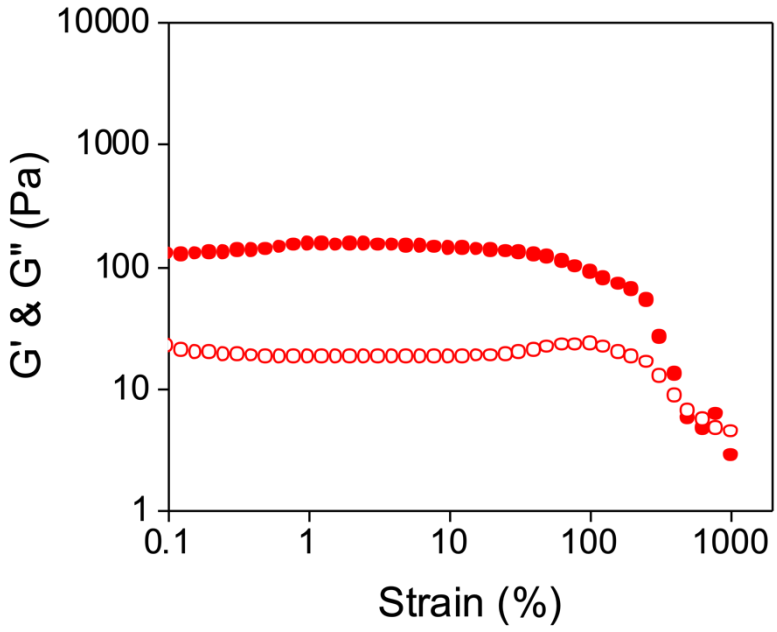

Figure A.1.6. Strain sweep of gels formed from a solution of **PBI-A** starting at pD 6 (Gel-2). Closed circles represent G′ and open circles represent G″. Strain sweeps were performed at a frequency of 10 rad/s at 25°C. Data shown are averaged data for triplicate runs of the samples, with error bars representing standard deviation.

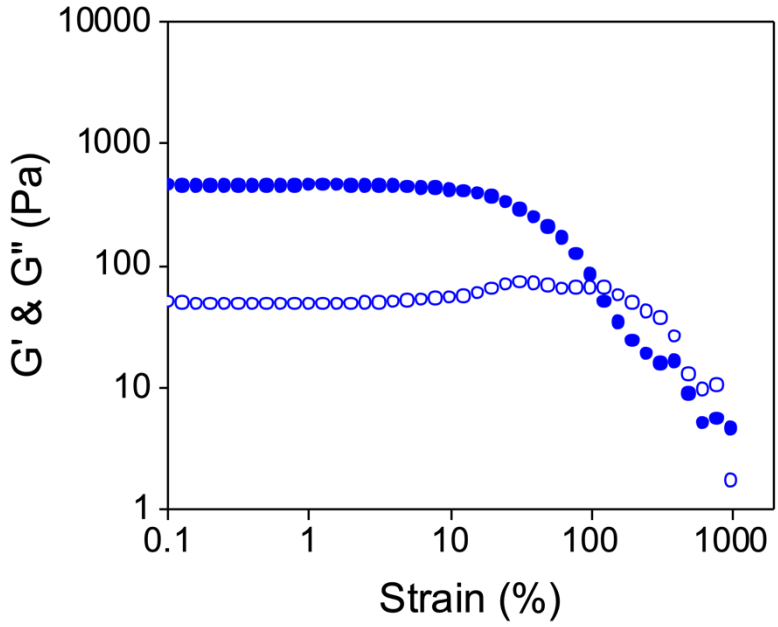

Figure A.1.7. Strain sweep of gels formed from a solution of **PBI-A** starting at pD 9 (Gel-1). Closed circles represent G′ and open circles represent G″. Strain sweeps were performed at a frequency of 10 rad/s at 25°C. Data shown are averaged data for triplicate runs of the samples, with error bars representing standard deviation.

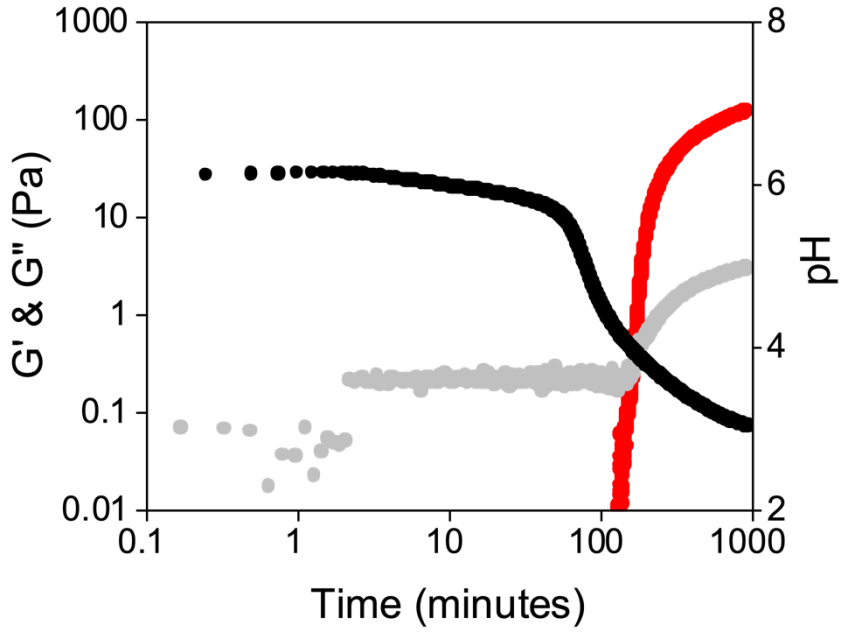

Figure A.1.8. Evolution of pH (black) and the gel networks of a solution of **PBI-A** starting at pD 6 (Gel-2). G′ is the red data and G″ is the grey data. Measurements were performed under a strain of 0.5%, a frequency of 10 rad/s and at 25°C.

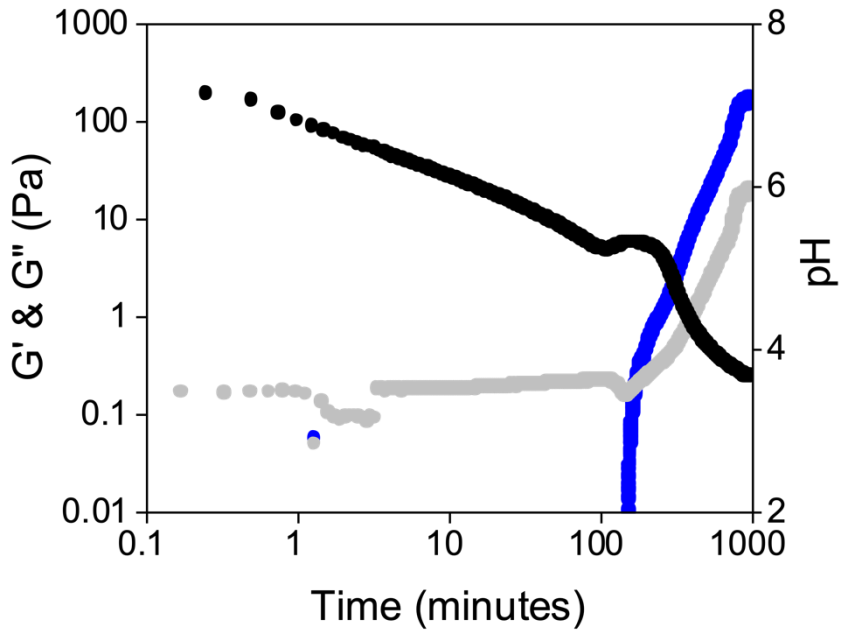

Figure A.1.9. Evolution of pH (black) and the gel networks of a solution of **PBI-A** starting at pD 9 (Gel-1). G′ is the blue data and G″ is the grey data. Measurements were performed under a strain of 0.5%, a frequency of 10 rad/s and at 25°C.

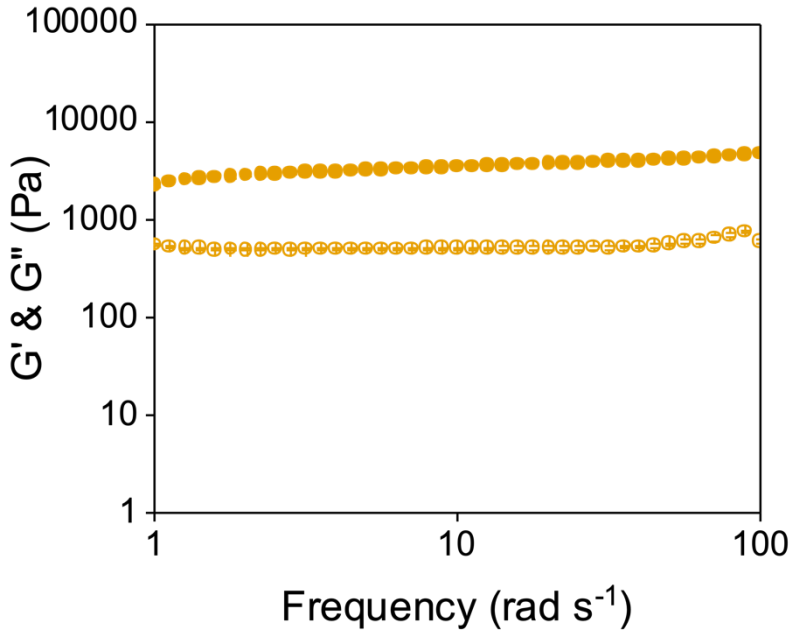

Figure A.1.10. Frequency sweep of gels formed from a solution of **PBI-A** starting at pH 6* (Gel-4). Closed circles represent G′ and open circles represent G″. Frequency sweeps were performed at 0.1% strain at 25°C. Data shown are averaged data for triplicate runs of the samples, with error bars representing standard deviation.

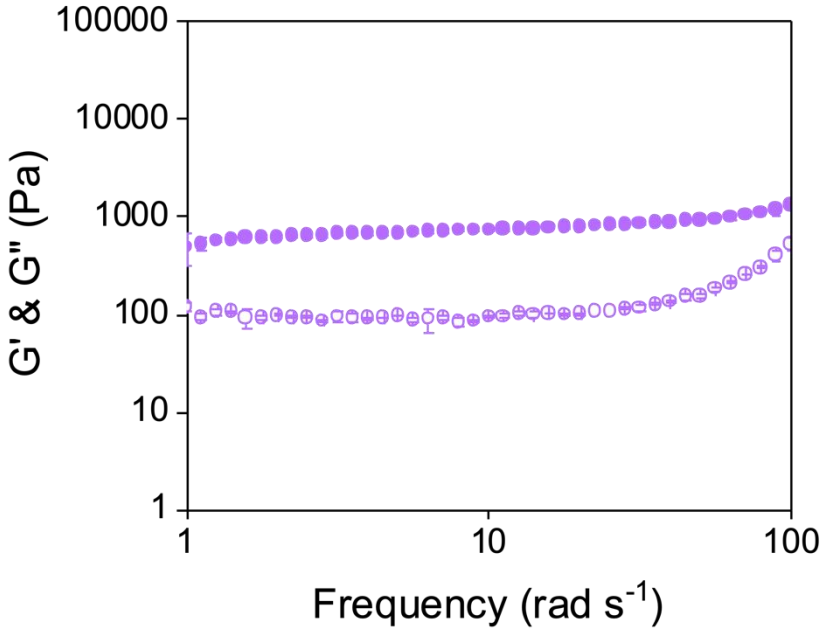

Figure A.1.11. Frequency sweep of gels formed from a solution of **PBI-A** starting at pH 9* (Gel-3). Closed circles represent G′ and open circles represent G″. Frequency sweeps were performed at 0.1% strain at 25°C. Data shown are averaged data for triplicate runs of the samples, with error bars representing standard deviation.

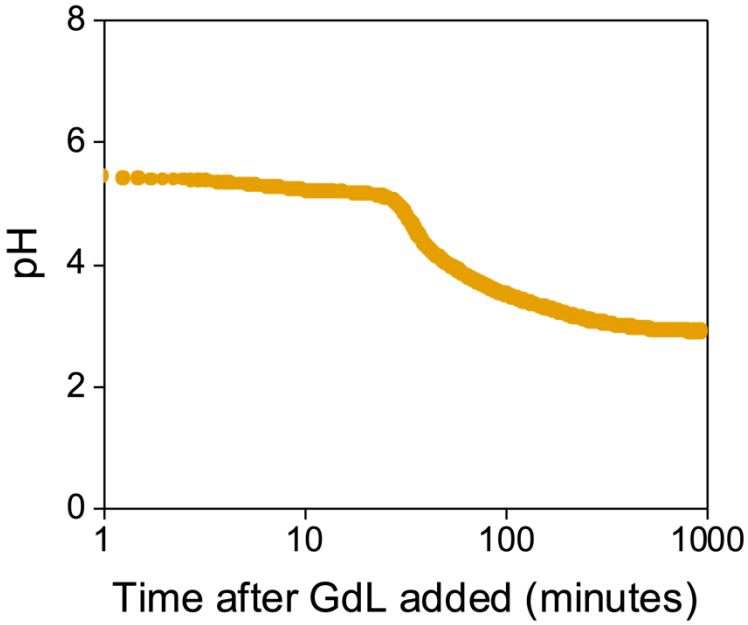

Figure A.1.12. Change in pH upon addition of GdL to a solution of **PBI-A** at pH 6*. Measurements were performed at 25°C.

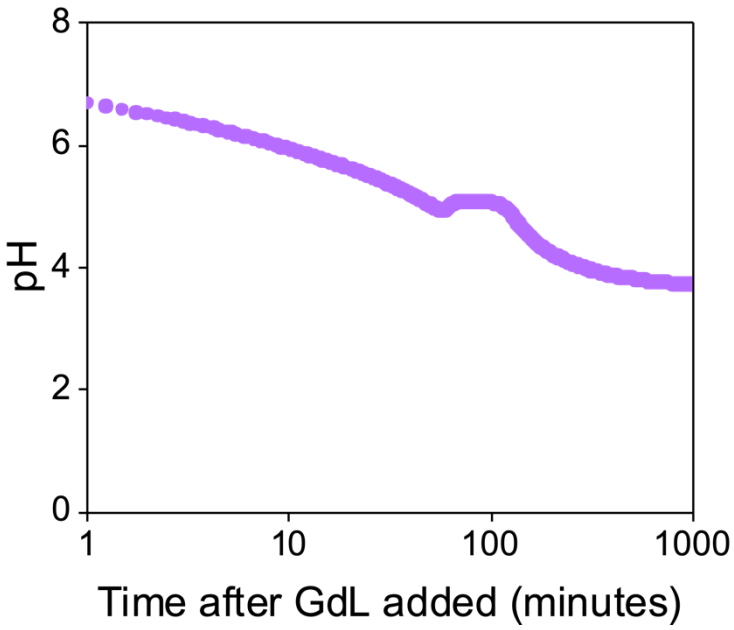

Figure A.1.13. Change in pH upon addition of GdL to a solution of **PBI-A** at pH 9*. Measurements were performed at 25°C.

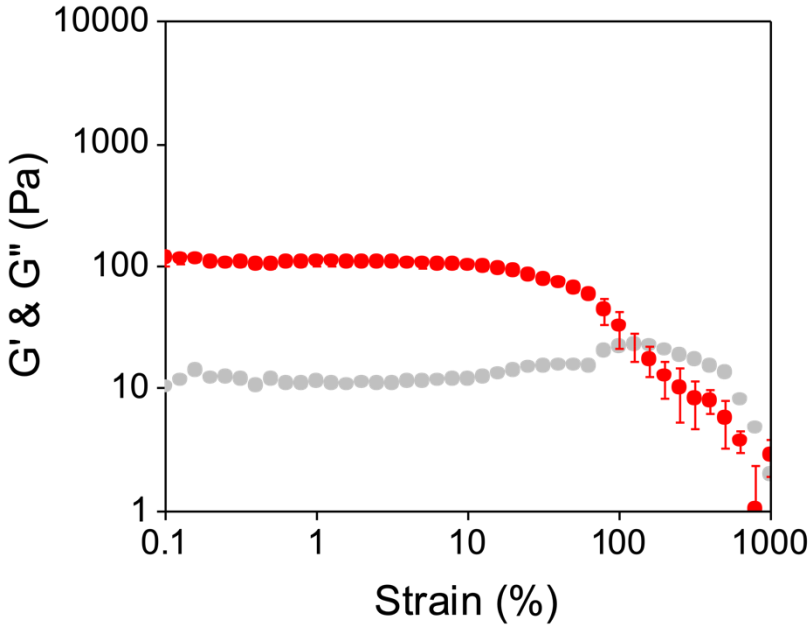

Figure A.1.14. Strain sweep of gels formed from a solution of **PBI-A** starting at pH 6 with 1 equivalent of NaCl (0.1 M, aq). Red circles represent G′ and grey circles represent G″. Strain sweeps were performed at a frequency of 10 rad/s at 25°C. Data shown are averaged data for triplicate runs of the samples, with error bars representing standard deviation.

A.2 Chapter 3 Appendix

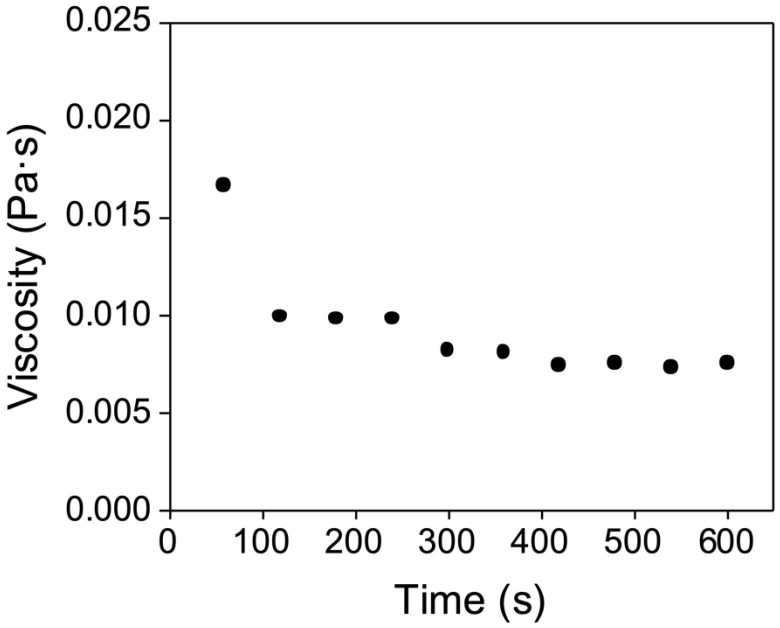

Figure A.2.1. Viscosity of **PBI-A** at a constant shear rate of 10 s^{-1} at 25°C.

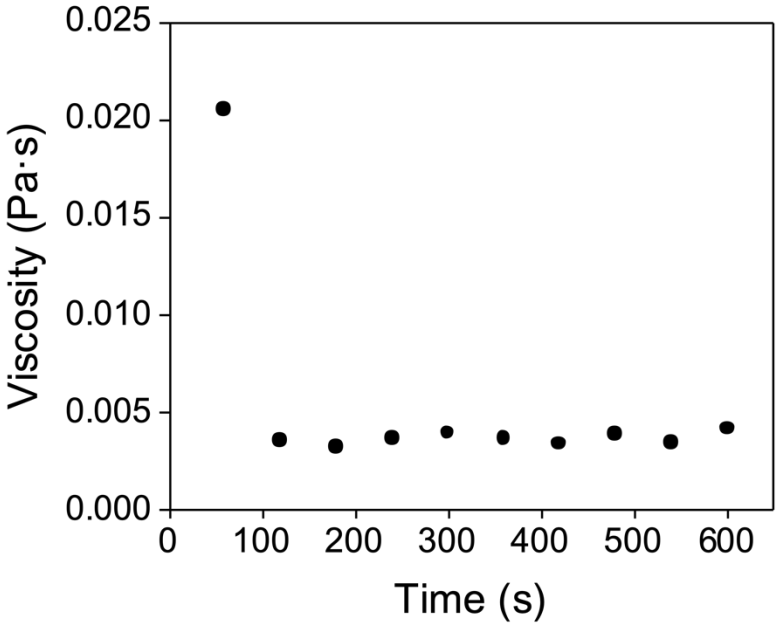

Figure A.2.2. Viscosity of **PBI-L** at a constant shear rate of 10 s^{-1} at 25°C.

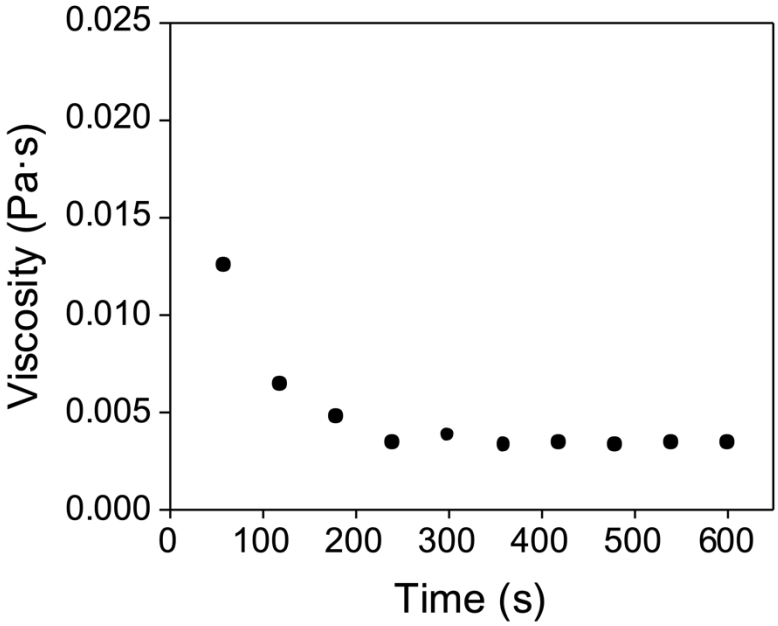

Figure A.2.3. Viscosity of **PBI-Y** at a constant shear rate of 10 s^{-1} at 25°C.

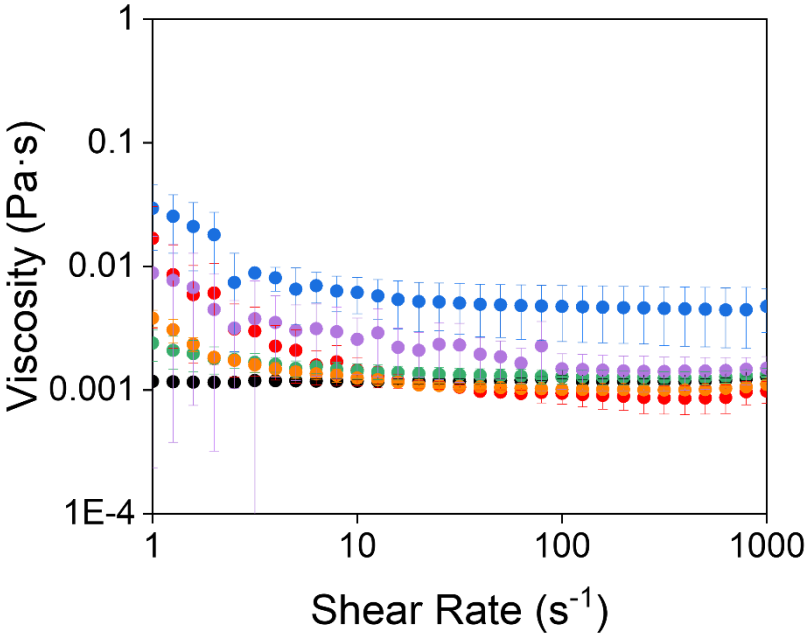

Figure A.2.4. Dynamic viscosity of **PBI-A** solutions at 25°C (black) and heated to 30°C (red), 40°C (blue), 50°C (green), 60°C (purple), and 70°C (orange).

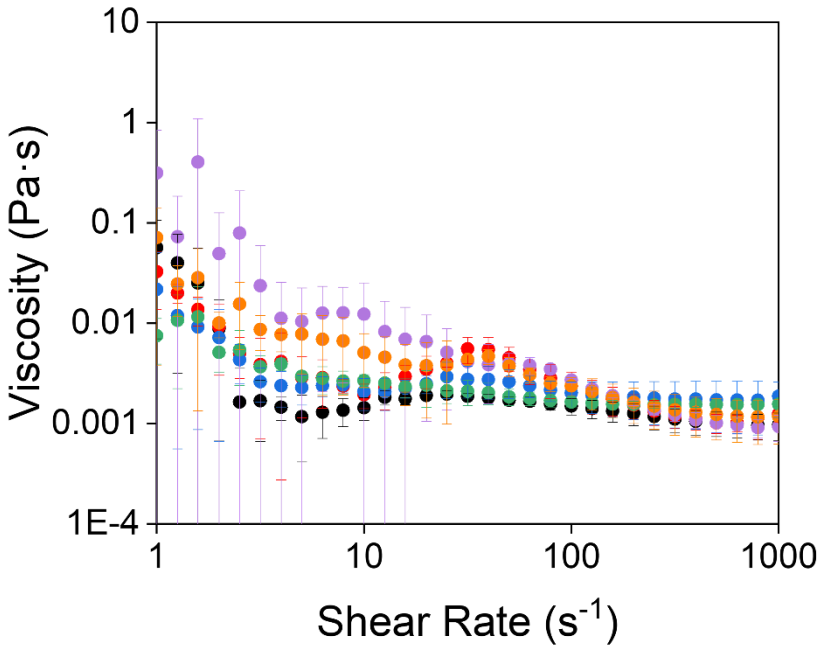

Figure A.2.5. Dynamic viscosity of **PBI-L** solutions at 25°C (black) and heated to 30°C (red), 40°C (blue), 50°C (green), 60°C (purple), and 70°C (orange).

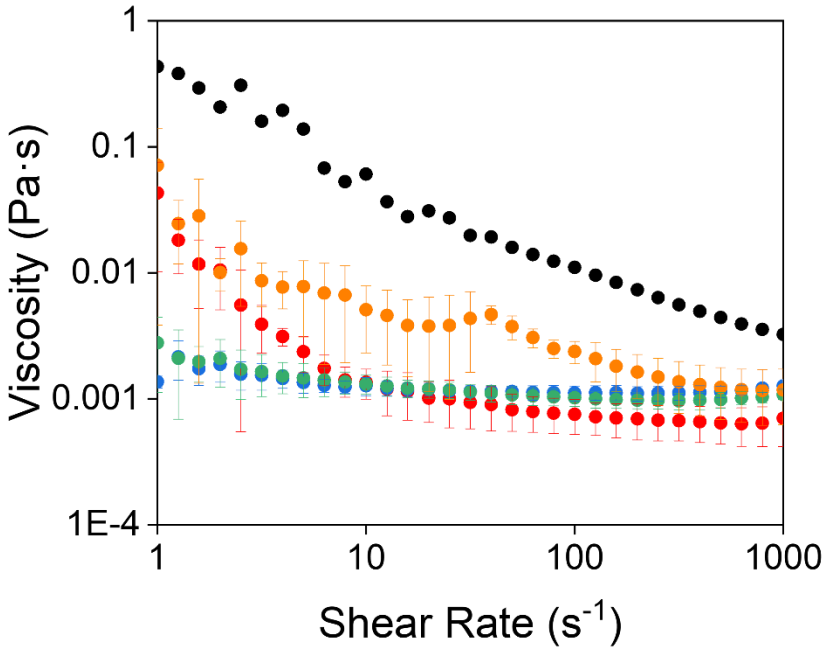

Figure A.2.6. Dynamic viscosity of **PBI-Y** solutions at 25°C (black) and heated to 30°C (red), 40°C (blue), 50°C (green), 60°C (purple), and 70°C (orange).

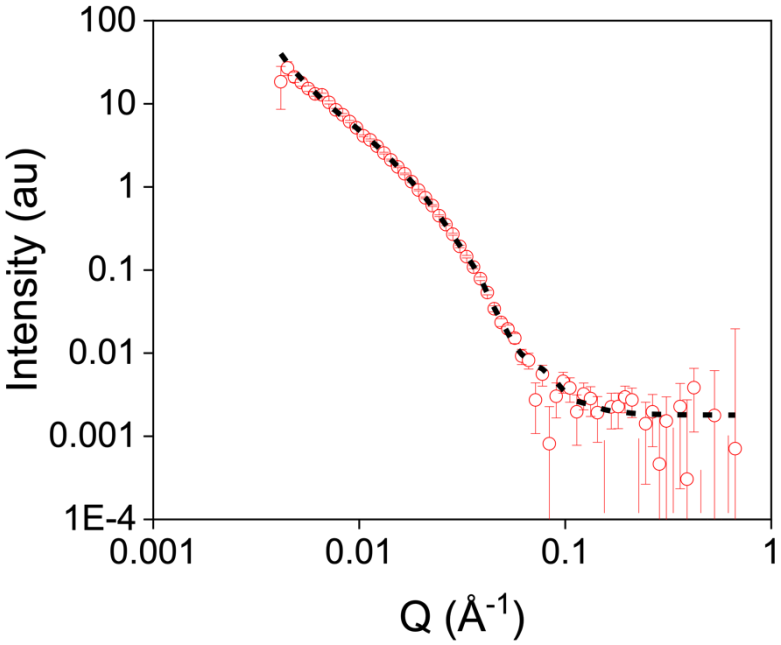

Figure A.2.7. Small-angle scattering pattern from a **PBI-A** solution heat-cooled from 30°C to 25°C.

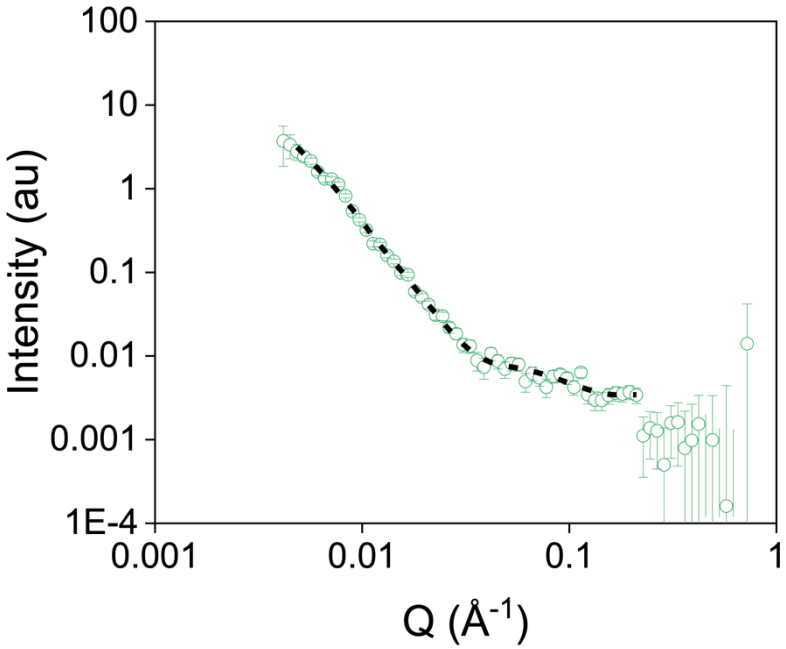

Figure A.2.8. Small-angle scattering pattern from a **PBI-A** solution heat-cooled from 50°C to 25°C.

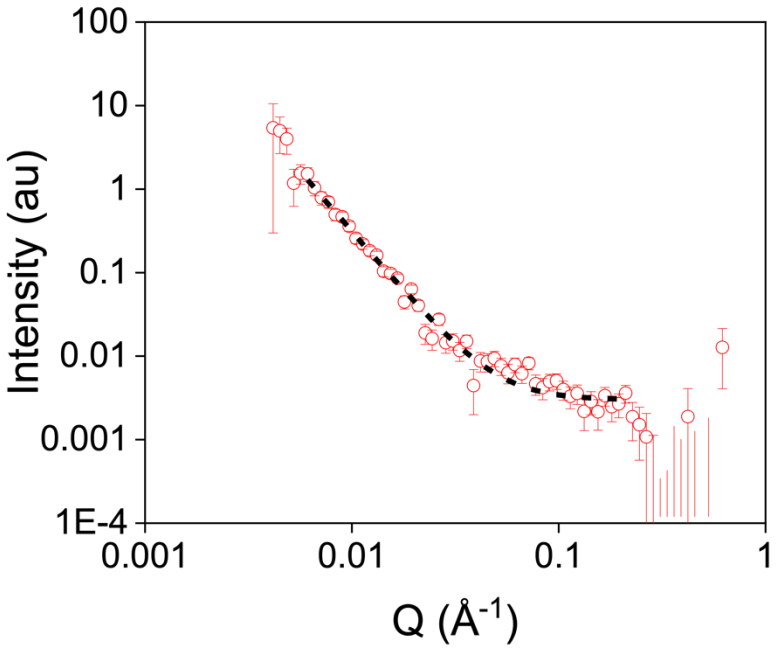

Figure A.2.9. Small-angle scattering pattern from a **PBI-L** solution at 30°C.

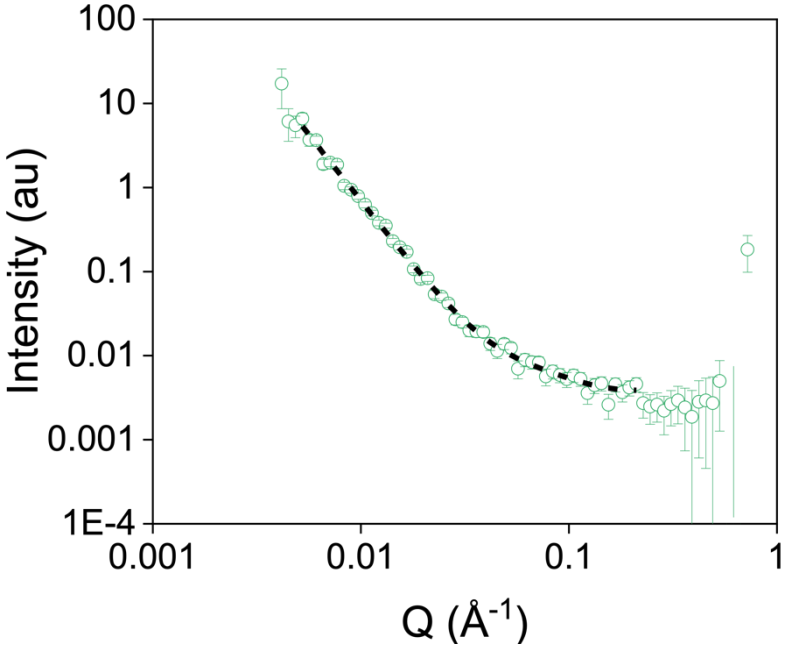

Figure A.2.10. Small-angle scattering pattern from a **PBI-L** solution at 50°C.

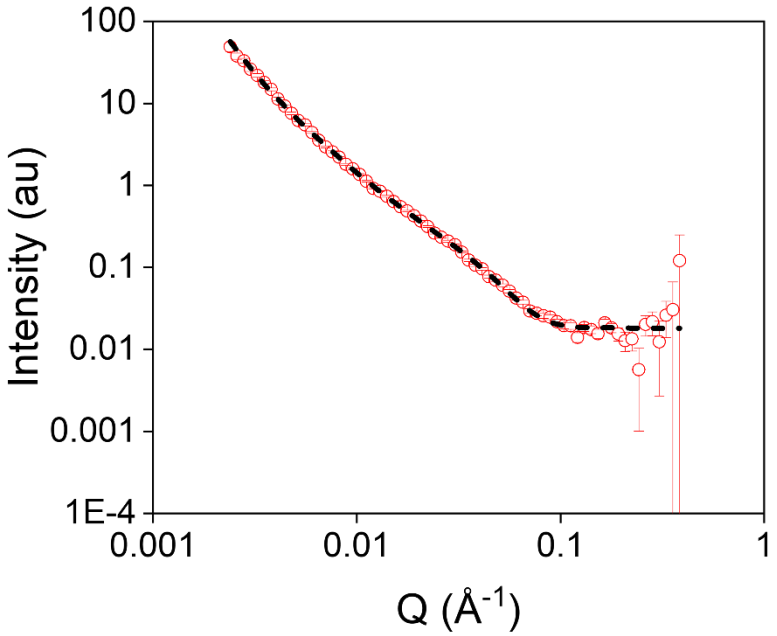

Figure A.2.11. Small-angle scattering patterns from a **PBI-L** solution heat-cooled from 30°C to 25°C.

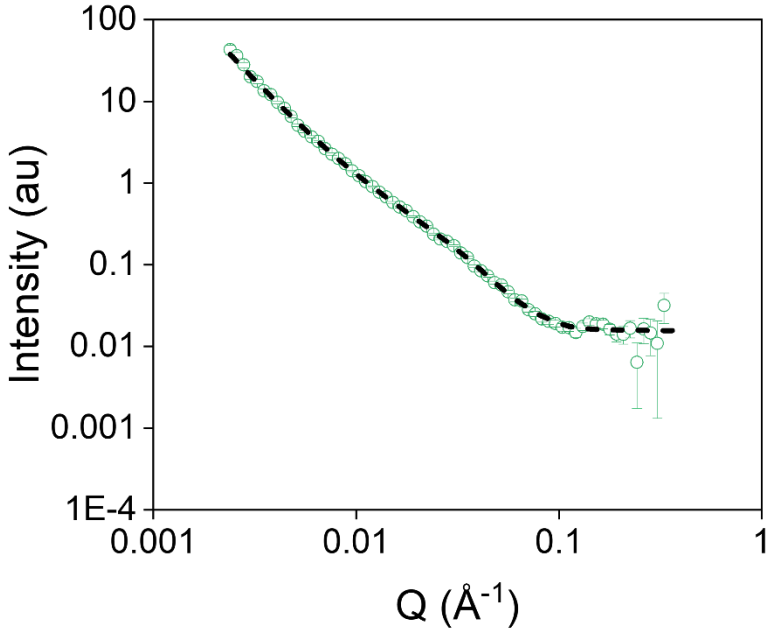

Figure A.2.12. Small-angle scattering pattern from a **PBI-L** solution heat-cooled from 50°C to 25°C.

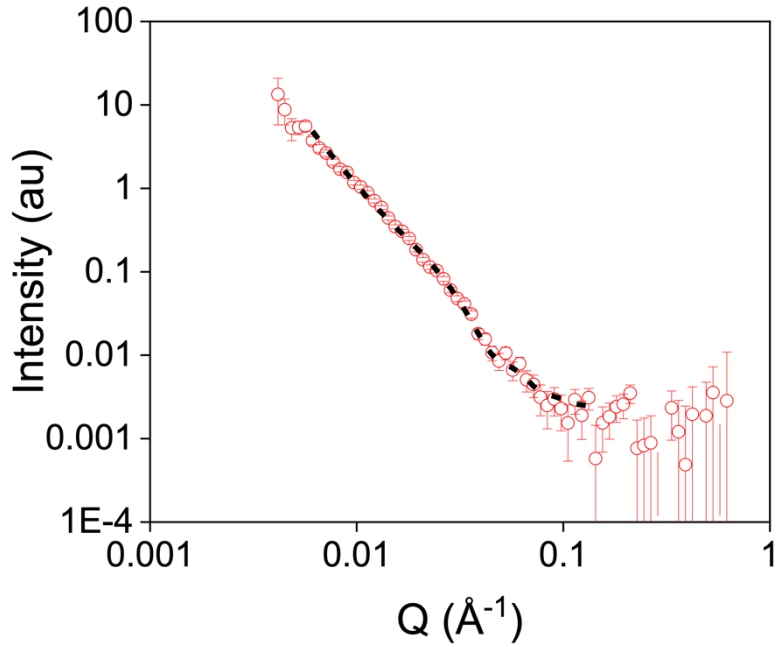

Figure A.2.13. Small-angle scattering pattern from a **PBI-Y** solution at 30°C.

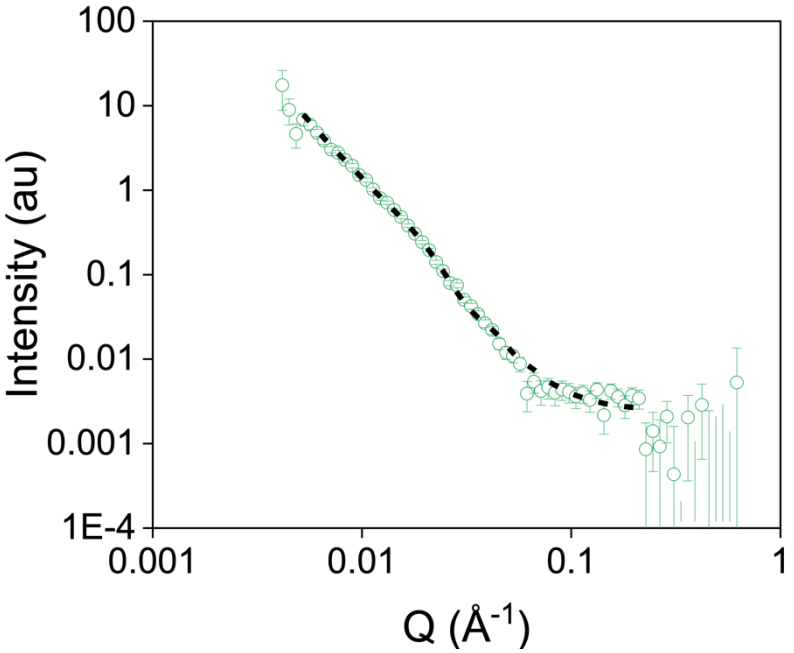

Figure A.2.14. Small-angle scattering pattern from a **PBI-Y** solution at 50°C.

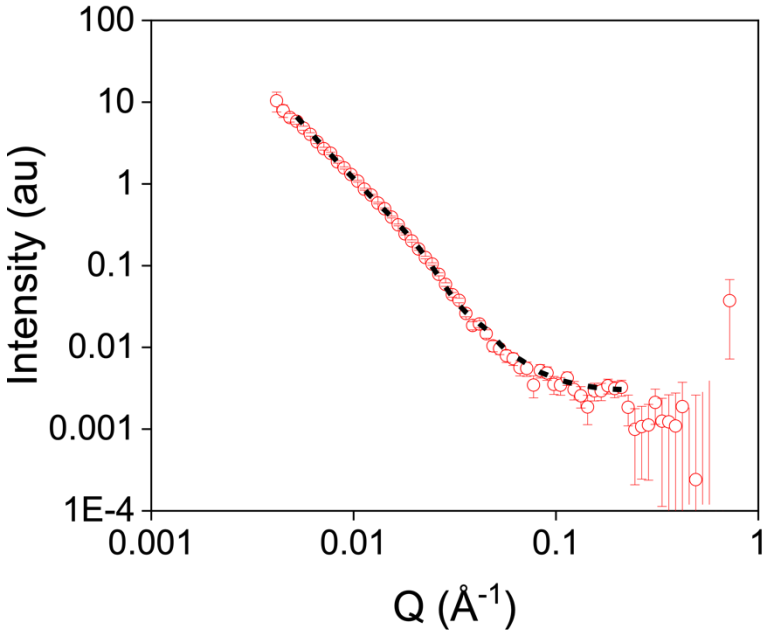

Figure A.2.15. Small-angle scattering pattern from a **PBI-Y** solution heat-cooled from 30°C to 25°C.

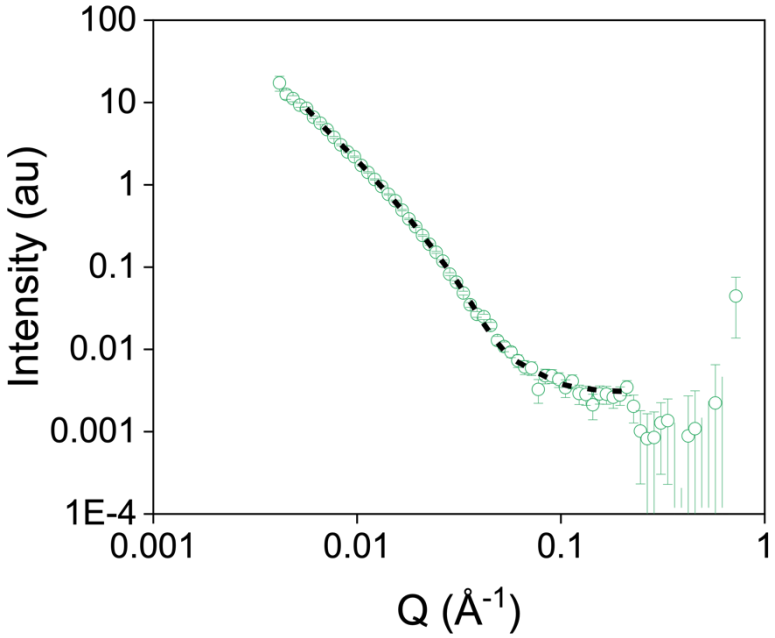

Figure A.2.16. Small-angle scattering patterns from a **PBI-Y** solution heat-cooled from 50°C to 25°C.

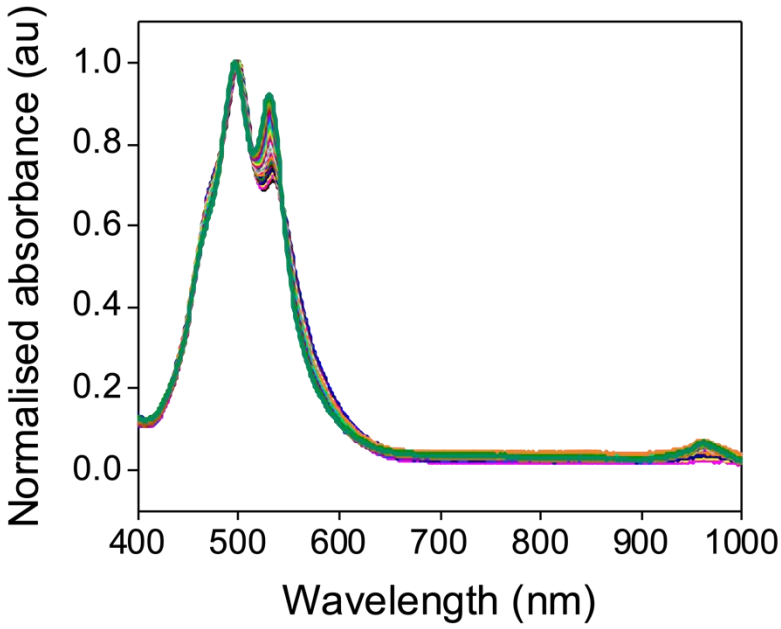

Figure A.2.17. Full normalised UV-vis absorption spectrum of **PBI-A** with increasing temperature. The temperature range was 25-70°C. Data is normalised to the highest absorption of each spectrum.

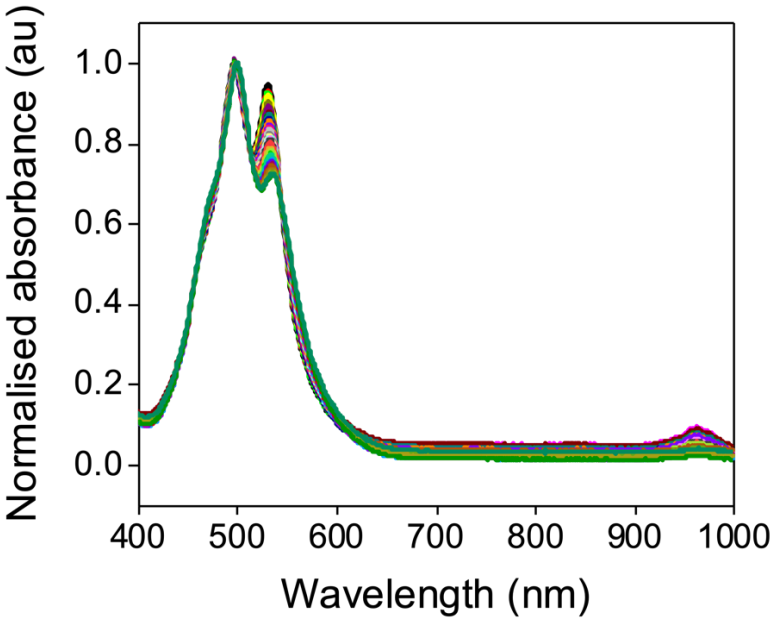

Figure A.2.18. Full normalised UV-vis absorption spectrum of **PBI-A** with decreasing temperature. The temperature range was 25-70°C. Data is normalised to the highest absorption of each spectrum.

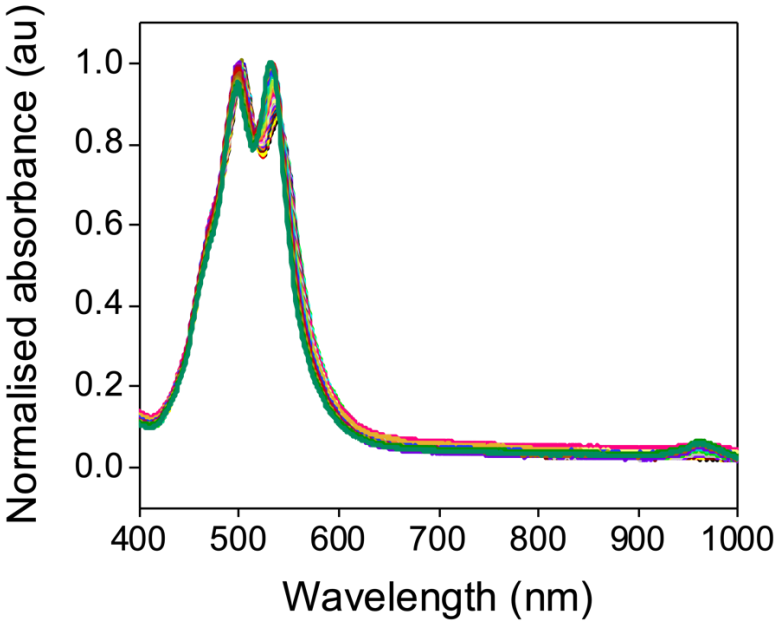

Figure A.2.19. Full normalised UV-vis absorption spectrum of **PBI-L** with increasing temperature. The temperature range was 25-70°C. Data is normalised to the highest absorption of each spectrum.

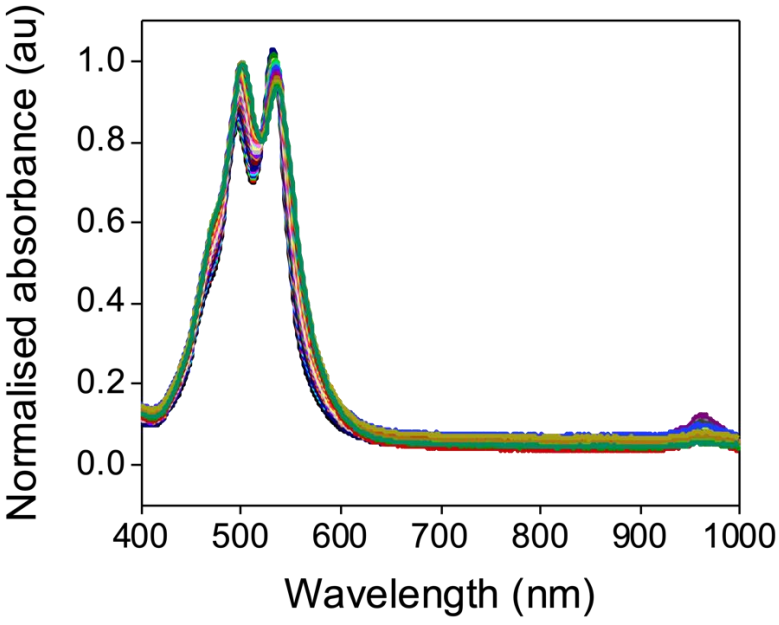

Figure A.2.20. Full normalised UV-vis absorption spectrum of **PBI-L** with decreasing temperature. The temperature range was 25-70°C. Data is normalised to the highest absorption of each spectrum.

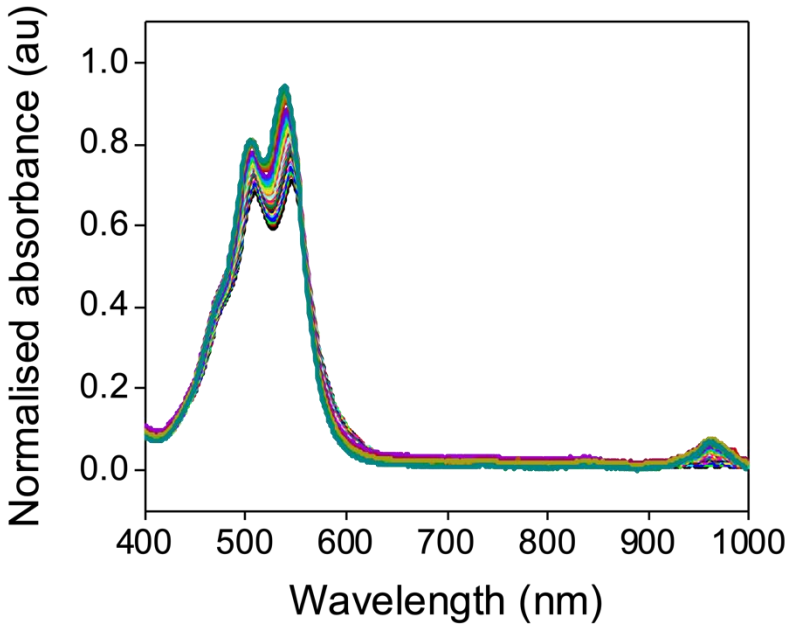

Figure A.2.21. Full normalised UV-vis absorption spectrum of **PBI-Y** with increasing temperature. The temperature range was 25-70°C. Data is normalised to the highest absorption of each spectrum.

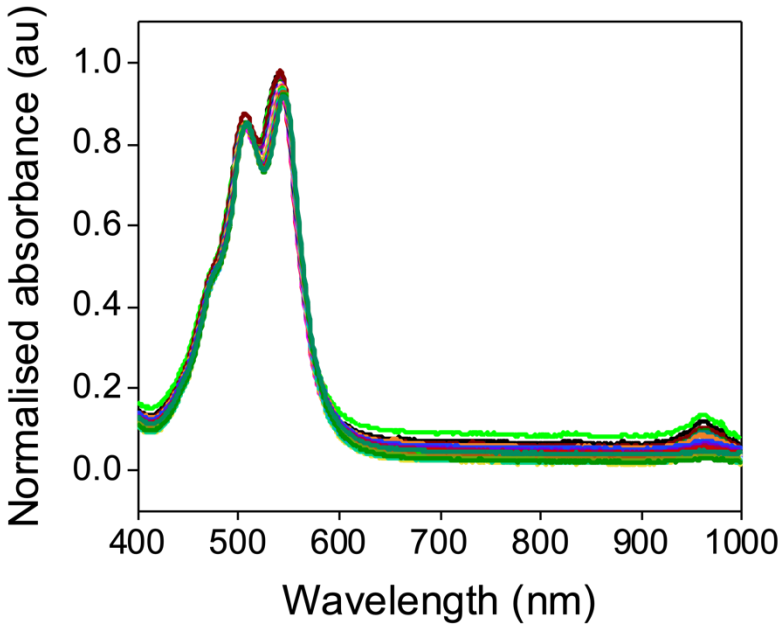

Figure A.2.22. Full normalised UV-vis absorption spectrum of **PBI-Y** with decreasing temperature. The temperature range was 25-70°C. Data is normalised to the highest absorption of each spectrum.

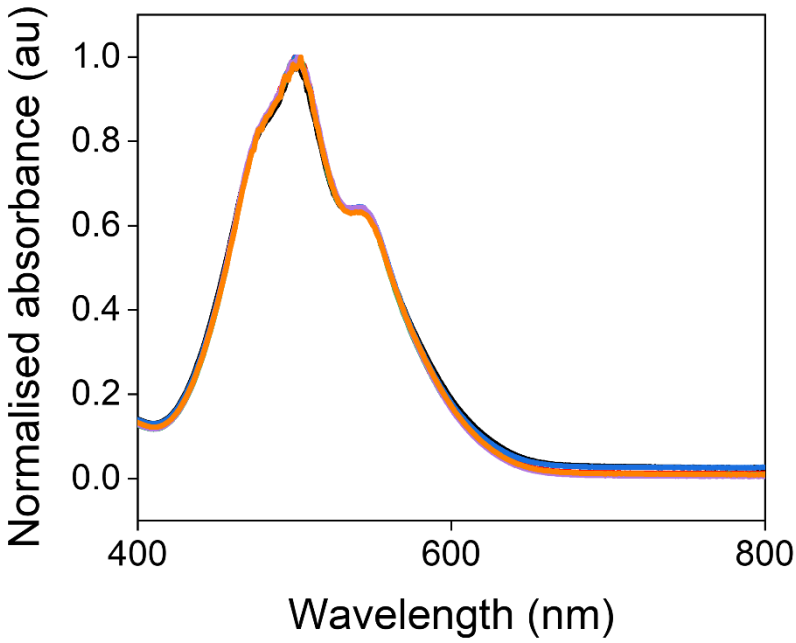

Figure A.2.23. UV-vis absorption spectra of **PBI-A** solutions at 25°C (black) and heated to 30°C (red), 40°C (blue), 50°C (green), 60°C (purple), and 70°C (orange) before cooling to 25°C. Data is normalised to the highest absorption of each spectrum.

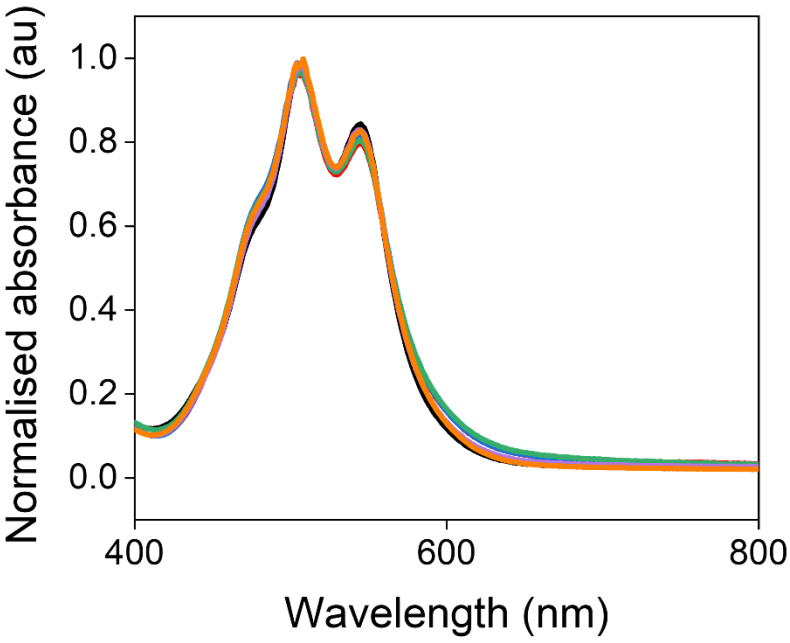

Figure A.2.24. UV-vis absorption spectra of **PBI-L** solutions at 25°C (black) and heated to 30°C (red), 40°C (blue), 50°C (green), 60°C (purple), and 70°C (orange) before cooling to 25°C. Data is normalised to the highest absorption of each spectrum.

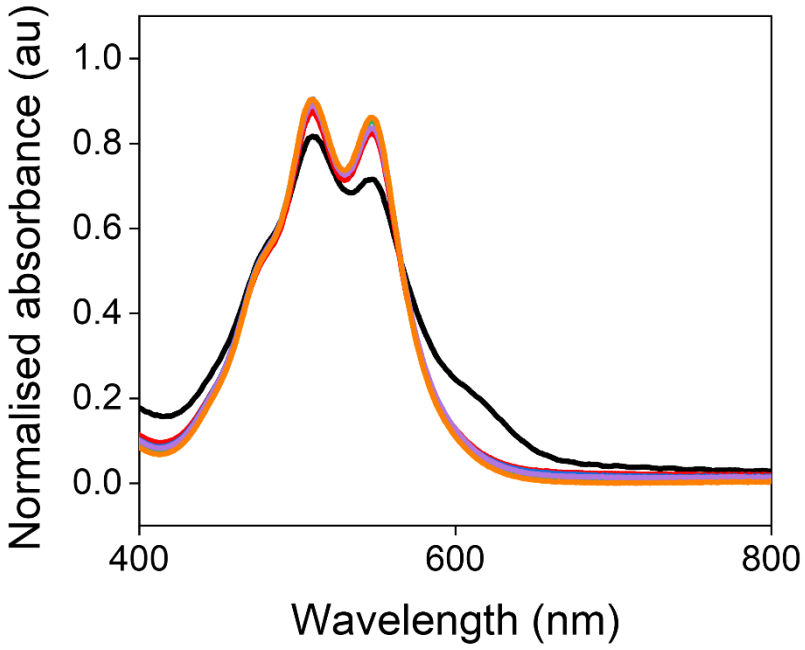

Figure A.2.25. UV-vis absorption spectra of **PBI-Y** solutions at 25°C (black) and heated to 30°C (red), 40°C (blue), 50°C (green), 60°C (purple), and 70°C (orange) before cooling to 25°C. Data is normalised to the highest absorption of each spectrum.

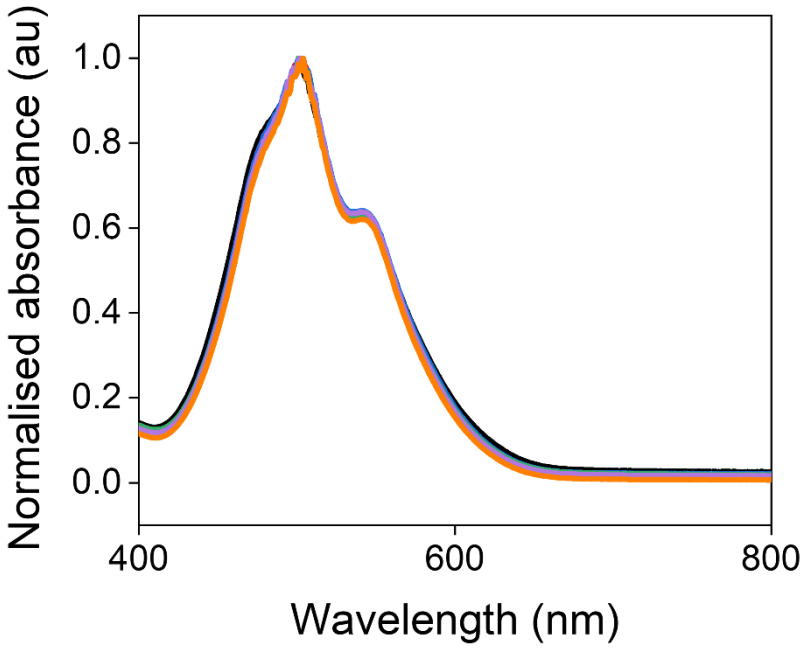

Figure A.2.26. UV-vis absorption spectra of **PBI-A** solutions at 25°C (black) and heated to 30°C (red), 40°C (blue), 50°C (green), 60°C (purple), and 70°C (orange). Data is normalised to the highest absorption of each spectrum.

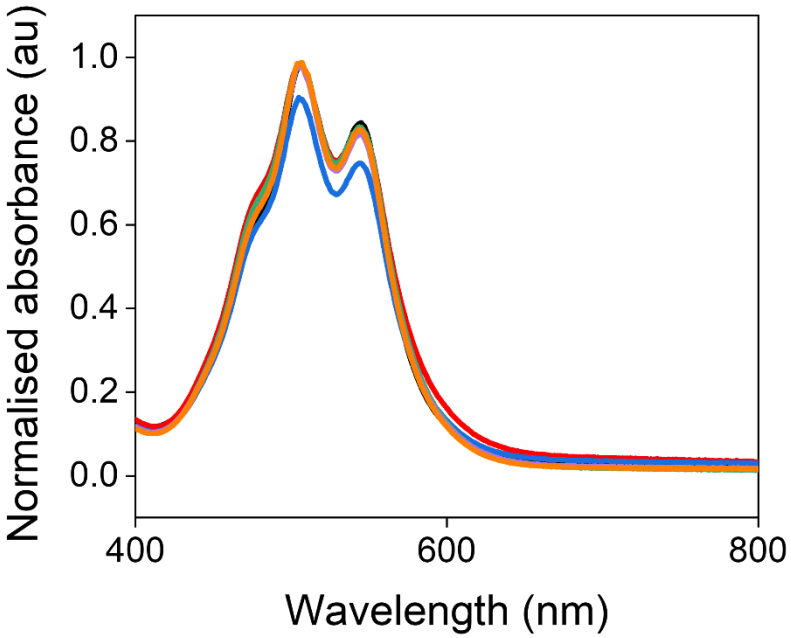

Figure A.2.27. UV-vis absorption spectra of **PBI-L** solutions at 25°C (black) and heated to 30°C (red), 40°C (blue), 50°C (green), 60°C (purple), and 70°C (orange). Data is normalised to the highest absorption of each spectrum.

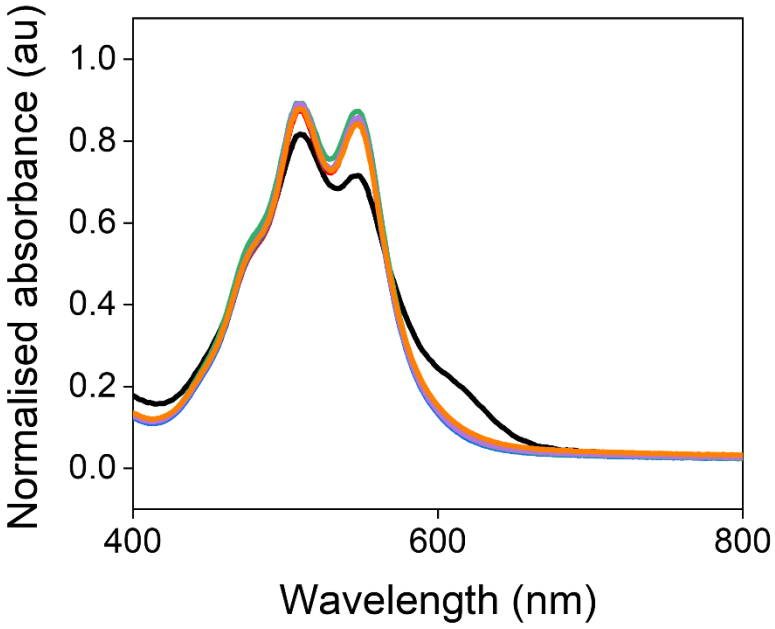

Figure A.2.28. UV-vis absorption spectra of **PBI-Y** solutions at 25°C (black) and heated to 30°C (red), 40°C (blue), 50°C (green), 60°C (purple), and 70°C (orange). Data is normalised to the highest absorption of each spectrum.

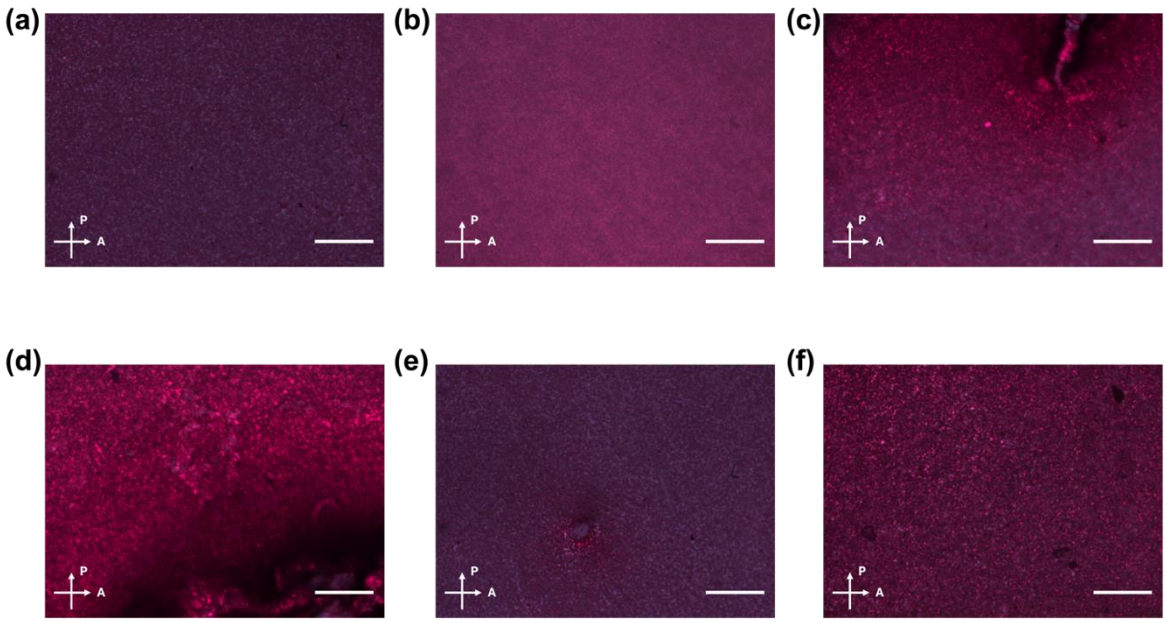

Figure A.2.29. Cross-polarised optical microscope images of **PBI-A** films prepared from solutions at (a) 25°C and solutions heated to (b) 30°C, (c) 40°C, (d) 50°C, (e) 60°C, and (f) 70°C and cooled to 25°C before casting. Scale bars represent 100 μm.

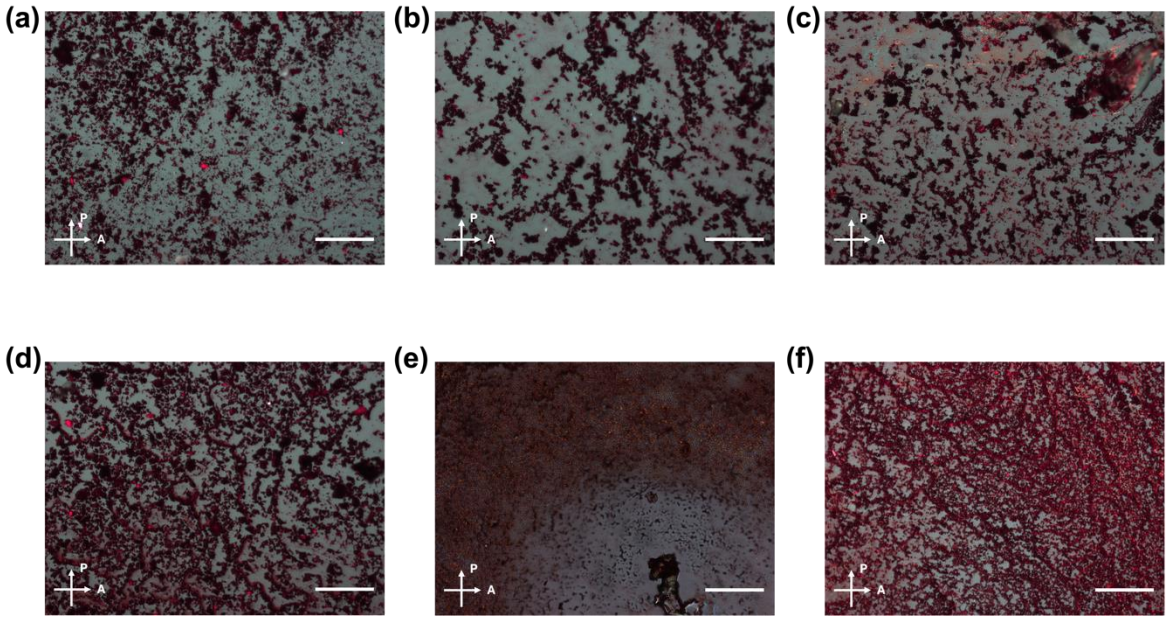

Figure A.2.30. Cross-polarised optical microscope images of **PBI-L** films prepared from solutions at (a) 25°C and solutions heated to (b) 30°C, (c) 40°C, (d) 50°C, (e) 60°C, and (f) 70°C and cooled to 25°C before casting. Scale bars represent 100 μm.

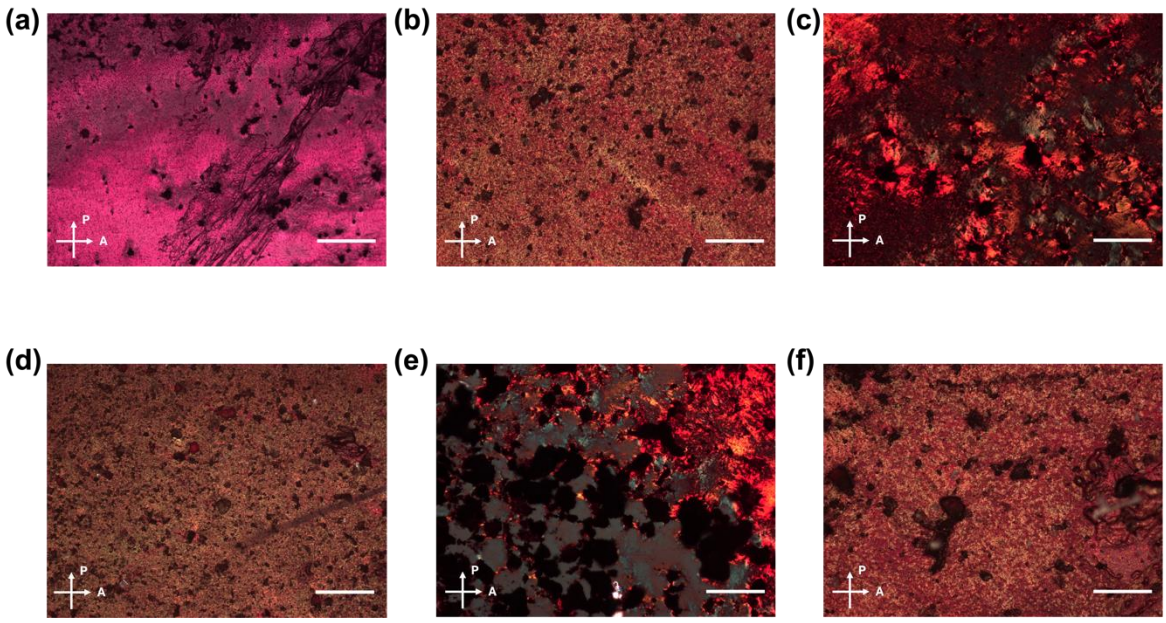

Figure A.2.31. Cross-polarised optical microscope images of **PBI-Y** films prepared from solutions at (a) 25°C and solutions heated to (b) 30°C, (c) 40°C, (d) 50°C, (e) 60°C, and (f) 70°C and cooled to 25°C before casting. Scale bars represent 100 μm.

Table A.2.1. Concentrations of glucono-δ-lactone required to form hydrogels from **PBI-A**, **PBI-L**, and **PBI-Y** solutions with an initial pH of 6 and a final pH of approximately 3.2. pH data shown are averaged data for triplicate samples, with errors representing standard deviation.

PBI	GdL concentration (mg/mL)	Average pH
PBI-A	7.5	3.22 ± 0.0010
PBI-L	10	3.20 ± 0.020
PBI-Y	10	3.18 ± 0.005

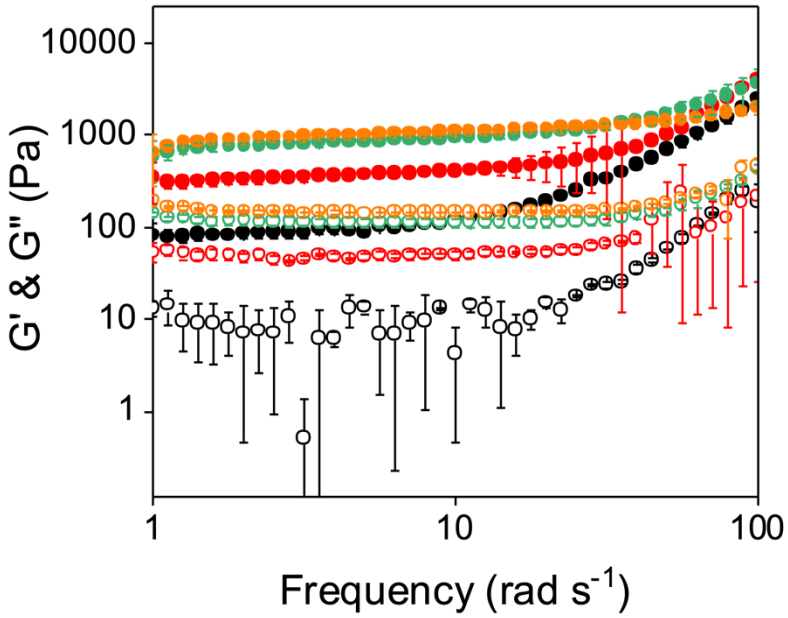

Figure A.2.32. Frequency sweep of gels formed from a solution of **PBI-A** at 25°C (black) and those heated to 30°C (red), 50°C (green), and 70°C (orange) before cooling to 25°C with a controlled cooling rate before triggering gelation. Closed circles represent G′ and open circles represent G″. Data shown are averaged data for triplicate runs, with error bars representing standard deviation.

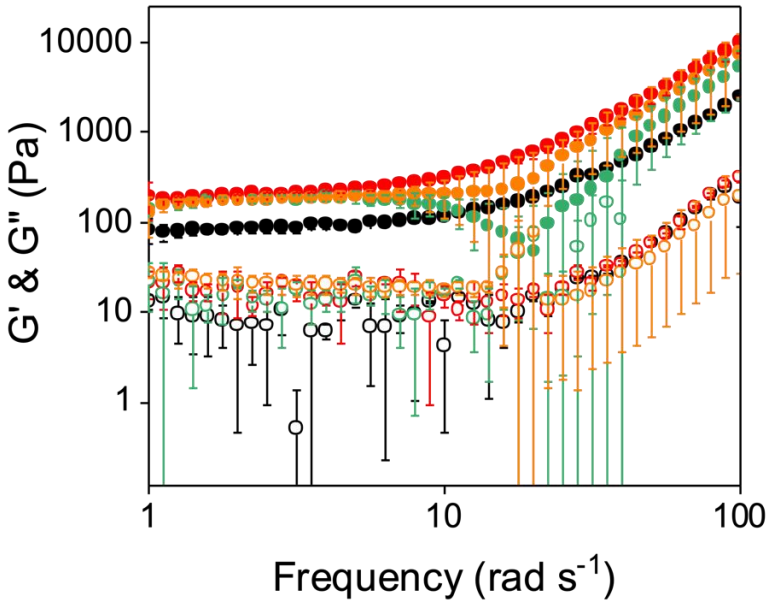

Figure A.2.33. Frequency sweep of gels formed from a solution of **PBI-A** at 25°C (black) and those heated to 30°C (red), 50°C (green), and 70°C (orange) before cooling to 25°C with an uncontrolled cooling rate before triggering gelation. Closed circles represent G′ and open circles represent G″. Data shown are averaged data for triplicate runs, with error bars representing standard deviation.

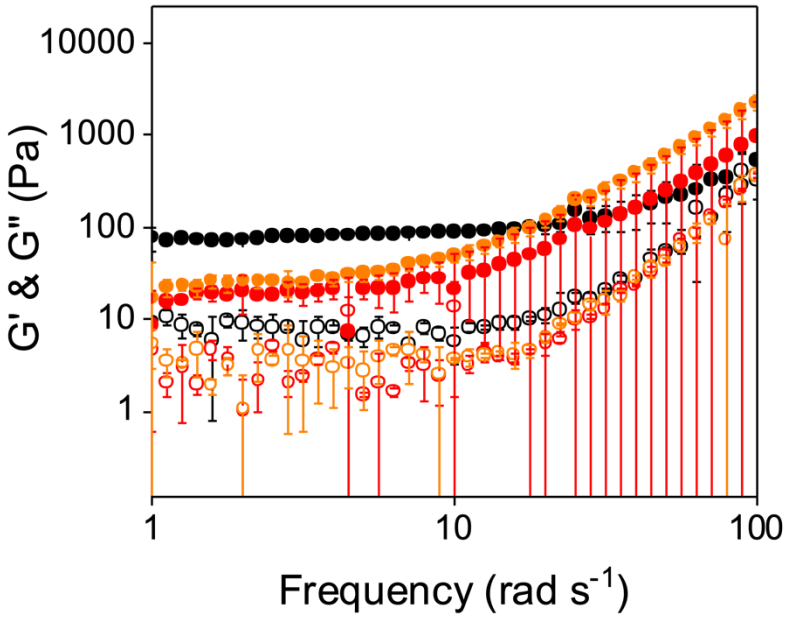

Figure A.2.34. Frequency sweep of gels formed from a solution of **PBI-L** at 25°C (black) and those heated to 30°C (red), 50°C (green), and 70°C (orange) before cooling to 25°C with a controlled cooling rate before triggering gelation. Closed circles represent G′ and open circles represent G″. Data shown are averaged data for triplicate runs, with error bars representing standard deviation.

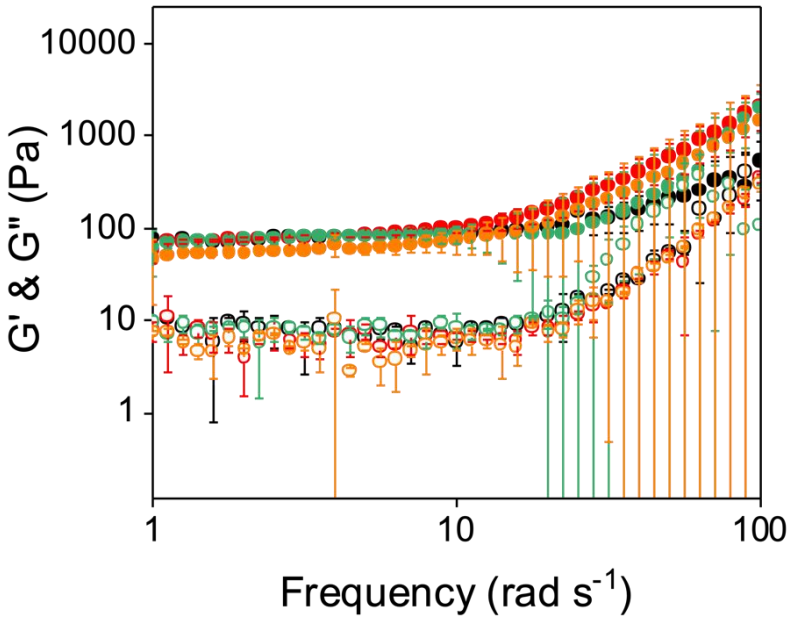

Figure A.2.35. Frequency sweep of gels formed from a solution of **PBI-L** at 25°C (black) and those heated to 30°C (red), 50°C (green), and 70°C (orange) before cooling to 25°C with an uncontrolled cooling rate before triggering gelation. Closed circles represent G′ and open circles represent G″. Data shown are averaged data for triplicate runs, with error bars representing standard deviation.

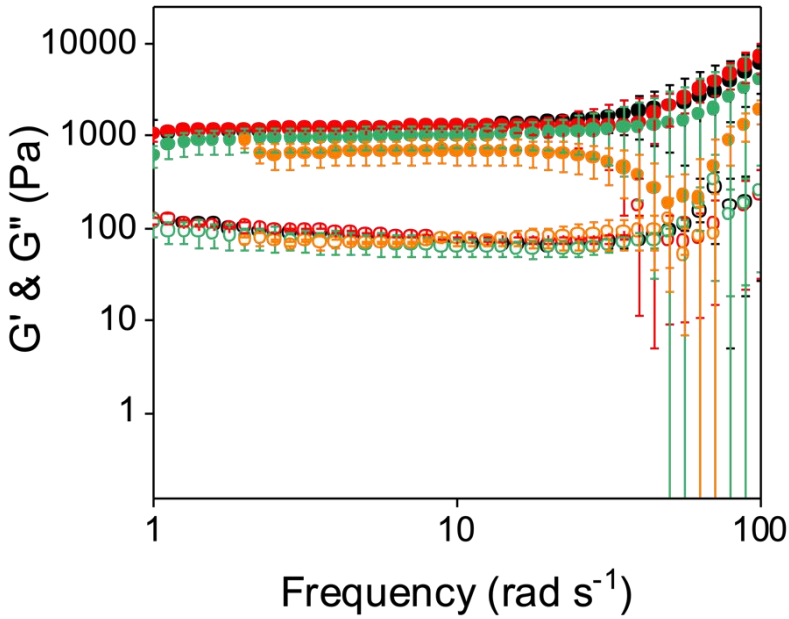

Figure A.2.36. Frequency sweep of gels formed from a solution of **PBI-Y** at 25°C (black) and those heated to 30°C (red), 50°C (green), and 70°C (orange) before cooling to 25°C with an uncontrolled cooling rate before triggering gelation. Closed circles represent G′ and open circles represent G″. Data shown are averaged data for triplicate runs, with error bars representing standard deviation.

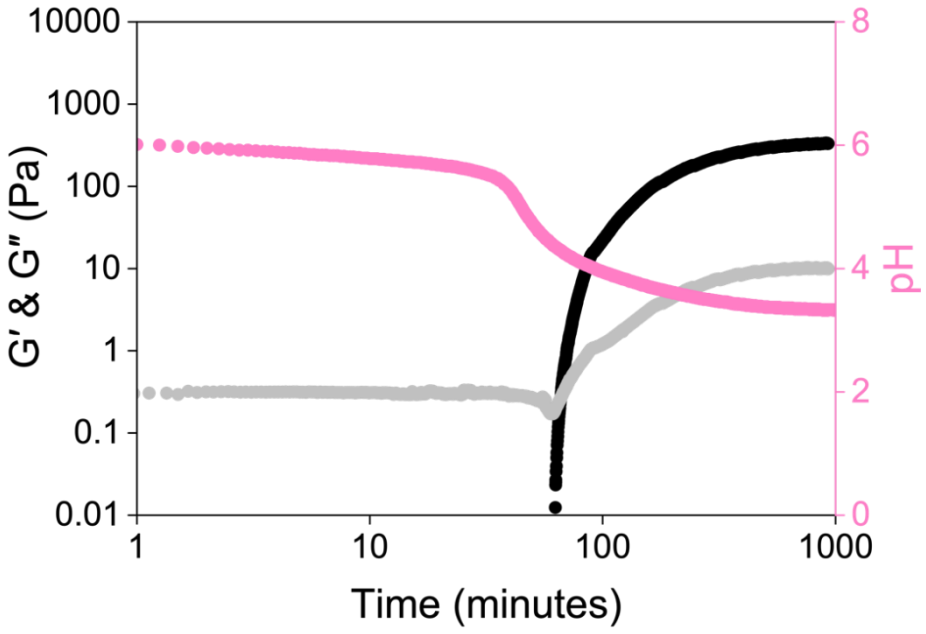

Figure A.2.37. Plots showing the evolution of the gel networks of a **PBI-A** solution at 25°C. The graph shows the development of G′ (black) and G″ (grey) with time and change in pH (pink).

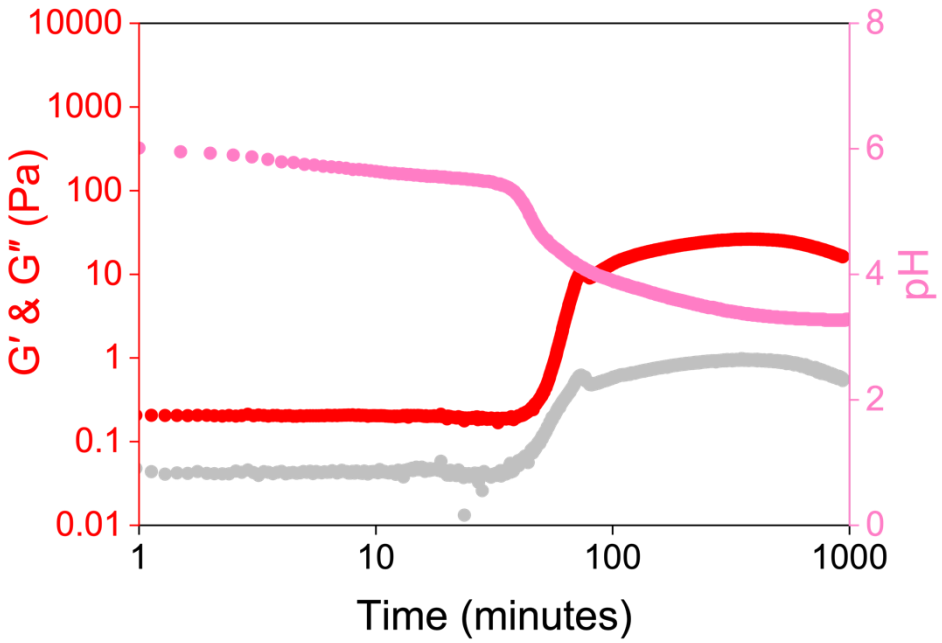

Figure A.2.38. Plots showing the evolution of the gel networks of a **PBI-A** solution heated to 30°C and cooled to 25°C with a controlled cooling rate. The graph shows the development of G′ (red) and G″ (grey) with time and change in pH (pink).

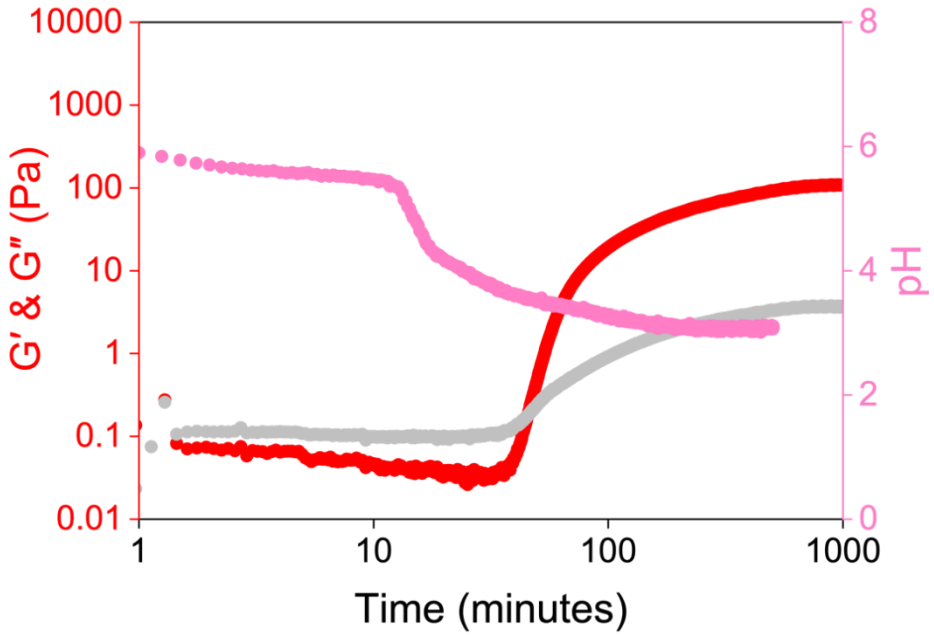

Figure A.2.39. Plots showing the evolution of the gel networks of a **PBI-A** solution heated to 30°C and cooled to 25°C with an uncontrolled cooling rate. The graph shows the development of G′ (red) and G″ (grey) with time and change in pH (pink).

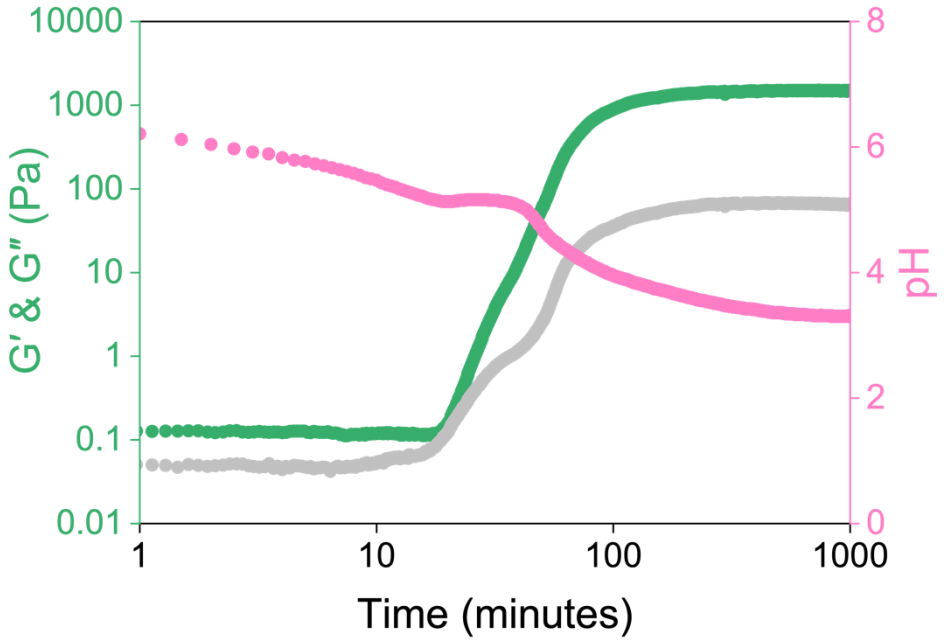

Figure A.2.40. Plots showing the evolution of the gel networks of a **PBI-A** solution heated to 50°C and cooled to 25°C with a controlled cooling rate. The graph shows the development of G′ (green) and G″ (grey) with time and change in pH (pink).

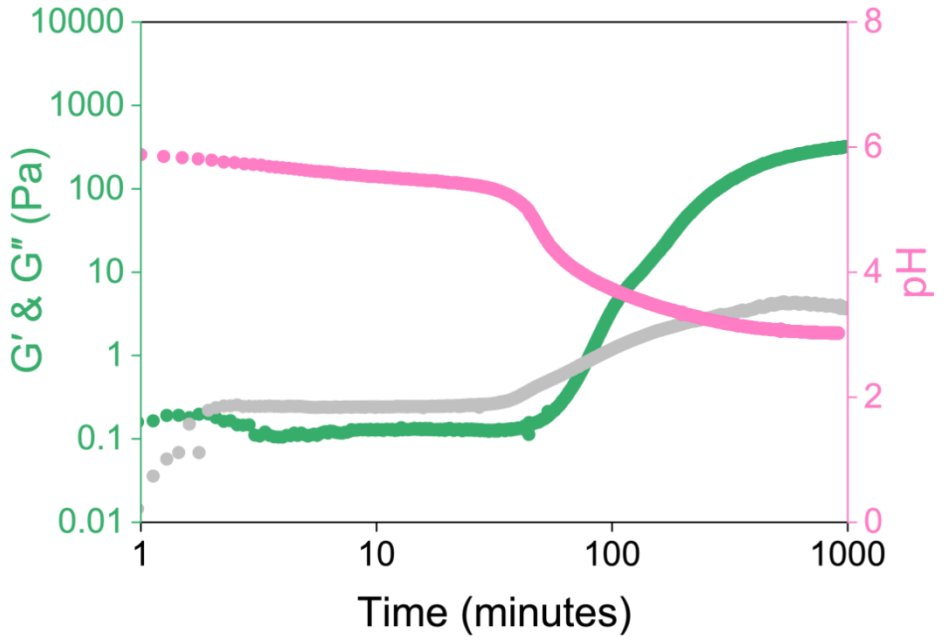

Figure A.2.41. Plots showing the evolution of the gel networks of a **PBI-A** solution heated to 50°C and cooled to 25°C with an uncontrolled cooling rate. The graph shows the development of G′ (green) and G″ (grey) with time and change in pH (pink).

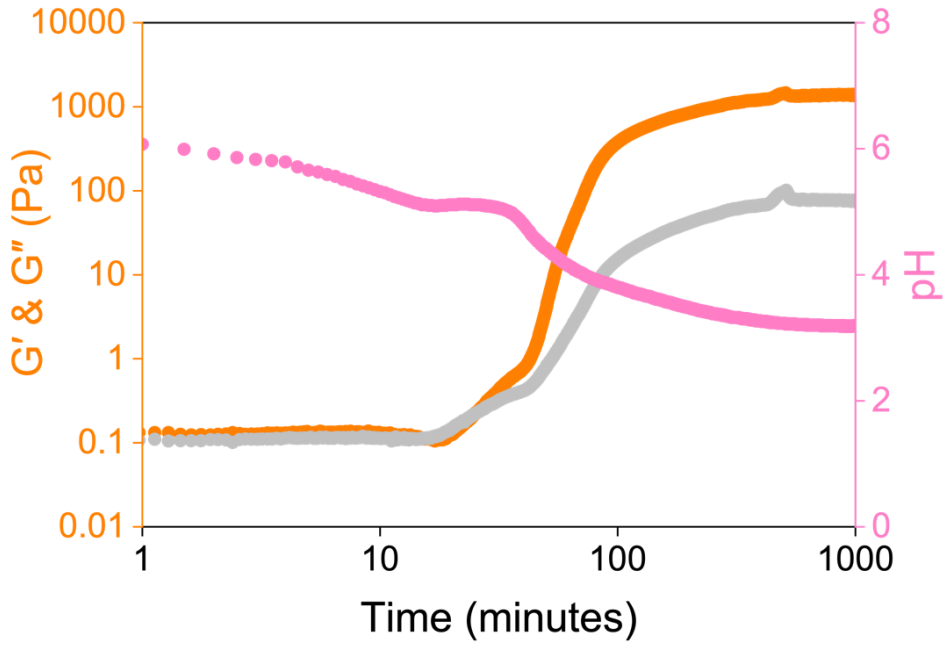

Figure A.2.42. Plots showing the evolution of the gel networks of a **PBI-A** solution heated to 70°C and cooled to 25°C with a controlled cooling rate. The graph shows the development of G′ (orange) and G″ (grey) with time and change in pH (pink).

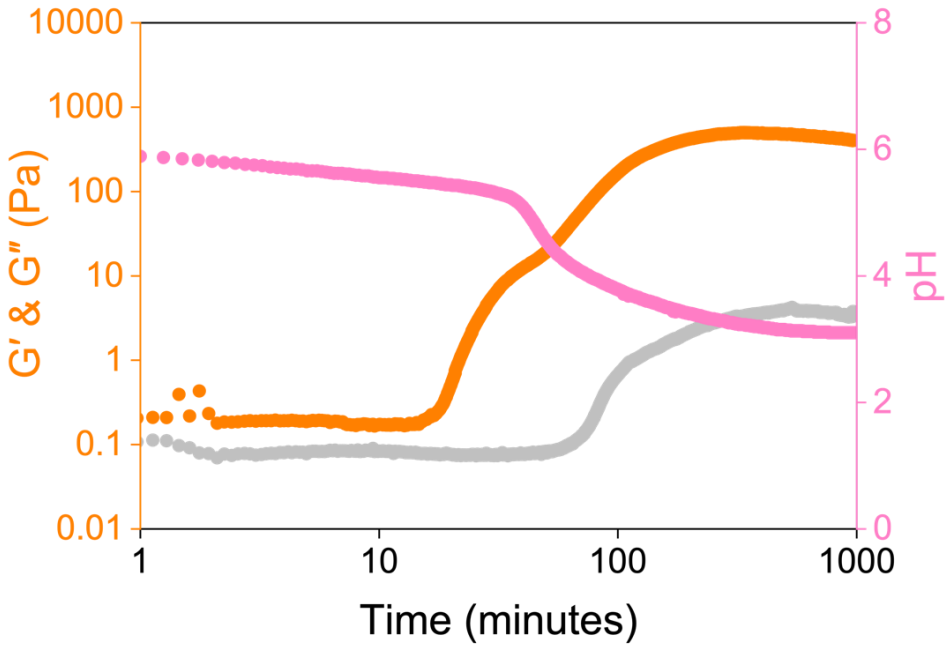

Figure A.2.43. Plots showing the evolution of the gel networks of a **PBI-A** solution heated to 70°C and cooled to 25°C with an uncontrolled cooling rate. The graph shows the development of G′ (orange) and G″ (grey) with time and change in pH (pink).

A.3 Chapter 4 Appendix

Table A.3.1. Rheology of gels formed from **PBI-A**/polymer blends with an initial pH of 6. A dash represents gels which did not form upon the addition of GdL.

Sample	G′ (Pa)	G″ (Pa)	Yield point (%)	Flow point (%)	tanδ
PBI-A/PEG 25/75	163	12	7.94	316	0.07
PBI-A/PEG 50/50	387	43	7.94	126	0.11
PBI-A/PEG 75/25	166	11	10	158	0.07
PBI-A/PEO 25/75	1163	32	6.31	25.1	0.03
PBI-A/PEO 50/50	1017	102	5.01	1000	0.10
PBI-A/PEO 75/25	470	22	20	1000	0.05
PBI-A/PVA 25/75	157	23	20	398	0.15
PBI-A/PVA 50/50	-	-	-	-	-
PBI-A/PVA 75/25	76	76	15.8	501	0.10

Table A.3.2. Rheology of gels formed from **PBI-A**/polymer blends with an initial pH of 9.

Sample	G′ (Pa)	G″ (Pa)	Yield point (%)	Flow point (%)	tanδ
PBI-A/PEG 25/75	570	92	2.00	63.1	0.16
PBI-A/PEG 50/50	1048	187	2.51	39.8	0.18
PBI-A/PEG 75/25	1370	244	2.51	251	0.18
PBI-A/PEO 25/75	876	124	31.6	794	0.14
PBI-A/PEO 50/50	801	148	10	100	0.19
PBI-A/PEO 75/25	1089	164	5.1	501	0.15
PBI-A/PVA 25/75	1553	228	2.51	501	0.15
PBI-A/PVA 50/50	2016	299	3.16	501	0.15
PBI-A/PVA 75/25	2923	466	2.00	501	0.16

Table A.3.3. Concentrations of glucono-δ-lactone required to form hydrogels from different **PBI-A/PEO** blends with an initial pH of 6 and a final pH of approximately 3.2. pH data shown are averaged data for triplicate samples, with errors representing standard deviation.

PBI-A/PEO Blend	GdL concentration (mg/mL)	Average pH
25/75	10	3.24 ± 0.006
50/50	10	3.21 ± 0.030
75/25	5	3.20 ± 0.010

Table A.3.4. Concentrations of glucono-δ-lactone required to form hydrogels from different **PBI-A/PEO** blends with an initial pH of 9 and a final pH of approximately 3.2. pH data shown are averaged data for triplicate samples, with errors representing standard deviation.

PBI-A/PEO Blend	GdL concentration (mg/mL)	Average pH
25/75	12.5	3.29 ± 0.010
50/50	10	3.17 ± 0.010
75/25	12.5	3.24 ± 0.005

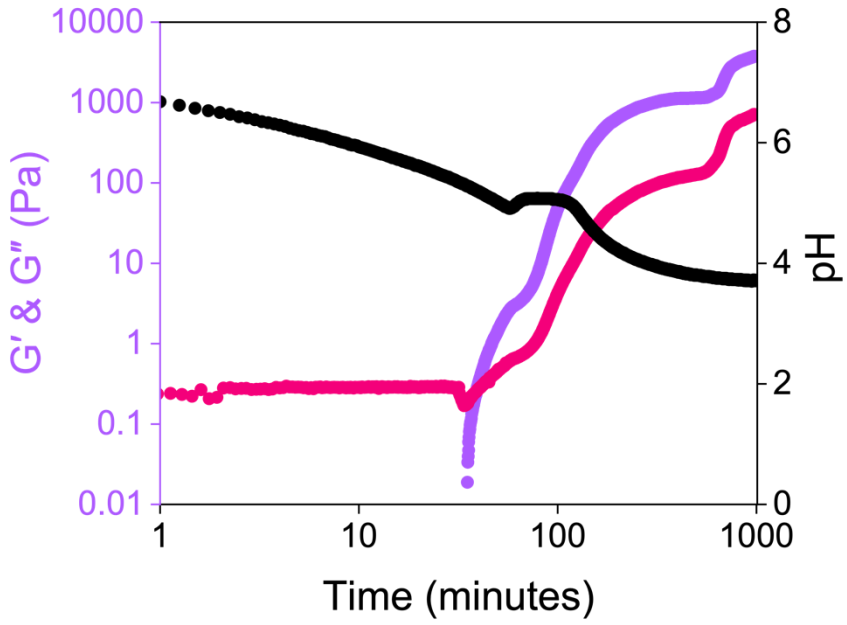

Figure A.3.1. Plots showing the evolution of the gel networks of **PBI-A** with an initial pH of 9. The graph shows the development of G′ (purple) and G″ (pink) with time and change in pH (black).

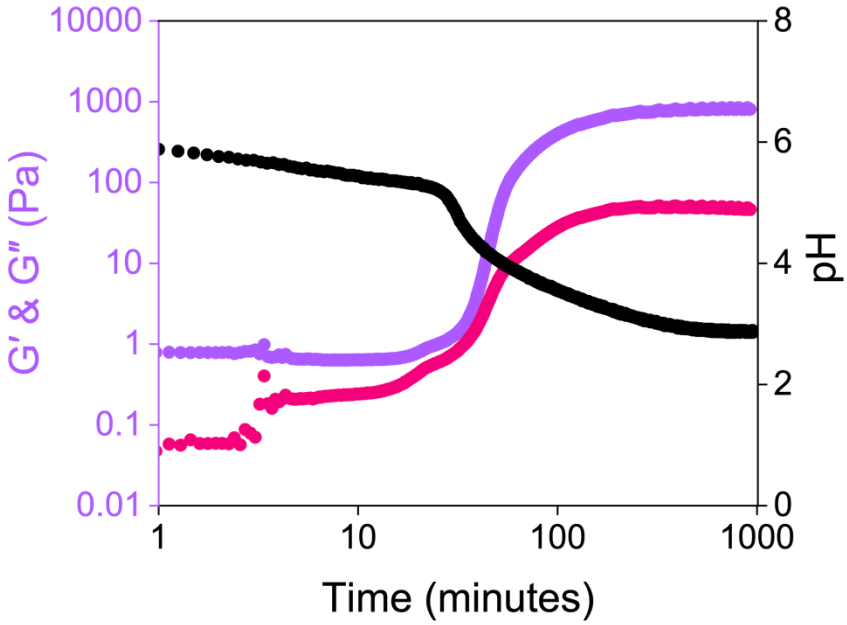

Figure A.3.2. Plots showing the evolution of the gel networks of **PBI-A/PEO** 25/75 blends with an initial pH of 6. The graph shows the development of G′ (purple) and G″ (pink) with time and change in pH (black).

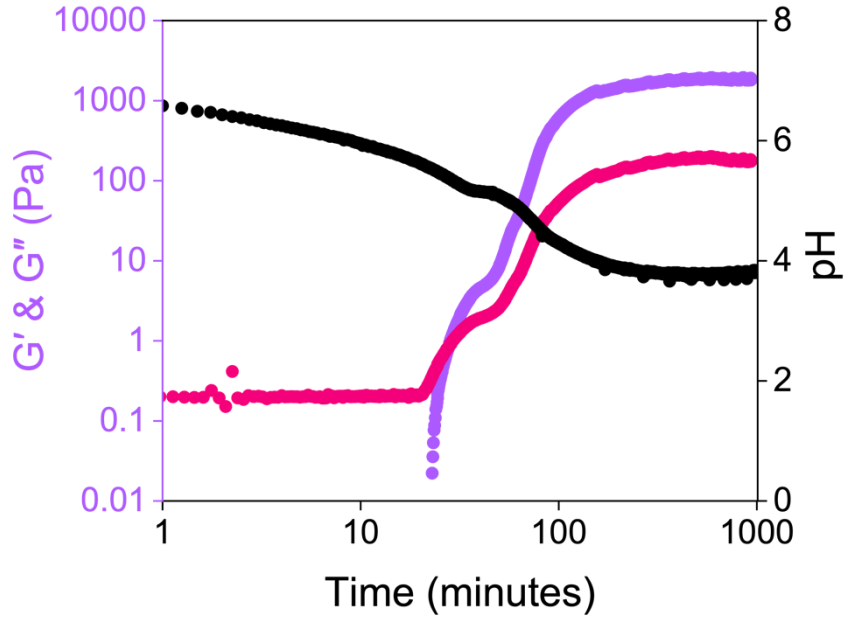

Figure A.3.3. Plots showing the evolution of the gel networks of **PBI-A/PEO** 25/75 blends with an initial pH of 9. The graph shows the development of G′ (purple) and G″ (pink) with time and change in pH (black).

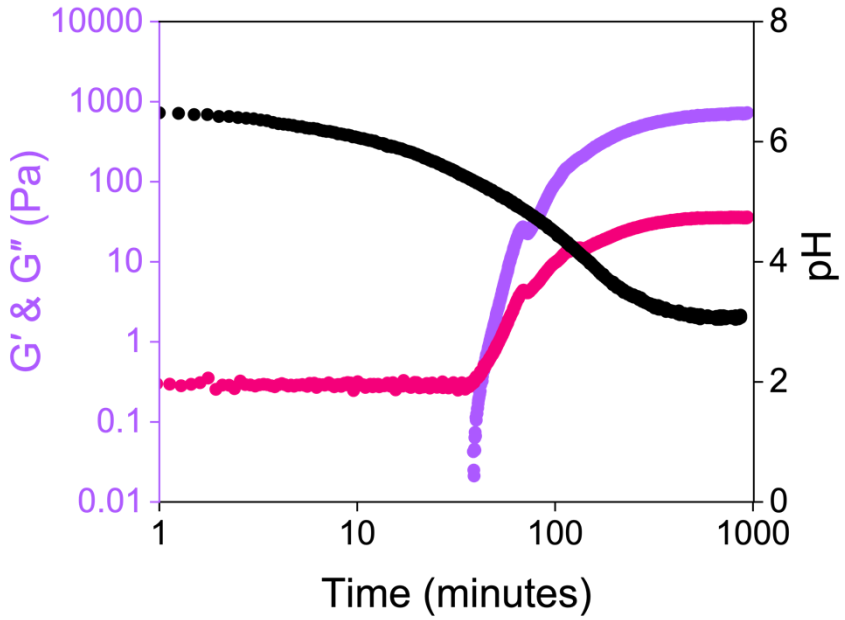

Figure A.3.4. Plots showing the evolution of the gel networks of **PBI-A/PEO** 50/50 blends with an initial pH of 6. The graph shows the development of G′ (purple) and G″ (pink) with time and change in pH (black).

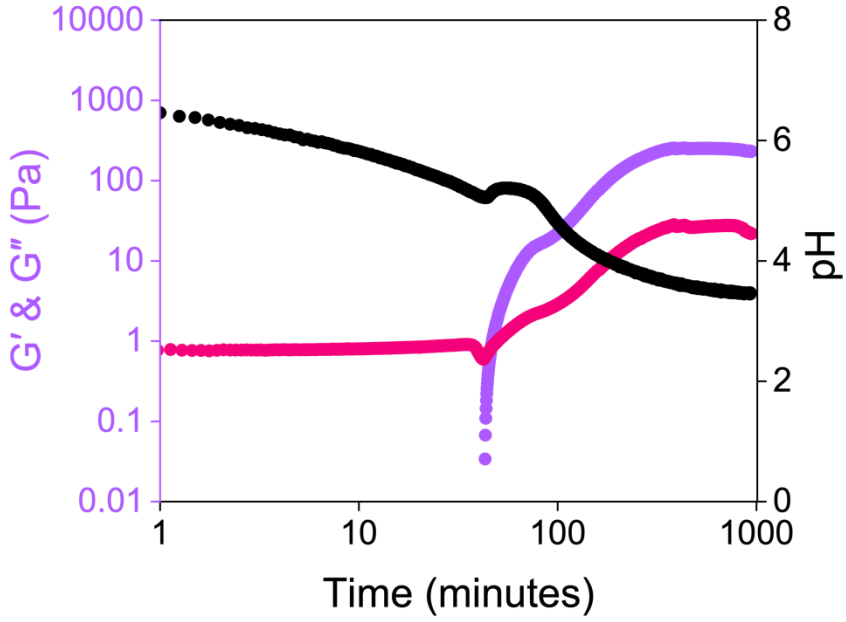

Figure A.3.5. Plots showing the evolution of the gel networks of **PBI-A/PEO** 50/50 blends with an initial pH of 9. The graph shows the development of G′ (purple) and G″ (pink) with time and change in pH (black).

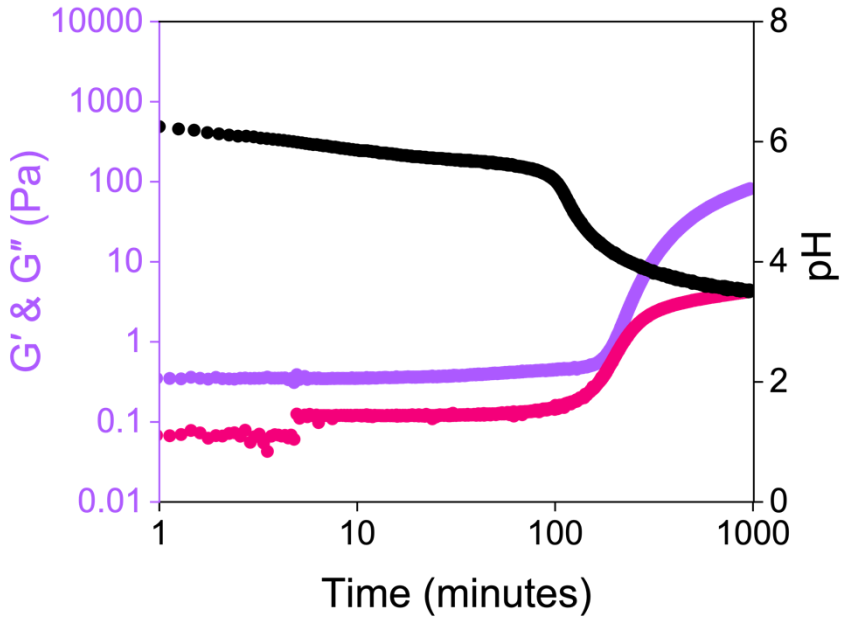

Figure A.3.6. Plots showing the evolution of the gel networks of **PBI-A/PEO** 75/25 blends with an initial pH of 6. The graph shows the development of G′ (purple) and G″ (pink) with time and change in pH (black).

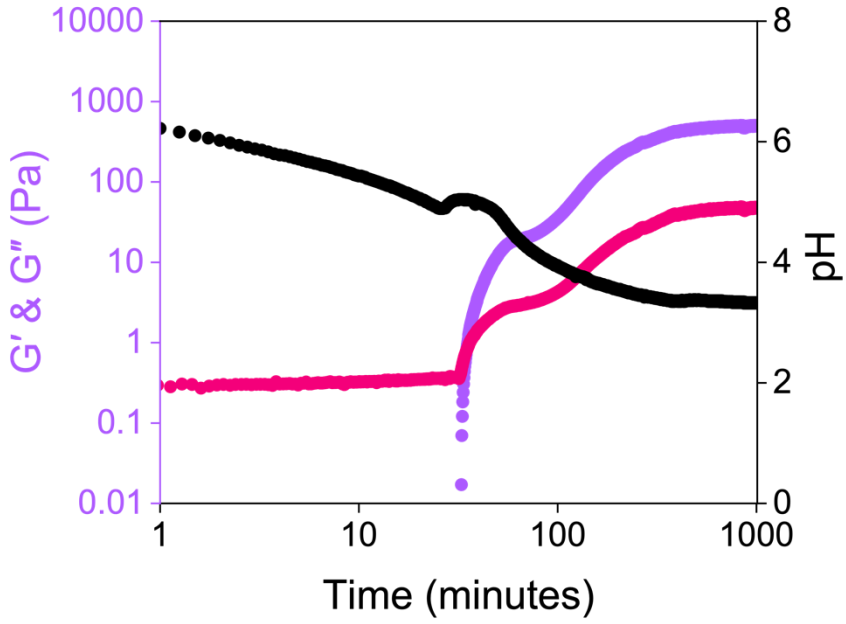

Figure A.3.7. Plots showing the evolution of the gel networks of **PBI-A/PEO** 75/25 blends with an initial pH of 9. The graph shows the development of G′ (purple) and G″ (pink) with time and change in pH (black).

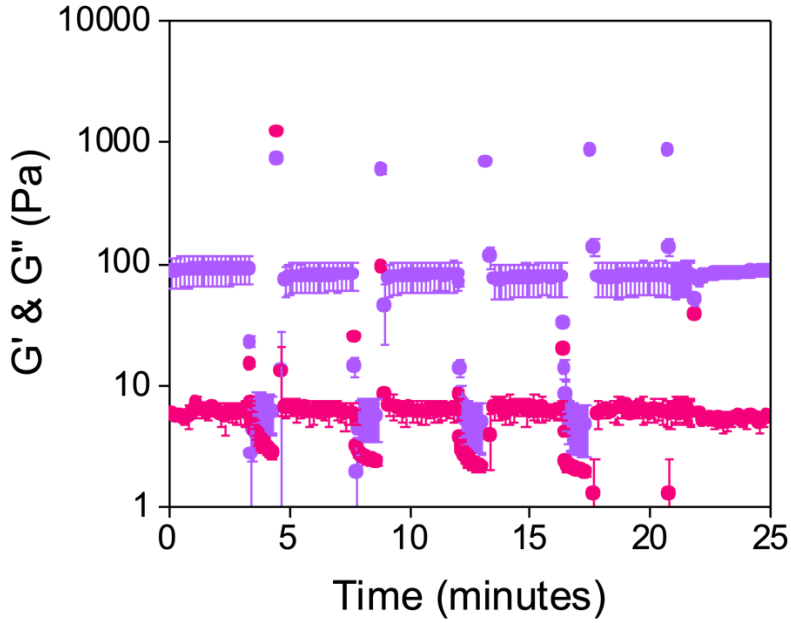

Figure A.3.8. Rheological recovery test for gels made from a **PBI-A** solution starting at pH 6. The gels were subjected to a constant frequency of 10 rad/s and a strain of 0.5% for 200 seconds followed by a higher strain of 300% for 60 seconds. These cycles were repeated five times. Purple circles represent G′ and pink circles represent G″. Data shown are averaged data for triplicate runs of the samples, with error bars representing standard deviation.

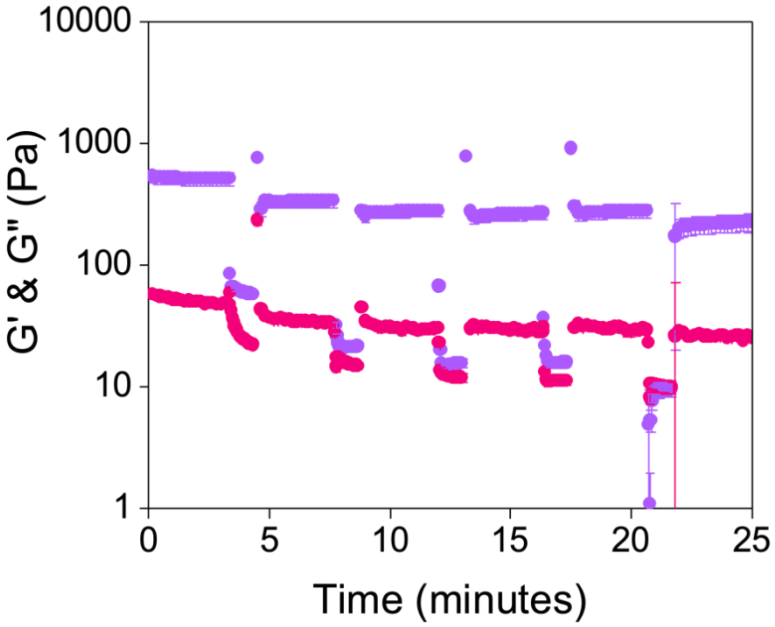

Figure A.3.9. Rheological recovery test for gels made from a 25/75 **PBI-A/PEO** blend starting at pH 6. The gels were subjected to a constant frequency of 10 rad/s and a strain of 0.5% for 200 seconds followed by a higher strain of 300% for 60 seconds. These cycles were repeated five times. Purple circles represent G′ and pink circles represent G″. Data shown are averaged data for triplicate runs of the samples, with error bars representing standard deviation.

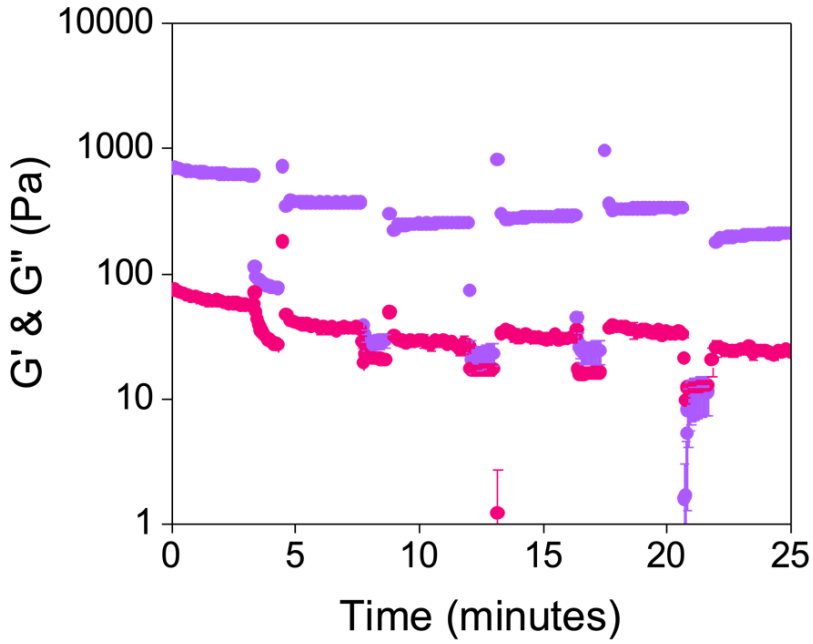

Figure A.3.10. Rheological recovery test for gels made from a 50/50 **PBI-A/PEO** blend starting at pH 6. The gels were subjected to a constant frequency of 10 rad/s and a strain of 0.5% for 200 seconds followed by a higher strain of 300% for 60 seconds. These cycles were repeated five times. Purple circles represent G′ and pink circles represent G″. Data shown are averaged data for triplicate runs of the samples, with error bars representing standard deviation.

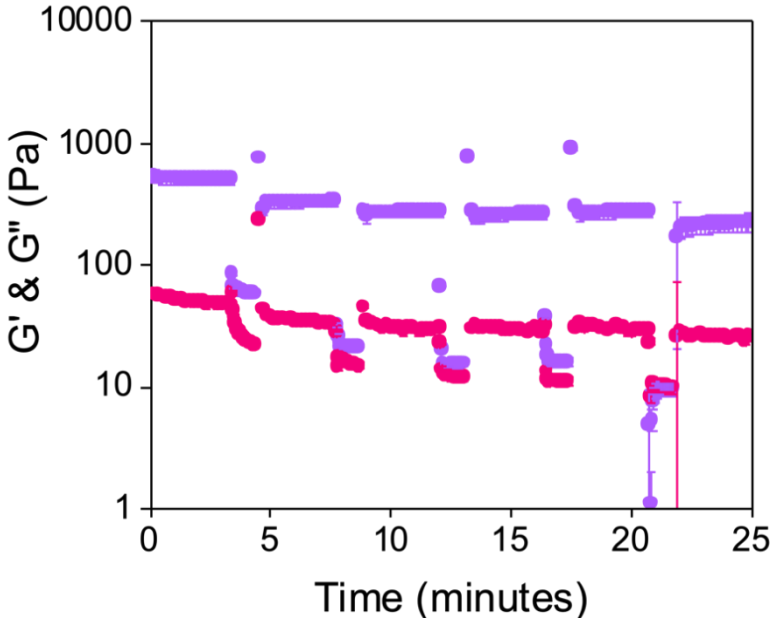

Figure A.3.11. Rheological recovery test for gels made from a 75/25 **PBI-A/PEO** blend starting at pH 6. The gels were subjected to a constant frequency of 10 rad/s and a strain of 0.5% for 200 seconds followed by a higher strain of 300% for 60 seconds. These cycles were repeated five times. Purple circles represent G′ and pink circles represent G″. Data shown are averaged data for triplicate runs of the samples, with error bars representing standard deviation.

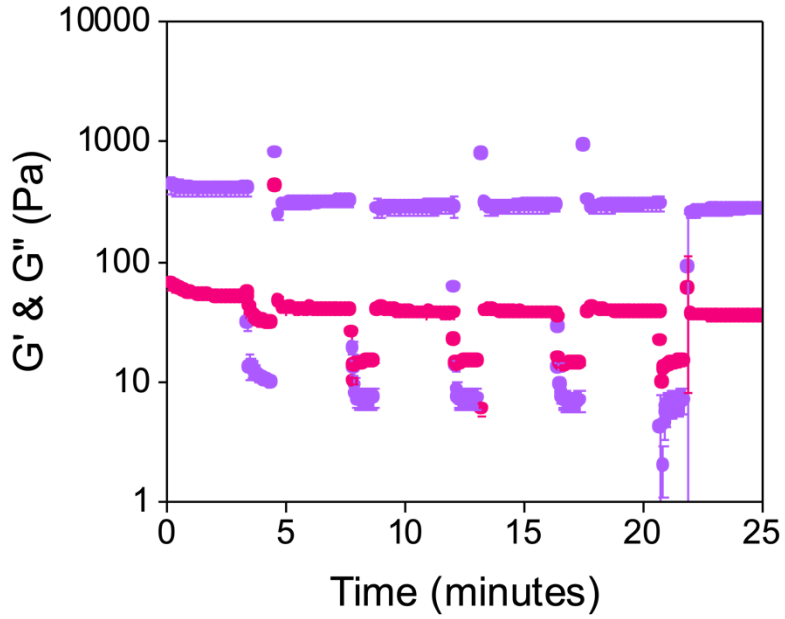

Figure A.3.12. Rheological recovery test for gels made from a **PBI-A** solution starting at pH 9. The gels were subjected to a constant frequency of 10 rad/s and a strain of 0.5% for 200 seconds followed by a higher strain of 300% for 60 seconds. These cycles were repeated five times. Purple circles represent G′ and pink circles represent G″. Data shown are averaged data for triplicate runs of the samples, with error bars representing standard deviation.

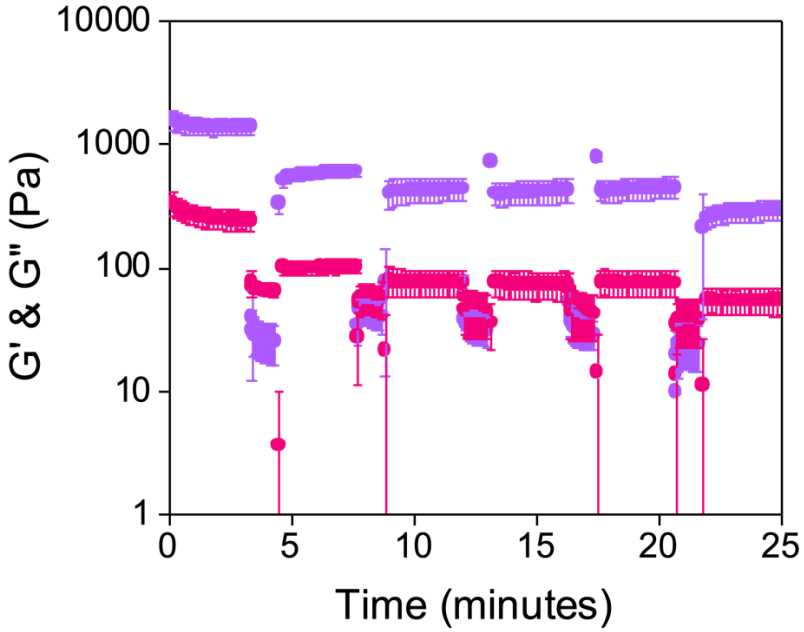

Figure A.3.13. Rheological recovery test for gels made from a 25/75 **PBI-A/PEO** blend starting at pH 9. The gels were subjected to a constant frequency of 10 rad/s and a strain of 0.5% for 200 seconds followed by a higher strain of 300% for 60 seconds. These cycles were repeated five times. Purple circles represent G′ and pink circles represent G″. Data shown are averaged data for triplicate runs of the samples, with error bars representing standard deviation.

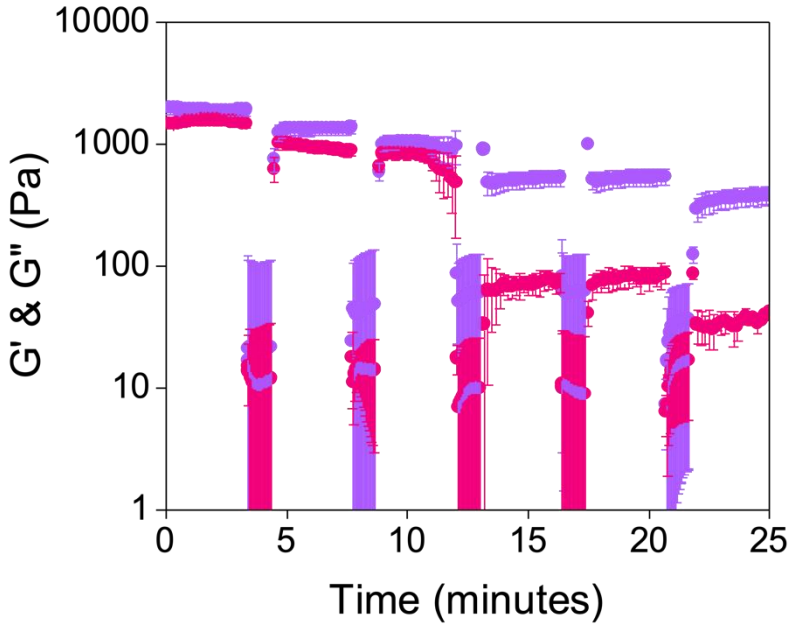

Figure A.3.14. Rheological recovery test for gels made from a 50/50 **PBI-A/PEO** blend starting at pH 9. The gels were subjected to a constant frequency of 10 rad/s and a strain of 0.5% for 200 seconds followed by a higher strain of 300% for 60 seconds. These cycles were repeated five times. Purple circles represent G′ and pink circles represent G″. Data shown are averaged data for triplicate runs of the samples, with error bars representing standard deviation.

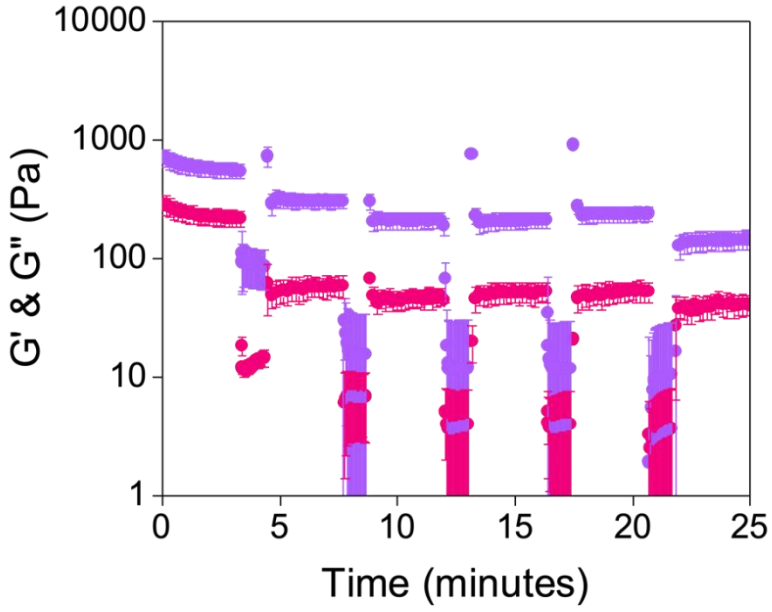

Figure A.3.15. Rheological recovery test for gels made from a 75/25 **PBI-A/PEO** blend starting at pH 9. The gels were subjected to a constant frequency of 10 rad/s and a strain of 0.5% for 200 seconds followed by a higher strain of 300% for 60 seconds. These cycles were repeated five times. Purple circles represent G′ and pink circles represent G″. Data shown are averaged data for triplicate runs of the samples, with error bars representing standard deviation.

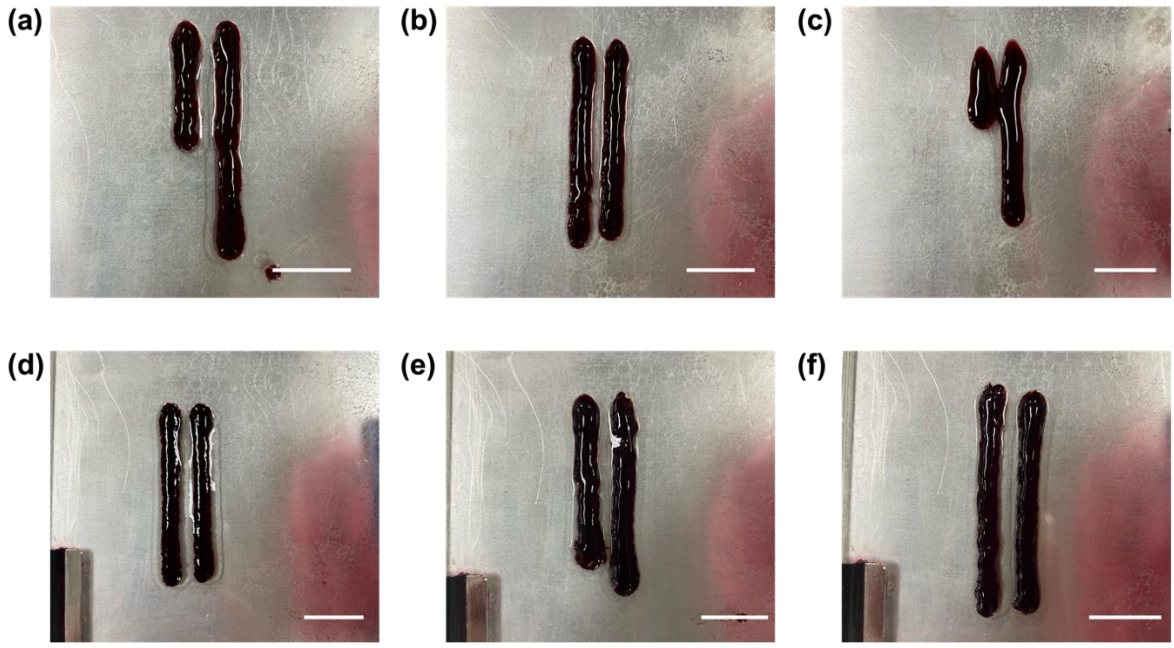

Figure A.3.16. Photographs of printed gels from **PBI-A/PEO** (a) and (d) 25/75, (b) and (e) 50/50 and (c) and (f) 75/25 blends with an initial pH of (a)-(c) 6 and (d)-(f) 9. Gels were printed at a total volume of 1000 μL, an accessory height of 3 cm, and a printing speed of 9408 mm/min. Scale bars represent 2 cm.

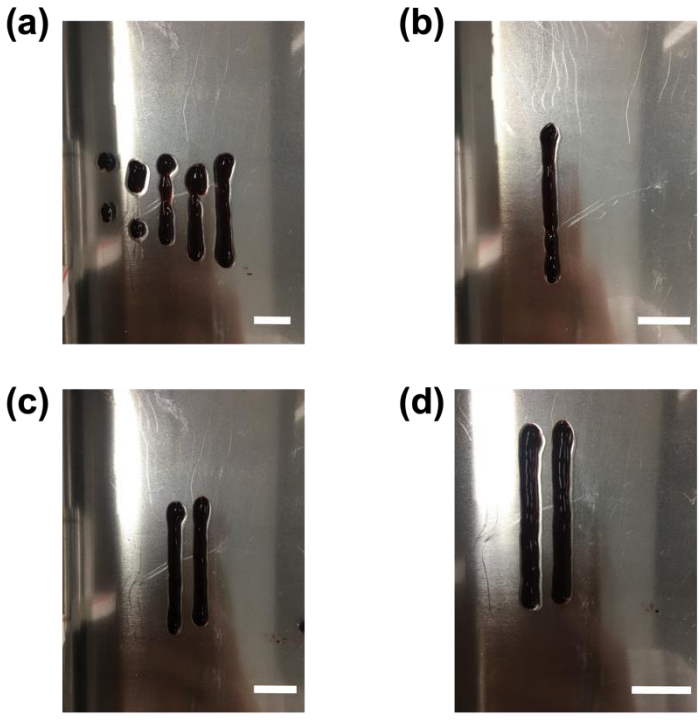

Figure A.3.17. Photographs of **Printed Gel-1** hydrogels printed at a total volume of (a) from left to right, 100, 200, 300, 400, and 500 μL; (b) 600 μL; (c) from left to right, 700 and 800 μL; and (d) from left to right, 900 and 1000 μL. An accessory height of 3 cm and a speed of 9408 mm/min was used for all prints. Scale bars represent 2 cm.

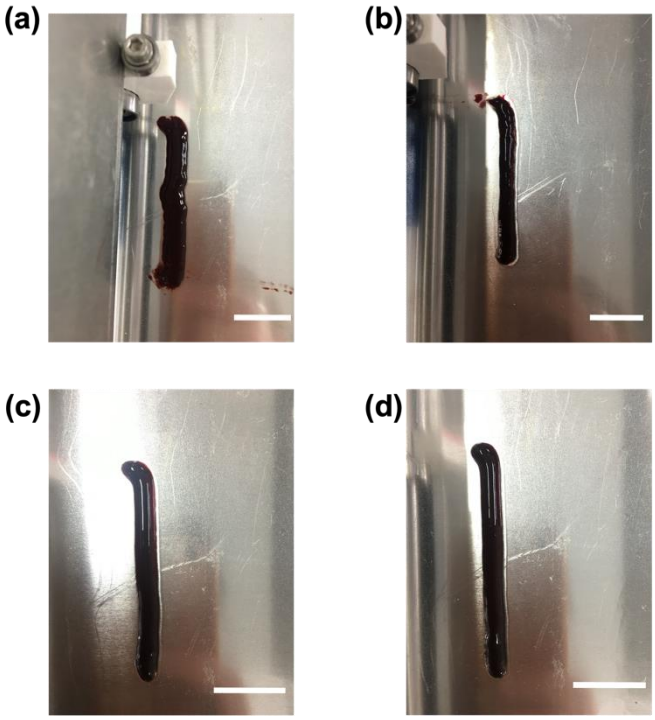

Figure A.3.18. Photographs of **Printed Gel-1** hydrogels printed at an accessory height of (a) 1 cm, (b) 2 cm, (c) 3 cm, and (d) 4 cm from the printing bed. A total volume of 1000 μL and a speed of 9408 mm/min was used for all prints. Scale bars represent 2 cm.

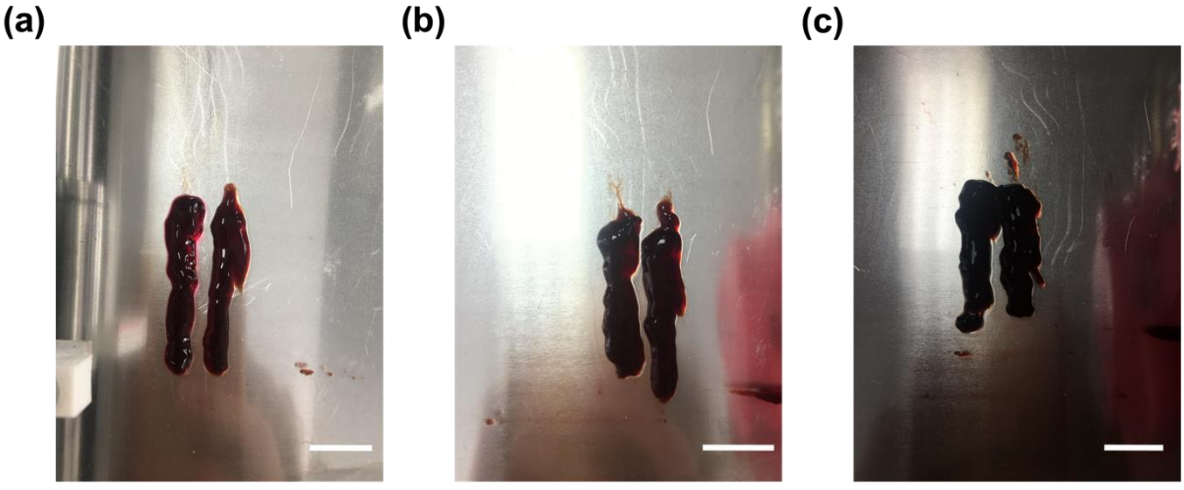

Figure A.3.19. Photographs of printed **Gel-1** hydrogels with a **PBI-A** concentration of (a) 10 mg/mL, (b) 15 mg/mL, and (c) 20 mg/mL. The concentration of **PEO** remained at 5 mg/mL in each blend. Hydrogels were printed at a total volume of 1000 μL, an accessory height of 3 cm, and a speed of 9408 mm/min. Scale bars represent 2 cm.

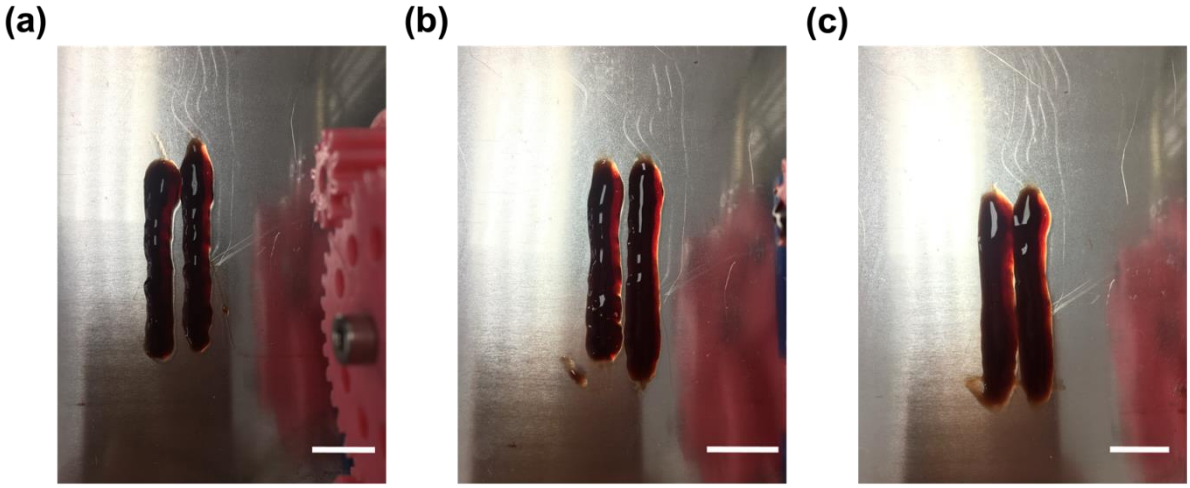

Figure A.3.20. Photographs of printed **Gel-1** gels with a **PEO** concentration of (a) 10 mg/mL, (b) 15 mg/mL, and (c) 20 mg/mL. The concentration of **PBI-A** remained at 5 mg/mL in each blend. Hydrogels were printed at a total volume of 1000 μL, an accessory height of 3 cm, and a speed of 9408 mm/min. Scale bars represent 2 cm.

Table A.3.5. Concentrations of glucono-δ-lactone required to form hydrogels from 25/75 **PBI-A/PEO** solutions starting at pH 9 with different concentrations of **PBI-A** with a final pH of approximately 3.2. pH data shown are averaged data for triplicate samples, with error bars representing standard deviation.

PBI-A concentration (mg/mL)	**GdL concentration (mg/mL)**	**Average pH**
5	12.5	3.29 ± 0.010
10	12.5	3.24 ± 0.010
15	15	3.23 ± 0.005
20	15	3.26 ± 0.005

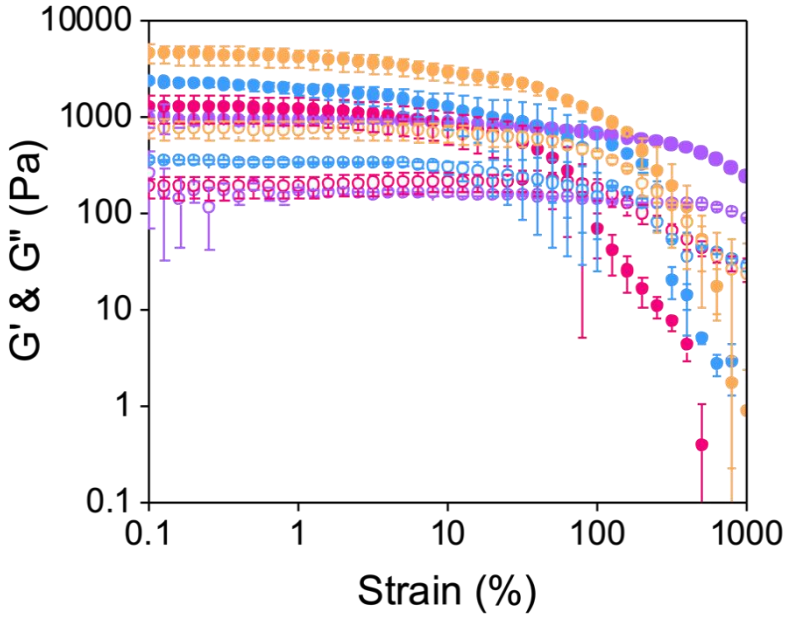

Figure A.3.21 Strain sweep of **Gel-1** hydrogels with different concentrations of **PBI-A**. Blends were made with PBI concentrations of 5 mg/mL (purple), 10 mg/mL (pink), 15 mg/mL (blue), and 20 mg/mL (orange), with the concentration of **PEO** remaining 5 mg/mL in each blend. Closed circles represent G′ and open circles represent G″. Strain sweeps were performed at a frequency of 10 rad/s at 25°C. Data shown are averaged data for triplicate runs of the samples, with error bars representing standard deviation.

Table A.3.6. Table highlighting the rheological properties of **Gel-1** with different concentrations of **PBI-A**. G′ and G″ are quoted at 1% strain. "–" means that the flow point was outwith the strain range of 0.1-1000%.

PBI-A concentration (mg/mL)	**Yield point (%)**	**Flow point (%)**	**G′ (Pa)**	**G″ (Pa)**	**tanδ (G″/G′)**
5	2.5	79.4	1156 ± 172	191 ± 48	0.16
10	25.1	-	893 ± 58	173 ± 9	0.19
15	12.6	-	2283 ± 71	352 ± 17	0.15
20	25.1	-	4493 ± 190	767 ± 165	0.17

Table A.3.7. Concentrations of glucono-δ-lactone required to form hydrogels from 25/75 **PBI-A/PEO** solutions starting at pH 9 with different concentrations of **PEO** with a final pH of approximately 3.2. pH data shown are averaged data for triplicate samples, with errors representing standard deviation.

PEO concentration (mg/mL)	GdL concentration (mg/mL)	Average pH
5	12.5	3.29 ± 0.010
10	8	3.28 ± 0.005
15	10	3.30 ± 0.010
20	10	3.27 ± 0.005

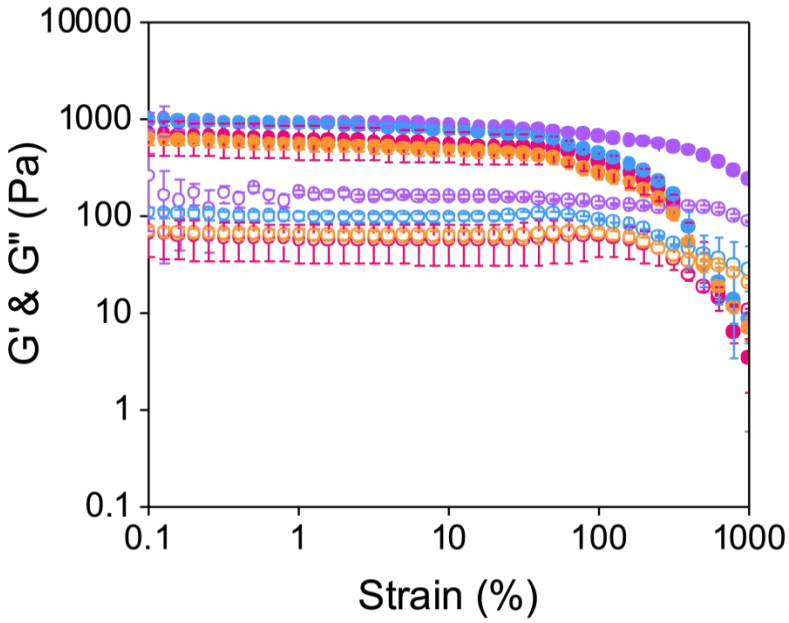

Figure A.3.22. Strain sweep of **Gel-1** hydrogels with different concentrations of **PEO**. Blends were made with **PEO** concentrations of 5 mg/mL (purple), 10 mg/mL (pink), 15 mg/mL (blue), and 20 mg/mL (orange), with the concentration of **PBI-A** remaining 5 mg/mL in each blend. Closed circles represent G′ and open circles represent G″. Strain sweeps were performed at a frequency of 10 rad/s at 25°C. Data shown are averaged data for triplicate runs of the samples, with error bars representing standard deviation.

Table A.3.8. Table highlighting the rheological properties of **Gel-1** with different concentrations of **PEO**. G′ and G″ are quoted at 1% strain.

PBI-A concentration (mg/mL)	Yield point (%)	Flow point (%)	G′ (Pa)	G″ (Pa)	tanδ (G″/G′)
5	2.5	79.4	1156 ± 172	191 ± 48	0.16
10	12.5	794	611 ± 229	57 ± 24	0.09
15	15.8	501	885 ± 79	98 ± 10	0.11
20	15.8	501	543 ± 68	64 ± 8	0.12

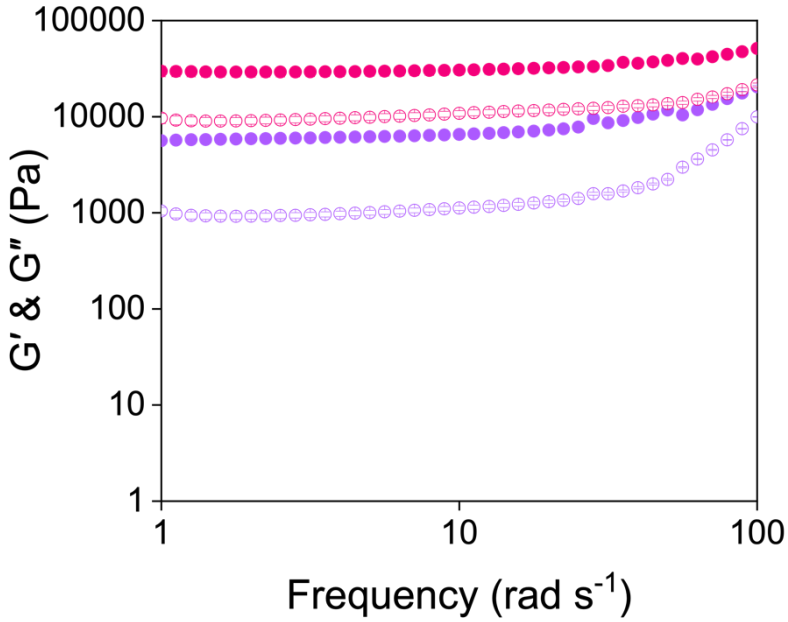

Figure A.3.23. Frequency sweeps of **Gel-1** before (purple) and after (pink) compression. Closed circles represent G′ and open circles represent G″. Frequency sweeps were performed at 0.1% strain at 25°C. Data shown are averaged data for triplicate runs of the samples, with error bars representing standard deviation.

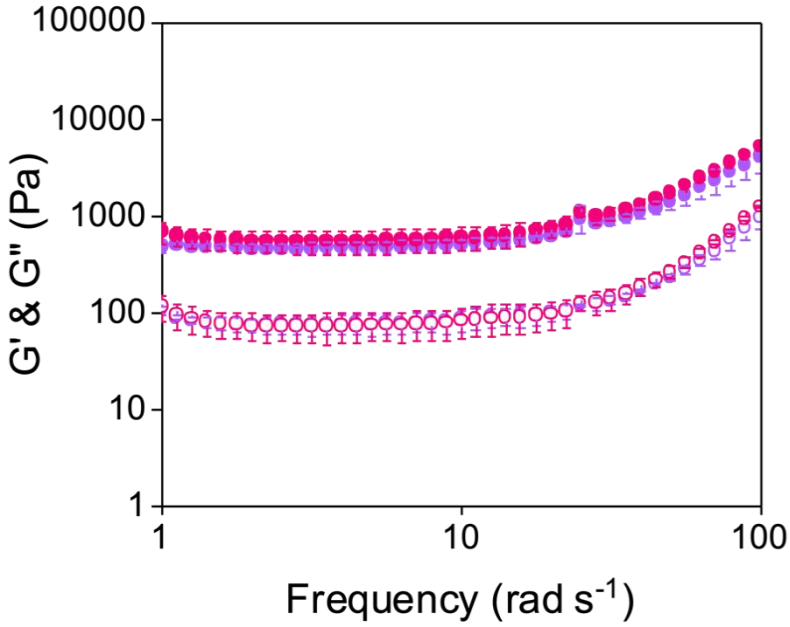

Figure A.3.24. Frequency sweeps of **Gel-1** syringe gels formed at the top (purple) and bottom (pink) of the syringe. Closed circles represent G′ and open circles represent G″. Frequency sweeps were performed at 0.1% strain at 25°C. Data shown are averaged data for triplicate runs of the samples, with error bars representing standard deviation.

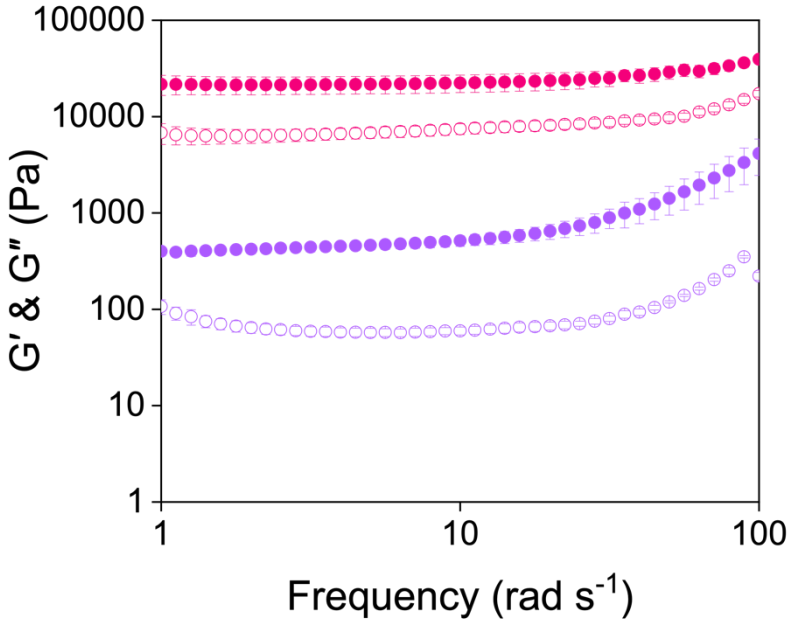

Figure A.3.25. Frequency sweeps of **Gel-1** (purple) and **Printed Gel-1** (pink). Closed circles represent G′ and open circles represent G″. Frequency sweeps were performed at 0.1% strain at 25°C. Data shown are averaged data for triplicate runs of the samples, with error bars representing standard deviation.

Table A.3.9. Reduction and oxidation potentials taken from cyclic voltammograms of 10 mg/mL hydroquinone with 10% 0.1 M NaCl. Cyclic voltammograms were performed in a 1 x 1 cm FTO window set-up. The scan rate of the cyclic voltammograms was 0.5 V/s.

Control	Reduction potential(s) (V)	Oxidation potential (V)
1 x 1 cm FTO window	-1.3, -2.0	0.7

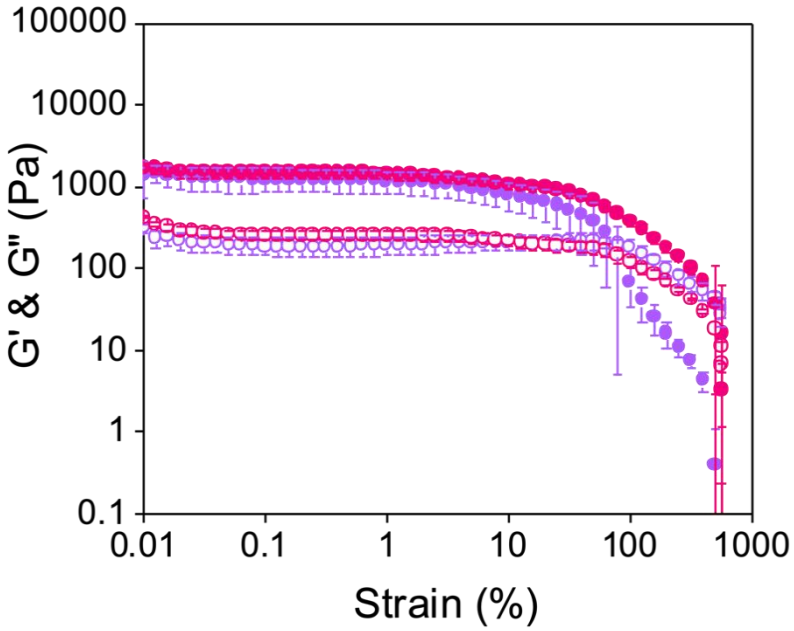

Figure A.3.26. Strain sweep of **Gel-1** without (purple) and with (pink) 1 equivalent of NaCl (0.1 M, aq). Closed circles represent G′ and open circles represent G″. Strain sweeps were performed at a frequency of 10 rad/s at 25°C. Data shown are averaged data for triplicate runs of the samples, with error bars representing standard deviation.

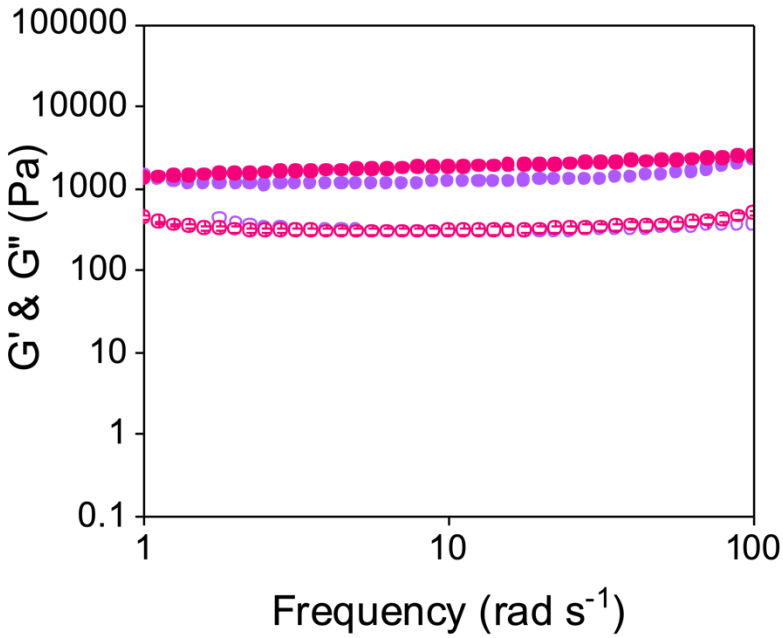

Figure A.3.27. Frequency sweep of **Gel-1** without (purple) and with (pink) 1 equivalent of NaCl (0.1 M, aq). Closed circles represent G′ and open circles represent G″. Frequency sweeps were performed at 0.1% strain at 25°C. Data shown are averaged data for triplicate runs of the samples, with error bars representing standard deviation.

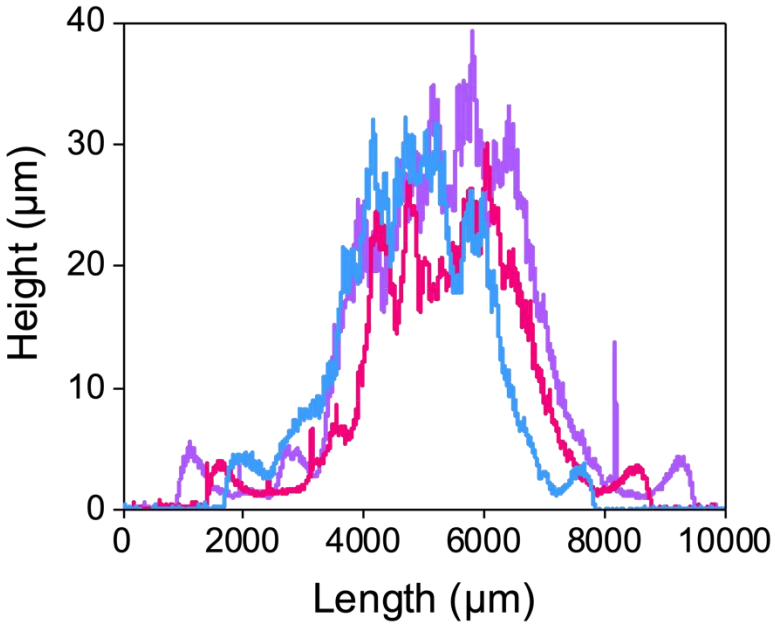

Figure A.3.28. Profilometry profile of **Printed Gel-1** xerogels measured 0.5 cm (purple), 1.0 cm (pink), and 1.5 cm (blue) along the printing axis.

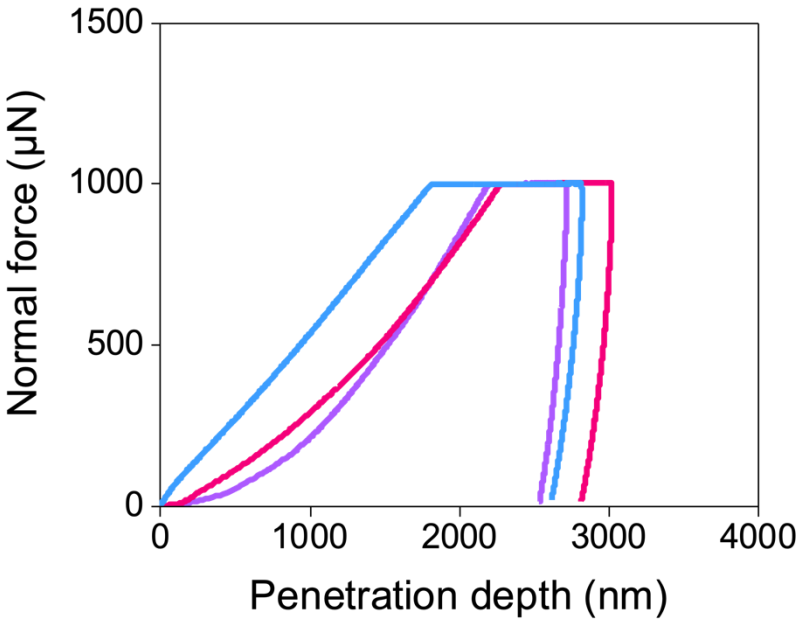

Figure A.3.29. Force-penetration depth curve obtained during nanoindentation of **Printed Gel-1** xerogels measured 0.5 cm (purple), 1.0 cm (pink), and 1.5 cm (blue) along the printing axis.

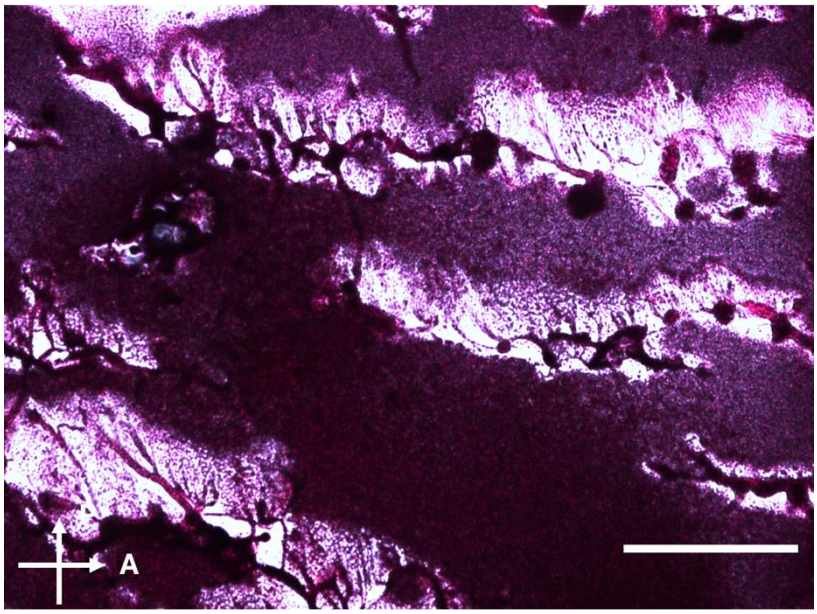

Figure A.3.30. Cross polarised optical microscope images of a **Gel-1** xerogel. Scale bar represents 100 μm.